

Submillimeter Properties of Sagittarius A*:

The Polarization and Spectrum

from 230 to 690 GHz

and the Submillimeter Array Polarimeter

A thesis presented

by

Daniel Patrick Marrone

to

The Department of Astronomy

in partial fulfillment of the requirements

for the degree of

Doctor of Philosophy

in the subject of

Astronomy

Harvard University

Cambridge, Massachusetts

31 August 2006

© 2006, by Daniel Patrick Marrone

All rights reserved.

Advisors: Drs. Raymond Blundell and James M. Moran Daniel Patrick Marrone

**Submillimeter Properties of Sagittarius A*:
The Polarization and Spectrum from 230 to 690 GHz
and the Submillimeter Array Polarimeter**

Abstract

Sagittarius A* is the supermassive black hole at the center of our galaxy; as the nearest example of a low-luminosity active galactic nucleus it provides an excellent opportunity to understand these objects. Submillimeter data are particularly important for examining this source because of the unique polarization and spectral features in this band. In this thesis I report several new observations of the polarization and spectrum of Sgr A* obtained with the Submillimeter Array (SMA).

I present the first measurement of Faraday rotation in Sgr A*. The rotation measure is $(-5.6 \pm 0.7) \times 10^5 \text{ rad m}^{-2}$, restricting the accretion rate to the range 2×10^{-7} to $2 \times 10^{-9} M_{\odot} \text{ yr}^{-1}$. These boundaries jointly increase if the magnetic field is sub-equipartition or disordered. The stability in the rotation measure limits accretion variability to 25%. I find large variations in the linear polarization on timescales of minutes to months, the first measurements of variability on intraday timescales. I report the observation of an interesting polarization variation that may lead to future measurements of the black hole spin. I am also able to identify variations in the intrinsic polarization direction of the source. These results demonstrate the utility of polarization for examining changes very close to the black hole. Finally, I show that the spectrum of Sgr A* peaks around 350 GHz, limiting the luminosity of the source to $200 L_{\odot}$, or $10^{-9} L_E$.

The majority of these results rely on observations obtained with the polarimeter

I constructed for the SMA. I discuss the design and testing of the instrument and its expected performance. I review the principles of interferometric polarimetry, polarization calibration, and the origins of non-ideal response (or “leakage”) in the polarimeter. Extensive calibration observations show that the leakages are extremely stable and exhibit the frequency behavior expected from theory. The precision of the calibration represents a factor-of-several improvement over that attained with the most similar instrument elsewhere; these careful measurements are crucial for other results in this thesis. The polarimeter now operates as a facility instrument of the SMA.

Contents

Abstract	iii
Acknowledgments	x
1 Introduction	1
2 The Submillimeter Array Polarimeter	30
2.1 Introduction	30
2.2 Interferometric Polarimetry	32
2.3 SMA Optical and Polarization Design	34
2.3.1 Optics Overview	34
2.3.2 Polarization Implications	37
2.4 Polarimeter Optics	40
2.4.1 Wave Plate Designs	40
2.4.2 Wave Plate Materials	42
2.4.3 Anti-Reflection Coatings	43
2.5 Positioning Hardware and Control System	47
2.6 Wave Plate Alignment	52
2.6.1 Optical Alignment	52
2.6.2 Polarization Alignment	56
2.6.3 Fast Axis Verification	57
2.7 Polarization Observations	58

2.7.1	Polarization Switching	58
2.7.2	Sensitivity	63
2.8	Future Modifications to the SMA Polarimeter	64
3	Polarization Calibration	67
3.1	Introduction	67
3.2	Interferometer Polarization Response	68
3.3	Leakage Calibration Observations	72
3.4	Wave Plate Cross-Polarization	77
3.5	Leakage Measurements	81
3.5.1	Leakage Variability	82
3.5.2	Frequency Dependence	88
3.6	Modified Polarization Response	92
3.6.1	Antenna Polarization	92
3.6.2	Impact of the Antenna Polarization	99
3.7	Astronomical Verification	102
4	Sgr A*: Variable 340 GHz Linear Polarization	104
4.1	Introduction	105
4.2	Observations	109
4.3	Results	114
4.3.1	Linear Polarization	114
4.3.2	Circular Polarization	119
4.3.3	Intraday Variability	120
4.4	Discussion	122
4.4.1	Rotation Measure	122
4.4.2	Accretion Rate Constraints	126
4.4.3	Linear Polarization and Variability	132

4.5	Conclusions	138
5	Sgr A*: Rotation Measure	141
5.1	Introduction	142
5.2	Observations	144
5.3	Rotation Measure and Intrinsic Polarization	148
5.4	Discussion	151
6	Sgr A*: Submillimeter Spectrum	155
6.1	Introduction	155
6.2	Observations and Results	157
6.3	Comparison with Previous Observations	161
6.3.1	Simultaneous Spectra	161
6.3.2	High-Frequency Photometry	165
6.3.3	Angular-Size Measurements	166
6.4	Discussion	167
7	Sgr A*: Light Curves	172
7.1	Introduction	172
7.2	Observations and Calibration	174
7.3	Light Curves	179
7.4	Variability Properties	195
7.5	Polarization Orbits	198
7.5.1	Flares and Polarization Light Curves	198
7.5.2	Future Prospects	200
8	Conclusions	204
A	SMA Polarimetry System	218

<i>CONTENTS</i>	viii
A.1 Hardware Components	218
A.1.1 Commercially Available Components	218
A.2 Wave Plates	219
A.2.1 Wave Plate Specifications	219
A.2.2 Anti-Reflection Coating Specifications	221
A.2.3 Vendors	221
A.2.4 Measured Coating Properties	223
A.3 Software Interface	223
B Optimal Walsh Functions	228
C Light Curve Data	234
C.1 Raw Data	234
C.2 $Q-U$ Light Curves	245
References	255

To Nicole and the rest of my family

Acknowledgments

It has been my great fortune to have Ray Blundell as my advisor since early in my first year of graduate school. Ray has directed me toward multiple interesting paths, given me support to pursue them, and constantly contributed scientific and general advice to keep me moving along. I have never wanted for opportunities, resources, or attention as his student. Although Jim Moran has been my advisor for a shorter period of time, he has been influencing my course since my first months here. It was his suggestion that led me to meet with Ray and join the Submillimeter Receiver Lab. In my second year, his excited talk on new results from a Galactic center workshop later created the polarimeter project and led to this thesis. He has been my mentor as I've tried to understand and relate the results of my measurements and to devise new experiments. He has been the origin of any scientific judgement I've developed in the last few years.

My time working in the Receiver Lab has been enormously beneficial to me. Although I have experienced several other labs, I have never before found a group of people so uniformly helpful, curious, creative, and interested. I've worked most closely with Scott Paine and Cosmo Papa, both of whom have generously shared their expertise and vast experience to make up for my lack of both. Everyone else in the lab (Jack Barrett, Todd Hunter, Robert Kimberk, Steve Leiker, Pat Riddle, Mike Smith, Edward Tong, Bob Wilson, the well-missed Hugh Gibson, and the predocs Denis Meledin, Denis Loudkov, and Sergey Ryabchun) has also contributed to my work, thoughts, knowledge, and happiness in individual interactions and through the general atmosphere of the lab. Ramprasad Rao, Ken Young, and Jun-Hui Zhao have

collaborated closely with me and been similarly giving of their time and knowledge.

My fellow graduate students have greatly improved my time at Harvard. Jenny Greene has been my officemate throughout and has been an unfailingly loyal and supportive friend. Brant Robertson has filled a similar role, although his chair has been located at least 15 feet further away. Jenny and Brant have enhanced my understanding of many areas of astronomy, provided what little information I retain in many others, and probably influenced my thinking in many ways that I'm not even aware of. Other students have also made my graduate experience happy and instructive including Yosi Gelfand, Craig Heinke, Maryam Modjaz, and Scott Schnee.

I thank my family for following along as I bounced from telescope to telescope and putting up with the increasingly short visits Nicole and I could make to Minnesota as we moved through graduate school. Of course, there's a long history of encouragement and interest from all of them that precedes the few years of work represented here. Finally, I must acknowledge my innermost circle of family, my wife Nicole and our dearly departed dog, Rukh. Nicole has propped me up for a very long time now, and since our second year here she has had to do this via long-distance telephone calls more often than either of us would like. The last two months of thesis writing demonstrated quite starkly the degree to which I depend on her constant support. Rukh spent many nights sleeping on my feet while I completed this work and in that way he is imprinted throughout.

Chapter 1

Introduction

The study of nuclear black holes is currently a very active area of research. The observation of a correlation between the mass of a black hole and the properties of its host galaxy, particularly the velocity dispersion of the spherical component (Gebhardt et al. 2000; Ferrarese & Merritt 2000), has sparked a wide variety of investigations of black hole properties in high and low accretion states, at large and small masses, at low and high redshift. The origin of the surprising connection between a galaxy's structure and the dynamically insignificant mass concentration at its center can now be scrutinized with powerful numerical simulations (Springel et al. 2005). Quasars at the edge of the universe are being used as backlights for the interstellar medium (Fan et al. 2006) and tests of structure formation models (Li et al. 2006), while their hosts are being examined by powerful telescopes (Walter et al. 2003).

The nearest supermassive black hole, located in our own galaxy, is also receiving great attention. 100 times closer than its nearest neighbor, it allows access to detail

on scales that cannot be observed in any other galaxy. It is the best available testbed for general relativity in the strong gravity limit (Broderick & Loeb 2006c). It provides a proving ground for models of accretion physics, in particular in the very low accretion state that likely dominates the life cycle of these objects. It even shows the stellar and gaseous vestiges of its more active past (Morris et al. 1999). Here I outline some highlights in the development of our understanding of this important object.

A Compact Mass

In February 1974, Balick & Brown (1974) detected a compact (sub-arcsecond) radio source in the center of the Milky Way at frequencies of 2.7 and 8.1 GHz. Subsequent connected-element and very-long-baseline interferometric (VLBI) observations (Lo et al. 1975; Davies et al. 1976; Kellermann et al. 1977) at multiple frequencies indicated that the angular size of Sgr A* varied like ν^{-2} as expected from foreground scattering (Davies et al. 1976). The possibility that the size of the underlying source might be less than the observed sizes, which were much too large to be a black hole of plausible mass, caused Kellermann et al. (1977) to mention the possibility that the radio source might harbor a black hole. These authors pointed to the “ingenious hypothesis” of Lynden-Bell (1969) (a quote from the *Nature* News and Views commentary on Lynden-Bell’s article) that there may be a “dead quasar” at the center of the Milky Way.

Confirmation of the presence of a black hole, or a very compact mass, had to wait for many more years. Genzel & Townes (1987) marshalled the available

dynamical indicators (H I, ionized gas, stellar velocity dispersions) to suggest that the enclosed mass may approach a constant value inside 1 pc ($25''$, or 3×10^6 Schwarzschild radii for a $3.5 \times 10^6 M_{\odot}$ black hole at 8.0 kpc). However, it was the advent of diffraction-limited near-infrared imaging techniques in the mid-1990s that finally solidified the case for a black hole in Sgr A*. Beginning in 1992, Eckart & Genzel (1996, 1997) used the 3-meter New Technology Telescope (NTT) to make diffraction-limited $2.2 \mu\text{m}$ images ($0.15''$ resolution) of the Galactic center through the shift-and-add speckle imaging technique. This was followed in 1995 by Ghez et al. (1998) with the 10-meter Keck I telescope, achieving $0.05''$ ($5800 r_S$) resolution. Repeated observations of the inner few arcseconds yielded proper motion measurements for tens of stars. No strong infrared source clearly identifiable as Sgr A* was detected in these images. Careful registration of the radio frame (where Sgr A* is readily identifiable at high-angular resolution) and the NIR frame, through the alignment of SiO and H₂O masers detected at radio frequencies and host stars seen in IR images (Menten et al. 1997), nevertheless allowed measurements of the distribution of two-dimensional velocity dispersions relative to Sgr A*. From the radial variation of the velocity dispersion, these groups inferred the enclosed mass distribution down to a radius of 0.01 pc ($0.25''$, $3 \times 10^4 r_S$). The distribution showed a constant mass of $2.6 \times 10^6 M_{\odot}$ at radii smaller than 0.1 pc, suggesting a dense object confined to a region smaller than 0.01 pc (Figure 1.1, *left*).

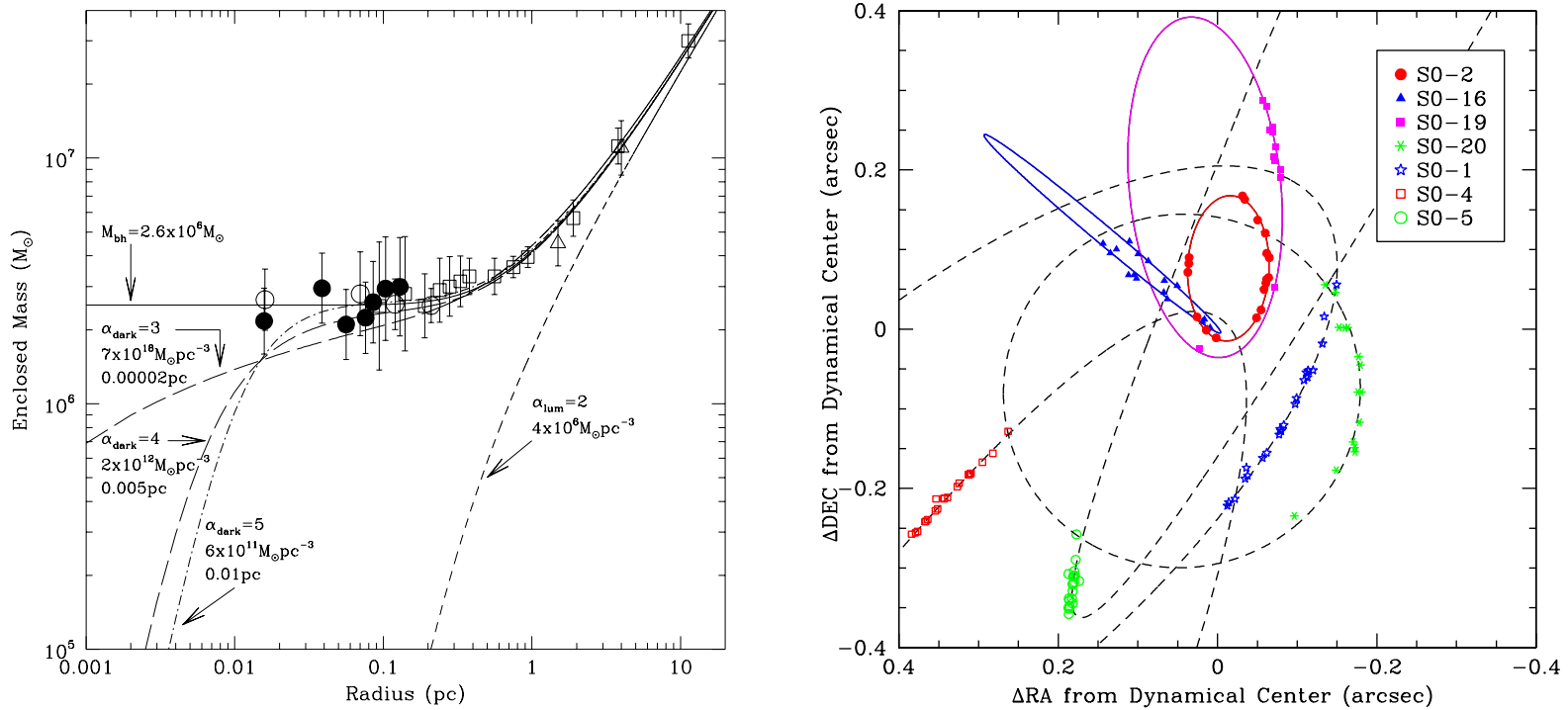


Fig. 1.1.— (*Left*): The enclosed mass as a function of projected distance from Sgr A*, based on NIR observations of stellar proper motions and radial velocities, and millimeter observations of molecular gas motions. Proper motion data are from Eckart & Genzel (1996, 1997), and Ghez et al. (1998), and are shown as open and filled circles. NIR radial velocity data from Genzel et al. (1996) are shown as open squares. The open triangles are from the millimeter data of Guesten et al. (1987). In addition to the constant mass fit (solid line), various cluster profiles described in Ghez et al. (1998) are also plotted. This figure appeared as Figure 7 in Ghez et al. (1998). (*Right*): Positions and orbital fits for seven stars in the Galactic center, Figure 2 of Ghez et al. (2005a). The positions were obtained between 1995 and 2003 using the Keck telescopes.

The conversion of one- and two-dimensional positions and velocity dispersions into enclosed mass measurements requires assumptions about the unknown phase space coordinates of the test particles. These assumptions are particularly prone to systematic error at small radii where the number of stars is limited. Fortunately, after several years of observations Ghez et al. (2000) detected acceleration (later confirmed by Eckart et al. 2002) in the proper motions of the closest stars. With the addition of radial velocity measurements (Schödel et al. 2003; Ghez et al. 2003; Eisenhauer et al. 2005), full orbital solutions became possible for the innermost stars, allowing direct measurement of the position and mass of the central object. The projected orbits of seven stars are shown in Figure 1.1 (*right*). Orbital solutions showed that the star with the closest known approach (S0-16) reached 0.0002 pc in 1999 (Ghez et al. 2005a), restricting the central mass to a region $600r_s$ in radius and excluding most alternatives to a black hole. As of April 2006, the two groups had converged on a mass of $3.6 \pm 0.2 \times 10^6 M_\odot$ for Sgr A* (Genzel et al., Ghez et al., in prep.) located precisely at the position of the radio source (to within the measurement error of 15 mas). An independent confirmation of the association of the radio source with a large, compact mass was provided by the lack of proper motion in Sgr A* (Reid & Brunthaler 2004).

Throughout this work I have adopted a mass of $3.5 \times 10^6 M_\odot$ for Sgr A*, in fortuitous agreement with the value eventually settled upon by the competing groups observing IR orbits. The corresponding Schwarzschild radius ($r_s = 2GM/c^2$) is 1.03×10^{12} cm, or 0.069 AU, or 34 light seconds. The orbital determinations from the NIR imaging and spectroscopy also provide a direct measurement of the distance to the Galactic center. At the recent (April 2006) Galactic Center Workshop, the two

groups reported a consensus distance of 7.4 ± 0.2 kpc (Lu et al. 2006; Trippe et al. 2006). Nevertheless, throughout this thesis I have adopted a distance of 8.0 kpc, the value suggested by Reid (1993) from a variety of different types of measurements, which has been the standard value over the past decade. At 8 kpc, the angular size of $1r_S$ is $8.6 \mu\text{as}$ and $1''$ corresponds to 0.039 pc or $1.16 \times 10^5 r_S$.

Source Structure

Although the mass measurements go a long way toward describing the space-time around the black hole powering Sgr A*, the emission structures that form the radio source Sgr A* must also be understood. Various classes of models for the emission from Sgr A* have been proposed, including a thin accretion disk (Zylka et al. 1992; Falcke et al. 1993a), analogues of the jets observed in external galaxies (Falcke et al. 1993b), and quasi-spherical accretion flows (Narayan & Yi 1994; Narayan et al. 1995). These models would be expected to present different (frequency-dependent) morphologies at the high angular resolution afforded by VLBI observations. Moreover, even the tightest constraints yet achieved on the size of the compact mass through IR stellar orbits (Ghez et al. 2005a) are several hundred Schwarzschild radii, not yet providing evidence of the general relativistic effects expected around a black hole. These questions continue to provide a compelling case for the pursuit of technically challenging VLBI observations.

Unfortunately, as mentioned above, the radio image of Sgr A* was found to be broadened by interstellar scattering (Davies et al. 1976). As VLBI observations pushed to higher frequencies, the ν^{-2} variation of the angular size was observed up

to 43 GHz (Lo et al. 1981, 1985; Alberdi et al. 1993; Backer et al. 1993; Bower & Backer 1998). Lo et al. (1998) compiled the observations to show an axial ratio of very nearly 2 in the scatter-broadened image, with the major axis position angle around 80° . The orientation is unfavorable because the VLBA (and other millimeter antennas) are predominantly located at northerly latitudes, resulting in projected baselines that are much longer (and provide much higher angular resolution) in the E–W direction, along the major axis. Because the minor axis (N–S) is less scattered, it should more easily show the deviations from ν^{-2} size variation that would be evidence of intrinsic structure. In fact, Lo et al. (1998) claimed to detect such deviations at 43 GHz along the minor axis, a claim that cannot be substantiated after more careful data analysis (Bower et al. 2004). VLBI observations have been extended to 86 GHz (Rogers et al. 1994; Krichbaum et al. 1998; Doeleman et al. 2001; Shen et al. 2005), and even one inconclusive one-baseline 215 GHz observation (Krichbaum et al. 1998). Even at these frequencies deviations from the scattering law, if any, are very small. Extrapolation of the major-axis scattering size predicts that the scattering diameter will be larger than $2r_S$ until 270 GHz (180 GHz for the minor axis), so scattering remains the dominant contributor to the measured size at all available frequencies. Recent measured sizes are shown in Figure 1.2.

The intrinsic source size is derived from the observed size through quadrature subtraction of the extrapolated scattering size, so the derived sizes are strongly dependent on the form and normalization of the scattering extrapolation. The exponent of the frequency dependence can be determined to be very close to -2 from the data (e.g. Bower et al. 2004). However, if the density variations in the scattering screen have a bounded power-law spectrum (e.g. the Kolmogorov

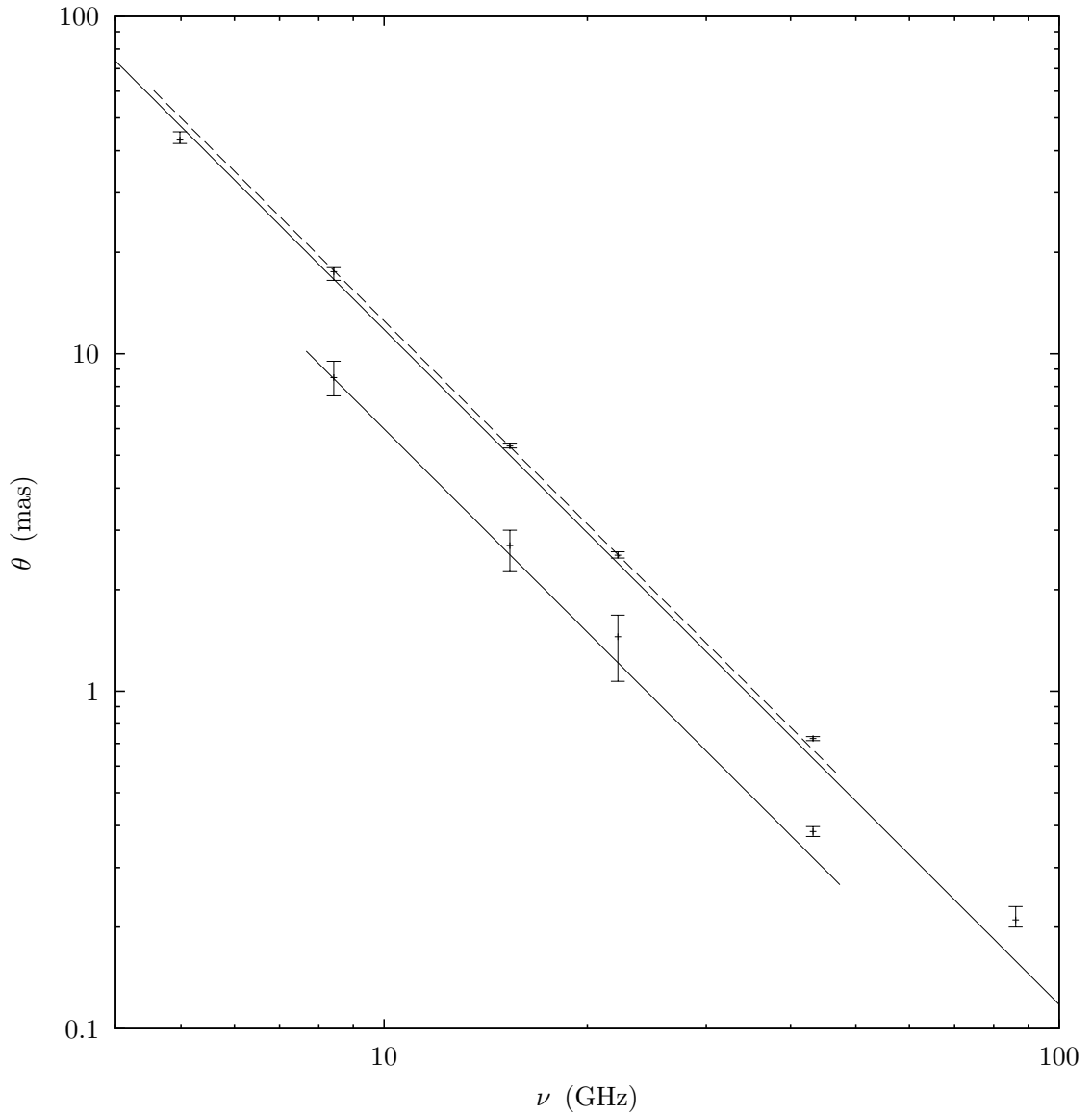


Fig. 1.2.— Angular size measurements of Sgr A* through very-long-baseline interferometry. The data points shown are taken from Shen et al. (2005). Minor axis sizes appear below major axis sizes at the frequencies where they are available. The minor axis scattering law shown is the average of the Bower et al. (2004) and Shen et al. (2005) curves, as their difference is not significant. The solid line through the major axis points uses the Bower et al. (2006) normalization for the scattering law, which is extrapolated from measurements near 1.4 GHz. The dashed curve has the Shen et al. (2005) normalization, derived from the points below 50 GHz. The intrinsic size of Sgr A* manifests itself as a deviation from the scattering law, with significant deviations visible at the highest frequencies.

spectrum, which has a power-law index of $11/3$), this exponent is identically -2 when the interferometer baselines are shorter than the inner scale of the turbulence (e.g. Thompson et al. 2001). Note that observations through a scattering screen with a single scale should also observe ν^{-2} scattering, while observations through a screen described by a Kolmogorov spectrum on baselines longer than the inner scale would measure an exponent of $-11/5$, but this is excluded by the observations. The latest results by Bower et al. (2004, 2006) and Shen et al. (2005) adopted ν^{-2} frequency dependence for the scattering law, but differed significantly on the normalization by calibrating their scattering laws across different frequency ranges. Shen et al. (2005) used nearly simultaneous 5 to 43 GHz data for calibration and applied the scattering law to measurements at 43 and 86 GHz to determine intrinsic sizes. They found an intrinsic source size of $14.7r_S$ at 86 GHz with a frequency-size relationship proportional to $\nu^{-\beta}$, with $\beta = -1.09^{+0.34}_{-0.32}$. Bower et al. (2004) calibrated their scattering law between 1.4 and 15 GHz and determined that the intrinsic size variation has exponent $\beta = -1.6 \pm 0.2$ between 22 and 86 GHz. Finally, Bower et al. (2006) revisited the calibration of the scattering size with new low-frequency data (1.26 – 1.71 GHz), where the intrinsic size contribution can be completely neglected but where any deviation from ν^{-2} in the scattering would be greatly amplified at 43 GHz. With their lower normalization, they found measurable intrinsic size starting at 8 GHz, with a β of -1.5 ± 0.1 . If the normalization is moved toward the Shen et al. (2005) value, β increases, although only to -1.3 for a 3σ change in the normalization. The fairly small span in ν^{-2} of the calibration sample (less than a factor of two) is a result of the frequency coverage of the VLA and will undoubtedly be revisited when ongoing improvements to the VLA receivers are complete.

These measurements of the intrinsic size of Sgr A* are beginning to make important contributions to our understanding of the source. First, the diameter of the emission region around Sgr A* at 86 GHz appears to be $14.7\text{--}15.8r_S$, a volume 40^3 times smaller than the size constraints imposed by stellar orbits. The frequency dependence of the size can also be compared to emission models, although this work is just beginning. Falcke & Markoff (2000) predicted $\beta = -1$ for a jet model, although Bower et al. (2006) suggest that more general jet models allow β as steep as -1.4 . Yuan et al. (2006) predict $\beta = -1.1$ for a quasi-spherical accretion flow (Yuan et al. 2003), although that model is also somewhat poorly constrained. To get tighter constraints, efforts are now underway to fit the VLBI visibilities directly with jet models (Markoff 2006). Test observations have also been made for 230 GHz VLBI observations of Sgr A*, where strong gravitational effects around the event horizon could be visible if the optical depth is low enough (e.g. Falcke et al. 2000; Broderick & Loeb 2006a).

Spectrum

Most of our current understanding of the physics of Sgr A* has been derived from measurements of its spectral energy distribution (SED), shown in Figure 1.3. Detections at the shortest wavelengths (near-IR, X-ray) were first obtained relatively recently; for most of the thirty years since Sgr A* was discovered only radio-frequency flux densities were available. Within the atmosphere's radio window (0.1–1000 GHz), Sgr A* has been detected from 0.33 GHz (Nord et al. 2004) to 850 GHz (Serabyn et al. 1997; Yusef-Zadeh et al. 2006). The emission at the highest frequencies

show evidence for great variability, as discussed below. At frequencies where interferometers have provided arcsecond or better angular resolution (≤ 230 GHz) the many components of the crowded Galactic center field can be separated and the flux density of Sgr A* reliably determined. At higher frequencies, single-aperture instruments with angular resolution of $10''$ or more have difficulty isolating the contribution of Sgr A* to the observed emission, as can be seen in the 350–650 GHz maps of Zylka et al. (1995). The low-frequency (below 10 GHz) spectrum of Sgr A* slowly rises, with a spectral index of 0.1–0.3, while at higher frequencies it appears to rise more steeply, with an index closer to 0.5. This latter feature is called the “submillimeter bump”. Given the uncertainty in the highest frequency measurements, the bump may extend beyond 850 GHz. Uncertainty in this peak of the spectrum contributes significantly to the uncertainty in the total luminosity. Between 1000 GHz ($300 \mu\text{m}$) and 10^4 GHz ($30 \mu\text{m}$) the atmosphere is completely opaque, apart from a few small windows at the driest locations (e.g. Paine et al. 2000; Marrone et al. 2005). Satellites and airborne observatories designed to observe at these frequencies (e.g., Infrared Space Observatory, Kuiper Airborne Observatory) have lacked the angular resolution required to separate Sgr A* from very strong dust emission at the center of the Galaxy (e.g. Davidson et al. 1992). The atmosphere again opens up to ground-based instruments between 30 and $0.3 \mu\text{m}$, although new problems arise for the detection of Sgr A*. Thirty magnitudes of visual extinction through the Galactic plane ensure that Sgr A* is unobservable shortward of $1 \mu\text{m}$. Inadequate angular resolution, even on 10-meter telescopes, has prevented a clear identification of Sgr A* amid a dusty and star-filled field longward of $4 \mu\text{m}$. In their review, Melia & Falcke (2001) compiled the mid-IR upper limits on emission

from Sgr A* based on the best available images between 8 μm and 30 μm (Telesco et al. 1996; Cotera et al. 1999). They appear to err in quoting a limit of 1.4 Jy at 30 μm , the Telesco et al. (1996) limit was 20 Jy and was shown correctly in the Morris & Serabyn (1996) review. Subsequent VLT observations have tightened these limits somewhat (Eckart et al. 2006a). Between 1.7 μm and 3.8 μm , adaptive optics systems on the VLT and Keck have enabled detections of flares of Sgr A*, with quiescent emission also possibly observed (e.g. Genzel et al. 2003), although the low level of the emission and previous observations that appear to show lower flux at other times (Hornstein et al. 2002; Ghez et al. 2005b) may indicate that truly “quiescent” emission is not yet detected. At X-ray wavelengths, Sgr A* is again observable, thanks to the sub-arcsecond angular resolution afforded by *Chandra*. Baganoff et al. (2003) found faint, extended (1.4'') emission at the position of Sgr A*, with unresolved emission at the same location during flares.

The SED of Sgr A* shows it to be exceptionally faint. Its bolometric luminosity is around $L_{\text{Sgr A}^*} = 10^{36}$ ergs s^{-1} , just a few hundred times the luminosity of the sun (Narayan & Quataert 2005). An instructive scale for the luminosity is the Eddington luminosity (L_{E}), the limit imposed by radiation pressure acting on infalling material. L_{E} is equal to

$$\begin{aligned} L_{\text{E}} &= \frac{4\pi GMm_{\text{p}}c}{\sigma_{\text{T}}} \\ &= \frac{3GMm_{\text{p}}c}{2r_{\text{e}}^2} \\ &= 1.3 \times 10^{38} \left(\frac{M}{M_{\odot}} \right) \text{ergs s}^{-1}, \end{aligned} \tag{1.1}$$

where M is the central mass and all other quantities are fundamental constants.

The Eddington luminosity of Sgr A* is 4×10^{44} ergs s^{-1} (for $M = 3.5 \times 10^6 M_{\odot}$),

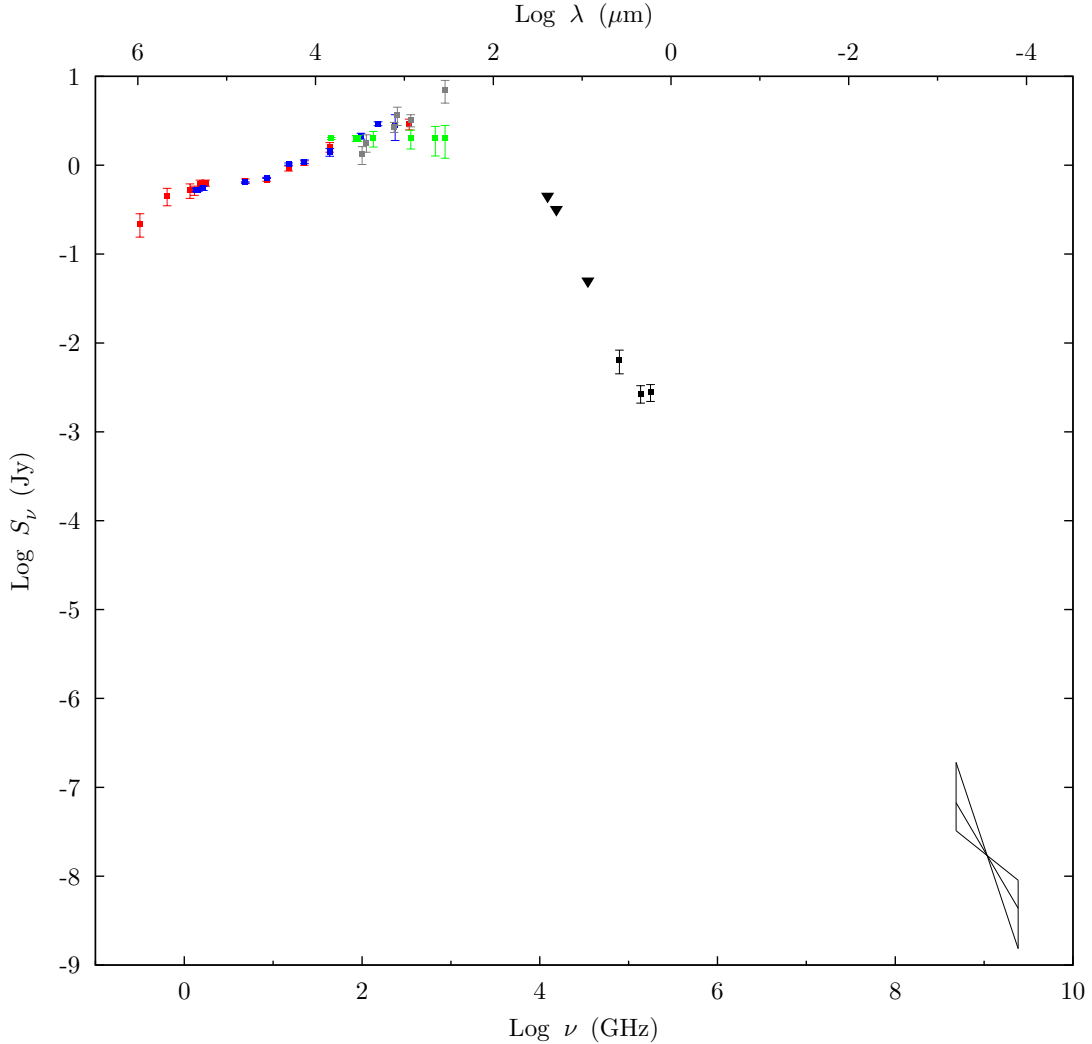


Fig. 1.3.— The spectral energy distribution of Sgr A*. The spectrum covers the range from 300 MHz to 10 keV (2.4×10^9 GHz), the nearly 10 decades in frequency/wavelength/energy over which Sgr A* has been detected. Blue points are taken from Falcke et al. (1998), red from An et al. (2005), and green from Yusef-Zadeh et al. (2006), all of which were multi-observatory campaigns to observe the simultaneous spectrum of Sgr A*. Additional high-frequency radio observations are provided by Serabyn et al. (1997) (grey). Mid-infrared upper limits are marked with upside-down triangles and are taken from Cotera et al. (1999) and (two from) Eckart et al. (2006a), in order of increasing frequency. The Telesco et al. (1996) $30 \mu\text{m}$ limit is substantially weaker and is not shown. The three detections in the near infrared were selected to represent quiescent emission rather than a flare, and are taken from Genzel et al. (2003). The quiescent X-ray emission is from Baganoff et al. (2003).

at least 10^8 times larger than what is observed. This is an extremely low Eddington ratio (L/L_E); a study of nearby active galactic nuclei (AGN) with well-measured SEDs found a few with ratios as small as a few times 10^{-6} (e.g., M84*, M87*, M104*), while the black hole often cited as the nearest analogue of Sgr A*, M81*, has an Eddington ratio of 2×10^{-5} (Ho 1999; black hole masses updated with the measurements of Marconi & Hunt 2003). Sgr A* is almost certainly not the only object with such a low Eddington ratio, but it would be difficult to detect an AGN so faint in all but the nearest galaxies.

The low luminosity of Sgr A* can be partially explained by the accretion rate, which is much lower than the Eddington rate. The resolved X-ray emission around Sgr A* observed by Baganoff et al. (2003) allows an estimate of the gas captured by the gravitational influence of the black hole. At the Bondi radius (Bondi 1952), gravitational forces balance gas pressure and material inside this radius should fall toward the black hole. The Bondi radius (r_B) is determined by the sound speed ($c_s^2 = \gamma kT / \mu m_H$, for adiabatic index γ , temperature T , and mean atomic weight μ) and the central mass (M)

$$r_B = \frac{2GM}{c_s^2} . \quad (1.2)$$

For Sgr A* r_B should be a few times $10^5 r_S$ or $1.6''$ (Baganoff et al. 2003; Yuan et al. 2003). The temperature and density of the X-ray gas indicate that the accretion rate at this radius (Bondi rate, \dot{M}_B) is around $10^{-5} M_\odot \text{ yr}^{-1}$, four orders of magnitude below the Eddington accretion rate ($L_E / (0.1c^2) \equiv \dot{M}_E \simeq 0.07 M_\odot \text{ yr}^{-1}$). A comparable accretion rate ($10^{-4} M_\odot \text{ yr}^{-1}$) had been predicted based on the Bondi model and expected conditions in stellar winds (Melia 1992) and through hydrodynamic simulations of the winds (Coker & Melia 1997; later, Cuadra et al.

2005, 2006). Radiatively efficient accretion at \dot{M}_B would produce a luminosity (L_B) several orders of magnitude greater than $L_{Sgr A^*}$, although it is possible that gas captured at large radius may be lost before reaching the black hole. The accretion rate at very small radii is unknown and is one of the important unknown parameters of Sgr A*.

Models

The enormous difference between expectations for $L_{Sgr A^*}$ (L_E, L_B) and observations (Figure 1.3) has led to a variety of models for the emission from Sgr A*. The models must explain the apparent radiative inefficiency of the accreted material in order to explain the four orders of magnitude between L_B and $L_{Sgr A^*}$. Alternatively, some of the captured material could be lost far from the black hole in the form of an outflow, which could ease the stringent requirements on the radiative efficiency somewhat. Such an outflow might even be a generic consequence of low efficiency, as the accreted gas will be heated to higher temperatures if it cannot cool radiatively, allowing the hottest material to escape the potential well.

The proposed models of Sgr A* can be crudely separated into two categories based on the radiatively important component in the model. In the first class of models, the accreting material is responsible for the observed emission. The classic thin-disk accretion flow (Shakura & Sunyaev 1973) is an example of this type of model. Thin disks were applied to Sgr A* (Zylka et al. 1992) before its spectrum was well understood, when much higher luminosities were admitted by the observations, but the current luminosity requires a very low accretion rate

($10^{-10} M_{\odot} \text{ yr}^{-1}$; Narayan 2002) and the spectrum does not resemble a thin disk. The following models, which suppress radiation instead of (or in addition to) suppressing accretion, fall under the general heading of radiatively-inefficient accretion flows (RIAFs). Narayan & Yi (1994, 1995) proposed a two-temperature accretion flow where the decoupling of the (radiating) electrons and (non-radiating) ions allowed gravitational potential energy to be stored in the ions and swallowed by the black hole (advected) without producing significant radiation. This type of flow is known as an advection-dominated accretion flow (ADAF). The accretion is quasi-spherical, although non-zero angular momentum in the accreted gas leads to circularization rather than radial infall. The accretion rate in this type of flow is comparable to the Bondi rate at all radii. Variants of this type of flow have also been proposed, usually with lower accretion rates. Because the ADAF is convectively unstable, the structural changes created by strong convection were incorporated into the convection-dominated accretion flow (CDAF) by Narayan et al. (2000) and Quataert & Gruzinov (2000b). The radial density profile (n) in this type of flow is much flatter, $n \propto r^{-1/2}$ instead of $r^{-3/2}$ in an ADAF, and the accretion rate is much lower ($\dot{M} \sim \dot{M}_{\text{B}}(r_{\text{S}}/r_{\text{B}})$). Blandford & Begelman (1999) proposed that the gas heated in an ADAF is unbound and should form outflows. The resulting density profile in the advection-dominated inflow-outflow solution (ADIOS) is a parameter in the model and can vary between those of the ADAF and CDAF. Finally, Yuan et al. (2003) introduced another variant of the ADAF in which the turbulent heating is increased, the density profile is a parameter, and a small fraction of the electrons are accelerated into a non-thermal distribution in order to match the radio and IR spectrum (see also Mahadevan 1998; Özel et al. 2000). It appears that many variants

of RIAFs provide a reasonable match to the SED of Sgr A* (e.g. Mahadevan 1998; Yuan et al. 2003; Goldston et al. 2005). However, other constraints have caused difficulty for some models, as discussed below.

The second type of model invokes a jet as the primary emission source. The progenitor of the current line of jet models for Sgr A* was provided by Falcke et al. (1993b), an extension of their accretion disk model (Falcke et al. 1993b). The motivation for the addition of a jet was the $100 r_S$ elongation (perpendicular to the major axis of the scatter-broadening) observed by Krichbaum et al. (1993) in the first 43 GHz VLBI image of Sgr A*, a feature that has never been observed since and was almost certainly in error (Bower & Backer 1998). This model required a low accretion rate ($10^{-7} - 10^{-8.5} M_\odot \text{ yr}^{-1}$) to explain the faint emission from Sgr A*, although the emission was assumed to be at least two orders of magnitude larger than the current estimate. The model has since been revisited, most recently by Falcke & Markoff (2000), who showed that it matched well with the spectrum of Sgr A*, including the newly discovered X-ray emission (Baganoff et al. 2003), at a similarly low accretion rate. The low-frequency radio spectrum is contributed by self-absorbed synchrotron emission along the jet, while the submillimeter bump originates in thermal (or nearly so) electrons at the “nozzle” from which the jet is launched. The X-ray emission is the result of inverse-Compton (IC) scattering of the submillimeter-bump photons, although the apparent thermal bremsstrahlung origin of the extended X-ray emission caused a downward revision in the IC component in Markoff & Falcke (2003). Near-IR emission is under-produced by the steep electron distribution in the submillimeter bump, although the deficit may be resolved through, for example, low-level flaring emission. The absence of an observable jet

can be understood from scaling arguments based on the small jet in M81* and the broadened image of Sgr A*. Other jet models (e.g. Beckert & Falcke 2002) have focused on polarization aspects of Sgr A* and are discussed below.

Finally, these classes of models have also been mixed to improve the match to the SED of Sgr A*. Although jet models can match the observed X-ray emission, its extended, thermal nature is more readily explained by the accreting plasma in a RIAF model. Similarly, ADAF models without non-thermal electrons cannot produce the flat low-frequency radio spectrum, and although a small power-law component to the electron distribution can fill the deficiency, placing the power-law component in a jet may be more aesthetically pleasing. An initial attempt at merging of these models was made by Yuan et al. (2002).

Several models presently exist that adequately match the SED of Sgr A* on their own or in combination. In addition to these analytic examples, magnetohydrodynamic (MHD) simulations resembling RIAFs have been used to calculate emergent spectra with some success (e.g. Goldston et al. 2005; Ohsuga et al. 2005). The ability of a variety of models to match the spectrum leaves the physics underlying the emission substantially unconstrained. Consensus may have been reached on the most basic components of the source: optically thick, non-thermal synchrotron emission producing radio emission below the submillimeter bump, with a thermal or similarly steep non-thermal component very near to the black hole producing the submillimeter photons. However, the overall accretion rate, the density structure, the size of the emission region as a function of wavelength, and polarization and variability properties discussed below remain undetermined.

Variability

Repeated observations of Sgr A* over more than thirty years have shown it to be variable at all frequencies. The longest time baselines are available at low radio frequencies, beginning with the three-year campaign of Brown & Lo (1982). Zhao et al. (2001a) provided a 20-year data set from the VLA and the Green Bank Interferometer, and Falcke (1999), Zhao et al. (2001a), and Herrnstein et al. (2004) added shorter, well-sampled observational campaigns. Intraday variability at radio frequencies has been observed as well, as in Bower et al. (2002c), Eckart et al. (2006a), and Yusef-Zadeh et al. (2006). These observations have produced two claims of periodic modulation (Falcke 1999; Zhao et al. 2001a), with periods of 57 and 106 days. The relative importance of intrinsic and extrinsic origins for the radio variability, the latter due to refractive scintillation in the scattering medium that broadens the radio image of Sgr A*, has long been debated. The presence of periodicities in the modulation would strongly favor intrinsic origins for the changes. However, in an analysis of the available data between 1.4 and 43 GHz, Macquart & Bower (2006) concluded that no periodicities of statistical significance are present on timescales longer than a few days, and that the characteristics of this variability are consistent with expectations from scintillation. The 10% variation on timescales shorter than four days does appear to be intrinsic.

At higher frequencies scintillation should not be an important source of variability, as shown by Macquart & Bower (2006) and as measured with rapid photometry by Gwinn et al. (1991). Variability was evident from the inconsistency of early observations at and above ~ 100 GHz (e.g. Zylka et al. 1992; Serabyn et al.

1992), although calibration errors were also present, and repeated observations with the same instruments showed clear changes (e.g. Wright & Backer 1993). More recent campaigns designed to measure these variations in a more systematic way, including Zhao et al. (2003), Miyazaki et al. (2004), and Mauerhan et al. (2005), have found 10% to 20% variations on timescales of hours to days, with occasional large (factor of two or more) outbursts on the shorter timescales (Miyazaki et al. 2004). At the highest submillimeter frequencies, Sgr A* may be very variable (compare Serabyn et al. 1997 and Yusef-Zadeh et al. 2006 at 850 GHz). Infrared flares have also been observed (e.g. Genzel et al. 2003; Ghez et al. 2004, 2005a), with amplitudes as large as several times the quiescent flux density. X-ray flares (e.g. Baganoff et al. 2001; Goldwurm et al. 2003; Bélanger et al. 2005) can be the most dramatic of the known outbursts, with the largest flare representing a $160\times$ increase in X-ray emission (Porquet et al. 2003). The timescales of the flaring emission can be quite short, with rise and fall times of just minutes in the IR and X-ray and total durations of less than an hour. The rapidity of the changes suggests very compact regions, most likely in the hot plasma in the immediate vicinity of the black hole.

When taken alone, flare data from a single wavelength provide little constraint on the flare mechanism. Observations of the X-ray and NIR spectral indices during flares (Ghez et al. 2005a; Eisenhauer et al. 2005; Gillessen et al. 2006b; Krabbe et al. 2006) may be useful for determining emission mechanisms, but a wide variety of spectral indices are observed. A few flares have been detected simultaneously in the IR and X-ray bands (Eckart et al. 2004, 2006a; Yusef-Zadeh et al. 2006), with one radio flare observed shortly after an X-ray flare (Zhao et al. 2004). These observations provide more information about the flaring process and a variety of

attempts have been made to interpret them. These have included perturbations (accretion rate changes, electron acceleration) to accretion models (Yuan et al. 2004), jet models (Markoff et al. 2001; Markoff & Falcke 2003), and somewhat independent examination of electron population changes (Liu et al. 2004). Because of the large energy separation between the IR and X-ray there is still a great deal of freedom in these observations and various mechanisms are possible. Given the range of submillimeter variability shown in these models, stronger constraints may come from submillimeter/IR/X-ray observations.

Searches for periodic features in the variations of Sgr A* have attracted renewed interest of late. However, the timescales currently of interest are those relevant to orbits at very small radii, rather than the periods of months that were investigated in radio frequency measurements. The orbital period (τ) for an object at radius r around a black hole with spin parameter a is

$$\tau = (108 \text{ s}) \left(\frac{M}{3.5 \times 10^6 M_\odot} \right) \left[\left(\frac{2r}{r_S} \right)^{3/2} \pm a \right]. \quad (1.3)$$

The upper and lower signs refer to prograde and retrograde orbits, respectively. Not all radii are permitted, the radius of the innermost stable orbit in a non-rotating black hole is $3r_S$, and is $r_S/2$ and $9r_S/2$ for prograde and retrograde orbits around a maximally rotating black hole ($a = 1, -1$), respectively. These orbits have periods of roughly 27, 4, and 47 minutes, respectively. Under the assumption that periodic signals observed in Sgr A* are the result of a persistent plasma hot spot orbiting the black hole, the identification of a period shorter than 27 minutes implies that Sgr A* must be rotating and puts a lower bound on the spin parameter. Three such claims have now been made, a period of 17 minutes in an IR flare (Genzel et al. 2003), a

period of 22.2 minutes in an X-ray flare (Belanger et al. 2006), and five different periods in X-ray flares and quiescent emission (Aschenbach et al. 2004), although this latter claim does not appear to be very significant. Periodic signals have not been observed in other flares in these bands. Observations in the submillimeter, where the synchrotron lifetime of flaring electrons should be much longer and thus any of the putative hot spots should be visible for many orbits, may be a better probe of these periodicities, although no well calibrated periodicity searches have been undertaken to date.

Polarization

Although linear polarization (LP) is very common in AGN (e.g. Aller et al. 2003) and very large polarization fractions can be generated in synchrotron sources, LP was not observed in Sgr A* in any early observations, nor in focused multi-frequency searches by Bower and collaborators. Using very sensitive VLA observations, Bower et al. (1999a) limited the polarization at 4.8 and 8.4 GHz to 0.2%. Extending the observations to much higher frequencies, Bower et al. (1999c) limited the LP fraction to 0.2%, 0.4% and 1% at 22, 43, and 86 GHz. These observations did detect variable circular polarization (CP) in Sgr A*, unusual for AGN in general and even within the low-luminosity AGN subclass (Bower et al. 2002b). Bower et al. (1999b, 2002c) and Sault & Macquart (1999) found that the CP fraction and its variability increased between 1.4 and 15 GHz, with variations observed within a single night during a flare. The unusual circular polarization properties (and the lack of linear polarization at the same frequencies) are only known to exist in one other object,

M81* (Brunthaler et al. 2001, 2006), suggesting that these low-luminosity AGN are physically similar. A variety of possible mechanisms have been proposed to generate the CP (see several options in Bower et al. 2002c; also Ruszkowski & Begelman 2002; Beckert & Falcke 2002), but it remains poorly understood.

Propagation effects provide a possible explanation for the lack of linear polarization at low frequencies. Of particular interest is Faraday rotation, a plasma effect with a ν^{-2} frequency dependence. For electromagnetic radiation in a plasma with a magnetic field parallel to the direction of propagation the indices of refraction differ for left- and right-circular polarization, producing a rotation of the linear polarization position angle (χ) that depends upon the integrated electron density and magnetic field. This integral is known as the rotation measure (RM) and the Faraday rotation at a given frequency is $\Delta\chi = \text{RM}c^2/\nu^2$. At low frequencies, a large RM can rotate the position angle several times across the bandwidth of the observation and wash out the signal (bandwidth depolarization). Bower et al. (1999a) searched for this polarization wrapping in their data, finding that there was no evidence of any LP in their data for any RM up to 1.5×10^7 rad m⁻² (a very large value compared to those measured in the region), the largest value they could test with their spectral resolution. Alternatively, the known scattering screen might have produced an inhomogeneous RM across the scattered image of Sgr A*, leading to a cancellation of the source-integrated polarization (referred to as beam depolarization). However, these authors excluded this possibility on the grounds that the required ambient density and field were too large. Depolarization within the accreting material or intrinsically low polarization in the emission remained plausible explanations for the lack of LP.

Linear polarization was successfully detected in Sgr A* in 1999 at 150, 220, 375, and 400 GHz, by Aitken et al. (2000). The observations were made using the 15-meter James Clerk Maxwell Telescope (JCMT), which provides an angular resolution between 34'' and 13'' at these frequencies. They found polarization fractions between 11 and 22%, with a possible rise toward high frequencies. The lack of bandwidth depolarization across the 40 GHz-wide 150 GHz band placed an upper limit of 10^6 rad m⁻² on the magnitude of the RM, demonstrating that the low-frequency non-detections of LP are not the result of a very large RM. In order to determine the polarization arising in Sgr A* they were forced to subtract the polarized and unpolarized contributions from the dust and free-free emission within the beam at the position of Sgr A*, between 65% and 80% of the emission in the central pixel. This made the polarization fractions very uncertain and the detection itself was met with some skepticism. Bower et al. (2001) used the Berkeley-Illinois-Maryland Association array (BIMA) to look for polarization at 112 GHz and found none at the level of 2%, well below the 150 GHz value. In subsequent BIMA observations at 230 GHz Bower et al. (2003) detected LP of 7% in four epochs, with sufficient angular resolution that there was no longer any possibility of significant polarized dust contamination. These authors boldly used three of the χ measurements from Aitken et al. (2000), discarding the 220 GHz point because it disagreed with their own, and found that the χ variation with frequency was well fit by an RM of -4.3×10^5 rad m⁻². Further BIMA observations showed that the 230 GHz χ was variable, casting doubt on the RM determined from widely separated measurements (Bower et al. 2005a). The variability in χ and the stability in the polarization fraction (at the precision of the measurements) led

Bower et al. (2005a) to conclude that the position angle changes were probably due to RM fluctuations in the accretion flow. If this mechanism were confirmed, the variability in χ could be used to examine the turbulence in the flow, but with repeated polarization measurements at just one frequency it was impossible to separate intrinsic changes from RM changes. Recently Macquart et al. (2006) have detected LP in Sgr A* at 83 GHz using the BIMA array. They used the very large baseline in ν^{-2} between these data and all previous measurements (including some of the results presented in this work) to claim a RM of -4.4×10^5 rad m⁻², although on close inspection the evidence for this conclusion is very weak. Because the position angle is 180°-degenerate, they must select between unwrappings of the position angle at 83 GHz and they do not have the statistical power to do so. Using the numbers reported in the paper, the formal significance at which they can exclude a RM fit with zero unwrappings (their preferred RM uses a -180° unwrapping) is 90%, which is not usually considered significant. Achieving this level of significance requires almost unsupportable choices about which data to include and how to define errors, and more appropriate choices allow the alternate fit at 26% or greater probability.

Despite some concerns about the veracity of the result, the Aitken et al. (2000) detection of linear polarization immediately advanced the theoretical understanding of Sgr A*. Quataert & Gruzinov (2000a) and Agol (2000) pointed out that the RM allowed by the LP detection was much smaller than would be predicted by models, such as the ADAF, where the accretion rate at small radii is comparable to \dot{M}_B . Thus the original form of the ADAF model, an acceptable model on the basis of the SED alone, was excluded on the basis of the very different constraints provided by polarization. Subsequent polarization observations have been examined

in context of the accretion rate that can be supported by measured upper limits on the RM, although significant assumptions about field order, direction, strength, the electron temperature variation with radius, and even viewing geometry are required to perform such comparisons outside an individual model.

The theoretical discussion of the polarization properties of Sgr A* remains somewhat underdeveloped. Immediately after the first polarization detection, Agol (2000) and Melia et al. (2000) attempted to understand the origin of the rapid polarization rise with frequency (between 86 and 150 GHz) as the revelation of a compact central emission component revealed at higher frequencies as the optical depth declines. Yuan et al. (2003) calculated the polarization expected from their model, with results similar to those of Melia et al. (2000). These analytic approaches to the polarization properties uniformly over-predict the polarization, which is unsurprising given the large difference between the high intrinsic polarization of the synchrotron radiation inputs to the models and the low observed polarization. Beckert & Falcke (2002) and Beckert (2003) attempted to match the LP and CP properties of Sgr A* through consideration of the turbulence and polarization conversion in a jet, a technique that includes disorder as a parameter. Simulations may be more successful in treating the polarization properties of this source. Goldston et al. (2005) calculated the radiation (and polarization) from an MHD simulation, producing a polarization spectrum and variability properties. The very ordered field at small radius in this simulation led to a very large polarization fraction, but the polarization variability spectrum may be useful for comparison to observations. Future simulations will almost certainly have to include the effects of radiative transfer in strong gravity (as in, e.g., Broderick & Loeb 2006a), as the

polarization is only observed in the submillimeter, which is expected to originate at the smallest radii.

The Submillimeter Array

The Submillimeter Array (SMA, Figure 1.4) is the first dedicated submillimeter interferometer, a predecessor to the Atacama Large Millimeter Array (ALMA), and a successor to the various millimeter interferometers. It was conceived of at the Smithsonian Astrophysical Observatory and is now a joint project between the Smithsonian Astrophysical Observatory and the Academia Sinica Institute of Astronomy and Astrophysics, with funding from the Smithsonian Institution and the Academia Sinica. The SMA has been sited at one of the better submillimeter sites, the summit of Mauna Kea, Hawaii, to provide access to higher frequency emission that is absorbed by tropospheric water vapor at wetter locations. The SMA is designed for observations between 183 and 900 GHz and is presently capable of observations in three bands centered near 215, 310, and 650 GHz. With eight 6-meter antennas and a maximum baseline in excess of 500 meters, the collecting area is slightly larger and the angular resolution is $30\times$ finer than those of the largest single-aperture submillimeter telescope. The SMA was dedicated in November 2003.

The SMA is a powerful new instrument for the study of the Galactic center. Confusion in this region has magnified the uncertainty and limited the impact of past submillimeter observations of Sgr A*. Although this wavelength regime may contain the emission peak for this source, the location of this peak and the variability in the spectrum are very poorly known because of the lack of angular

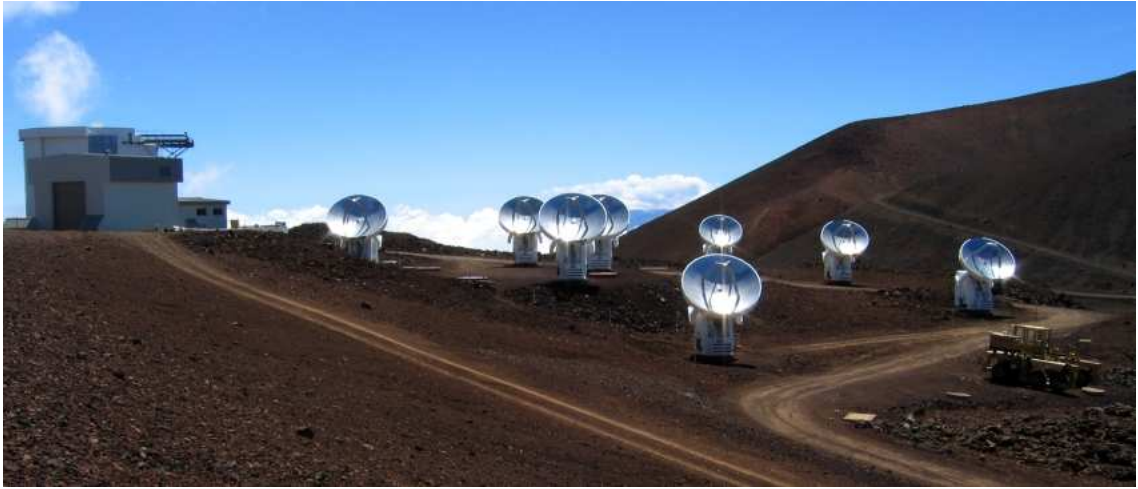


Fig. 1.4.— The Submillimeter Array on Mauna Kea, Hawaii. Photo by Nimesh Patel.

resolution. Arguably the most significant measurement of Sgr A* yet made at these frequencies was the Aitken et al. (2000) detection of linear polarization, but resolution problems led to very weak polarization constraints at most frequencies and interferometric followup at 230 GHz (Bower et al. 2003) was required to confirm the measurement. The Berkeley-Illinois-Maryland Association array (BIMA) has routinely observed Sgr A* at 230 GHz with high angular resolution, but the northerly latitude of the array, poor site, and narrow instrumental bandwidth have limited the sensitivity of this instrument for this southern source. The SMA's advantages in all of these respects should yield a 230 GHz sensitivity 5 (or more) times better than the BIMA sensitivity, a factor of 25(!) in integration time. This dramatic improvement should increase the precision and temporal resolution of total intensity and polarization measurements, in addition to opening up entirely new frequencies for these observations, without interference from the surrounding contaminant emission.

This Work

The completion of the Submillimeter Array was fortuitously timed for my graduate career, providing me with an opportunity to exploit this new telescope for observations of Sgr A*. The next chapter of this thesis describes the instrument I have constructed to allow linear polarimetry with the SMA in all three of its completed receiver bands. Because persistent linear polarization is unique to the submillimeter band in Sgr A*, this capability greatly increases the potential impact of the SMA for this source. Chapter 3 explains the polarization calibration that is crucial for the observations that follow. Chapter 4 reports the first scientific results of the SMA polarimeter, measurements of the linear polarization of Sgr A* at 340 GHz. These observations were the first of their kind and showed the sensitivity advantages of the SMA in detecting polarization variability on timescales never before accessible. Chapter 5 provides the first detection of the rotation measure and intrinsic linear polarization changes (separated from the effects of rotation measure fluctuations) in Sgr A*. The peak in the spectrum of Sgr A* is measured in Chapter 6, without the uncertainty previously created by the large variability at high frequencies. In Chapter 7 the very-short timescale variations of the polarization of Sgr A* are shown and the signatures of orbiting material are considered for these and future observations. Finally, Chapter 8 reviews the results of this thesis and the associated improvements in our knowledge. Followup observations, pending results, and prospects are also summarized.

Chapter 2

The Submillimeter Array

Polarimeter

2.1 Introduction

As the first dedicated submillimeter interferometer, the Submillimeter Array provides an opportunity to extend the high-angular resolution polarization observations made with millimeter interferometers to higher frequencies. Dust polarization measurements, which trace the structure of the magnetic field in the plane of the sky (B_{\perp}), benefit greatly from the move to higher frequency because of the steep dust spectrum. The flux density from optically thin warm dust emission (warm enough to keep the spectral peak well above SMA frequencies, at least 10 – 20 K) rises like ν^{3-4} , multiplying the emission by factors of several even between the two lowest SMA bands (230 and 345 GHz). The spectral advantages combined with the resolution increase over past measurements made with single-aperture

instruments (e.g. CSO, JCMT, KAO) created great interest in adding polarization capabilities to the array very early in the design process. As a result, significant polarization considerations were included in the optics design and receiver plans, as described below. Schemes for implementing polarimetry and recommendations for future work were even outlined in a 1998 workshop that drew on the expertise of other millimeter and submillimeter observatories (Wilner 1998). In particular, the conferees concluded that:

The SMA should provide for computer controlled rapid switching between polarizations using quarter wave plates. This simple hardware extension will allow for some polarization experiments, in any SMA band, without any new receivers and just half of the final correlator. This mode of operation requires the construction of appropriate polarizers for the frequencies of interest. Some investigation should be made into the availability of achromatic polarizers.

Despite this recommendation, the required hardware was a low priority during the construction and testing phases of the array and no attempt was made to field an instrument for the subsequent five years. Although I was unaware of the memo at the inception of this project, this is exactly the system I undertook to build.

The polarization system that exists today is not the result of the science case made for dust (and CO) polarization observations early in the history of the SMA. Instead, my interest in this instrument was attracted by Sgr A* and the recent detections (Aitken et al. 2000; Bower et al. 2003) of polarized emission from the immediate vicinity of the black hole, as described to the graduate students by Jim

Moran in late 2002. Along with fellow students Jenny Greene and Robin Herrnstein, I offered to construct a simple instrument to allow polarimetry with a subset of SMA antennas at 345 GHz. Our hope was that a small hardware effort, drawing on my experience building a wave plate positioner for a CMB polarization experiment as a freshman at Caltech, could allow a fast interferometric detection of polarization in Sgr A* at a new frequency. The project has greatly evolved from my original plan of a month's work and a three antenna experiment. That initial system was deployed in August 2003 with the assistance of many on the SMA project (particularly Ken Young and Ram Rao), in the Receiver Lab, and Greene, who came to the SMA to take half the observing load in the first run. In 2004 the hardware grew to eight systems for 345 GHz, then in 2005 it was expanded again to cover all three SMA bands. The full polarization system, now a facility instrument on the SMA, is described in this chapter, with further details on its astronomical calibration provided in Chapter 3. The scientific results, beyond the simple goal of a higher frequency measurement of Sgr A* polarization, are discussed later.

2.2 Interferometric Polarimetry

The measurement of polarized emission from astronomical sources requires sensitivity to both orthogonal components of the polarization; however, the choice of the polarization basis sampled by the detectors must be carefully considered. The common bases are the orthogonal linear polarizations (LP: X and Y), and circular polarizations (CP: right- and left-circular, or R and L). For interferometers, complete polarization measurements require all four correlations of the two polarization states

(e.g.: RR, RL, LR, LL). This is easily demonstrated for the circular basis; it can be shown that full sampling of the uv -plane for measurement of LP requires both LR and RL correlations (e.g. Roberts et al. 1994), while separation of the total intensity and circular polarization requires both RR and LL.

The choice of feed polarization depends significantly on the type of polarization to be investigated. In terms of the Stokes visibilities of the source emission (I , Q , U , and V), the visibilities for the four cross correlations of perfect linear feeds are

$$\begin{aligned}
 \mathcal{V}_{XX} &= g_{Xa}g_{Xb}^*(I + Q\cos 2\phi + U\sin 2\phi) \\
 \mathcal{V}_{YY} &= g_{Ya}g_{Yb}^*(I - Q\cos 2\phi - U\sin 2\phi) \\
 \mathcal{V}_{XY} &= g_{Xa}g_{Yb}^*(-V_Q\sin 2\phi + U\cos 2\phi + iV) \\
 \mathcal{V}_{YX} &= g_{Ya}g_{Xb}^*(-V_Q\sin 2\phi + U\cos 2\phi - iV), \tag{2.1}
 \end{aligned}$$

where the gain of the X polarization feed in antenna a is g_{Xa} and ϕ is the parallactic angle of the feed polarization on the sky. For alt-az telescopes, the feed polarization rotates across the sky. For perfect CP feeds we have

$$\begin{aligned}
 \mathcal{V}_{RR} &= g_{Ra}g_{Rb}^*(I + V) \\
 \mathcal{V}_{LL} &= g_{La}g_{Lb}^*(I - V) \\
 \mathcal{V}_{RL} &= g_{Ra}g_{Lb}^*(Q + iU)e^{-2i\phi} \\
 \mathcal{V}_{LR} &= g_{La}g_{Rb}^*(Q - iU)e^{2i\phi}. \tag{2.2}
 \end{aligned}$$

Although feed imperfections alter these equations somewhat (see Chapter 3), astronomical considerations allow us to discriminate between the two bases. The significant polarization at submillimeter wavelengths is LP, represented by Q and U , while circular polarization (V) has not been observed. The LP visibilities (eq. [2.1])

mix the small but interesting Stokes Q and U with the dominant I , so the gains must be carefully determined in order to extract the linear polarization from differences of visibilities without introducing contamination from I . The CP visibilities fully separate the linear Stokes parameters from the total intensity, greatly reducing the potential for contamination. For this reason, linear polarization is usually measured interferometrically with CP feeds.

The SMA detectors are natively linearly polarized, so CP detection requires some mechanism for converting the polarization sensitivity of the feeds. Moreover, the SMA measures only a single polarization in each antenna at a time at a given frequency (although this will change for some frequencies in the future, see § 2.8), so polarization modulation is necessary to completely determine the incident polarization. The hardware described here serves to perform the linear-to-circular conversion and to allow rapid switching of the polarization sensitivity between LCP and RCP, so that all polarization information can be obtained nearly simultaneously.

2.3 SMA Optical and Polarization Design

2.3.1 Optics Overview

The Submillimeter Array is composed of eight 6-meter diameter antennas on alt-az mounts. The optical system was designed by Scott Paine and is described in detail in the SMA Project Book¹. SMA antennas are Cassegrain telescopes with receivers

¹http://sma-www.cfa.harvard.edu/private/eng_pool/table.html

mounted in a fixed cryostat at a Nasmyth focus, as shown in Figure 2.1. This receiver position assures that the receivers maintain a constant orientation relative to gravity, unlike the Cassegrain focus-mounted ALMA cryostat; this trivially eliminates the elevation-dependent changes in the receiver performance that might be expected from tilting the closed-cycle refrigerators.

Following the primary and secondary, the (up to) eight receivers in each antenna share mirrors 3 – 6 (Figure 2.1). Mirrors 3 (M3) and 6 (M6) are flat, when the telescope is pointed to the zenith they combine to form a periscope relaying the receiver beam to the secondary. M4 and M5 are curved and serve, with the lenses that are specific to each receiver band, to image the feedhorn aperture onto the secondary mirror. The lens and feed combination for each receiver creates a common virtual image and the feed illumination of the secondary is roughly independent of band and frequency. There is an intermediate image of the feed/secondary between the two mirrors that is likewise frequency independent, intended for use as a location for calibration loads and polarizing elements. M4 and M5 also form a periscope, which counterbalances the distortion from the two off-axis reflections.

No more than two receivers are usable at any one time, with the receiver selection made just after M6 through polarization splitting. In this design there are two types of receiver positions, “low” and “high” frequency, distinguished by their illumination. The low frequency receivers are illuminated by a rotating wire grid (the “combiner grid”). The grid wires are oriented in the plane of the page in Figure 2.2, so the reflected E-field polarization is also in the plane of the page. Although Figure 2.2 suggests four positions for receivers of this type, mechanical and polarization considerations make the primed positions (A', B') inconvenient

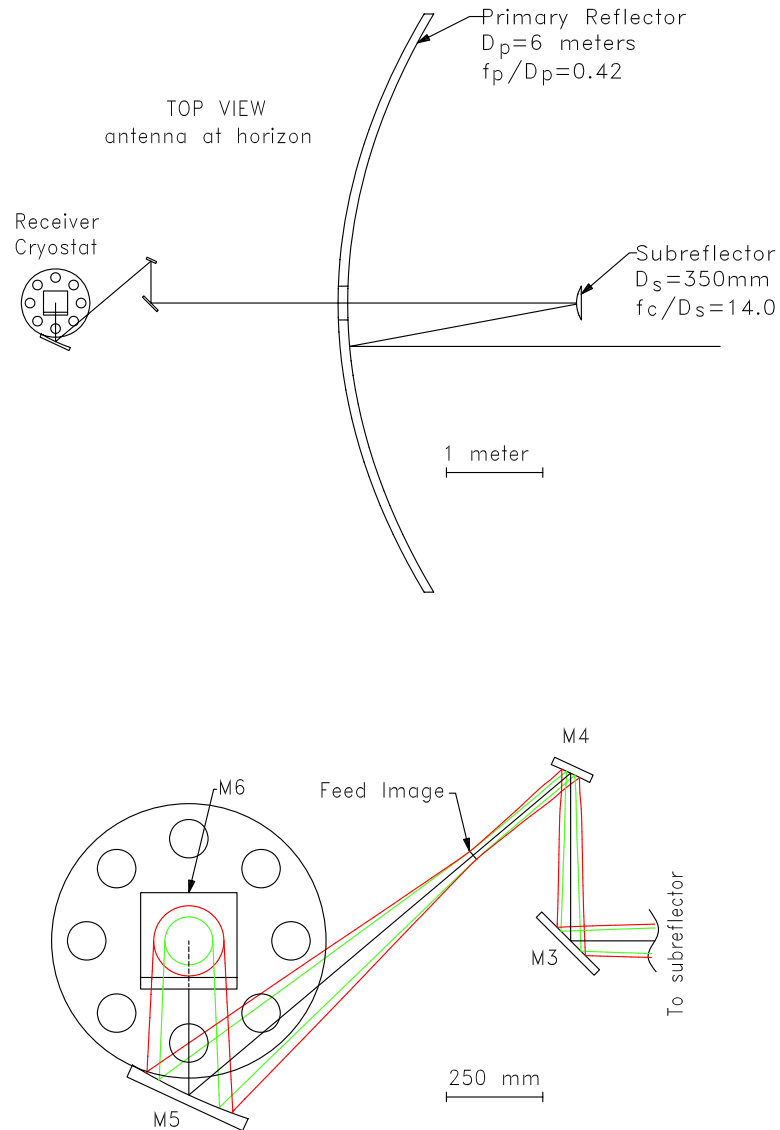


Fig. 2.1.— Scale drawing of the SMA optical system, adapted from the SMA Project Book. *Top:* The first six reflections of the SMA optics, viewed from above with the antenna pointed to the horizon. *Bottom:* An expanded view of the optics behind the primary mirror. Mirrors 3 and 4 (M3 and M4) are positioned along the elevation axis to relay the sky signal through a Nasmyth port. The 20 dB truncation levels for 216 and 460 GHz, representatives of the low and high frequency receiver beams are drawn from M3 onward. The 216 GHz beam is the larger of the two and approximates the largest receiver beam in the system. The receiver cryostat with its eight receiver ports is shown as well. Between M4 and M5 the beam converges to form an image of the secondary mirror (also the feed aperture) which is the approximate location of the calibration loads and wave plates.

and it is unlikely that these two will be installed. Thus the grid always points to position A or B and the low frequency receiver polarization at M6 is always along the A–B diameter. The high frequency receivers are illuminated by the polarization transmitted by the combiner grid, so their polarization at M6 is always perpendicular to the A–B diameter.

There are presently three receivers installed in all eight SMA antennas, the 230 GHz band (183 – 247 GHz) at position A, the 345 GHz band (265 – 355 GHz) at position B, and the 650 GHz band (600 – 700 GHz) at position E. The fourth receiver (320 – 430 GHz) is being installed at position C this year. The fifth and sixth bands will likely cover the 460 GHz atmospheric window and overlap with the 230 GHz band to provide dual polarization capabilities there, but it is not clear which will be built first or whether both will be built.

2.3.2 Polarization Implications

The early interest in polarimetry influenced the SMA optics design, which is in many ways very well suited for polarization observations. The Project Book specifies polarization-related design requirements including providing for a wave plate and limiting cross-polarization from the optics to less than that expected from the combiner grid. The cross-polarization requirement led to the choice of the M4–M5 relay, rather than the original single mirror turn between M3 and M6, because the smaller incidence angles on these mirrors reduced the induced cross-polarization. The image of the secondary between M4 and M5 naturally accommodates a wave plate.

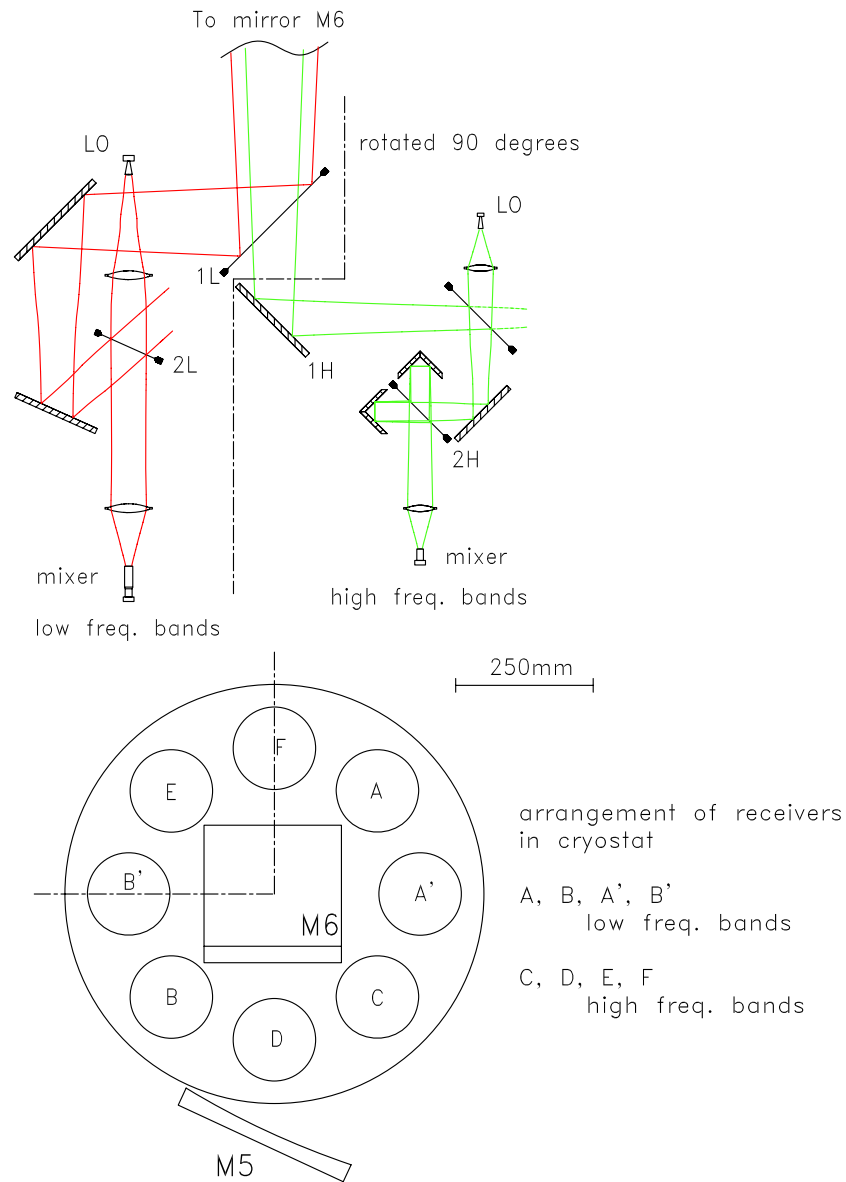


Fig. 2.2.— *Top*: Side view of the optics after M6. The low frequency beam is reflected off of the combiner grid (1L) and combined with the local oscillator (LO) through a beamsplitter (2L) before entering the cryostat. The high frequency beam is transmitted by the grid and directed toward the selected receiver by the combiner mirror (1H). For the high frequency receivers the LO is injected through a Martin-Puplett interferometer diplexer (2H), which more efficiently couples the LO to the mixer. *Bottom*: Another view of the receiver cryostat, shown in the same orientation as in Figure 2.1. Presently positions A, B, and E are occupied in all antennas by 230, 345, and 650 GHz receivers, respectively. Adapted from the SMA Project Book.

Other design requirements are also quite useful for polarimetry. The polarization diplexing that allows two receivers to observe simultaneously in the same beam will allow overlapping 345 GHz and 400 GHz receivers to obtain full polarization information in each integration. It also allows polarimetry at 230 and 690 GHz as discussed below. The combiner grid is also useful because it eliminates one source of instrumental polarization. Because there is an efficient (25 to 35 dB polarization purity) polarizer in the optical path (in transmission or reflection) the cross polarization of the receivers is rejected before reaching the sky. Such cross polarization can arise from angular misalignment of or imperfection in the feed. While the instrumental polarization (“leakage”) would be calibrated out, it would be expected to change each time a receiver insert is changed (a frequent occurrence with the SMA). Such polarization changes are evident in polarization calibration data from the BIMA array (Bower et al. 2002a), which shows large changes in polarization due to receiver modifications. This instrumental variability limited their ability to establish the stability of the instrumental polarization and required calibration after each receiver modification, something that may not be necessary if the stability of SMA leakages can be conclusively demonstrated.

The Nasmyth location of the SMA receivers differs from interferometers such as the VLA, BIMA array, Plateau de Bure Interferometer, and ALMA, which have their receivers at the Cassegrain focus. In alt-az antennas the feed polarization rotates relative to a polarization vector on the sky while tracking sources, unlike in equatorially-mounted antennas, but as discussed in Chapter 3 this behavior is useful for calibrating polarization. The Nasmyth mount introduces an additional elevation dependence to the parallactic angle that can be useful for calibration by further

modulating the parallactic angle, but it may also introduce problems that have not been examined at other observatories. Because instrumental polarization can arise on either side of M3, which creates the added elevation dependence of the parallactic angle as it rotates about the elevation axis, effects from the primary and secondary mirror are modulated differently than those from the receiver side of the mirror. The importance of this effect is discussed in the next chapter.

2.4 Polarimeter Optics

2.4.1 Wave Plate Designs

The fundamental piece of the polarimetry hardware is the linear-to-circular polarization converter, or quarter-wave plate (QWP). A QWP is an anisotropic optical element that introduces a delay of a quarter wavelength, a 90° phase shift, between orthogonal linear polarizations. The “fast axis” of the plate has a smaller index of refraction than the “slow axis”, and the thickness is tuned so that the path length difference is equivalent to a quarter of the observing wavelength. If the QWP axes are oriented at 45° to incident linear polarization, the polarization component along the slow axis is delayed relative to the component of equal magnitude along the fast axis and the output is pure circular polarization. By rotating the QWP by 90° the handedness of the circular polarization can be reversed.

Wave plates are ubiquitous in polarimetric experiments. Half-wave plates rotate linear polarization and are often used to modulate the polarization sensitivity of a detector of fixed polarization. Examples include the polarimeters for the

submillimeter cameras on the JCMT and CSO: SCUBA (Greaves et al. 2003) and SHARC (Novak et al. 2004), and various CMB polarization experiments including MAXIPOL (Johnson et al. 2003). Quarter-wave plates are often employed to generate circular polarization for interferometers with linear feeds, as was done with the BIMA array (Rao 1999). In the simplest case, free space half- or quarter-wave plates are single elements of birefringent material tuned in thickness to provide the appropriate path delay at a specific frequency. Because the delay is a propagation distance difference between the polarizations, the corresponding phase difference changes linearly with frequency. Multiple element designs can provide a nearly fixed phase delay over a large bandwidth, as was shown for three elements by Pancharatnam (1955) and more generally by Title (1975). These designs are less frequently used but may become common as a result of the bandwidth requirements of bolometer-based CMB polarization experiments (e.g. Hanany et al. 2005).

The SMA polarimeter uses two sets of single-element quarter wave plates to allow polarimetry in each of the three observing bands. One set of QWPs is tuned to 345 GHz, while the second set works as a QWP at 230 GHz and a three-quarter-wave plate at 690 GHz, achieving the same linear-to-circular conversion. Using the polarization diplexing discussed above, the 230/690 QWP allows polarimetry at both frequencies simultaneously. This scheme results in QWPs that are much easier to assemble and align than multi-element plates and limits internal absorption by reducing their thickness. The 12 GHz inter-sideband span of frequencies in a single observation is a small fractional bandwidth (5% at 230 GHz) and so this design does not prevent both sidebands from being simultaneously useful for tunings near to the design frequencies. A broadband design would allow coverage of the full

RF bandwidth of a given receiver band, or possibly all bands at once for very complicated designs (e.g. Masson & Gallot 2006), but there are few spectral lines that are interesting for polarimetry and little to be gained by continuum polarimetry at two frequencies widely separated within a single receiver band. The current QWPs do perform well at the CO lines, which have previously been seen to be weakly polarized, as well as at the strong maser lines at 217 GHz (SiO), 325 GHz (H₂O), and 658 GHz (H₂O).

2.4.2 Wave Plate Materials

Wave plates can be made from materials with natural or manufactured birefringence. The SMA wave plates are made from low-loss naturally anisotropic crystals; all of the plates are x-cut crystalline quartz except for a single sapphire plate from the original polarimeter prototype. Quartz has indices of refraction of 2.106 and 2.154 for its ordinary and extraordinary axes, respectively, so the index of refraction difference is $\Delta n = 0.048 \pm 0.005$ (Birch et al. 1994). For a design frequency ν , the QWP thickness is given by:

$$t_{QWP} = \frac{c}{4\nu\Delta n}, \quad (2.3)$$

so this 10% fractional uncertainty in Δn translates directly to uncertainty in the tuning frequency of the plates. However, calibration of the 340 GHz quartz QWPs show them to be tuned to their design frequency to within 3%, indicating that the literature value of Δn is similarly accurate. Sapphire has larger indices of refraction, 3.064 and 3.404 (Afsar 1987), and a much larger birefringence, $\Delta n = 0.3390 \pm 0.0001$, which allows sapphire plates to be about seven times thinner than quartz plates.

2.4.3 Anti-Reflection Coatings

To minimize sensitivity loss and standing waves resulting from the QWPs, anti-reflection (AR) coatings have been applied. The ideal (monochromatic) AR coating is a quarter-wave thick with an index of refraction that is the geometric mean of the indices of the materials on either side of it. For quartz in air this is roughly 1.46, which is fairly close to the index of low-density polyethylene (LDPE), $n_{LDPE} = 1.514$ (Lamb 1996). The larger index of sapphire is not particularly well matched by common polymer materials although Hanany et al. (2005) use a form of fused quartz known as Herasil with an index of refraction of 1.87 as an AR layer for a sapphire wave plate. Despite the poorer match, the SMA sapphire plate was also coated with LDPE. Figure 2.3 shows the expected normal-incidence transmission along both axes of the 345 GHz quartz and sapphire plates, ignoring the small ($< 1\%$) absorption expected in the plates.

AR coatings were permanently bonded to the QWPs through a process described in Paine (1992). The quartz or sapphire is sandwiched between sheets of LDPE which have a total thickness approximately 10% larger than the desired coating thickness. This stack is placed between sheets of polytetrafluoroethylene (PTFE, or Teflon) to prevent the LDPE from adhering to surfaces other than those of the wave plate. The whole stack was placed between two flat surfaces and baked at 170°C for four hours under 0.25 psi pressure to melt the LDPE onto the substrate. The 345 GHz SMA QWPs coated in this way have a typical coating thickness accuracy of $\pm 10\%$ and a similar degree of peak-to-peak thickness variation (wedge) across the surface.

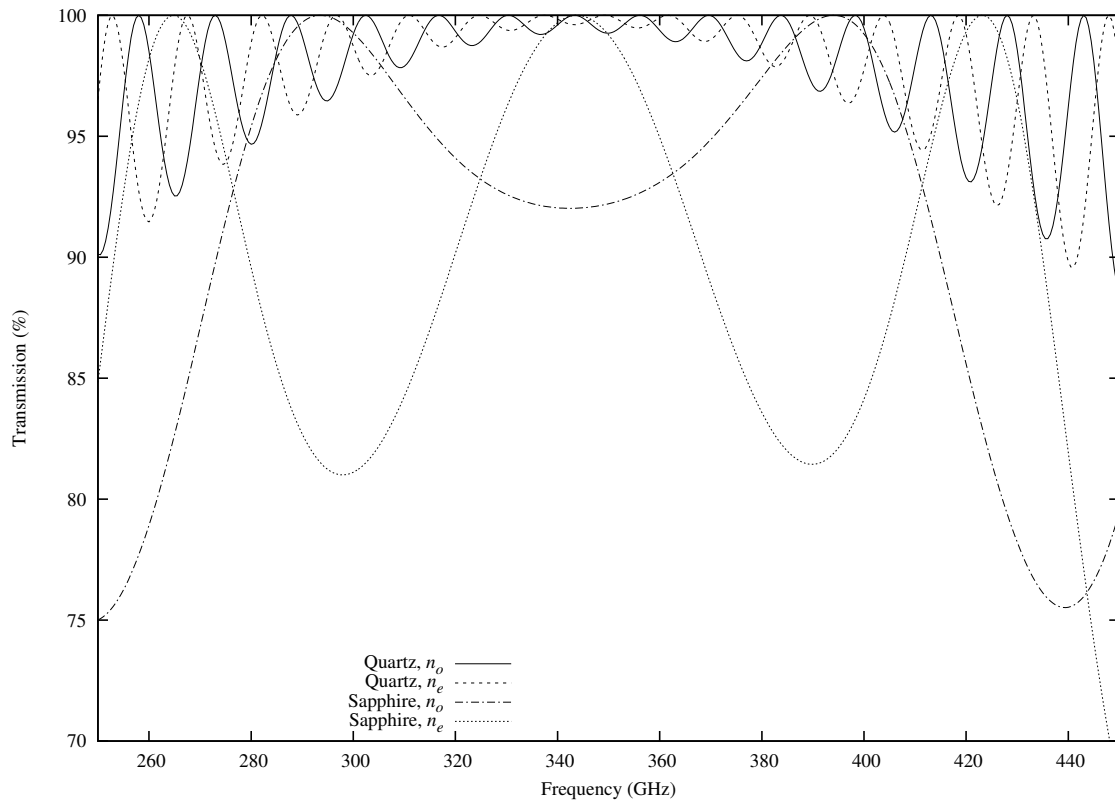


Fig. 2.3.— The expected transmission for quartz and sapphire QWPs with LDPE AR coatings, with transmission shown for both axes of each crystal. The plates and coatings are tuned for a frequency of 345 GHz. The sinusoidal modulation in the transmission ($c/2nt_{QWP} \simeq 16$ GHz for the quartz) results from reflection off of the back surface of the birefringent material, so the slow modulation in the sapphire reflects the fact that it is much thinner. The transmission calculation makes use of the characteristic matrix technique of Born & Wolf (1999).

Because of the difficulty of observing in the 650 GHz band, greater coating precision was desired for the 230/690 GHz QWPs to minimize their loss at 690 GHz. These QWPs were given a thicker coating than the target thickness of 215 μm and the LDPE was removed from three small pads at the edges on each side of the plate. These bare surfaces provided references from which the thickness of the coating could be measured directly. The coating thickness was then turned down in a precision lathe and specially designed collet. The frequency of peak transmission was then verified in the Fourier transform spectrometer (FTS), as shown in Figure 2.4. The coating thickness was tuned in steps as small as 10 μm based on the peak frequency measured with the FTS, corresponding to changes of approximately 16 GHz in the location of the transmission peak. Typical peak transmission near 690 GHz was around 95%, which reflects absorption in the quartz at this high frequency. At 230 GHz the absorption is expected to be less than 2%.

The transmission of the QWPs and their effect on SMA performance has also been measured at the telescope. The receiver temperature was measured with and without each QWP in the beam of one antenna and these were compared to determine the transmission. Measurements were made with the QWPs tilted slightly from the beam axis so that any reflected power was terminated in an ambient temperature load, rather than being directed back toward the cold receiver, just as the absorbed power is terminated in an ambient temperature QWP. The results of these measurements are reported in Table 2.1. The 684 GHz result is consistent with the transmission measured with the lab FTS for the 230/690 GHz waveplates. The wavelength scaling of the transmission is also consistent with the loss at all frequencies being due to absorption in the quartz, indicating that the AR

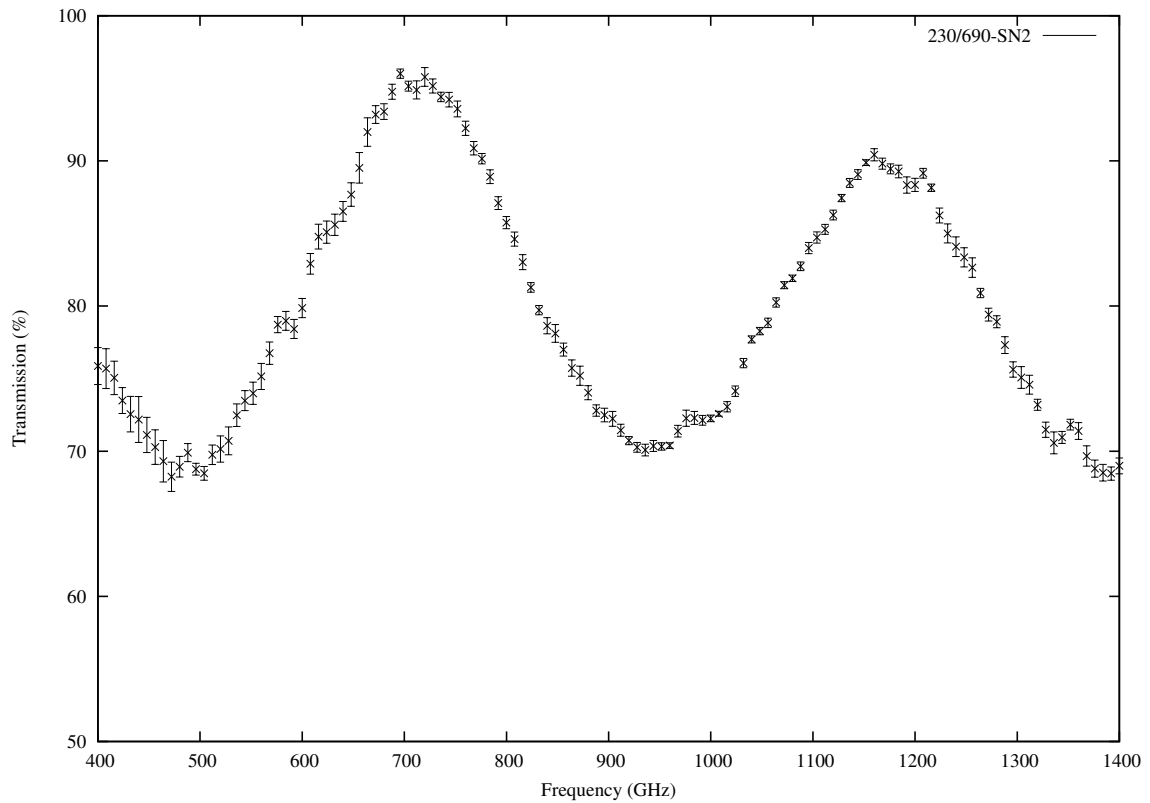


Fig. 2.4.— Transmission spectra of an SMA 230/690 GHz QWP. The spectrum was obtained with the Receiver Lab Fourier transform spectrometer at a resolution of 8 GHz. The sensitivity is limited below 400 GHz by the weak emission of the thermal backlight and above 1400 GHz by filters at the input to the bolometer detector.

coatings are well tuned to their design frequencies. The fractional change in receiver temperature is also shown to indicate the impact the waveplates have on the receiver performance. In real observations the waveplates are normal to the beam axis and much of the reflected power is terminated at low temperature in the receiver, so it is found that the change in T_{rx} at frequencies away from the optimum for the AR coating is not very much worse than that shown here.

2.5 Positioning Hardware and Control System

In order to convert the SMA to circular polarization sensitivity the QWPs must be repeatably aligned to the feed polarization and be rotatable to select LCP or RCP. This is achieved with a computer-controlled mount and rotation system, the wave plate positioning hardware. The QWPs are held in a commercially available rotation stage (Opto-Sigma Polarizer Holder 114-0250) with a PTFE slip ring bearing. A gear with a large clear central aperture is mounted to the rotation stage and driven by a gear attached to a small DC motor (Faulhaber Series 1319S). There is no encoder to monitor the motor position, rather, the wavplate positions are determined by two optical brakes (opto-interrupters) and four adjustable positioning flags on the circumference of the rotation stage. These flags determine four angular positions for the waveplate, two of which set the $\pm 45^\circ$ position angles that convert the feed polarization to left- and right-circular polarization. The other two flags are monitored by a second optical brake and set positions $\pm 22.5^\circ$, allowing half-wave plates to switch a feed between two linear polarizations 90° apart. See Figures 2.5 and 2.6.

The wave plate positioning hardware operates and interfaces with the rest of the array through dedicated control computers. Each wave plate mount is controlled by a compact (PC-104 form-factor) disk-less computer with a 66 MHz 486 processor and ethernet adapter, identical to those used to control the SMA optical guidescopes. The computers run a version of Red Hat Linux through a virtual filesystem mounted across the ethernet connection. A remote procedure call (RPC) server is kept running to respond to requests for position changes from the central observing computer, `ha19000`. The RPC server controls the plate movements, reports failures in acquiring positions, keeps track of the current position, and can re-initialize the rotation stage to re-establish the location should it be lost due to loss of power or a failure in positioning. The computer is packaged with circuitry to drive the motor and power supplies for the computer, motor, and opto-interrupters, so the entire polarimetry system consists of just the computer box and the wave plate mount. A single cable provides a connection between the motor, optical brakes, and computer, and a second cable provides an ethernet connection, computer reset line, and console output. The full system for eight antennas is shown in Figure 2.5. Circuit diagrams, part lists, and cable pinouts are provided in Appendix A.

Stability of the polarization properties of the SMA requires precisely repeatable positioning of the QWPs. Hard stops could be used to set the positions, but frequent impact against stops (as often as every 15 seconds) could accelerate wear on the drive system and cause the stop to move over time. Encoders were also deemed inadequate as it would usually be impossible to detect errors in the encoder from the appearance of the real time data and unnoticed position errors would render the data useless. Instead we rely on the optical brakes and a two-step positioning cycle. In

Table 2.1. Measured QWP Transmission

Waveplate	Frequency ¹ (GHz)	Transmission (%)	$\Delta T_{rx}/T_{rx}$ (%)
345	342	97.9	9
230/690	227	98.4	10
230/690	684	94.4	8

¹Denotes local oscillator frequency. The transmission measurement averages the response of the two sidebands.



Fig. 2.5.— The SMA wave plate positioning system. The eight wave plates and their positioning stages are in the foreground. See the rotation stage detail in Figure 2.6. The control computers and associated electrical components are in the enclosures at the back. The ruler in the foreground is 30 cm long.

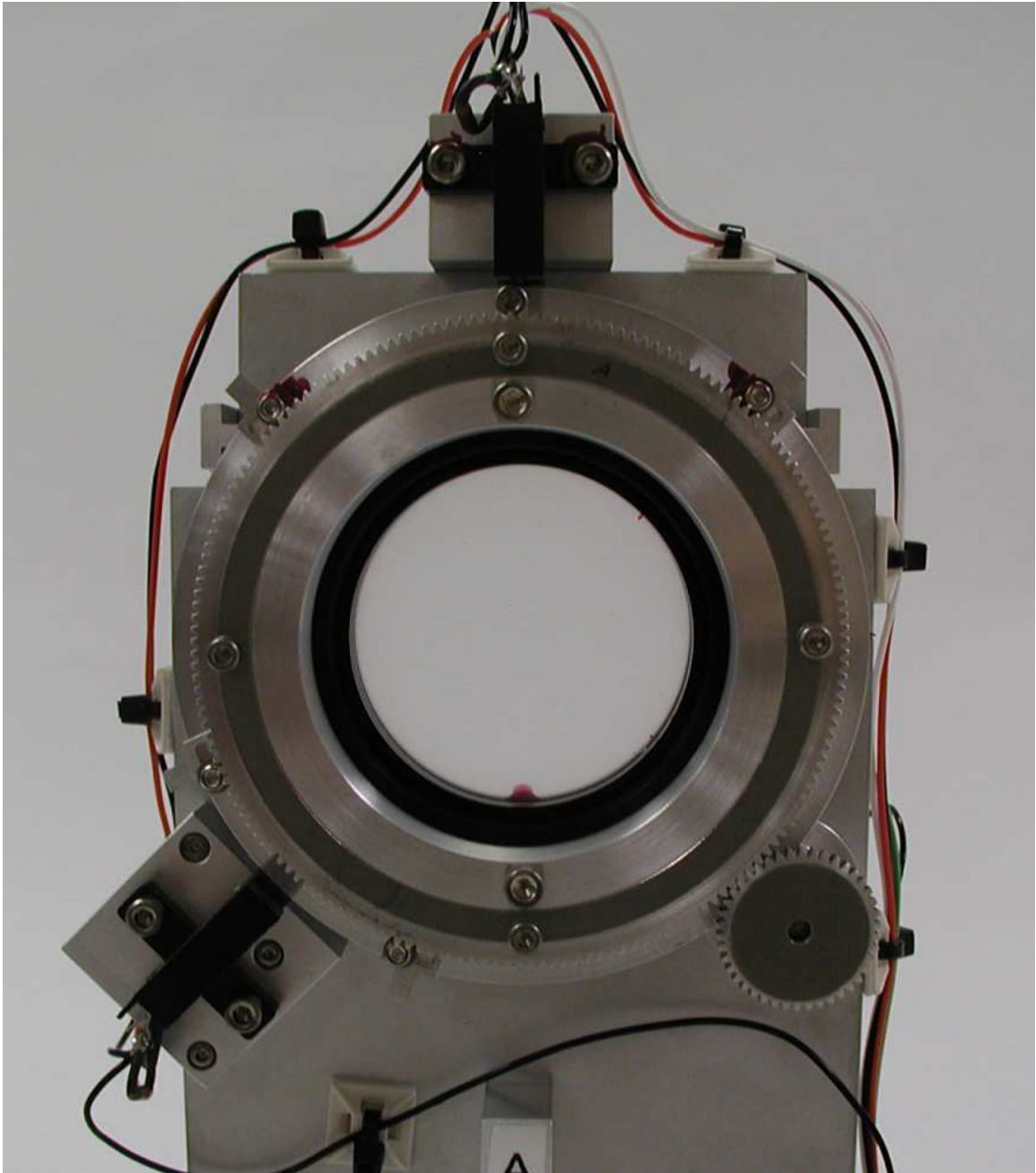


Fig. 2.6.— Closeup of the rotation stage and QWP in a wave plate positioner. Optical brakes are visible at the top and the bottom left. The adjustable flags that determine the wave plate positions are visible on the circumference of the rotation stage at $\pm 45^\circ$ from the top and at $\pm 22.5^\circ$ from the optical brake at the bottom left. The drive gear is visible at lower right. The alignment ring is affixed to the rear surface of the QWP.

the first step, the motor slews the QWP to the commanded position, stopping only when the appropriate optical brake (opto-interrupter) is interrupted by a flag. The rough angular difference between the initial and final positions allows the software to estimate the switching time and slow switches are reported as invalid. Because of the variable deceleration across the wave plate mounts, the position determined in this way can be inaccurate by a degree or more and might be expected to change with temperature as the frictional loading is changed. Much greater accuracy is obtained in the second step, where the motor makes rapid pulsed movements until the correct edge of the flag (depending on the initial and final positions) is driven out of the opto-interrupter beam. Measurements of the positional repeatability achieved through this procedure found it to be better than the measurement precision, around 0.2° , which is more than adequate given the astronomical calibration limitations.

The SMA polarimetry system uses two different QWPs to cover the three SMA receiver bands (§ 2.4.1), so provision has been made to allow the QWPs to be interchanged without loss of angular alignment. After the alignment procedure discussed below, an alignment ring is epoxied to each QWP. The ring fits snugly into the clear aperture of the rotation stage, ensuring that any non-centrality of the QWP in its mount is retained from installation to installation. The angular position is marked by machining alignment slots into the ring and rotation stage along a slightly off-center chord across the QWP. When switching plates, the position can be recovered by inserting a shim matched to the chord length and slot width into the alignment slots. The angular position can be established to around $20 \mu\text{m}$ on a roughly 50 mm diameter, or roughly a twentieth of a degree.

The SMA QWPs must switch rapidly between the left- and right-circular

polarization states to limit the observing time lost to switching. The motor and gear ratio have been chosen to ensure that the switch between the widely separated LCP and RCP positions can be achieved in less than 2 seconds in either direction on all bases. The friction of the commercial rotation stages was tuned by adjusting the pressure applied to the PTFE slip ring. In the final configuration, all the positioners switch in 1.5 – 1.9 seconds.

2.6 Wave Plate Alignment

The wave plate positioning hardware, when properly aligned, switches wave plates through 90° with the QWP axes positioned exactly vertical or horizontal in each position. This alignment was achieved in two steps, one to optically establish the switching angle and transfer the vertical and horizontal axes to a polarizing grid, and a second to align the QWP axes to the grid through measurements made at the QWP operating frequency. A separate measurement was also made to verify the identification of the fast axis of the QWPs (lower index of refraction), so that the left- and right-circular polarization states could be properly identified. These procedures are described in this section.

2.6.1 Optical Alignment

The initial alignment procedures for the SMA polarimetry system address mechanical aspects of the system rather than polarization response, and therefore were performed with visible light techniques. The optical alignment provided horizontal, vertical,

and beam center references that were later transferred to components throughout the alignment setup. An alignment telescope with rotatable crosshairs was used to retain and transfer the reference positions and directions. The telescope line of sight was aligned to be parallel to the surface of the underlying optics bench (and aligned to the grid of holes for the sake of convenience) through adjustment of the two mirrors seen in Figure 2.7. The parallelism and height were set through observations of a combination square at different distances along the line of sight. With the reference line established, components used in the polarization alignment, such as the bolometer, were centered on the reference line. The vertical axis (the normal to the optics bench surface) was also obtained from the combination square. One axis of the telescope crosshair was aligned to edge of the scale; for the telescope and scale used in these measurements this crosshair should be normal to the surface to a small fraction of a degree, limited by the distortion of the image of the scale at the edge of the field.

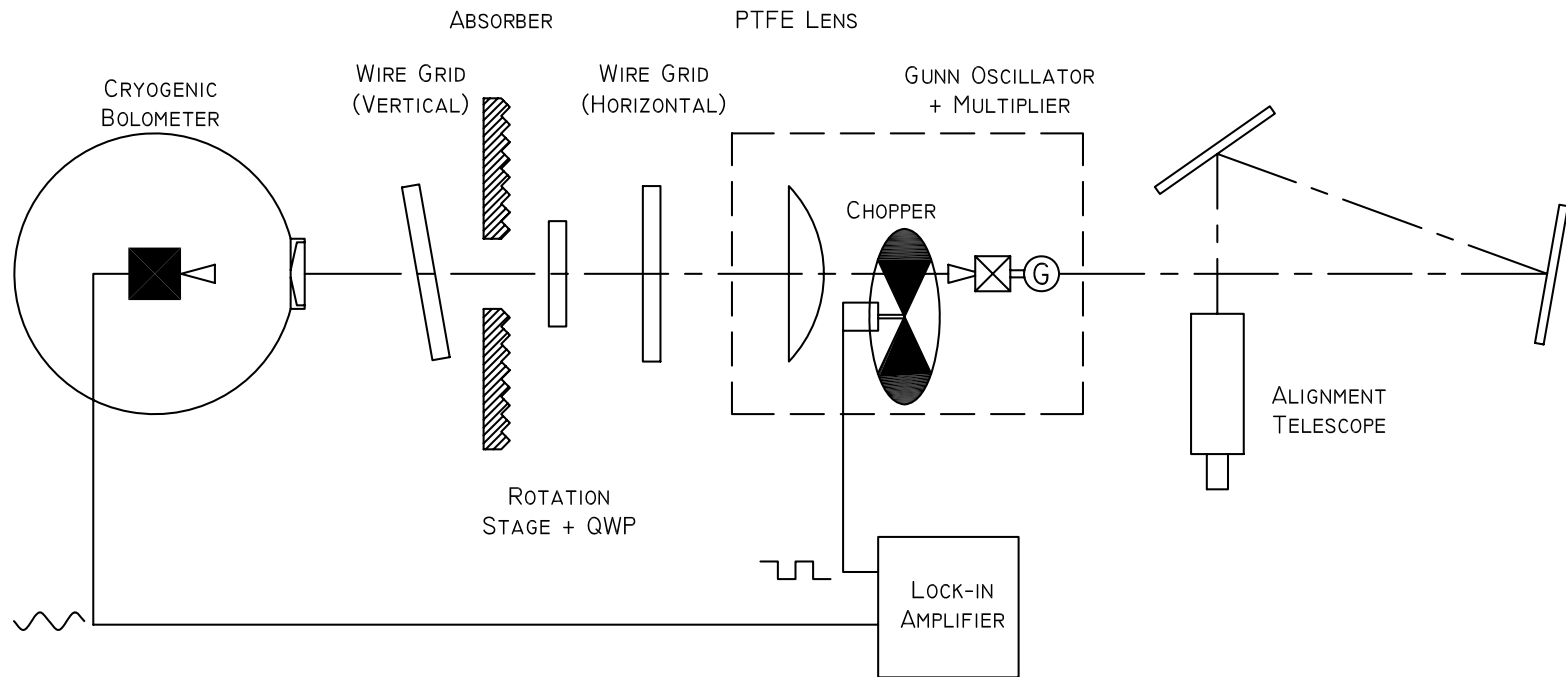


Fig. 2.7.— The alignment setup used with the wave plate positioning hardware. Components are arranged on an optical bench. For the optical alignment the components in the dashed box are removed and the other components are centered on the axis established by the alignment telescope line of sight. The polarization alignment procedure makes use of a lock-in amplifier, which synchronously detects the modulated power from the local oscillator (as measured by the bolometer) using the reference signal (~ 100 Hz) from the rotating chopper wheel.

The angular position of the rotation stage in each of the available polarization states was also determined through optical alignment. The positions are determined by the “flags”, seen in Figure 2.6, which interrupt the beam of the optical brakes. A paper target, affixed with double-sided tape for easy repositioning, provided diameters matched to the size of the rotation stage and spaced by 45° . For each wave plate positioner the paper target was iteratively centered on the axis of rotation of the rotation stage and this axis aligned with the line of sight from the telescope. Each flag was carefully adjusted to align a diameter on the target with the telescope crosshairs. The upper two flags were set 90° apart for switching a QWP between circular polarization states, while the lower two were set 45° apart for a half-wave plate switching between linear polarization states. Based on the linewidth on the target and the size of the split crosshair used for the fine alignment, each flag should be correctly set to $\pm 0.2^\circ$. After all the flags were set for a given positioner, the rotation stage was clamped in the position for left-circular polarization. The act of immobilizing the stage can cause rotation, so the angular position was monitored with a loupe while clamping. The monitoring ensured that the locked stages were within 0.3° of the positions acquired under computer control. Finally, the alignment telescope was used to align the nearest wire grid (Figure 2.7) so that its wires were horizontal. This step tied polarization coordinates for the subsequent alignment steps to the normal to the bench surface. With the optical alignment complete, the paper target was removed, and the PTFE lens and local oscillator (LO) chain (Gunn oscillator with frequency multiplier) were inserted along the optical axis.

2.6.2 Polarization Alignment

Polarization alignment was performed separately with each QWP through measurements made at its design frequency (either 230 or 345 GHz). The alignment procedure used crossed wire grids to null a large modulated signal from the LO, with the bolometer readout synchronously detected in a lock-in amplifier (see Figure 2.7). A QWP inserted between the crossed grids converts a component of the vertical polarization transmitted by the first grid into horizontal polarization that will be transmitted by the second grid, except when one of the QWP axes is aligned with the incident polarization. This allowed direct access to the QWP axes for alignment to the rotation stage.

The procedure outlined above produced very sensitive alignment of the QWPs. The wire grids were manufactured in the lab and have 20 μm dia. wires on a 60 μm pitch, with a typical r.m.s. pitch variation of a few microns. The far (vertical) grid was aligned by minimizing the LO signal that reaches the bolometer in the absence of a QWP. The power reflected by the grid was largely terminated on the absorber, which has a 3 cm diameter aperture centered on the telescope line of sight, and the grid is skewed from the beam axis to prevent polarization-converting back reflections from the absorber and QWP. The signal attenuation from the crossed grids (referenced to the signal transmitted by the first grid) was typically 33 and 30 dB for 230 and 345 GHz measurements. With the QWP installed the minimum power was comparable to that measured without the plate, typically $\pm 10\%$ or less. Small QWP rotations showed a quadratic variation of transmitted power with angular shift, allowing calibration of position errors from measurements of power

changes. After locking the QWP in place, the transmitted power was measured for both CP positions under computer control. The power in the state used for alignment was well reproduced, indicating that the rotation stage was not rotated when clamped at the level of 0.2° . Power transmitted in the other circular position was often different by several percent, probably indicating differences in the AR coating performance along the two axes, but again corresponded to local minima at the level of 0.3° . Because the crystal axes are orthogonal, this indicates that the switching angles are 90° to within approximately 0.3° in most cases. One exception was observed where the switching angle was smaller by 0.5° .

Each wave plate positioner required two polarization alignment steps to prepare QWPs for both frequencies. After the alignment of each QWP an alignment ring was installed and its alignment slot machined. The registration of the rotation axis of the positioner to the line of sight in the alignment setup was re-established through the use of stops or with new paper target measurements, depending on the interval between the alignment of the first and second QWPs.

2.6.3 Fast Axis Verification

The circular polarization handedness is determined by the relative orientation of the feed polarization and the fast axis of the QWP. For the SMA, with four reflections between the QWP and the sky, each of which reverses the CP handedness, the fast axis should be oriented vertically for detection of RCP, as shown in Figure 2.8. Here we employ the handedness convention from IAU (1974), where the electric field from the sky rotates counter-clockwise (position angle increases) with time when viewed

from the ground.

In order to establish the correct orientation of the QWPs we need only determine the direction of the fast axis. The QWPs were manufactured with a small flat marking the position of one axis, but the accompanying documentation was not clear about whether the flat runs parallel or perpendicular to the direction of the fast axis. To resolve the ambiguity, the fast axis orientation was measured directly in the lab. A QWP was placed between a Gunn oscillator with a tripler and a detector. The Gunn was locked to a harmonic of a synthesizer at 16–20 GHz and with a phase-lock IF of 80 MHz provided by another synthesizer. The high frequency synthesizer was used to down-convert the detected signal through a harmonic mixer. The resulting IF signal was compared to the tripled 80 MHz signal in a vector voltmeter. The phase change between the two QWP axes was noted and the sign of positive delay was determined by introducing a sheet of paper to the beam and observing the sign of the phase change. This experiment indicated that the flat is parallel to the fast axis direction, as shown in Figure 2.8. This determines the expected polarization handedness, a result which has been confirmed astronomically (§ 3.7).

2.7 Polarization Observations

2.7.1 Polarization Switching

At present the SMA has only a single feed in each band and therefore cannot sample both polarizations at the same frequency simultaneously. To recover the full polarization information we use the wave plates to switch the antennas between

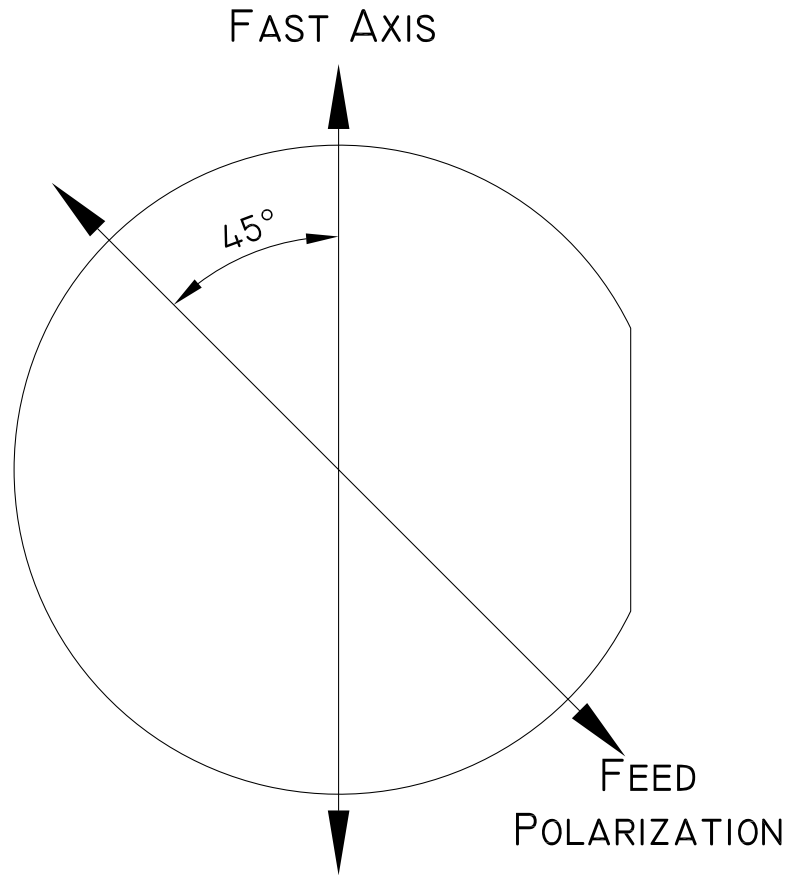


Fig. 2.8.— Orientation of the SMA QWPs for the detection of right-circular polarization. The view is from M5 looking toward M4 (see Figure 2.1). The feed polarization for low frequency receivers and the QWP fast axis are marked. The flat on the edge of the QWP is also shown, exaggerated in size for clarity. This configuration is valid for the SMA 230 and 345 GHz receivers, which have the same polarization at the QWP. The 230/690 QWP oriented in this way also yields RCP at 690 GHz because the orthogonal feed polarization for this receiver and the three-quarter wave delay of the plate each reverse the handedness and result in no net change in sky polarization.

LCP and RCP in a coordinated temporal sequence. The switching patterns of the antennas are described by orthogonal two-state sequences known as Walsh functions. Walsh function phase modulation is already employed in the SMA to permit separation of the sidebands from the double-sideband mixers and to suppress low frequency noise. By carefully selecting from the 16 period-16 Walsh function patterns, as described for up to seven antennas in Rao (1999), it is possible to quickly sample all four polarized correlations on each baseline (Appendix B). In the optimum choice of functions, 22 out of the 28 baselines in the full array obtain all four polarizations each quarter cycle, four baselines sample all four polarizations twice each half cycle, and two baselines require averaging over the full cycle of 16 steps to sample all the polarization states (four times each). Averaging the visibilities over the cycle time (or shorter times with the loss of a few baselines) results in quasi-simultaneous measurements of all polarizations.

Integrating the polarization switching into the existing SMA observing infrastructure required a great deal of software development and the use of careful observational techniques. The most significant change was the introduction of a new correlator capability to reduce the data loss resulting from the wave plate switching. Normally the SMA correlator runs continuously, accumulating data into integrations of tens of seconds (typically 30 seconds), with several integrations obtained consecutively on each source. Integrations obtained while slewing between sources are automatically discarded, but these are a small fraction of the total integration time. In polarimetry, however, the polarization of at least one antenna (on average, half of the antennas) will be altered after each integration and during the switch the incoming data samples are invalid because the wave plate is not yet

in position. Rather than discarding the first integration of each polarization state, Ken Young has created a paused state for the correlator that is activated while the wave plates switch. The correlator remains paused for integral periods of the SMA phase switching cycle, 2.58111 seconds when 8 antennas are in use (although it could be made a factor of four shorter with 7 antennas) and resumes once the software is notified that all wave plates are ready. This correlator integration quantization was the motivation for the 2 second upper limit on the switching time described in § 2.5, but in practice the correlator always remains paused for two cycles, most likely because of the large number of communications across the summit network required in order to notify all the relevant computers of the correlator pause, start the switch, detect its completion, and start the next integration. With this 5 second loss per integration, complete 16-step polarization cycles require 4–7 minutes for 10–20 second integrations, yielding temporal efficiency of 67%–80% within the cycle, rather than the 50% that we would obtain without the pauses. Unfortunately, the pauses make the correlator much more prone to losing synchronization than it otherwise would be. This can manifest itself as complete stoppages of the correlator, or more insidiously as a loss of synchronization in a subset of the (twelve) correlator crates. This latter problem allows data from a previous integration in one sixth or more of the bandpass (each crate correlates this fraction of the bandpass) to be combined with the current integration on one or more of the baselines. This problem may be present quite frequently, but it would not affect normal observations that integrate on the same source for several integrations and flag all integrations at source transitions. The modulation introduced into polarimetry data by the switching requires that each integration be clean, otherwise the contamination makes it appear

that the polarized leakages (see Chapter 3) are unphysically large. As of April 2006 the correlator software problem that admits this loss of synchronization was still unsolved, although there is some as-of-yet unconfirmed hope that a recent bug fix will be the cure. In the face of this potentially catastrophic problem, polarization observations have required heightened vigilance and real-time examination of the correlations on strong sources to catch and correct the error immediately. A simple restart of the correlator (typically requiring a few minutes) is usually adequate to restore normal correlations.

To limit the signal loss resulting from rotation of the baseline vectors in the uv -plane over the polarization cycle averaging interval we must keep the cycle length short. Losses from time averaging depend on the direction of the baseline, source declination, and offset from the phase center (there is no effect for sources located at the phase center). To estimate the longest averaging time we could use, we consider the longest baseline achievable with the SMA, around 500 meters, a source point at the eastern or western edge of the primary beam, and for convenience assume an east-west baseline (as in, e.g., Thompson et al. (2001); Taylor et al. 1999). For averaging time τ , synthesized beam radius θ_b , and angular offset from the phase center θ_s , the small loss approximation of the response to a point source is (Thompson et al. 2001 eq. [6.81]):

$$R \simeq 1 - 0.231 \left(\frac{\omega_e \tau \theta_s}{\theta_b} \right)^2, \quad (2.4)$$

where ω_e is the angular velocity of the Earth. Because θ_b and θ_s appear as a ratio, the frequency dependences of the synthesized beam and the offset from the phase center (bounded by the radius of the primary beam, θ_B below) cancel, and we are

left with the ratio of the baseline length to the antenna diameter (or the number of synthesized beamwidths across the primary beam). For our 6 meter antennas this ratio is around 100 for 500 meter baselines. We can then rewrite equation 2.4 as:

$$R \simeq 1 - \left(\frac{\tau}{300s}\right)^2 \left(\frac{\theta_s}{\theta_B}\right)^2 \left(\frac{D}{500m}\right)^2. \quad (2.5)$$

This suggests that for polarization observations in the very extended configuration, we will lose significant information on the smallest angular scales at the edge of our primary beam with our typical cycle times of a few minutes. However, the losses drop quadratically as the distance from the center of the field decreases and as the baseline length (D) decreases. While losses of this type may be of concern for very long baselines and large fields, the effect will be 5 and 50 times smaller in the extended and compact arrays, respectively. Polarimetry of an extended source has not yet been attempted in even the extended configuration (although the point source Sgr A* was observed with the very extended array in July 2006). On the longest baselines in that configuration, using a 4 minute cycle, an image of the inner quarter of the primary beam would produce a loss of only a few percent at the edge of the field. For few minute cycles in the compact array, the effect should be negligible across the field.

2.7.2 Sensitivity

The sensitivity achieved during SMA polarimetry is degraded relative to normal observations by three effects: the switching overhead, the time-sharing between co- and cross-polarized integrations, and the system temperature degradation caused by the wave plates. As discussed above, the current dead time of 5 seconds leads to

67%–80% temporal efficiency for 10–20 second integrations. However, only half of the remaining integration time can be counted toward the sensitivity in any one Stokes parameter, because each polarization state (RR, LL, RL, LR) measures just two of the four Stokes parameters. Therefore, within a one-hour segment of polarimetric data, just 20–24 minutes of integration time will sample each Stokes parameter. Finally, the reflectivity and absorptivity of the wave plates add roughly 10% to the receiver temperatures, as shown in Table 2.4.3. In total, the noise in polarimetric data should be increased by a factor of 1.7–1.9 over conventional SMA observations.

The noise in polarization maps is consistent with the measured system temperatures, within the $\sim 10\%$ uncertainties from pointing errors, variable antenna efficiencies, and other low-level effects. For example, within a 230 GHz track on 2005 July 20, the predicted r.m.s. noise in each Stokes parameter is 5.7 and 6.3 mJy for the observations of the quasars NRAO 530 and BL Lac, respectively. The observed noise levels are 5.2 ± 0.5 and 6.9 ± 1.0 mJy. Similarly, in the 345 GHz track on 2005 June 6, the expected noise for the same sources is 12.3 and 17.2 mJy, while the observed noise is 12.7 ± 0.5 and 15.6 ± 0.7 mJy.

2.8 Future Modifications to the SMA Polarimeter

The polarimeter is intended to be a permanent part of the SMA and has already been made available for public proposals. To become a regular observing mode it is important that the hardware transition from an experimental state to something more integrated with normal SMA operations. For example, in all past observations

the wave plates had to be placed in the telescope beam manually. However, the new SMA calibration load system has been designed with a mount for the wave plate positioning hardware to allow automatic wave plate installation. The positioners attach directly to a translation stage on the calibration system which inserts them into the beam under computer control just as it does for the hot and ambient calibration loads. This should allow polarimetry to be queue scheduled like other observations and should reduce the danger to the array presented by manual installations of hardware near to fragile optics. The control hardware for the wave plates remains intact and the alignment is unaffected, so no changes are required in the software or observing procedures.

The SMA is in the process of adding a fourth set of receivers to cover 320 – 430 GHz and provide overlap with the existing 345 GHz band (265 – 355 GHz). In the SMA optics scheme these two bands can observe orthogonal polarizations at the same frequency. The correlator can be configured to cross correlate the signal from each band and across both bands on each baseline (four cross-correlations per baseline), providing complete polarization information. For reasons discussed in §2.1 circular polarization is the preferred basis set for interferometric observations of linearly polarized sources, so the wave plates will still be required for polarimetry with two receivers. Sensitivity will increase by a factor of $\sqrt{2}$ because we will measure both polarizations simultaneously. However, because we can observe in a single wave plate orientation for longer periods instead of switching at each integration, we will greatly reduce the substantial switching overhead that presently degrades our time efficiency. The combination of these effects should increase the sensitivity by up to $\sqrt{3}$. The 230 GHz band may also be paired with a receiver of opposite polarization

but not before the fifth or sixth set of receivers, while the 650 GHz band can never be paired because of the layout of the receiver selection scheme. For the foreseeable future these two bands will require the rapid polarization switching technique used for all polarimetry to date.

Chapter 3

Polarization Calibration

3.1 Introduction

Polarization is usually neglected in millimeter and submillimeter observations because the thermal sources that dominate at these wavelengths typically have very low linear polarization fractions and no circular polarization. Nevertheless, in many types of objects there is important information encoded in the polarization properties. The SMA provides the first opportunity to examine polarization at both high frequencies and high angular resolution, but in order to obtain accurate polarization measurements the response of the array must be carefully calibrated. In this chapter I discuss the polarimeter calibration, beginning with the theory of interferometer polarization response (§ 3.2) and the observational techniques employed in calibration (§ 3.3). The relationship between wave plate properties and instrumental polarization are examined in § 3.4. The calibration results, the precision expected from the data, and other concerns are covered in the remaining

sections.

3.2 Interferometer Polarization Response

Interferometric polarimetry requires consideration of the polarization properties of individual antennas, the joint response of two antennas, and the polarization distribution of the sky. Single-antenna detection can be described with linear transformations of the input electric field (described by two orthogonal polarizations) to the output detection voltages. Through a product of these linear transformations, represented as 2×2 matrices known as Jones matrices (Jones 1941), the many physical effects of the antenna can be assembled into a single response function. As shown in Hamaker et al. (1996), the transformation resulting from the cross-correlation of two antennas (the interferometer response) can be described by the outer product of the individual antenna Jones matrices. Such a 4×4 matrix is known as a Mueller matrix (Mueller 1948) and relates the input distribution of polarized emission to the cross-correlations measured by the interferometer. For complete details on their mathematical framework and examples of its flexibility, see Hamaker et al. (1996). Here I will briefly review several of their results, most of which are also reproduced in similar forms in standard texts on interferometry (e.g. Thompson et al. 2001; Taylor et al. 1999).

The antenna response Jones matrix, \mathbf{J} , relates the input electric field (\mathbf{e}) and output voltage (\mathbf{v}) according to

$$\mathbf{v} = \mathbf{J}\mathbf{e}. \quad (3.1)$$

The input and output signals are two-element column vectors, with one complex element representing each polarization state. Here the polarization is expressed in the right-circular, left-circular basis. The response can be decomposed into a few generic Jones matrices representing the idealized gain, coupling between the polarization states, and the rotation of the feed polarization,

$$\mathbf{J} = \mathbf{GDP}. \quad (3.2)$$

The gain matrix, \mathbf{G} , subsumes pointing, atmospheric, and electronic effects into two coefficients

$$\mathbf{G} = \begin{pmatrix} g_R & 0 \\ 0 & g_L \end{pmatrix}. \quad (3.3)$$

The cross polarization response, or “leakage”, is the deviation from the ideal gain matrix

$$\mathbf{D} = \begin{pmatrix} 1 & d_R \\ -d_L & 1 \end{pmatrix}. \quad (3.4)$$

The sources of leakage are obscured in the Jones matrix \mathbf{D} ; connections between physical properties of wave plates and the imperfections in this matrix are explored in § 3.4. Finally, the parallactic angle of the feed (ϕ) creates a phase shift in the measured circular polarization described by

$$\mathbf{P} = \begin{pmatrix} e^{-i\phi} & 0 \\ 0 & e^{+i\phi} \end{pmatrix}. \quad (3.5)$$

With the antenna response defined, the interferometer response can be obtained from the outer product¹ of antenna matrices. The output (\mathcal{V}) from an interferometer

¹The outer product of two matrices, $\mathbf{A} \otimes \mathbf{B}$, is the matrix formed by replacing each element (a_{ij})

consisting of antennas a and b , in response to sky polarization \mathbf{s} is

$$\mathcal{V} = (\mathbf{J}_a \otimes \mathbf{J}_b^*) \mathbf{S} \mathbf{s}. \quad (3.6)$$

Here \mathcal{V} represents the four polarized cross correlations of the RCP and LCP feeds. The sky polarization could be expressed as a similar time-averaged cross-correlation of circular polarization (the circular polarization “coherency” vector), but these correlations are not the quantities of astronomical interest. Instead, it is conventional to express the sky polarization in terms of the Stokes visibilities (I, Q, U, V); these are the Fourier transform of the intensity distribution in each Stokes parameter (definitions of the stokes parameters in terms of electric fields can be found in, e.g., Kraus 1966; Born & Wolf 1999). The conversion between the Stokes coordinates and the circular coherency vector is specified by \mathbf{S} ,

$$\begin{pmatrix} v_{RR} \\ v_{RL} \\ v_{LR} \\ v_{LL} \end{pmatrix} = \mathbf{S} \begin{pmatrix} I \\ Q \\ U \\ V \end{pmatrix}, \quad \mathbf{S} = \frac{1}{2} \begin{pmatrix} 1 & 0 & 0 & 1 \\ 0 & 1 & +i & 0 \\ 0 & 1 & -i & 0 \\ 1 & 0 & 0 & -1 \end{pmatrix}. \quad (3.7)$$

By use of equations (3.2) to (3.7), the interferometer response in all four polarized

of \mathbf{A} with $a_{ij} \mathbf{B}$. See Appendix A of Hamaker et al. (1996) for comments on the properties of this operator.

visibilities can be written

$$\begin{aligned} \mathcal{V}_{RR} = \frac{1}{2} g_{Ra} g_{Rb}^* & \left[(I + V) + d_{Ra} d_{Rb}^* (I - V) \right. \\ & \left. + d_{Ra} (Q - iU) e^{2i\phi} + d_{Rb}^* (Q + iU) e^{-2i\phi} \right], \end{aligned} \quad (3.8)$$

$$\begin{aligned} \mathcal{V}_{RL} = \frac{1}{2} g_{Ra} g_{Lb}^* & \left[(Q + iU) e^{-2i\phi} + d_{Ra} (I - V) \right. \\ & \left. - d_{Lb}^* (I + V) - d_{Ra} d_{Lb}^* (Q - iU) e^{2i\phi} \right], \end{aligned} \quad (3.9)$$

$$\begin{aligned} \mathcal{V}_{LR} = \frac{1}{2} g_{La} g_{Rb}^* & \left[(Q - iU) e^{2i\phi} - d_{La} (I + V) \right. \\ & \left. + d_{Rb}^* (I - V) - d_{La} d_{Rb}^* (Q + iU) e^{-2i\phi} \right], \end{aligned} \quad (3.10)$$

$$\begin{aligned} \mathcal{V}_{LL} = \frac{1}{2} g_{La} g_{Lb}^* & \left[(I - V) + d_{La} d_{Lb}^* (I + V) \right. \\ & \left. - d_{La} (Q + iU) e^{-2i\phi} - d_{Lb}^* (Q - iU) e^{2i\phi} \right]. \end{aligned} \quad (3.11)$$

The terms are arranged with the leading term representing what would be observed by ideal antennas, followed by the terms resulting from instrumental polarization. For most sources of interest here, the linear polarization fraction ($m = \sqrt{(Q^2 + U^2)}/I$) is less than a few to ten percent and the circular polarization fraction ($m_C = V/I$) is very small. Moreover, a well-performing system should have leakages (d) that are 10% or less. Terms that are second or third order in m , m_C , or d are therefore often disregarded. In this case, the remaining terms make up the linearized response equations

$$\mathcal{V}_{RR} \simeq \frac{1}{2} g_{Ra} g_{Rb}^* [I + V] \quad (3.12)$$

$$\mathcal{V}_{RL} \simeq \frac{1}{2} g_{Ra} g_{Lb}^* [(Q + iU) e^{-2i\phi} + (d_{Ra} - d_{Lb}^*) I] \quad (3.13)$$

$$\mathcal{V}_{LR} \simeq \frac{1}{2} g_{La} g_{Rb}^* [(Q - iU) e^{2i\phi} - (d_{La} - d_{Rb}^*) I] \quad (3.14)$$

$$\mathcal{V}_{LL} \simeq \frac{1}{2} g_{La} g_{Lb}^* [I - V]. \quad (3.15)$$

These equations make clear the impact of the leakages in circularly polarized

antennas. To first order, the leakages transfer Stokes I into Q and U , the linear polarization. Stokes I and V are relatively unaffected, although V measurements remain difficult because the L and R gains must be perfectly matched to cancel the dominant I when differencing \mathcal{V}_{RR} and \mathcal{V}_{LL} .

3.3 Leakage Calibration Observations

The linearized response equations show a clear path to calibration of the instrumental polarization. First, the co-polar visibilities (\mathcal{V}_{RR} and \mathcal{V}_{LL}) can be used to solve for the antenna gains without first order dependence on the unknown leakages. Second, the leakage contribution can be separated from the source polarization in the cross-polar visibilities (\mathcal{V}_{RL} and \mathcal{V}_{LR}) through the 2ϕ parallactic angle phase rotation in the $Q \pm iU$ terms. Thus, calibration of the leakages should be achievable through observation of a point source over a range of parallactic angles.

The parallactic angle is the difference between north at the sky position being observed and a fixed direction in the antenna (the vertical direction). The angle is defined to increase east of north. In an alt-az telescope the feed polarization direction matches this angle (plus or minus some fixed offset due to its orientation in the antenna), which is given by

$$\sin \phi_{alt-az} = \frac{\cos \lambda \sin H}{\cos E}, \quad (3.16)$$

for latitude λ , hour angle H , and elevation angle E . A parallactic angle range of 90° is typically adequate for leakage calibration. The parallactic angle of the Nasmyth-mounted feeds in SMA (alt-az) antennas is somewhat different than that

given by equation (3.16). In particular, the rate of parallactic angle change is not symmetric across zero hour angle. The origin of the difference is the additional optics needed to relay the beam along the elevation axis; these optics add a rotation by the source elevation to the parallactic angle change. After including a fixed 45° rotation of the SMA feed polarization from the vertical direction, the polarization position angle of SMA receivers in “low frequency” receiver positions (the current 230 and 345 GHz band receivers, see § 2.3.1) is

$$\phi_{SMA} = 45^\circ - E + \phi_{alt-az}. \quad (3.17)$$

All “high frequency” positions have orthogonal polarization and thus have a position angle different by 90° . The addition of the E term destroys the simple hour angle anti-symmetry present in equation (3.16). Instead, ϕ_{SMA} varies in a more complicated fashion, as shown in Figure 3.1.

In the second paper of a series (after Hamaker et al. 1996), Sault et al. (1996) explore polarization calibration in much greater detail than the simple discussion above. They show that a long observation of a polarized point source with alt-az antennas does provide adequate information to solve for both the instrumental and the calibrator polarization. However, the calibration procedure leaves one degree of freedom unconstrained, the phase difference between the R and L feeds, which corresponds to a rotation of the linear polarization on the sky ($Q \leftrightarrow U$ contamination). This problem is circumvented at the VLA through observations of one of a few polarization calibrators that are known to have stable polarization position angles. None of the bright quasars observed with the SMA has shown stability in its polarization position angle (χ). Fortunately, this final ambiguity is

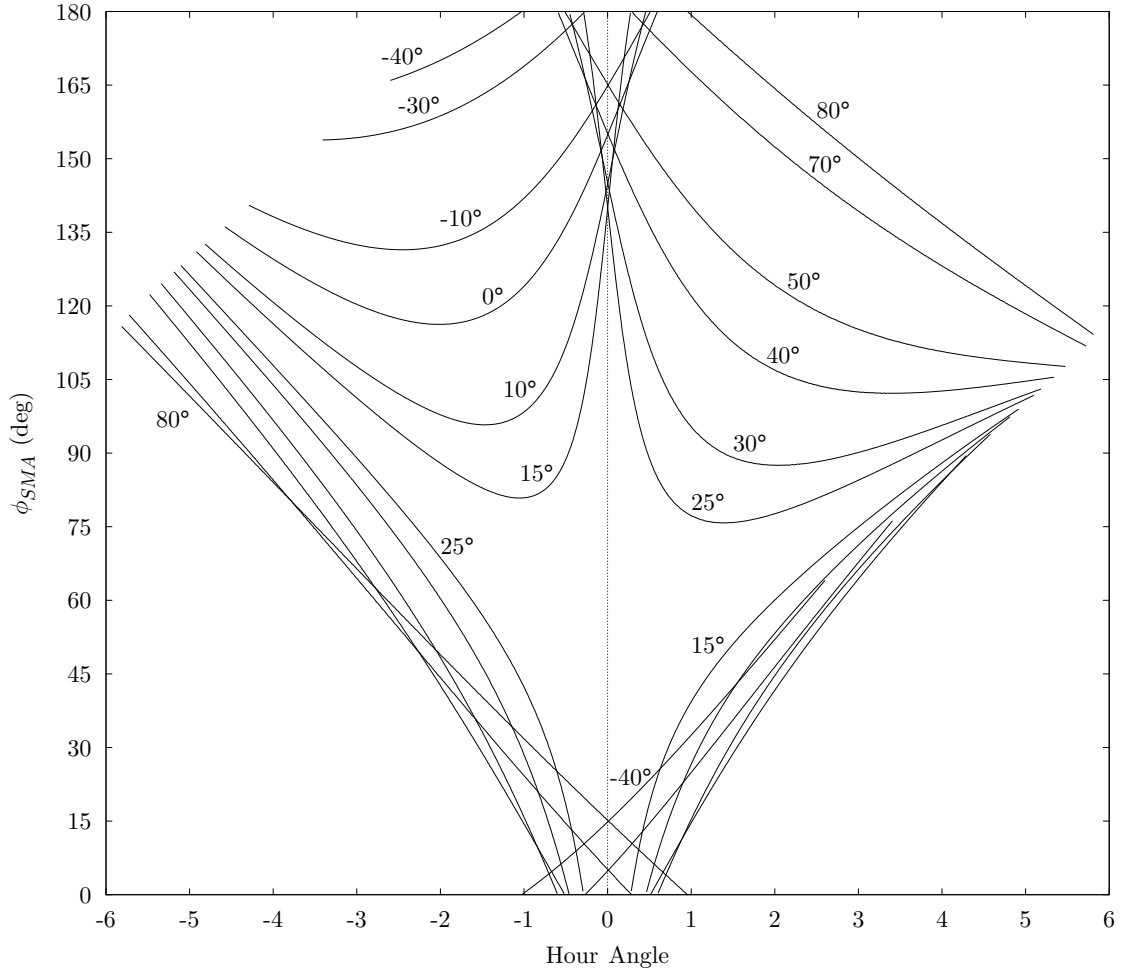


Fig. 3.1.— The parallactic angle of the SMA 230 and 345 GHz receivers (ϕ_{SMA} , equation [3.17]) as a function of hour angle. A range of declinations are plotted, with each curve limited to hour angles where the elevation is greater than 20° . The unlabeled curves correspond to unwrapped portions of the same declinations labeled in the center of the plot.

removed from the SMA observations by the time-multiplexing technique used to perform polarization observations. A phase difference cannot arise between SMA R and L “feeds”, as just one linearly-polarized feed receives both RCP and LCP. The polarization switching is achieved with the wave plate, with the handedness alternating rapidly and both signals traversing the same RF and IF electronics paths. Even if off-center rotation of the wave plates (not believed to exist) presented different sections of the plate in the two polarization states and changed the optical path length, the resulting phase change would be chromatic (a fixed length, not a fixed phase difference) and would be removed by the passband calibration. However, when dual-polarization observations become possible with the SMA (§ 2.8) some wave plate switching will still be desirable in order to calibrate the electronic phase difference between the two feeds.

Sault et al. (1996) also analyze the impact of errors in the gain and leakage solutions. They point out that the single-baseline Mueller matrix has just seven complex degrees of freedom, eight from the two four-element Jones matrices that generate the Mueller matrix less one for the arbitrary phase of one element. This suggests that there are just seven types of calibration errors. When properly composed from combinations of errors in the real or imaginary parts of the gains and leakages, each error can be identified with an interconversion of Stokes parameters (six possible combinations) plus an overall error in the flux density scale. The error definitions, causes, and effects for both linear and circularly-polarized feeds are summarized in their Table 1. The three errors involving the complex gains are the least troublesome for linear polarimetry with the SMA. These are the flux scale error, R–L gain imbalance leading to $I \leftrightarrow V$ conversion, and an R–L phase

offset discussed in the previous paragraph. The second of these is a reminder of the difficulty of measuring very small V with circular feeds. The third is excluded by the SMA observing technique. Real or imaginary offsets to the leakages produce conversion of V to and from Q and U . Fortunately, the low fractional flux density in all of these Stokes parameters ensures that errors of a percent or so of Q and U (10^{-3} or less of I) are unimportant. Finally, incorrect solutions for the calibrator linear polarization lead to $I \leftrightarrow Q, U$ corruption. This type of error is of most concern. The possible magnitude of such errors is discussed by use of the scatter in the measured leakages in § 3.5.

The Sault et al. (1996) leakage error analysis also allows us to understand the limitations imposed by leakage calibration with an unpolarized calibrator. This may be relevant for SMA 690 GHz polarimetry, as very bright quasars are only rarely available at this frequency (3C 454.3 reached 20 Jy at 690 GHz in July 2005 in an exceptional outburst). Instead, unresolved Solar system objects, such as asteroids or planetary satellites, may be the only compact sources available for calibration. Sault et al. (1996) show that calibration with an unpolarized source leaves three degrees of freedom undetermined, the R–L phase and an arbitrary complex offset to the leakages. Since the phase is not a problem for the SMA system and a leakage offset merely leads to conversion between linear and circular polarization, this type of calibration should be adequate. Unfortunately, planets are not free of polarization. In the case of solid surfaces, the polarization of thermal emission from any point on the surface of a planet depends on the angle between the surface and the line of sight to the telescope, with maximum polarization achieved at the Brewster angle for the emitting material (Heiles & Drake 1963). Thus the polarization of

a planet is radial at all points, although the full-disk average of a circular planet will have no net polarization. Similarly, scattering by atmospheric particles will polarize the emission from gas-enshrouded bodies (e.g., Titan). The importance of this effect in interferometric observations depends on the degree to which the planet is resolved. In particular, at the baseline distances where the total intensity is resolved out (the nulls in the visibility function) the polarized intensity is maximum, while the polarization is minimized when the total intensity is maximized. The peak polarization fraction across a planetary disk is typically a few percent, so by observing planets that are much smaller than the fringe spacing of the longest baselines, good polarization calibration is possible.

3.4 Wave Plate Cross-Polarization

Under the Jones matrix formalism introduced above it is possible to make predictions about the behavior of the leakages on the basis of certain effects expected in the wave plates. The SMA optical path is fairly simple and has been designed to have good polarization performance (low coupling of orthogonal linear polarization to the linearly polarized SMA feeds), so it is expected that the wave plates will cause a significant portion of the leakages measured in each antenna. The leakage signatures of wave plate imperfections are derived here.

The product of the gain and leakage matrices (equations [3.3] and [3.4]) can be further expanded into physically motivated Jones matrices. Note that in the following discussion, the Jones matrices are defined for the linear polarization basis to match the SMA feed polarization. Transformation to the circular basis assumed

for the component matrices of equation (3.2) is made explicitly in a later equation. The first Jones matrix in an expansion of the wave plate behavior represents the intended function of the plate, the imposition of a propagation delay (Δ , expressed as a phase) between radiation polarized along its two principle directions. This retardation can be represented as

$$\mathbf{W}(\Delta) = \begin{pmatrix} e^{+i\Delta/2} & 0 \\ 0 & e^{-i\Delta/2} \end{pmatrix}. \quad (3.18)$$

The difference in the indices of refraction along the two wave plate axes leads to differential transmission/reflection, even in the presence of an anti-reflection coating (§ 2.4.3 and Figure 2.3). The fractional difference (ϵ) in the electric field transmission coefficient is expressed by

$$\mathbf{T}(\epsilon) = \begin{pmatrix} 1 + \epsilon/2 & 0 \\ 0 & 1 - \epsilon/2 \end{pmatrix}. \quad (3.19)$$

As discussed in the previous chapter, the wave plate axes must be oriented at $\pm 45^\circ$ to the feed polarization. Rotation of the coordinate system by an angle ψ is described by the rotation matrix

$$\mathbf{R}(\psi) = \begin{pmatrix} \cos \psi & -\sin \psi \\ \sin \psi & \cos \psi \end{pmatrix}. \quad (3.20)$$

Using these elements, the quarter wave plate can be expressed as a product of Jones matrices

$$\mathbf{Q}(\theta, \delta, \epsilon) = \mathbf{R}(\pi/4 + \theta) \mathbf{W}(\pi/2 + \delta) \mathbf{T}(\epsilon) \mathbf{R}(-\pi/4 - \theta) \mathbf{C}^+ \quad (3.21)$$

The arguments to the rotation, retardation, and transmission matrices are the values for a perfect quarter-wave plate (e.g. $/\pi/2$ in \mathbf{W}) plus error quantities that

represent non-ideal behavior. For example, θ is the orientation error, the offset from the ideal orientation with the crystal axes rotated 45° from the feed polarization direction. Similarly, δ is the offset from the ideal quarter-wave retardation. The final matrix (\mathbf{C}^+) acts to convert the input sky polarization, specified in circular polarization coordinates, to the linear polarization coordinate system at the feed,

$$\mathbf{C}^+ = \frac{1}{\sqrt{2}} \begin{pmatrix} 1 & 1 \\ -i & i \end{pmatrix}. \quad (3.22)$$

For the rotations used in equation (3.21), \mathbf{Q} represents the RCP orientation of the QWP. To obtain the LCP orientation, the signs of the angles in the \mathbf{R} matrices should be negated. Because \mathbf{Q} connects the sky polarization and feed polarization, the linear polarization coordinate system is aligned with the polarization direction of the SMA (low frequency) feed. The orthogonal polarization is directed to the high frequency feed, thus the lower row of the matrix represents the properties of the other receiver (the 690 GHz receiver, in the case of the 230/690 GHz wave plates) rather than the LCP feed.

Matrix \mathbf{Q} can be expanded in powers of the error quantities to determine their effects. Recall that \mathbf{Q} is a replacement for the product \mathbf{GD} in equation (3.2). The expansions will therefore determine the wave plate impact on the gains (g) and leakages (d). Because the RCP and LCP orientations are represented by two different matrices, only the top row of the \mathbf{Q} matrix is relevant for a single receiver band. Nevertheless, expansion of the two orientations yields identical results. The

expansions to second order in the error terms are

$$g \simeq 1 - \left(\theta^2 + \frac{\theta\epsilon}{2} + \frac{\delta^2}{8} \right) + \left(-\theta - \frac{\theta\epsilon}{2} + \frac{\delta\epsilon}{4} \right) i, \quad (3.23)$$

$$d \simeq \left(-\frac{\delta}{2} + \theta^2 - \frac{\theta\epsilon}{2} \right) + \left(-\theta + \frac{\epsilon}{2} - \frac{\theta\delta}{2} \right) i. \quad (3.24)$$

By the convention² of Sault et al. (1996), d_L has opposite sign from d_R , so the expansion in equation (3.24) should be negated when used for d_L . Equation (3.23) shows that the gain has a single first order correction, from the wave plate orientation. This is a frequency-independent quantity and should be small (0.5% for a 0.3° error) because of the careful alignment of the SMA system. If the wave plates are the dominant contributor to the leakage in the SMA the terms in equation (3.24) can be used to determine properties of the plates and their alignment. At first order, the real component of the leakage depends on the retardation error alone and the imaginary component arises from the orientation error and the transmission difference. In the SMA system the retardation error should be the same in both wave plate orientations, so the real components of d_R and d_L should be equal. The origin of the retardation error is the chromaticity of the wave plate; because the wave plates produce a fixed path length difference between the two polarizations, the phase delay is only a 90° at one frequency. Therefore, as pointed out in Rao (1999), to lowest order the real part of the leakage should be

$$\text{Re}[d] \simeq -\frac{\pi}{4\nu_0} (\nu - \nu_0), \quad (3.25)$$

where ν_0 is the frequency where the wave plate produces exactly $\lambda/4$ delay.

Equation (3.24) also shows that the imaginary part of the leakage should indicate

²Conventions vary. For example, Thompson et al. (2001) does not adopt this minus sign.

the alignment error in the absence of a transmission difference between its axes. Although ϵ should depend sensitively on the AR coating thickness and observing frequency, it should be constant between the two wave plate positions. The orientation error will differ for the two positions, so the sum of the imaginary components of d_R and d_L (with d_L appropriately defined to be negative, as in equation [3.4]) should measure the error in the nominal 90° rotation of the wave plate between the LCP and RCP orientations. In most cases we expect the second order terms to be negligible, although they may be significant when the observing frequency is far from the tuned frequency of the AR coating or the wave plate.

3.5 Leakage Measurements

Scientifically useful polarimetric data have been obtained on nearly thirty nights since May 2004. Leakage calibration observations have been included in the majority of these tracks, although they were often skipped when observing at frequencies with very recent calibration data. The frequency coverage of the leakage measurements has been determined by the science goals of the polarimetric projects, resulting in very redundant data at few frequencies. This type of sampling provides very good measurements of stability and reproducibility in the leakage determinations. The spectral properties of the leakages can also be examined from these data, but are less well determined.

3.5.1 Leakage Variability

The calibration data include three fairly well-measured tunings, one in the 230 GHz band and two in the 345 GHz band. During two months in the summer of 2005, calibration data were obtained five and four times at 221.9/231.9 GHz and 338.0/348.0 GHz, respectively, as part of Sgr A* observations with very stringent calibration requirements (Chapter 5). Two additional measurements at 221.9/231.9 GHz have been obtained in 2006. Four measurements at 336.5/346.5 GHz were obtained in late 2005 and 2006. The ensemble of leakage measurements probes possible instrumental polarization changes on short and long timescales. In addition, the wave plates in a few antennas were swapped between 2005 and 2006 observations, so the change or constancy of these leakages provides information on the antenna contribution to the leakages.

Leakages at the three repeatedly observed tunings are shown in Figures 3.2 and 3.3. The plots provide a graphical representation of average values of the measured leakages and their variability. At each frequency $\text{Re}[d_R]$ and $\text{Re}[d_L]$ are usually systematically offset from each other (by as much as 1%), which is not predicted for the wave plates themselves, as shown in § 3.4. This is probably the result of instrumental polarization elsewhere in the system. The imaginary component of d_R or d_L generally agrees across the two sidebands for each tuning, as would be expected if this leakage arises from the orientation error in the wave plate. There are a few exceptions in the 345 GHz leakages, but these may be a result of coupling between the imaginary parts of the leakages across the antennas owing to a constraint in the data reduction software. The MIRIAD (Sault et al. 1995) task GPCAL, used to

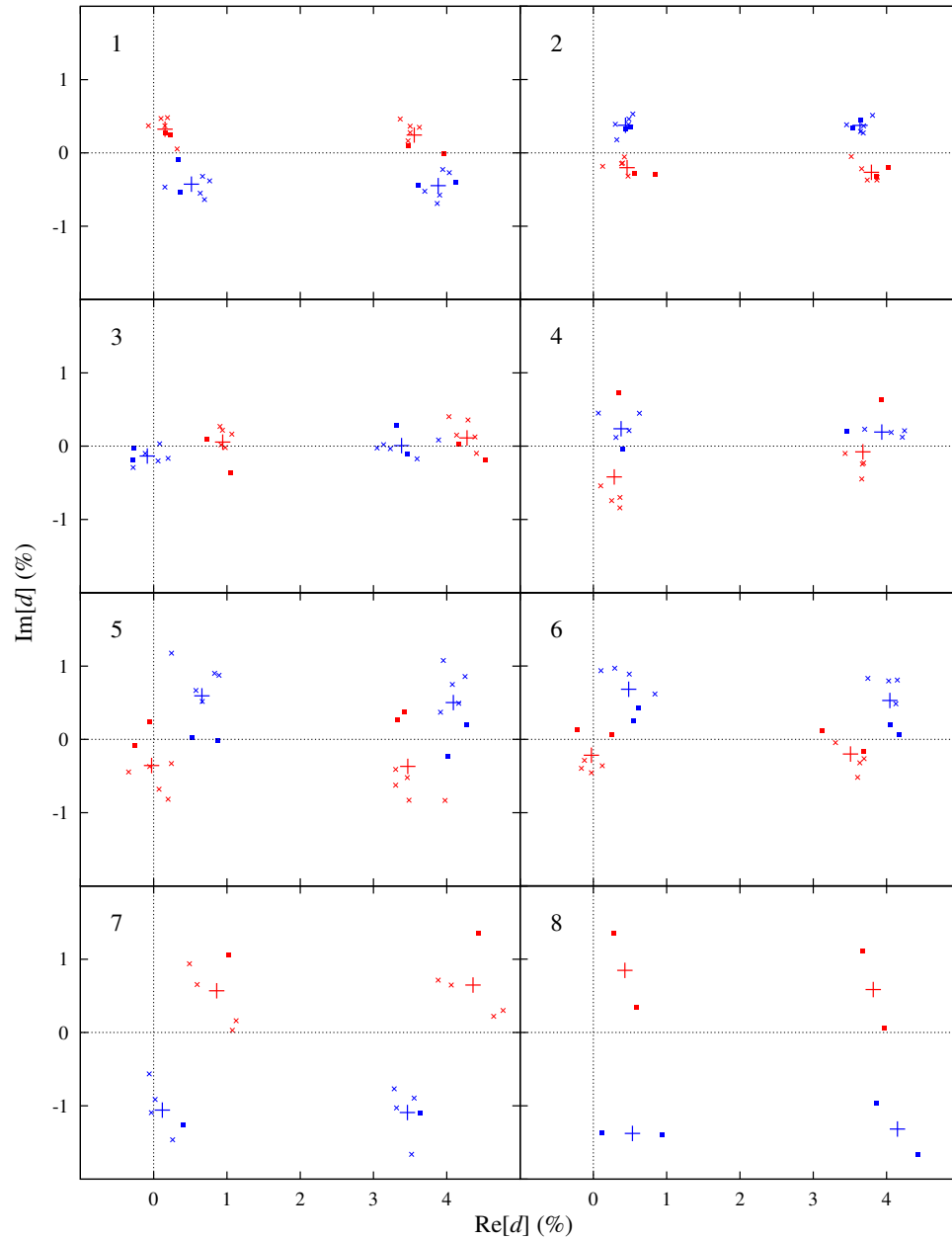


Fig. 3.2.— Leakages measured in the 230 GHz band. Each plot represents a single antenna, identified at the upper left. Leakages are plotted in the complex plane, with equal linear scales in the real and imaginary axes. The points at the left of each subplot are measurements at 231.9 GHz; those at the right are 221.9 GHz. The difference between them in the $\text{Re}[d]$ direction is expected from equation (3.25). Red points are d_R , blue points are d_L . The mean value of d_R (d_L) for each frequency is represented by a large red (blue) +. Individual measurements from 2005 (\times) and 2006 (\blacksquare) are marked with smaller symbols.

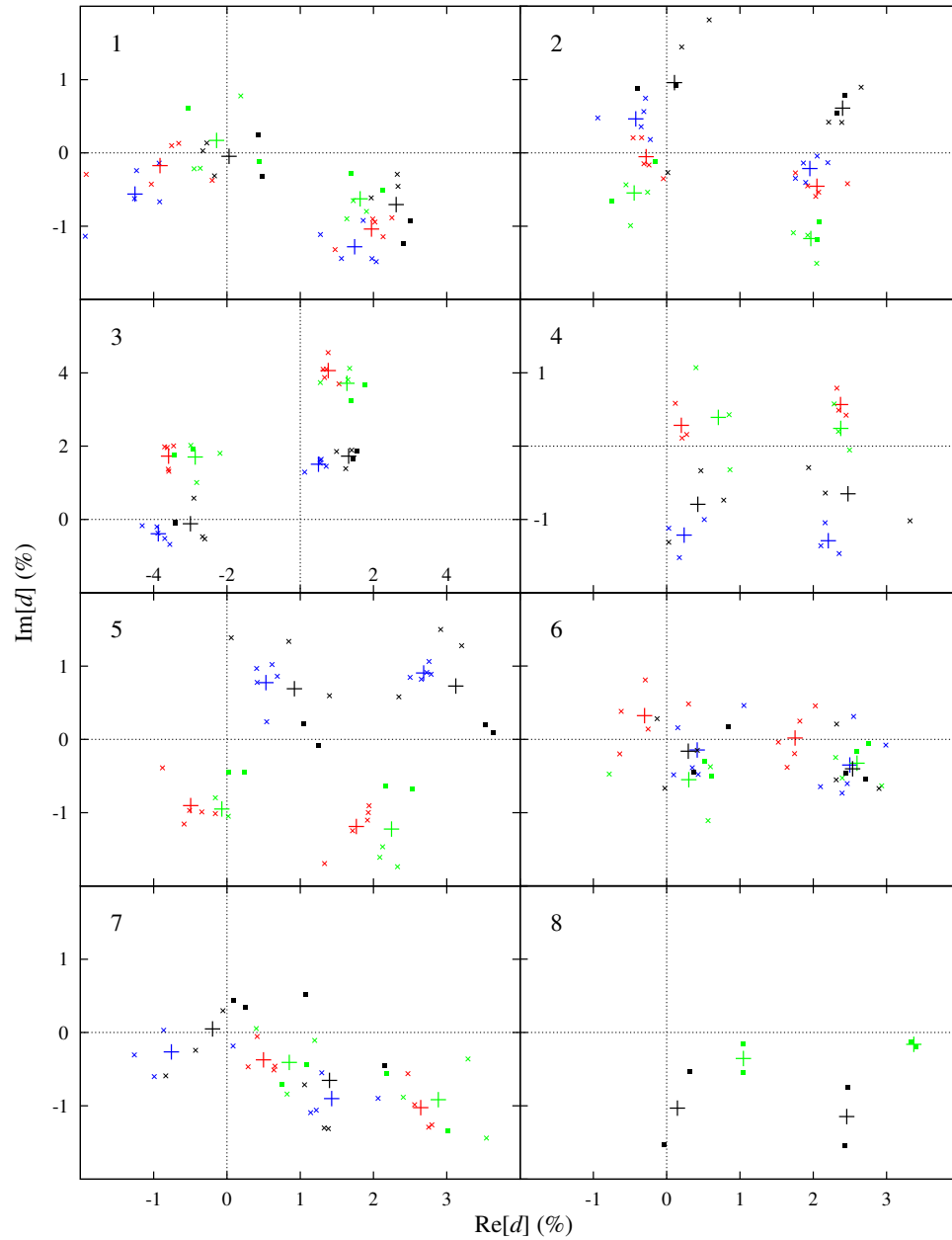


Fig. 3.3.— Leakages measured in the 345 GHz band. Subplots and symbols are as in Figure 3.2. Here the red and blue points represent d_R and d_L , respectively, at 338.0 GHz (points at right in each plot) and 348.0 GHz (points at left). Green and black points represent d_R and d_L , respectively, at 336.5 GHz (right) and 346.5 GHz (left). The subplot for antenna 3 has a linear scale twice as large as those for the other antennas, as shown by its labels. At 338.0/348.0 GHz, leakages were measured twice in the same track (2005 June 6) using different calibrators and both sets of leakages are shown. The same is true at 336.5/346.5 GHz for 2006 April 7.

determine leakages, imposes the condition

$$\sum_{Ant} \text{Im} [d_R] = - \sum_{Ant} \text{Im} [d_L], \quad (3.26)$$

except in the rare case where the calibrator has greater than 5% polarization. This possible imaginary offset is exactly the type that interconverts Stokes U and V , according to Table 1 of Sault et al. (1996), which causes no problems as long as neither of these Stokes parameters is large. Thus the aberrant 345 GHz band behavior of the antenna 3 imaginary components (a large difference between imaginary components across the sidebands) may also impose the smaller inter-sideband imaginary offsets observed in the other antennas.

Table 3.1 lists the average values and variability of the leakages at each frequency in Figures 3.2 and 3.3. At the two 230 GHz frequencies, the average leakage variations are 0.34%, while the four 345 GHz band frequencies have variations between 0.30% and 0.53%. If these represent a random uncertainty in the leakages, the expected false polarization signal introduced into an snapshot polarization observation would be 0.1% to 0.2% (reduced by the square root of the number of antennas). In a long synthesis this is further reduced by the parallactic angle rotation of the source polarization. In the other extreme, if the leakage changes in any given observation are fully correlated in a way that directly converts I to Q or U (errors in the linear polarization derived for the calibrator), as much as the full leakage error may be introduced into a snapshot polarization measurement. Just as in the case of random errors, parallactic angle rotation will reduce the average polarization error across the whole track. Although this type of fully-correlated and maximally damaging error is unlikely to be realized, there may be some correlations

between the leakage changes from the effect discussed in § 3.6.

The precision expected in the leakage measurements can be estimated for the case where systematic errors are unimportant. Holdaway et al. (1992) suggest that for self calibration on a source of flux density S measured with noise σ on a single baseline in an N antenna array, the expected error in the leakages (σ_d) is

$$\sigma_d = \frac{1}{\sqrt{N-1}-1} \frac{\sigma}{S}. \quad (3.27)$$

A typical 230 GHz band observation in 2005, when 3C 454.3 had a flux density of 30–40 Jy, should yield $\sigma_d \simeq 0.06\%$. For more typical conditions when calibrators are a few to 10 Jy, the precision should be more like 0.2%. This approaches the level of variation observed in the measured leakages. However, nearly all of the calibration observations in 2005 (the majority of data points included in Table 3.1 and the accompanying figures) were obtained with a flaring 3C 454.3 as the calibrator, so finite signal to noise should not be responsible for most of the observed changes.

Leakages appear to be as stable on long (one year) timescales as they are across periods of weeks. The 2005 and 2006 leakage points do not show obvious offsets from each other, except possibly in antenna 5. In this antenna there may be an offset of approximately 0.5% in $\text{Im}[d]$ at 221.9/231.9 GHz and 336.5/346.5 GHz between the two seasons. This could be explained by a change of 0.3° in the orientation of the wave plates; since it is similar for both sets of wave plates it suggests that the entire wave plate positioner is resting slightly differently than it was in 2005.

Between 2005 and 2006 the wave plates in antennas 2 and 4 were changed (to those from antennas 8 and 7, respectively). In antenna 2 there is no perceptible change in the leakages between the two years, in fact, this antenna has the most

Table 3.1. Measured Leakages

Frequency (GHz)	Ant.	Re[d_R] (%)	Im[d_R] (%)	σ_R (%)	Re[d_L] (%)	Im[d_L] (%)	σ_L (%)	N_{pts}	Ant. (%)	Re[d_R] (%)	Im[d_R] (%)	σ_R (%)	Re[d_L] (%)	Im[d_L] (%)	σ_L	N_{pts}
221.9	1	3.56	0.24	0.23	3.88	-0.45	0.23	7	5	3.47	-0.37	0.51	4.09	0.50	0.43	7
	2	3.79	-0.27	0.19	3.64	0.37	0.13	7	6	3.51	-0.20	0.30	4.04	0.53	0.34	6
	3	4.28	0.11	0.26	3.38	0.01	0.30	7	7	4.36	0.65	0.52	3.46	-1.09	0.34	5
	4	3.68	-0.08	0.40	3.94	0.19	0.31	5	8	3.82	0.58	0.54	4.15	-1.32	0.45	2
231.9	1	0.16	0.32	0.18	0.52	-0.43	0.27	7	5	-0.03	-0.36	0.39	0.66	0.59	0.47	7
	2	0.46	-0.20	0.22	0.44	0.38	0.13	7	6	-0.03	-0.22	0.28	0.48	0.68	0.36	6
	3	0.94	0.06	0.22	-0.09	-0.13	0.21	7	7	0.86	0.57	0.49	0.12	-1.06	0.36	5
	4	0.28	-0.42	0.59	0.38	0.24	0.27	5	8	0.43	0.85	0.53	0.53	-1.38	0.41	2
336.5	1	1.82	-0.63	0.28	2.31	-0.70	0.38	5	5	2.25	-1.22	0.50	3.12	0.73	0.73	5
	2	1.97	-1.17	0.23	2.40	0.61	0.24	5	6	2.60	-0.32	0.32	2.54	-0.40	0.39	5
	3	1.27	3.72	0.49	1.32	1.73	0.27	5	7	2.89	-0.92	0.67	1.40	-0.65	0.78	5
	4	2.37	0.24	0.27	2.47	-0.65	0.67	3	8	3.37	-0.16	0.05	2.46	-1.15	0.39	2
338.0	1	1.97	-1.04	0.31	1.74	-1.28	0.36	5	5	1.77	-1.19	0.36	2.68	0.91	0.13	5
	2	2.05	-0.45	0.26	1.95	-0.21	0.21	5	6	1.75	0.02	0.35	2.50	-0.35	0.50	5
	3	0.77	4.06	0.33	0.50	1.51	0.24	5	7	2.64	-1.02	0.32	1.43	-0.90	0.43	4
	4	2.37	0.57	0.17	2.21	-1.29	0.21	3	8	0
346.5	1	-0.14	0.17	0.58	0.03	-0.05	0.42	5	5	-0.07	-0.95	0.62	0.92	0.69	0.75	5
	2	-0.44	-0.55	0.36	0.11	0.96	0.77	5	6	0.30	-0.55	0.62	0.29	-0.16	0.50	5
	3	-2.87	1.70	0.54	-3.00	-0.12	0.53	5	7	0.85	-0.41	0.44	-0.20	0.05	0.56	5
	4	0.71	0.39	0.61	0.42	-0.79	0.50	3	8	1.05	-0.35	0.19	0.15	-1.03	0.53	2
348.0	1	-0.91	-0.17	0.62	-1.25	-0.56	0.51	5	5	-0.49	-0.90	0.36	0.53	0.77	0.30	5
	2	-0.28	-0.05	0.26	-0.42	0.46	0.32	5	6	-0.30	0.32	0.48	0.42	-0.15	0.52	5
	3	-3.59	1.73	0.32	-3.87	-0.39	0.32	5	7	0.50	-0.37	0.24	-0.76	-0.26	0.56	4
	4	0.20	0.28	0.22	0.24	-1.21	0.30	3	8	0

Note. — The leakage errors (σ_R , σ_L) are the quadrature sums of the dispersions in the real and imaginary components. For the frequencies in the 345 GHz band, all of the antennas were measured on four or fewer nights, but the statistics include two leakage measurements in the same night using different sources.

stable leakage at nearly all frequencies with measurements from both years. This suggests good uniformity in the wave plates and their alignment, a conclusion that is supported by the results of the next section. In antenna 4, some 2006 leakages (230 GHz only) resemble those in antenna 7 in 2005, while others do not. Antenna 8 inherited the wave plate of antenna 4 in 2006, but the leakage properties of antenna 4 do not seem to have followed the plate. These results again imply uniform wave plates, with the antenna 8 leakages suggesting a significant antenna impact on the leakages. It therefore appears that leakages cannot be transferred from one antenna to another when a wave plate is moved, an important result for calibration planning.

3.5.2 Frequency Dependence

With the limited frequency coverage available it is possible to investigate some of the spectral properties predicted for the leakages in § 3.4. First, equation (3.25) predicts that to first order the slope in the real part of the leakages should be inversely proportional to the design frequency of the wave plate, the point at which the real component goes to zero. The 230/690 GHz wave plates were designed to have a $\lambda/4$ delay at 229.7 GHz (Appendix A), although the birefringence of quartz is not known to better than a few percent (§ 2.4.2). Figure 3.4 shows the frequency dependence of the real part of the 230 GHz band leakages. In order to eliminate effects believed to arise outside the wave plate, the real parts of d_R and d_L have been averaged together to produce this figure. The plates are remarkably uniform, the measured $\text{Re}[d] = 0$ intercepts are $\nu_0 = 233.0 \pm 0.3$ GHz, where the error represents the scatter in the seven plates. The slopes, while less well measured, vary by just

2.5% from the mean of 0.342%/GHz, corresponding to a ν_0 of 229 GHz, consistent with the intercepts. The real components of the 345 GHz band leakages are plotted in the same way in Figure 3.5. The unusual behavior of the sapphire wave plate in antenna 3 is apparent in the plot, but the seven quartz plates match each other well. The intercepts show $\nu_0 = 347.7 \pm 1.5$ GHz, while the slopes have an average value of 0.223%/GHz with 7% variation, implying $\nu_0 = 353$ GHz. Reversing equation (2.3), these measurements can be used to determine the birefringence of quartz. Both sets of wave plates agree with a value of Δn that is $1.5 \pm 0.1\%$ lower than that assumed in the wave plate design, or $\Delta n = 0.0473 \pm 0.0001$ after including the uncertainty in the wave plate thicknesses. This is fifty times more precise than the error in the literature value for this quantity.

Another prediction of § 3.4 is that the sum of the imaginary components of d_R and d_L should indicate the error in the nominal 90° switch between the two wave plate positions. A complication is introduced by the imaginary normalization imposed by the reduction software (equation [3.26]). In any leakage solution the total imaginary component ($\text{Im}[d_R + d_L]$) is constrained to be zero, so an offset from 90° that is constant across all antennas would be missed. With that caveat, the 230 GHz band leakage data (Figure 3.6) show small total imaginary components that are roughly constant between the two frequencies, indicating switching errors of 0.3° or less. The same result should be obtained in the 345 GHz band as both sets of wave plates use the same rotation stages. However, the 345 GHz results in Figure 3.7 are quite different from those in the previous figure. The total imaginary component is not constant with frequency and is often large. This is most likely due to the behavior of antenna 3, which has a large total imaginary component, coupling

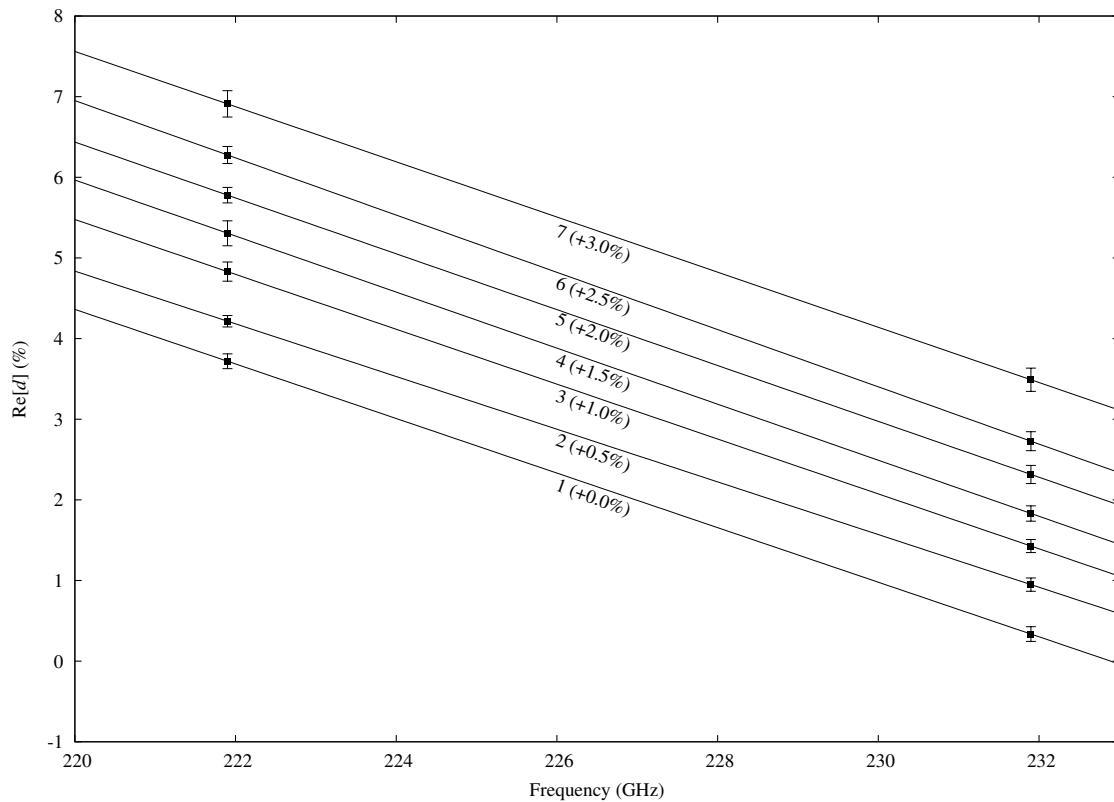


Fig. 3.4.— The variation of the real part of SMA leakages with frequency in the 230 GHz band. The average of $Re[d_R]$ and $Re[d_L]$ is plotted for each antenna at the two frequencies in the 230 GHz band where leakages have been measured more than once. There is a progressively increasing vertical offset in the antennas for easier interpretation. Linear fits, here a fully constrained line between the two data points, are shown for each antenna. The error bars are plotted as the standard error of the mean in the real component of the leakage for fitting purposes, as this accounts in the fitting for the different number of samples at some 345 GHz frequencies.

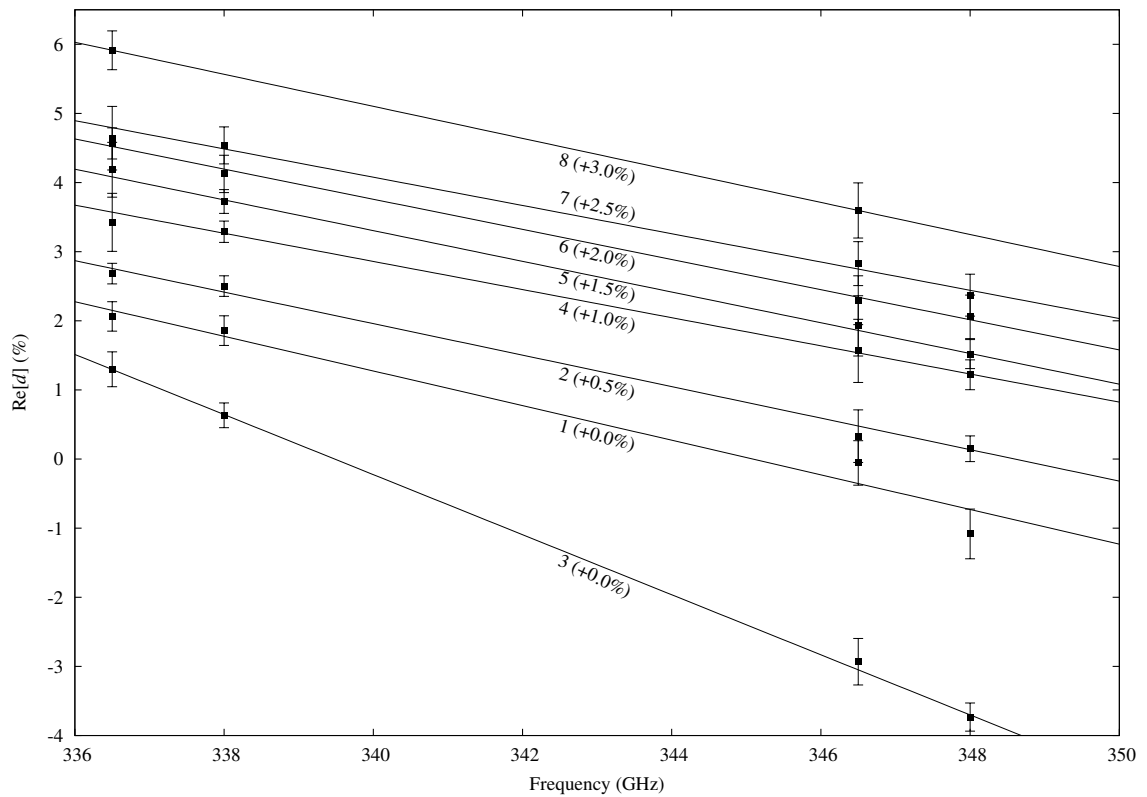


Fig. 3.5.— The variation of the real part of SMA leakages with frequency in the 345 GHz band. The points and fits are as in Figure 3.4. Antenna 3 is excepted from the pattern of increasing vertical offsets because it is the sole sapphire wave plate and behaves differently with frequency.

into the other antennas through the normalization constraint. The imaginary components of antenna 3 are not believed to be the result of orientation error based on the performance at 230 GHz in the same rotation stage. Instead, they probably arise from large transmission differences between the axes created by the large birefringence of sapphire.

3.6 Modified Polarization Response

3.6.1 Antenna Polarization

The polarization response theory described in § 3.4 is limited to effects from the wave plates and therefore may not encompass all of the relevant cross-polarization coupling processes. Evidence for leakage arising outside the wave plates is provided by the significant offsets between the real parts of d_R and d_L at most frequencies, for example. Because instrumental polarization and source polarization vary differently with parallactic angle (equations [3.13] and [3.14]), the leakage solutions in each track can be tested by generating polarization light curves of the polarized sources. In particular, the quasar 3C 454.3, which was extremely bright (up to 40 Jy) during the summer 2005 observing campaign, provides high signal-to-noise ratio polarized light curves. Although the curves do not show evidence of source polarization changes within a single night, there is a systematic pattern in the polarization versus hour angle in all of the nights. The deviation from the average Q and U polarization on each night as a function of hour angle is shown in Figures 3.8 and 3.9 for the 230 and 345 GHz bands, respectively.

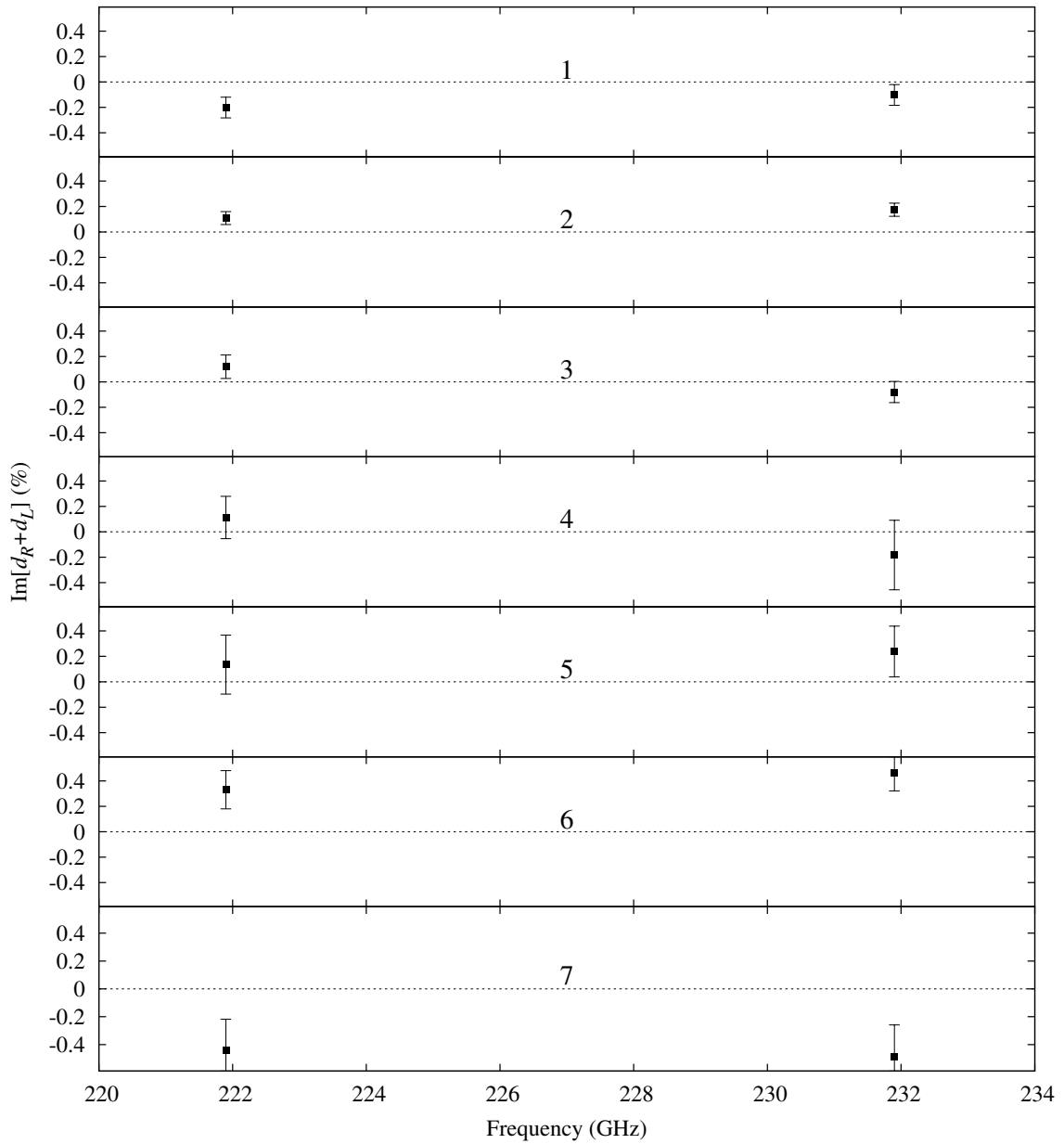


Fig. 3.6.— The variation of $\text{Im}[d_R + d_L]$ for the 230 GHz band. Ignoring the effect of frequency-dependent ϵ (§ 3.4), this sum should represent the deviation from the ideal switch of 90° between the two orientations of the wave plates and should be frequency independent. In this interpretation, a total imaginary component of 1% corresponds to a switching error of 0.6° .

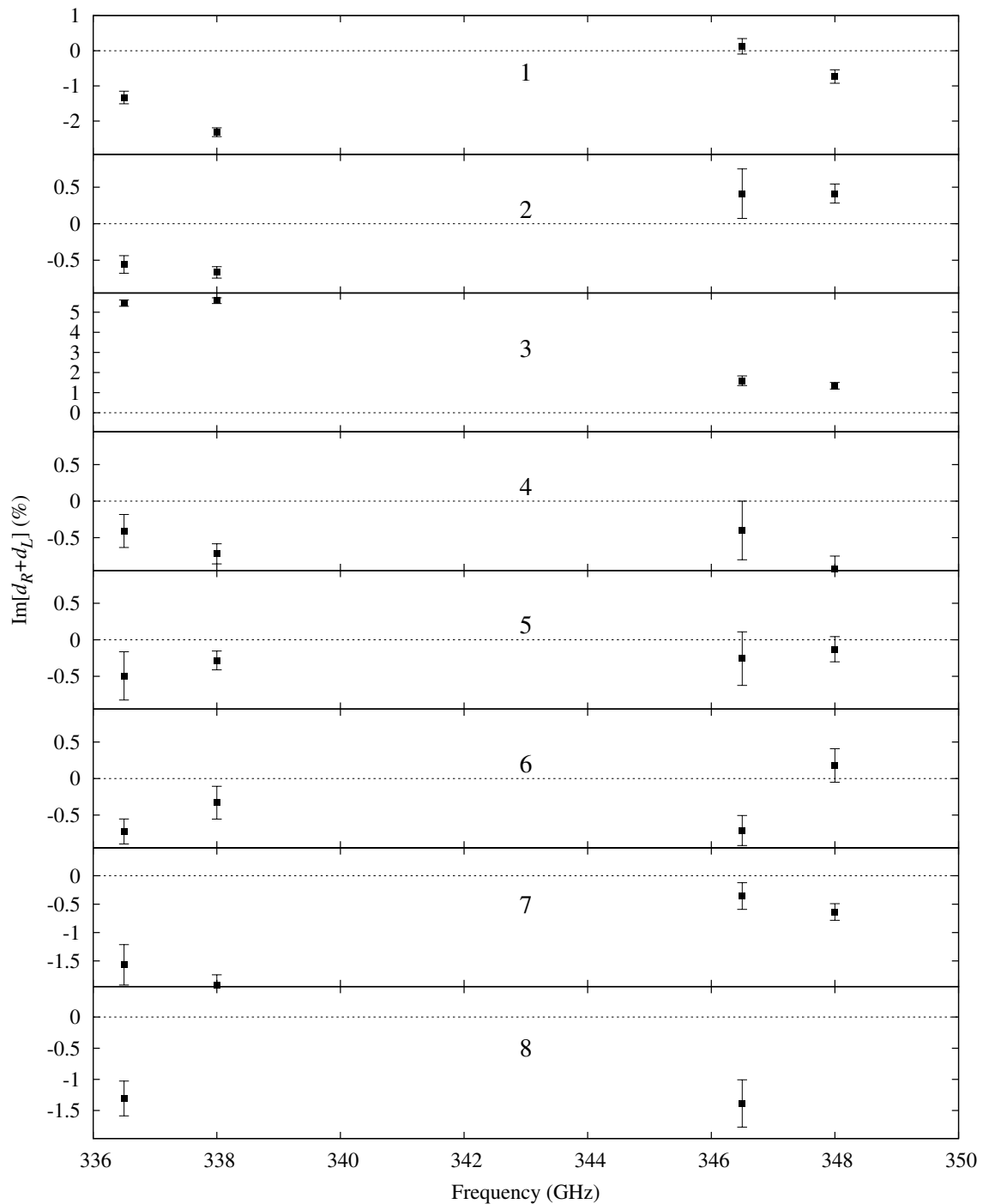


Fig. 3.7.— Same as Figure 3.6, for the 345 GHz band. The results for various antennas are not as uniform as they are in the 230 GHz band. This is likely to be the result of normalization imposed by the data reduction software, see the discussion in § 3.5.2.

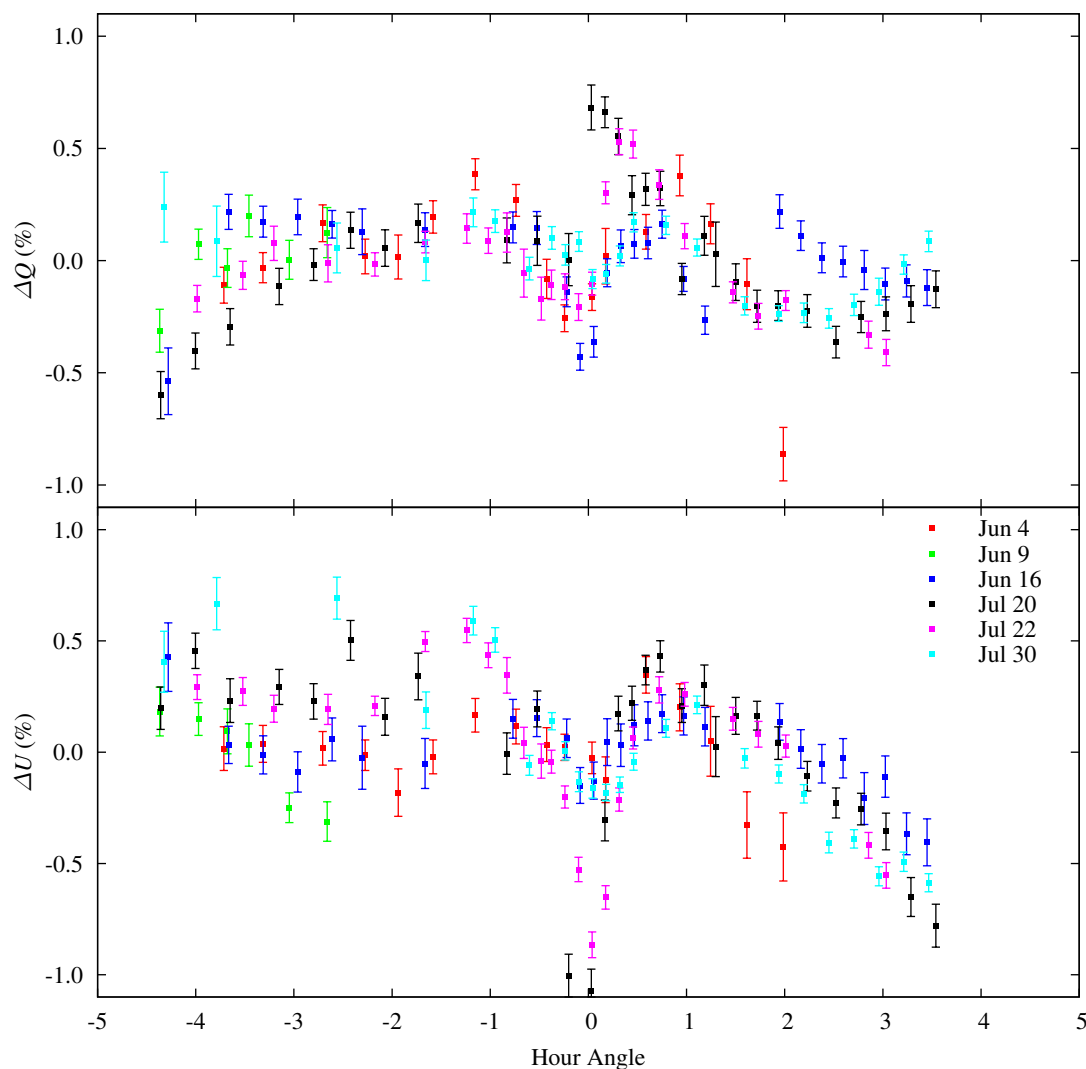


Fig. 3.8.— Variations in the polarization of 3C 454.3 as a function of hour angle for six 230 GHz band observations in 2005. In each epoch the two sidebands have been summed to increase the signal-to-noise ratio, the two sidebands always show nearly identical variations. The changes in Q and U are similar in all epochs, suggesting a systematic error rather than intrinsic polarization changes.

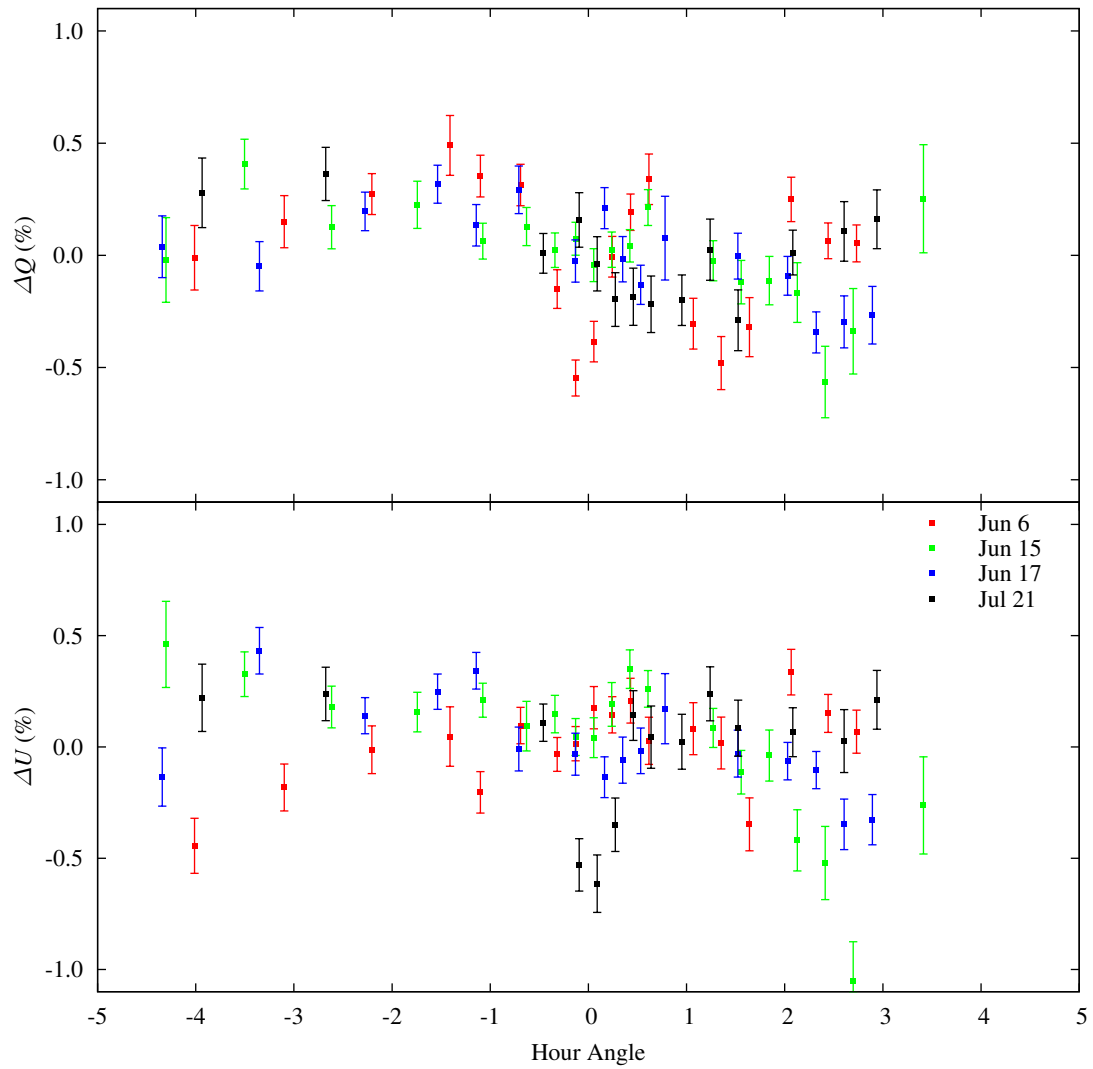


Fig. 3.9.— Same as Figure 3.8, except using 345 GHz measurements from 2005.

The polarization deviations are believed to arise from a combination of two symptoms. First, there is a smooth variation in both Q and U across the entire track with an amplitude of approximately 0.2%, most pronounced in U near the end of each track. Near transit ($HA = 0$) there is also a cusp in the polarization error, often with large amplitude, superimposed on the smooth variation. The cusp is almost certainly a side effect of the high transit elevation of 3C 454.3 ($E = 86.35^\circ$), as it does not appear prominently in lower signal-to-noise ratio observations of the next strongest quasar, 3C 279. Kesteven (1997) describes the field rotation introduced by an antenna's pointing model (particularly the tilt of the elevation and azimuth axes) near transit, finding that these imperfections are magnified by the tangent of the elevation (up to $16\times$ for this source). His equations do not account for the additional rotation caused by the Nasmyth position of the receivers, but it appears that for typical SMA pointing models and this source, the resulting field rotation can be as large as a degree, a significant fraction of the $2^\circ - 5^\circ$ position angle change observed near transit. Another cause is suggested by the significant decrease in visibility amplitude near transit (as much as 25%) visible on most baselines. These are caused by pointing errors at high elevation. SMA visibility phases are also known to be altered by pointing errors, so gain errors (both amplitude and phase) may be corrupting the derived polarization properties through the phase difference between RR and LL. Finally, the imprint of leakage errors during transit can also resemble the observed polarization cusp, due to the rapid change in parallactic angle near transit. Since these effects are all tied to the high transit elevation and since a similar cusp is not seen in other objects, this type of error is not a cause for general concern.

The smooth polarization variation is more important because it is seen in all sources where adequate signal-to-noise ratio measurements are available. The variation could be attributed to errors in the leakage measurements, so the leakages have been investigated in several ways. In most of these observations 3C 454.3 was also used as the polarization calibrator, so it is plausible that the gain changes near transit could affect the leakage determination. However, excluding the high-elevation data from the leakage solution does not change the shape of these deviations. The July 20 and July 22 curves in Figure 3.8 were both derived with the transit data ($E > 82^\circ$) excluded and show larger cusp amplitudes near transit but still retain the overall pattern of variation. Using leakages derived from another calibrator (3C 279), when available, similarly does not produce flat polarization. Light curves were also derived using various forms of averaged leakages, including averages between real or imaginary components of d_R and d_L , with no effect.

With simple leakage errors excluded as the cause of the smooth variation, the most likely explanation arises from the Nasmyth optics configuration used in the SMA. To this point it has been assumed that the cross-polarization coupling occurs inside the receiver cabin, that is, after the full parallactic angle change specified in equation (3.17) and thus with constant orientation relative to the receiver. This is the behavior assumed in the *MIRIAD* software (Sault et al. 1995) that derives the leakages from the data. However, any cross-polarization coupling caused by the optics on the sky side of the elevation mirror (M3 in Figure 2.1) will rotate by ϕ_{alt-az} (equation [3.16]) relative to the sky, but will also rotation by E relative to the receiver. In principle, the Cassegrain SMA telescopes should not have significant cross-polarization for on-axis sources because of the symmetry of the design, but

effects such as the illumination offsets measured in nearly all of the telescopes break the symmetry.

Addition of leakage at a second point in the optical path significantly complicates the response equations. The response can be calculated after appropriately redefining \mathbf{J} (equation [3.2]). Decomposing the leakage into one component (\mathbf{D}) fixed relative to the receiver and a second component (\mathbf{D}') referred to as the antenna polarization or leakage, defined as in equation (3.4), and originating on the sky side of M3, equation (3.2) becomes

$$\mathbf{J}' = \mathbf{G} \mathbf{D} \mathbf{P}(\pi/4 - E) \mathbf{D}' \mathbf{P}(\phi_{alt-az}). \quad (3.28)$$

This equation can be used with (3.6) to determine analogues of equations (3.8–3.11). When the antenna polarization (\mathbf{D}') is included, the response equations have terms that vary with $2\phi_{alt-az}$, $2\phi_{SMA}$, $2E$, and $2(\phi_{alt-az} + E)$, and the sums and products of the two types of leakages, making them sufficiently complex that they will not be reproduced here. Implementation of a polarization calibration routine that incorporates these terms is underway. The program will be based on the *MIRIAD* task GPCAL, which is used to determine leakages in the absence of this complication. The modifications are being made by R. J. Sault, the author of the original program, who will be resident in Cambridge in October 2006.

3.6.2 Impact of the Antenna Polarization

Because the antenna polarization cannot be corrected with existing software, it is important to evaluate its impact on polarization data obtained from the SMA. The data reduction procedures assume a constant leakage within each observation, while

the combination of antenna and wave plate leakages behave roughly like a total leakage of the form $(d + d'e^{-2iE})$, plus cross terms that should be unimportant. The most obvious impact of this behavior is that the leakages derived in a given observation will depend on the parallactic angle (or hour angle) coverage of the track. This is almost certainly responsible for much of the interday variability observed in the leakages (§ 3.5.1), as the expected measurement error is well below the observed changes and time-ordered leakages do not show permanent shifts or trends that might be expected from changes in the instrument. Because most of the parallactic angle change on the usual calibrator, 3C 454.3, occurs within an hour of transit, the derived leakages will depend heavily on the sampling within this hour. The question of leakage variability will need to be revisited once the software infrastructure required for determining antenna leakage has been completed. It is important to note, however, that the leakage repeatability achieved thus far is already five times better than was obtained at BIMA for 230 GHz band leakages, the best previous example of polarimetry at comparable frequency. The ability to measure these small effects is largely the result of the availability of very strong calibrators, good weather, and a sensitive and stable instrument, rather than an indication of poor performance.

The antenna polarization could also have consequences for the polarization properties derived for science target sources. Since the leakage error enters as a fractional contamination of the source polarization (in the case of leakage errors corresponding to $I \leftrightarrow Q, U$ corruption), the effects will be most important for low-polarization sources. For a 1% polarized source, contamination of 0.2% could change the measured position angle by as much as 12° . At 5% polarization this

maximum position angle error is down to just 2° . These represent the errors in snapshot polarization observations, but as in the previous discussion of leakage errors (§ 3.5.1), parallactic angle rotation will reduce the impact of these errors for full-track averages.

Of particular concern are the effects on the precision polarimetry of Sgr A* discussed in subsequent chapters. A primary motivation for the construction of the polarimeter was the measurement of position angle changes with frequency indicative of Faraday rotation. The results of Chapter 5 indicate that the position angle difference introduced by Faraday rotation across the 10 GHz SMA sideband separation is just 5° at 230 GHz and just 1° at 345 GHz. Given the variations of several tenths of a percent in Q and U in Figures 3.8 and 3.9, it seems somewhat implausible to measure position angle differences to such precision. Fortunately, because the antenna polarization properties should change very slowly with frequency (negligible change across a 10 GHz interval), the ΔQ and ΔU versus hour angle curves for the two sidebands track each other well across the sky. As a result, there is no systematic difference between the polarizations derived in the two sidebands for polarized sources (excluding Sgr A*). The polarization data obtained in good weather are also of such quality as to allow polarization light curves to be created for Sgr A* with single-sample integration times as short as four minutes (Chapter 7). At present, these curves are afflicted by the effects of antenna leakage at a low level. The peak ΔU of approximately 0.5% could alter the instantaneous position angle of Sgr A* by several degrees when it drops to 5% polarization, and much lower polarization fractions are observed in these light curves. Although such changes are small compared to the polarization variability of the source, they are a troublesome

contaminant and a primary motivation for the development of improved software.

3.7 Astronomical Verification

The sky at submillimeter wavelengths is almost devoid of sources with known polarization for comparison with SMA results. Quasar polarimetry from the SMA and other observatories at these frequencies (e.g. Nartallo et al. 1998) show that the polarization of these objects is not often stable, so non-contemporaneous measurements at the same frequency cannot usefully be compared. Comparison with the VLA/VLBA Polarization Calibration Database³ (Taylor & Myers 2000) also shows that the polarization at lower frequencies (5 – 43 GHz) need not be correlated with the submillimeter polarization. Although many galactic sources have measured polarization properties, previous submillimeter polarimetry examines very different angular scales than the SMA. There are, however, a very few sources that have been observed with BIMA at 230 GHz at comparable angular resolution.

Two tests of the calibration of the absolute polarization position angles measured with the SMA have been undertaken. First, the polarization of 3C 286 was measured at 230 GHz in June 2005. This source is one of the position angle calibrators used with the VLA and VLBA to determine absolute polarization directions because it is believed to have a stable polarization direction at the relevant frequencies (5 – 43 GHz). 3C 286 is a weak source (0.4 Jy in June 2005) in the submillimeter band, so the 45 mJy polarization was detected at just 5σ . Nevertheless, the

³<http://www.vla.nrao.edu/astro/calib/polar/>

polarization fraction ($11.5\% \pm 2.5\%$) and position angle ($35^\circ 6' \pm 5.9''$) from the SMA agree well with the 11–12% polarization reported in VLA/VLBA Polarization Calibration Database and the 33° position angle assumed for this source in VLA calibration. The second test compared polarization measured at 230 GHz by BIMA in the binary protostar NGC 1333 IRAS4A (Girart et al. 1999) with observations at 345 GHz with the SMA (Girart et al. 2006). After smoothing the SMA data to the angular resolution of the earlier BIMA data, the polarization direction at the total intensity peak is $143^\circ 0' \pm 1.6''$, compared to the $146^\circ \pm 7''$ measured by Girart et al. (1999). Because the polarization direction is believed to be determined by the ordered magnetic field of the system (Girart et al. 2006), we expect the true polarization direction to be the same at these frequencies.

Chapter 4

Sgr A*: Variable 340 GHz Linear Polarization

Daniel P. Marrone, James M. Moran, Jun-Hui Zhao & Ramprasad Rao 2006,
“Interferometric Measurements of Variable 340 GHz Linear Polarization in
Sagittarius A*”, *The Astrophysical Journal*, **640**, 308

Abstract

Using the Submillimeter Array, we have made the first high angular resolution measurements of the linear polarization of Sagittarius A* at submillimeter wavelengths, and the first detection of intraday variability in its linear polarization. We detected linear polarization at 340 GHz (880 μm) at several epochs. At the typical resolution of $1''.4 \times 2''.2$, the expected contamination from the surrounding (partially polarized) dust emission is negligible. We found that both the polarization

fraction and the position angle are variable, with the polarization fraction dropping from 8.5% to 2.3% over 3 days. This is the first significant measurement of variability in the linear polarization fraction in this source. We also found variability in the polarization and total intensity within single nights, although the relationship between the two is not clear from these data. The simultaneous 332 and 342 GHz position angles are the same, setting a 1σ rotation measure (RM) upper limit of $7 \times 10^5 \text{ rad m}^{-2}$. From position angle variations and comparison of “quiescent” position angles observed here and at 230 GHz we infer that the RM is a few times 10^5 rad m^{-2} , a factor of a few below our direct detection limit. A generalized model of the RM produced in the accretion flow suggests that the accretion rate at small radii must be low, below $10^{-6} - 10^{-7} M_{\odot} \text{ yr}^{-1}$ depending on the radial density and temperature profiles, but in all cases below the gas capture rate inferred from X-ray observations.

4.1 Introduction

The radio source Sagittarius A* (Sgr A*) has been conclusively identified in the radio and infrared with a black hole of mass $\sim 3.5 \times 10^6 M_{\odot}$ at the center of our Galaxy (Reid & Brunthaler 2004; Schödel et al. 2003; Ghez et al. 2005a; Eisenhauer et al. 2005). Sgr A* is the nearest supermassive black hole, 100 times closer than its nearest neighbor, M31*, and therefore should provide a unique opportunity to understand the physics and life cycle of these objects. For a black hole of its size, Sgr A* is extremely under luminous, only a few hundred solar luminosities and $10^{-8} L_{\text{Edd}}$. This surprisingly low luminosity has motivated many theoretical and

observational efforts to understand the processes at work very near to Sgr A*.

Accretion models of Sgr A* generally seek to explain its faintness through inefficient radiative and accretion processes. A variety of physical mechanisms can be invoked to suppress accretion and radiation, including convection (Narayan et al. 2000; Quataert & Gruzinov 2000b), jets (Falcke et al. 1993b), advection of energy stored in non radiating ions (Narayan & Yi 1994), and winds (Blandford & Begelman 1999). Many models incorporating combinations of these and other phenomena are able to account for the spectrum and low luminosity of Sgr A*. Therefore, the physics of this source is not well constrained by these observations alone.

In recent years, millimeter and submillimeter polarimetry has emerged as an important tool for studies of Sgr A*. Linear polarization and its variability can be used to understand the structure of the magnetic field in the emission region and turbulence in the accretion flow, and possibly to constrain the mechanisms responsible for the multi-wavelength variability of this source. Through Faraday rotation of the linear polarization, we can examine the density and magnetic field distributions along the line of sight, and eventually, in the context of more comprehensive models of the accretion flow structure, infer an accretion rate at the inner regions of the accretion flow (Quataert & Gruzinov 2000a; Agol 2000; Melia et al. 2000).

Previous observations of the linear polarization of Sgr A* have found low (<1%) upper limits at 22, 43, and 86 GHz (Bower et al. 1999c), with a 2% limit at 112 GHz (Bower et al. 2001). The lowest frequency detection of linear polarization is at 150 GHz (Aitken et al. 2000), suggesting that these polarimetric probes of

Sgr A* can only be exploited at short millimeter and submillimeter wavelengths. Aitken et al. (2000) found that the polarization fraction rises steeply from 150 to 400 GHz, although these observations were made with a single-aperture instrument and therefore required careful removal of contaminant emission within the telescope beam. The steep spectrum and a jump in the polarization position angle between 230 and 350 GHz in the Aitken et al. (2000) data have been taken as evidence of a transition to optically thin synchrotron emission (e.g., Aitken et al. 2000; Agol 2000; Melia et al. 2000). Subsequent interferometric monitoring of the 230 GHz polarization, with angular resolution sufficient to avoid contamination from the surrounding emission, has shown that the 230 GHz polarization fraction appears to remain constant over 5 yr, despite variations in the position angle on timescales of months to years (Bower et al. 2003, 2005a). This variability reduces the significance of the observed position angle jump and demonstrates the need for contemporaneous measurements at multiple frequencies. Bower et al. (2005a) attribute the variations in the 230 GHz polarization to changes of a few times 10^5 rad m^{-2} in the rotation measure (RM), probably in the accretion medium, rather than to changes in the intrinsic source polarization. As of yet, no observations have been able to determine the RM, but they can place upper limits on the magnitude of the RM and infer temporal variations that are within a factor of a few of the upper limits.

Circular polarization has also been detected in this source, with a rising polarization fraction from 1.4 to 15 GHz (Bower et al. 1999b; Sault & Macquart 1999; Bower et al. 2002c). Some models seeking to explain the millimeter/submillimeter linear polarization have also predicted appreciable circular polarization at these high frequencies due to the conversion of linear to circular polarization in a turbulent jet

(Beckert & Falcke 2002; Beckert 2003). However, measurements to date that are at or above 100 GHz (e.g., Tsuboi et al. 2003; Bower et al. 2003, 2005a) have not shown circular polarization at the percent level.

The Submillimeter Array (SMA) has the potential to contribute many new capabilities to these studies. It provides the first opportunity to measure the polarization above 230 GHz at an angular resolution sufficient to separate Sgr A* from its surroundings. Its large bandwidth (2 GHz per sideband), low latitude, and dry site make it far more sensitive for studies of this southern source than the 230 GHz observations of Bower et al. (2003, 2005a), which were made with the Berkeley-Illinois-Maryland Association array at Hat Creek, California. Given the sensitivity and the large (10 GHz) sideband separation, 340 GHz polarimetry with the SMA should improve limits on the RM, and future 230 GHz polarimetry may measure it directly. These advantages also apply to measurements of variability in total intensity and polarization, and of circular polarization. Here we present the first high angular resolution observations of the submillimeter polarization of Sgr A*, using the newly dedicated SMA and its polarimetry system. We discuss our observations and data reduction in § 4.2, the data and their relation to previous polarimetry in this source in § 4.3, and the implications of these new results in § 4.4. We offer concluding remarks in § 4.5.

4.2 Observations

Sgr A* was observed on several nights in 2004 using the Submillimeter Array¹ (Blundell 2004; Ho et al. 2004). The observing dates, zenith opacity, number of antennas used in the reduction, and on-source time are given in Table 4.1. The local oscillators were tuned to a frequency of 336.7 GHz, centering the 2 GHz wide upper and lower sidebands (USB and LSB) on 341.7 and 331.7 GHz, respectively. This frequency choice avoided strong spectral lines and provided a reasonable match to the frequency response of the SMA polarimetry hardware, as discussed below. Our Sgr A* tracks generally included source elevations between 20° and 41° (transit), a period of 7 hr, although weather, calibration, and technical problems caused variations in the coverage. In the SMA “Compact-North” configuration we sampled projected baselines between 8 and 135 k λ . The average synthesized beam was approximately 1".4 \times 2".2. According to the estimate in Aitken et al. (2000), polarized emission within the 14" beam of the James Clerk Maxwell Telescope (JCMT) at 350 GHz contributes 100 mJy of polarized flux density. With a beam smaller by a factor of 60 and reduced sensitivity to large-scale emission, we expect that this contaminant will be negligible in our data.

Each SMA antenna was equipped with a single linearly polarized (LP) feed in each of its three observing bands. Ideally, interferometric observations of linear polarization are made with dual circularly-polarized (CP) feeds as they separate the

¹The Submillimeter Array is a joint project between the Smithsonian Astrophysical Observatory and the Academia Sinica Institute of Astronomy and Astrophysics, and is funded by the Smithsonian Institution and the Academia Sinica.

Table 4.1. Observing Parameters

Date	τ_{337}^a	N_{ant}	t_{int} (minutes)
2004 May 25	0.16	7	100
2004 May 26	0.28	6	160
2004 Jul 5	0.11	7	160
2004 Jul 6	0.15	7	180
2004 Jul 7	0.29	6	170
2004 Jul 14	0.23	6	100

^aMean zenith opacity at the LO frequency of 337 GHz.

total intensity (Stokes I) from the linear polarization Stokes parameters (Q and U). For polarimetry we have converted the 340 GHz LP feeds to left- and right-hand circularly polarized (LCP and RCP) feeds using positionable quartz and sapphire quarter-wave plates. The polarization handedness was selected by switching the angular position of the wave plate crystal axes between two positions at $\pm 45^\circ$ from the polarization angle of the receiver. Although we could only measure a single polarization in each antenna at a given time, we sampled all four polarized correlations (LL, LR, RL, and RR) on each baseline by switching antennas between LCP and RCP in period 16 Walsh function patterns (e.g., Rao 1999). For 20 s integrations, a full cycle required just under 7 minutes. These observations were made during the commissioning phase of the SMA polarimetry hardware; details of this instrument can be found in D. P. Marrone (2005, in preparation).

The conversion of LP to CP was not perfect, but we calibrated the (frequency dependent) leakage of cross-handed polarization into each CP state of each antenna in order to properly determine source polarizations. We used a long observation of a polarized point source (in this case, the quasar 3C 279) to simultaneously solve for the quasar polarization and leakage terms (e.g., Sault et al. 1996). This polarization calibration was performed twice, on May 25 and July 14, yielding consistent leakages. The derived polarization leakages were at or below 3% in the USB and 5% in the LSB, with the exception of antenna 3, which used a sapphire wave plate with different frequency response and poorer performance (6% LSB leakage) than the other wave plates. Theoretical considerations of our design suggest that the real components of the L \rightarrow R and R \rightarrow L leakages should be identical for a given wave plate at a given frequency, and a comparison of the results on the two

nights (a total of four measurements of each real component) show that the rms variations in the measured leakage terms were below 1% for all antennas except antenna 7. One measured leakage on July 14 was responsible for this antenna's large rms, and because of the disagreement between the real part of the L→R and R→L leakages, we know that this measurement was in error. Using the same comparison on the other antennas, we found that on average the solutions for this date were of poorer quality, probably due to the difference in weather. Accordingly, we adopted the May 25 leakage values for all dates, although that required that we not use antenna 8, which was absent from that calibration track. Errors in the leakage calibration produce effects of varying importance, as outlined in Sault et al. (1996); the most important for our purposes are the contamination of Q and U by Stokes I due to errors in the determination of the leakage calibrator polarization. We have examined this effect by comparing the Q and U fractions across sidebands on the high signal-to-noise ratio 3C 279 data sets of May 25 and July 14; the two sidebands should give identical measurements of Q and U from the source, and differences can be ascribed to noise in the images and the difference of the independent errors in the leakage solutions in the two sidebands. With this procedure we found no inter-sideband differences that were consistent across the two data sets, and the differences present were consistent with the noise level, roughly 0.3% or smaller. Because an important part of our analysis is the comparison of position angles across sidebands, we had to ensure that the calibration did not create a position angle offset between the sidebands. Fortunately, although leakage errors could introduce spurious Stokes Q or U polarization, the phase difference between the RCP and LCP feeds, corresponding to a rotation of the sky polarization, is identically zero, because

each pair of CP feeds is in reality a single LP feed looking through both crystal axes of the same wave plate. Therefore, the only way to create a relative position angle difference between the sidebands would be through the leakage errors and the resulting contamination of Q and U , an effect that appears to be small in our data.

The flux density scale was derived from observations of Neptune on all nights except May 25 and July 14. We expect that the absolute calibration will be accurate to about 25% on these nights. The May 25 flux density scale was transferred from three quasars that were also observed on May 26; these appeared to have the same relative flux densities on both nights to better than 10%, consistent with the overall uncertainty on that night, so we do not expect that the May 25 flux densities are any more uncertain than the others. The July 14 data were obtained in an engineering track primarily aimed at obtaining a second polarization calibration, so only three sources are present (*Sgr A**, 3C 279, and 1743-038). Fortunately, 1743-038 has been very stable during more than two years of monitoring observations with the SMA (an rms flux density variation of only 20% in that time; M. Gurwell, private communication), with even smaller ($< 10\%$) variations observed from July 5 to July 7, so we have used it as our flux density standard for the final track.

The data were averaged over the 7 minute polarization cycle to simulate simultaneous measurement of all four polarized visibilities and were then phase self-calibrated using the LL and RR visibilities. Quasars were interleaved into the observations of *Sgr A** to allow variability monitoring and independent gain calibration. Transferring gains from the quasars, rather than self-calibrating, generally resulted in slightly lower signal-to-noise ratios but did not change the polarization. We attribute the increased noise ($\sim 20\%$) to the 16° – 40° angular

separation between Sgr A* and the quasars. Following calibration, each sideband was separately imaged in Stokes I , Q , U , and V , using only baselines longer than $20 \text{ k}\lambda$, and then cleaned. Sample Stokes images are shown in Figure 4.1. On July 14, due to poorer coverage in the uv -plane in the short track, we increased the cut to $30 \text{ k}\lambda$. Flux densities were extracted from the center pixel of each image, and these are listed in Table 4.2. We also examined the polarization by fitting point sources to the central parts of the images; the point-source flux densities matched well with those obtained from the central pixel when the signal was well above the noise, but the point-source positions and peak flux densities became erratic for low signal-to-noise ratio images (most Stokes Q and V images). Table 4.2 also includes the polarization fraction (m), which has been corrected for the noise bias (through quadrature subtraction of a 1σ noise contribution; e.g., Wardle & Kronberg 1974), and the electric vector position angle (χ , determined as $2\chi = \tan^{-1}(U/Q)$).

4.3 Results

4.3.1 Linear Polarization

The polarization fraction and position angle for each sideband on each night are plotted in Figure 4.2. It can be seen from the figure and the data in Table 4.2 that we have clear detections of the linear polarization in both sidebands on all nights. Among the six nights of our observations, July 7 stands out for its low polarization fraction, around 2%. The polarization was only detected at the $2 - 3\sigma$ level in each sideband, so the polarization position angle was poorly constrained.

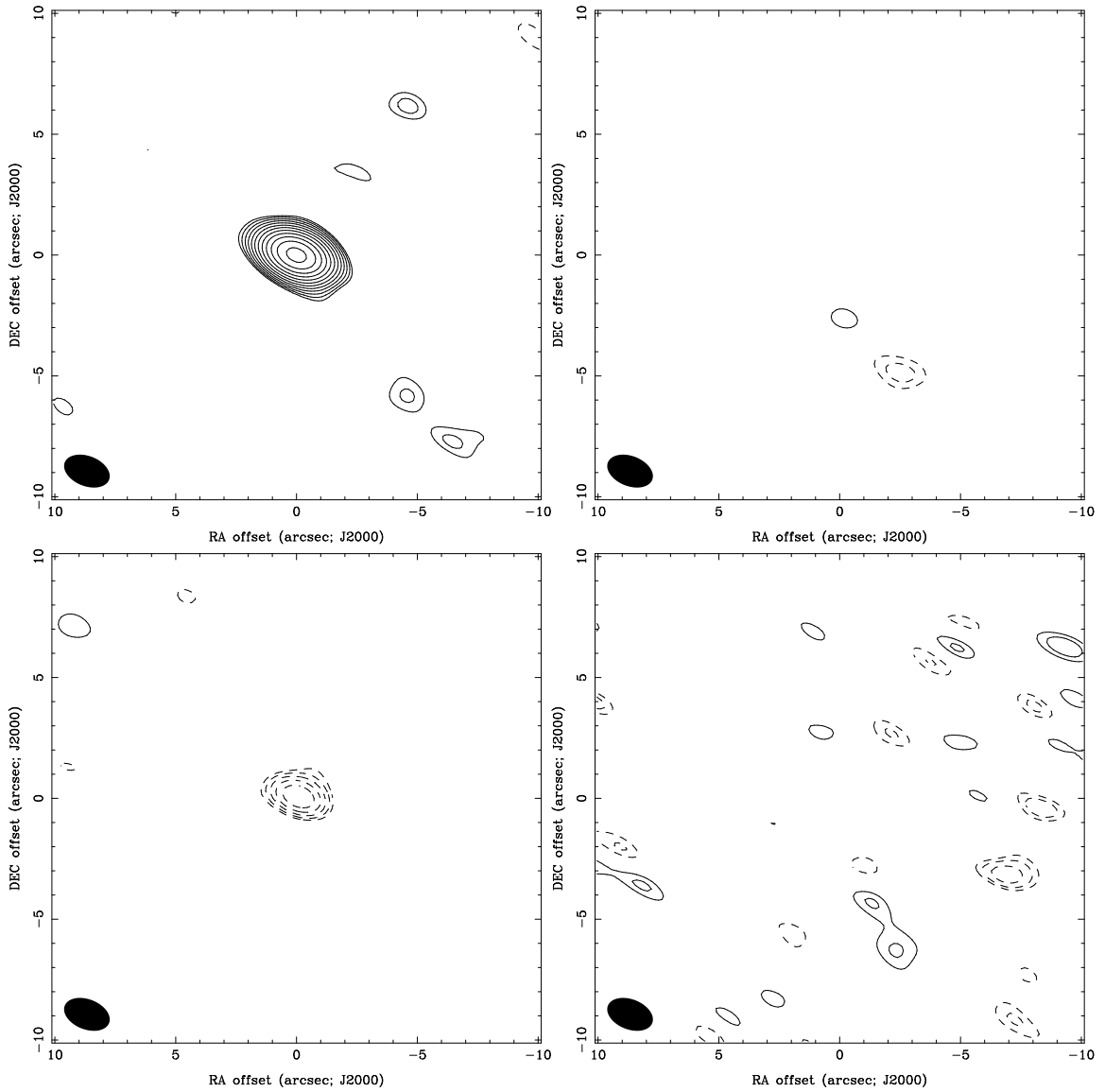


Fig. 4.1.— Sample Stokes images of Sgr A*, from the USB data (341.7 GHz) of 2004 May 25. The synthesized beam is $2''.0 \times 1''.2$. Panels clockwise from top left show I , Q , V , U . Contours are spaced by geometrical factors of $\sqrt{2}$. For Stokes I they are drawn at -4.2 (absent), -3, 3, 4.2, 6, 8.5, 12, 17, 24, 34, 48, 68, 96, and 136 times the 25 mJy beam^{-1} noise in the image, and for Q , U and V they are drawn at -12, -8.5, -6, -4.2, -3, 3, 4.2, and 6 (absent in all three images) times the 15 mJy beam^{-1} rms noise in the Q and U images (0.4% of I_{peak}). The V contours match the Q and U contours to highlight the increased noise introduced by the contamination of V by I , which is due to relative gain variations between LCP and RCP.

Table 4.2. 340 GHz Polarization Measurements of Sagittarius A*

Date	I (Jy)	Q (mJy)	U (mJy)	V (mJy)	m (%)	χ (deg)
2004 May 25:						
USB ...	3.79 ± 0.03	9 ± 15	-244 ± 15	-5 ± 22	6.43 ± 0.39	136.1 ± 1.7
LSB	3.79 ± 0.02	13 ± 17	-201 ± 17	-9 ± 21	5.28 ± 0.45	136.8 ± 2.4
Both ...	3.79 ± 0.02	13 ± 11	-230 ± 11	-5 ± 17	6.07 ± 0.28	136.7 ± 1.3
2004 May 26:						
USB ...	3.19 ± 0.03	145 ± 20	-97 ± 20	-14 ± 21	5.43 ± 0.63	163.0 ± 3.3
LSB	3.11 ± 0.02	104 ± 18	-138 ± 18	-10 ± 22	5.53 ± 0.58	153.5 ± 3.0
Both ...	3.16 ± 0.02	118 ± 13	-138 ± 13	-17 ± 19	5.75 ± 0.43	155.3 ± 2.1
2004 July 5:						
USB ...	3.23 ± 0.04	42 ± 14	-267 ± 14	-37 ± 17	8.35 ± 0.44	139.5 ± 1.5
LSB	3.13 ± 0.02	41 ± 12	-273 ± 12	-19 ± 17	8.84 ± 0.38	139.3 ± 1.2
Both ...	3.20 ± 0.02	42 ± 10	-270 ± 10	-38 ± 13	8.52 ± 0.31	139.5 ± 1.0
2004 July 6:						
USB ...	3.19 ± 0.02	58 ± 21	-169 ± 21	-15 ± 25	5.56 ± 0.65	144.4 ± 3.3
LSB	3.15 ± 0.03	29 ± 18	-164 ± 18	-16 ± 22	5.27 ± 0.56	140.1 ± 3.0
Both ...	3.18 ± 0.02	52 ± 15	-177 ± 15	-18 ± 19	5.78 ± 0.49	143.2 ± 2.4
2004 July 7:						
USB ...	2.71 ± 0.03	38 ± 22	-35 ± 22	-8 ± 29	1.72 ± 0.82	158.8 ± 13.7
LSB	2.78 ± 0.04	31 ± 22	-67 ± 22	-13 ± 38	2.53 ± 0.80	147.6 ± 9.0
Both ...	2.75 ± 0.03	44 ± 17	-49 ± 17	-17 ± 25	2.32 ± 0.61	156.1 ± 7.5
2004 July 14:						
USB ...	3.00 ± 0.03	37 ± 27	-243 ± 27	14 ± 32	8.14 ± 0.91	139.3 ± 3.2
LSB	3.00 ± 0.03	29 ± 19	-175 ± 19	-17 ± 25	5.87 ± 0.64	139.7 ± 3.1
Both ...	3.02 ± 0.03	75 ± 16	-236 ± 16	-15 ± 24	8.17 ± 0.55	143.8 ± 1.9
All days:						
USB ...	3.33 ± 0.02	57 ± 10	-197 ± 10	-9 ± 15	6.15 ± 0.29	143.1 ± 1.3
LSB	3.29 ± 0.02	49 ± 10	-202 ± 10	-8 ± 13	6.32 ± 0.29	141.8 ± 1.3
Both ...	3.31 ± 0.02	59 ± 7	-204 ± 7	-17 ± 11	6.39 ± 0.23	143.1 ± 1.0

Note. — Errors in the flux density columns are from the image rms only; they do not include the 25% absolute calibration uncertainty, which applies equally to all flux densities and does not affect the m or χ columns.

This is the lowest linear polarization fraction measured at or above 150 GHz, the lowest frequency at which polarization has been detected. The weather on this night was the poorest of all the tracks, but only marginally worse than May 26, which did not show an unusually low polarization. Other sources in the July 7 track with measurable polarization, such as 3C 279, did not show a significantly lower polarization than on other nights, as one might have expected from a systematic problem in that track. An obvious systematic error would be a substantial change in the leakages with respect to previous nights; this would most easily be caused by large changes to the alignment of the polarization hardware. However, the hardware was not moved between installation on July 5 and removal after the July 7 track, and the July 5 and 6 tracks show substantially larger polarization, so this possibility seems very unlikely. Moreover, because the leakages measured on July 14 are consistent with the May 25 leakages, as discussed in § 4.2, any change between July 6 and 7 would have to have been reversed when the hardware was reinstalled on July 14. This low polarization fraction, along with the unusually high polarization two nights before, clearly demonstrates that the polarization fraction is variable. Moreover, the polarization variations are present both in the polarization fraction and the polarized flux density, even after accounting for the 25% uncertainty in the overall flux density scale, and are not merely the result of a constant polarized emission component with a changing total intensity.

Variability was also observed in the polarization position angle. Polarization over four of the nights ranged between roughly 137° and 143° , at a weighted average position angle of 139.6° . The position angle determined for May 26 differed significantly from this range, and July 7 had an extremely uncertain position angle

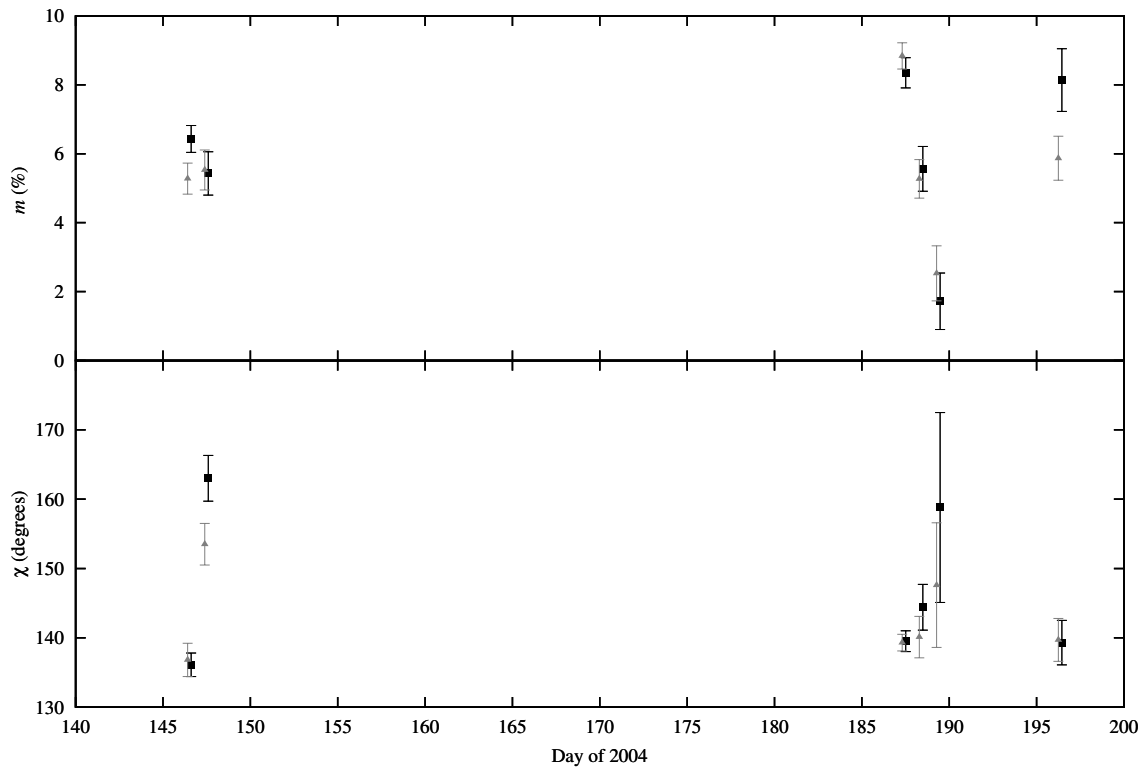


Fig. 4.2.— Plots of the 340 GHz Sgr A* polarization fraction (m ; *top*) and position angle (χ ; *bottom*). The USB (*black squares*) and LSB (*gray triangles*) data are plotted separately for each night. The two sidebands are slightly offset in time for clarity, but both sample the same time interval. The large χ error bars on day 189 (July 7) are due to the low polarization signal on that night.

due to the very low polarization fraction. Neither the combined six-night data set nor the individual nights showed significant inter-sideband differences, with the possible exception of May 26. On that night $\chi_{\text{LSB}} - \chi_{\text{USB}} = (153^{\circ}.5 \pm 3^{\circ}.0) - (163^{\circ}.0 \pm 3^{\circ}.3) = -9^{\circ}.5 \pm 4^{\circ}.5$, which is marginally significant for the quoted errors. As we discussed in § 4.2, although it is possible for Stokes I to contaminate Q and U (which determine χ), this appears to be unimportant in these data. The 0.3% limit on this effect is smaller than the Q and U errors on May 26, which are 0.6% of the Stokes I . Furthermore, any other systematic source of inter-sideband position angle offsets would show up equally on all nights, but the six-night average $\chi_{\text{LSB}} - \chi_{\text{USB}}$ is $1^{\circ}.3 \pm 1^{\circ}.8$, which is consistent with zero. The May 26 result is considered further in the context of a Faraday rotation measure in § 4.4.1.

4.3.2 Circular Polarization

Neither the averaged data nor the individual nights show CP at a level that is significant. The greatest deviation from zero is -38 ± 13 mJy on July 5, corresponding to $-1.2\% \pm 0.4\%$. However, in addition to the quoted error, which is the measured noise in the cleaned map, there are well-known systematic effects. The MIRIAD reduction package (Sault et al. 1995) uses linearized equations when solving for the polarized leakages, ignoring second-order terms in the leakages (d) and linear polarization fraction. These terms contribute a systematic error in Stokes V of the form Id^2 and md (Roberts et al. 1994), which may be on the order of a few tenths of a percent for our leakages and the polarization of Sgr A*. Moreover, the small difference in the sample times of the LL and RR correlations on a given

baseline permit gain differences due to weather, pointing, and system changes to introduce differences between the LL and RR visibilities that would not be present if these were actually measured simultaneously (as our reduction assumes). These gain variations contaminate Stokes V with Stokes I and make the value of V at the peak of the I map more uncertain than the map rms would indicate. The average of all six tracks shows $-0.5\% \pm 0.3\%$ CP, consistent with zero, with an additional systematic error of perhaps another 0.3%. The 0.5% sum of these errors can be taken as a limit on any persistent level of CP across the six nights and is the most stringent limit yet on CP in Sgr A* above 90 GHz.

4.3.3 Intraday Variability

Intraday variability in the total intensity (Stokes I), the polarization fraction, and position angle are shown in Figure 4.3. The July 5–7 observations were obtained as part of a coordinated multi wavelength Sgr A* monitoring program, and the observed temporal variability in Stokes I on these nights is discussed in conjunction with results at other wavelengths in Eckart et al. (2006a). In order to prevent antennas with variable performance from falsely modulating Stokes I , we use only the five antennas with the best gain stability for these light curves. Slow variations in the gain of the other antennas are likely due to pointing errors. We have reduced the effects of changing spatial sampling of extended emission by removing the two baselines that project to less than $24 \text{ k}\lambda$ (angular scales $>9''$) during the Sgr A* observations. Further details of the light curve reduction can be found in Eckart et al. (2006a). The variability in the linear polarization is much harder to measure;

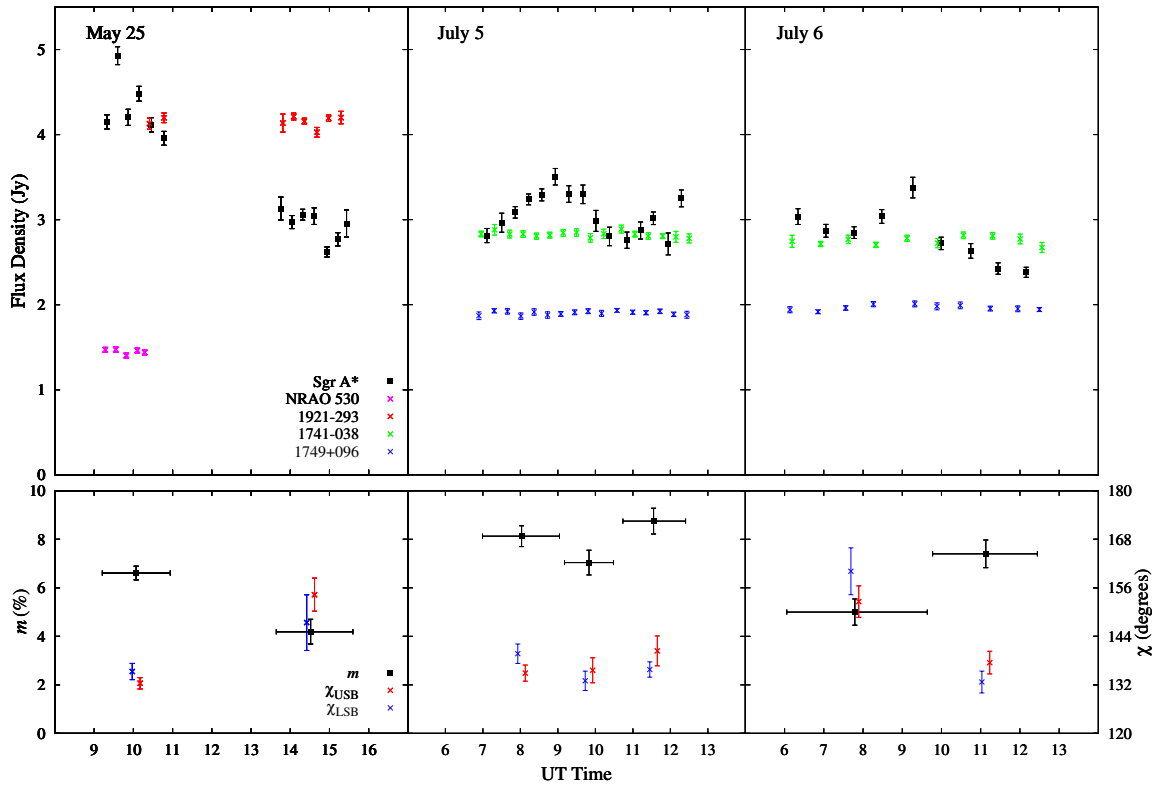


Fig. 4.3.— Variability in the total intensity (*top*) and polarization (fraction and position angle; *bottom*) of Sgr A* at 340 GHz. The three nights with the best weather are shown, as these permit the most accurate determinations of the polarization variation. The total intensity light curves of the quasar calibrators, 1741–038, 1749+096, and 1921–293, are also shown. In the lower plots, the binned intervals are demarcated by the horizontal bars on the polarization fraction points. This polarization fraction is the double-sideband value. The USB and LSB position angles sample the same time bin but have been offset slightly from the bin center for clarity.

with signals 1 – 2 orders of magnitude weaker than Stokes I , it is difficult to obtain reliable results from a subdivided track, and we could not be as selective about which data to exclude in the hope of removing the imprint of instrumental variations from the polarization variation. Accordingly, polarized light curves could not be reliably extracted for May 26 and July 14 due to poor weather, nor for July 7, due to both weather and very low polarization fraction. The remaining three nights have been subdivided into two or three segments at boundaries in the Stokes I curves, and the polarization has been extracted as described in § 4.2. The large (160 minute) gap on May 25, due to instrument difficulties, served as one of the boundaries.

A great deal of variability is visible in the Stokes I curve on all three nights, with the most notable feature being the ~ 1.5 Jy difference between the flux densities of the first and second halves of the May 25 data. No such difference shows up in the light curve of the calibrator, 1921–293, a source at nearly identical declination, suggesting that this result is not an instrumental artifact. Clear polarization variability is also measured on May 25 and July 6 in both m and χ . At all times the position angles in the USB and LSB are found to be very similar, as was observed in the full track averages reported above.

4.4 Discussion

4.4.1 Rotation Measure

The rotation measure associated with a plasma screen located between the source and observer can be inferred from the measurement of χ at two frequencies, since it

introduces a frequency-dependent change in the position angle given by

$$\chi(\nu) = \chi_0 + \frac{c^2}{\nu^2} \text{RM}, \quad (4.1)$$

where the RM is given by (e.g., Gardner & Whiteoak 1966)

$$\text{RM} = 8.1 \times 10^5 \int n_e \mathbf{B} \cdot d\mathbf{l} \quad (4.2)$$

for the electron density n_e in units of cm^{-3} , the path length $d\mathbf{l}$ in pc, and the magnetic field \mathbf{B} in Gauss. The greatest obstacle to such a detection, as previously noted, is the variability in the polarization, which may prevent polarization measured at different times from being reliably compared.

The best method for measuring the RM from our data comes from the observed difference in the simultaneous position angles in the USB and LSB. If we apply equation (4.1) to the two sideband frequencies of these observations, for position angles in degrees, we obtain

$$\text{RM} = (3.7 \times 10^5) (\chi_{\text{LSB}} - \chi_{\text{USB}}). \quad (4.3)$$

Equation (4.3) implicitly assumes that the Faraday rotation occurs outside of the plasma responsible for the polarized emission. This assumption seems reasonable for Sgr A*; very long baseline interferometry (VLBI) measurements (Krichbaum et al. 1998; Shen et al. 2005; Bower et al. 2004) suggest intrinsic sizes of $13 - 24r_S$ at 215, 86, and 43 GHz, and for reasons described in § 4.4.2 we expect little contribution to the RM inside $300r_S$. One other potential complication arises if the source polarization changes with radius and the two frequencies being compared probe different radii. For our 3% sideband separation, if we assume that the polarized submillimeter emission is thermal synchrotron (as is expected in ADAF models;

Yuan et al. 2003), we expect a 5% opacity difference between our sidebands, while for nonthermal synchrotron emission (taking an electron energy spectral index of 2-3.5; e.g., Markoff et al. 2001; Yuan et al. 2003) the difference is 9%–12%. Emission will be contributed from a range of radii around the $\tau = 1$ surfaces, so we would have to postulate a large gradient in the source polarization to produce a large intrinsic inter-sideband polarization difference over such a small frequency range. Finally, the 2 GHz bandwidth at 340 GHz limits the allowed RM to approximately 2×10^7 rad m⁻² if polarization is detected, as this RM would rotate the polarization by more than a radian across the band and wash out the signal (bandwidth depolarization). For highly polarized emission, the vector average of the polarization may still be detectable, but the position angles of the two sidebands are very unlikely to agree in this case. We can therefore ignore the possibility of full 180° wraps between sidebands, as a wrap requires a RM of 7×10^7 rad m⁻².

As is clear from Table 4.2, we do not see a significant change in the position angle between the two SMA sidebands on most of the observing nights (disregarding the uncertain position angle of July 7). In the most sensitive track, July 5, the sideband difference places a 1σ limit of 7.1×10^5 rad m⁻² on the RM on that particular night, which is the most sensitive limit to date from simultaneous interferometric observations. If the full data set is considered together (i.e., with Stokes images derived from the ensemble of data), the limit drops by a small amount to 6.8×10^5 rad m⁻², although if the RM is varying between observations this average will not actually represent a measurement of a RM. It should be noted here that the broadband observations of Aitken et al. (2000) were able to place a similar limit of approximately 5×10^5 rad m⁻² on the RM in 1999 August because of the

large bandwidth of their 150 GHz bolometer.

The May 26 sideband difference of $-9.5^\circ \pm 4.5$ is possibly significant, with an inferred rotation measure of $(-3.5 \pm 1.7) \times 10^6 \text{ rad m}^{-2}$. If this RM had been present on the previous night, it would have shown up as a similarly large sideband difference instead of the observed 0.7 ± 3.1 , which corresponds to a RM of $(0.3 \pm 1.1) \times 10^6 \text{ rad m}^{-2}$. We can check the large RM by comparing the position angles on May 25 and 26, on the assumption that the emitted polarization (χ_0 from eq. [4.1]) is constant over timescales of a few days and observed position angle changes are due to RM changes. At this frequency, the relationship between the position angle change ($\Delta\chi$, in units of degrees) and the RM change is (see eq. [4.1])

$$\Delta\text{RM} = (2.2 \times 10^4) \Delta\chi. \quad (4.4)$$

We observed an increase in the position angle from May 25 to May 26 of 18.6 ± 2.5 . If this is not a change in the intrinsic polarization, it corresponds to an increase in the RM of $4 \times 10^5 \text{ rad m}^{-2}$, which is inconsistent with the small sideband difference on May 25 and the large difference on May 26. The position angle is 180° degenerate, however, and a change in χ of $18.6 - 180^\circ = -161.4$ requires a RM change of $-3.6 \times 10^6 \text{ rad m}^{-2}$, which agrees well with the RM inferred from the May 26 sideband difference. It is therefore possible that we have observed a large change in the RM between these two nights, with the May 26 value far in excess of the limits on the other five nights. We discuss this further in § 4.4.2.

In the existing polarization data at 230 and 340 GHz, the position angle seems to frequently return to the same value. The Bower et al. (2005a) 230 GHz data are clustered around 111° between 2002 October and 2004 January, while four of

our observations at 340 GHz have a mean position angle of 140° . Assuming that these two angles sample the same χ_0 (no source polarization changes between the two observing periods or observing frequencies), we can infer a “quiescent” RM of $-5.1 \times 10^5 \text{ rad m}^{-2}$. This is just below the RM upper limit from our most sensitive night. If the idea of a quiescent RM is correct, then the change in the mean 230 GHz position angle observed between early 2002 (Bower et al. 2003) and 2003 (Bower et al. 2005a) merely reflects a change in this RM by $-3 \times 10^5 \text{ rad m}^{-2}$. This implies that the quiescent RM in early 2002 was around $-8 \times 10^5 \text{ rad m}^{-2}$, which is conveniently below the detection limit of the Bower et al. (2003) observations. If this scenario is correct, the RM should be detectable by the SMA at 230 GHz, where it would be observable as a 5° sideband difference.

4.4.2 Accretion Rate Constraints

Much of the importance placed on the RM determination stems from its use as a probe of the accretion rate near the black hole. However, the interpretation of a RM detection, or limit, in terms of an accretion rate requires a model for the density and magnetic field in the accretion flow, as these quantities actually determine the RM through equation (4.2).

To estimate the RM predicted for a variety of accretion models, we make several simplifying assumptions. First, we assume a generic picture with a central emission source surrounded by a roughly spherical accretion flow. Given the previously mentioned limits on the millimeter size of *Sgr A**, we could also accommodate models where the observed 340 GHz emission arises in a small jet component, as the jet

would have to lie within $\sim 10r_S$ of the black hole and would effectively be a central emission source as seen from a Faraday screen tens to hundreds of r_S further out.

We characterize the radial density profile, $n(r)$, as a power law,

$$n(r) = n_0(r/r_S)^{-\beta}, \quad (4.5)$$

where $r_S = 2GM_{\text{BH}}/c^2$ is the Schwarzschild radius of Sgr A* (10^{12} cm for $M_{\text{BH}} = 3.5 \times 10^6 M_\odot$), and n_0 is the density at this radius. In the case of free-falling gas we have $\dot{M}(r) \propto r^p$ with $\beta = 3/2 - p$, as in Blandford & Begelman (1999). For spherical accretion (Bondi 1952) or an advection-dominated accretion flow (ADAF; Narayan & Yi 1994), we have $\beta = 3/2$, while for a convection-dominated accretion flow (CDAF; Narayan et al. 2000; Quataert & Gruzinov 2000b), formally an $\dot{M} = 0$ limiting case of convection-frustrated accretion, we have $\beta = 1/2$. Intermediate values are also possible: the best-fit radiatively inefficient accretion model in Yuan et al. (2003) has $\beta = 0.8$, and accretion flow simulations (e.g., Pen et al. 2003) typically produce values between 1/2 and 1 (Quataert 2003). We take the ADAF and CDAF values as bounds on β (i.e., from 1/2 to 3/2).

Rather than using a separate parameter to describe the magnetic field profile, we tie it to the density by assuming equipartition between magnetic, kinetic, and gravitational energy, as many other modelers have done (e.g., Melia 1992). For pure hydrogen gas, with the use of equation (4.5), we obtain

$$B(r) = \sqrt{4\pi c^2 m_H n_0} \left(\frac{r}{r_S} \right)^{-(\beta+1)/2}. \quad (4.6)$$

We additionally assume that the magnetic field contains no reversals along the line of sight and is entirely radial, which should contribute only a small error unless the field is very nearly toroidal. The former simplification is a good approximation for

strongly peaked RM versus r profiles (large β), where only a small radial range contributes significantly. For smaller values of β and many field reversals, the effective field will only drop as the square root of the number of reversals.

In the Sgr A* accretion flow we expect that the electron temperature (T_e) will rise to smaller radii, eventually bringing the electrons to relativistic temperatures ($T_e > 6 \times 10^9 \text{K} = m_e c^2/k$) at some radius r_{in} . The RM contribution from relativistic electrons is suppressed [by as much as $\log(\gamma)/2\gamma^2$ for the Lorentz factor γ in the ultra-relativistic thermal plasma limit; Quataert & Gruzinov 2000a], so we approximate this effect by truncating the RM integration at r_{in} and by treating r_{in} as a variable. From the density profile, if we assume that gas at r_{in} is in free fall, we can determine a mass flux across the $r = r_{\text{in}}$ surface:

$$\begin{aligned} \dot{M}_{\text{in}} &= 4\pi r_{\text{in}}^2 m_{\text{H}} n(r_{\text{in}}) v(r_{\text{in}}) \\ &= 4\pi r_{\text{S}}^2 m_{\text{H}} n_0 c (r_{\text{in}}/r_{\text{S}})^{3/2-\beta}. \end{aligned} \quad (4.7)$$

This equation does not require that the density profile be followed down to $r = r_{\text{S}}$; $n_0 = n(r_{\text{S}})$ is merely a convenient quantity to normalize the power-law density relation we are assuming for larger radii. The mass flux at r_{in} (\dot{M}_{in}) can be taken to be an upper limit on the accretion rate at r_{S} , but the true rate of accretion onto the black hole could be lower if the loosely bound plasma falling from r_{in} escapes as a wind or jet. By substituting equations (4.5), (4.6), and (4.7) into equation (4.2), and converting \dot{M}_{in} to units of $M_{\odot} \text{yr}^{-1}$ and r to r_{S} , we obtain

$$RM = (3.4 \times 10^{19}) \left(\frac{M_{\text{BH}}}{3.5 \times 10^6 M_{\odot}} \right)^{-2} \quad (4.8)$$

$$\times r_{\text{in}}^{(6\beta-9)/4} \dot{M}_{\text{in}}^{3/2} \int_{r_{\text{in}}}^{r_{\text{out}}} r^{-(3\beta+1)/2} dr. \quad (4.9)$$

Integrating and simplifying yields

$$RM = (3.4 \times 10^{19}) \left[1 - (r_{\text{out}}/r_{\text{in}})^{-(3\beta-1)/2} \right] \quad (4.10)$$

$$\times \left(\frac{M_{\text{BH}}}{3.5 \times 10^6 M_{\odot}} \right)^{-2} \left(\frac{2}{3\beta-1} \right) r_{\text{in}}^{-7/4} \dot{M}_{\text{in}}^{3/2}. \quad (4.11)$$

To obtain an RM from a given β and \dot{M}_{in} we must also choose r_{in} and r_{out} . The inner radius will vary by model, but it is typically around $300r_{\text{S}}$ (e.g., Yuan et al. 2003). For these calculations we consider values of r_{in} from $300r_{\text{S}}$ to $3r_{\text{S}}$ in order to account for variations among models and to allow for the possibility that the electrons do not become highly relativistic interior to r_{in} , in which case the RM would not be strongly suppressed. The outer radius depends on the coherence of the radial field. We examine two cases: a fully coherent field ($r_{\text{out}} \approx \infty$), and a field that persists for a factor of 3 in radius from r_{in} .

Figure 4.4 shows the accretion rate limits imposed by our RM limit of $7 \times 10^5 \text{ rad m}^{-2}$, based on the model described above. From the two choices of r_{out} we see that the effect of the magnetic field coherence is larger at small values of β . As mentioned before, for steep density profiles (large values of β) we expect that only a small range in radius around r_{in} contributes to the RM, making the inferred accretion rate limit insensitive to the field coherence length. If we assume that the density profile follows equation (4.5) down to $r = r_{\text{S}}$, our model imposes accretion rate limits that are a factor of $\dot{M}(r_{\text{S}})/\dot{M}_{\text{in}} = (r_{\text{in}}/r_{\text{S}})^{\beta-3/2}$ lower than those in Figure 4.4, but the transition to supersonic flow makes this density extrapolation uncertain. However, in cases like the basic ADAF model (Narayan & Yi 1995) in which the electron temperature ceases to rise at small radii and the electrons are only marginally relativistic, integration to smaller radii (the lower sets of curves)

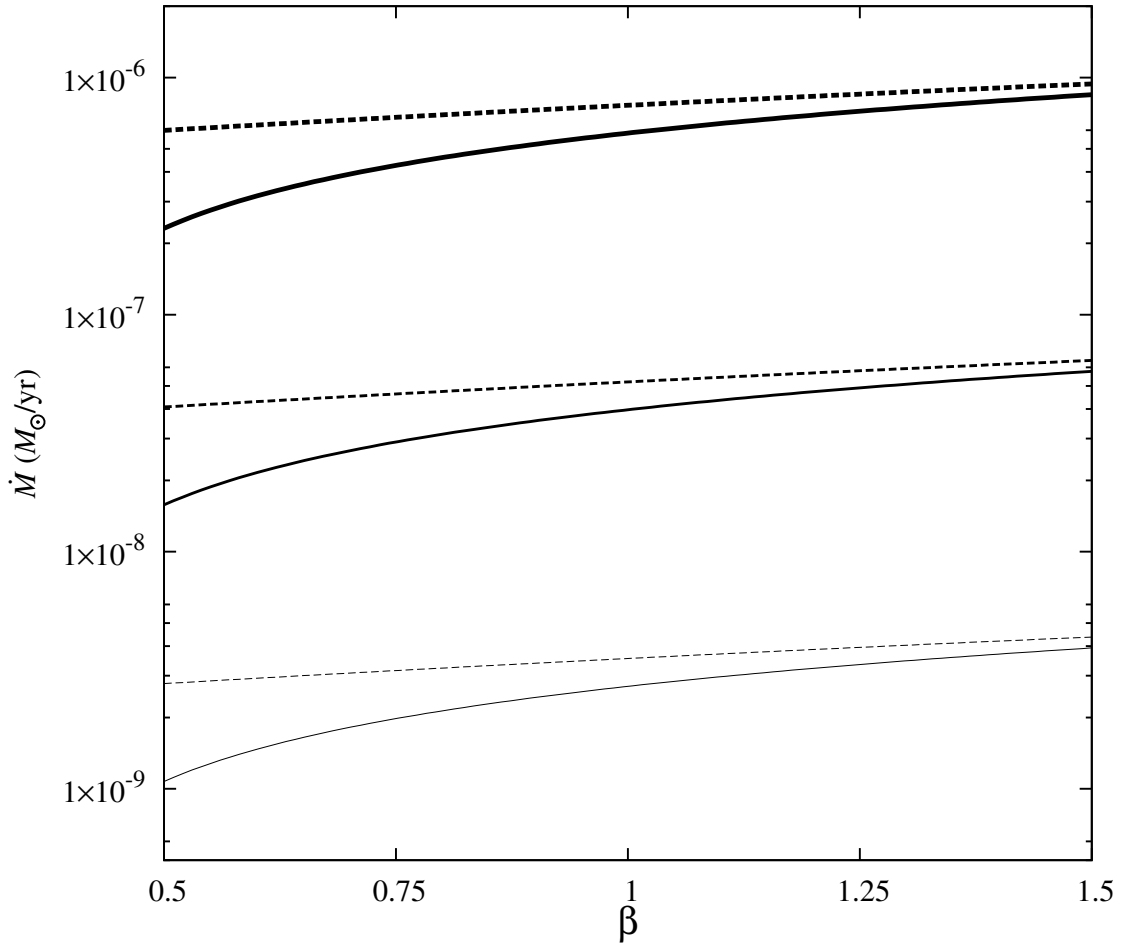


Fig. 4.4.— Accretion rate limits imposed by the rotation measure limit of $7 \times 10^5 \text{ rad m}^{-2}$ as a function of the density power law, given the accretion model described in § 4.4.2. The accretion rate plotted here is measured at the radius where the electrons become relativistic, r_{in} ; extrapolation to the black hole event horizon is discussed in § 4.4.2. Two sets of curves are plotted (see eq. [4.11]): three for a magnetic field that is coherent to large radius (*solid lines*), and three for a field that is coherent over a smaller range ($r_{\text{out}}/r_{\text{in}} = 3$; *dashed lines*). Within each set, the lines from thickest to thinnest represent $r_{\text{in}} = 300r_{\text{S}}$, then $30r_{\text{S}}$, and finally $3r_{\text{S}}$.

may set more relevant (and lower) accretion rate limits. In fact, by taking $\beta = 3/2$ and $r_{\text{in}} = 30r_{\text{S}}$, we roughly have the ADAF Bondi model used in Quataert & Gruzinov (2000a), and we reproduce their \dot{M} limit of $10^{-7} M_{\odot} \text{ yr}^{-1}$. The high- and low- β limits are similar, but the field coherence is a larger concern for shallow profiles. Since the prototype for a low- β model is a highly convective flow, we can expect a tangled field, but in this case the accretion rate limit (proportional to $B^{-2/3}$) will increase only as $\dot{M} \propto N^{1/3}$ for N field reversals. In summary, the figure shows that for any choice of density profile, the maximum allowed accretion rate is $10^{-6} M_{\odot} \text{ yr}^{-1}$ and may be much lower. This is an order of magnitude below the gas capture rate of $10^{-5} M_{\odot} \text{ yr}^{-1}$ inferred from X-ray observations (Baganoff et al. 2003; Yuan et al. 2003) and from simulations of stellar winds in the Galactic center (e.g., Quataert 2004; Cuadra et al. 2006). It is therefore likely that there is substantial mass lost between the gas capture at $r \sim 10^5 r_{\text{S}}$ and the event horizon.

Finally, this model of the accretion flow can be used to examine the proposed $-3.5 \times 10^6 \text{ rad m}^{-2}$ RM from May 26 (§ 4.4.1). This RM would require a change of more than $2 \times 10^6 \text{ rad m}^{-2}$ between consecutive nights. This is very large compared to the RM changes implied by other position angle changes (again assuming that the source polarization remains constant). On the basis of the four other nights with strong polarization detections, all of which have position angles near 140° , the peak-to-peak change in χ corresponds to an RM change of $1.5 \times 10^5 \text{ rad m}^{-2}$, and the rms variation is only $5 \times 10^4 \text{ rad m}^{-2}$. The largest change on similar timescales (days to weeks) observed at 230 GHz is $3 \times 10^5 \text{ rad m}^{-2}$ (between 2003 December 27 and 2004 January 5; Bower et al. 2005a). The longer timescale 230 GHz position angle changes and the difference between our position angles and the Aitken et al.

(2000) 350 GHz position angle (reinterpreted as described in § 4.4.3 or otherwise) also correspond to RM changes of a few times 10^5 rad m⁻². We expect that these variations are not more than order unity fractional RM changes, so they are all quite consistent with our inferred -5×10^5 rad m⁻² quiescent RM from § 4.4.1. The May 26 RM would then correspond to a factor of 7 increase in the density or line-of-sight magnetic field. Such a change is difficult to accomplish with any density profile but is particularly difficult for small values of β , where the entire line of sight contributes significantly to the RM. If the fluctuation is real, it suggests a steep density profile, as the associated density/field change should not be extended over decades of radius. Unless such an event is observed again in future observations, the more likely interpretations appear to be that the position angle change from May 25 represents a RM fluctuation of 4×10^5 rad m⁻² observed between consecutive nights or a transient change in the source polarization, and the May 26 difference in the USB and LSB position angles is merely a 2σ measurement noise event.

4.4.3 Linear Polarization and Variability

Our 340 GHz observations show a typical polarization fraction of 6.4%, with a range of 2.3%–8.5%, and an rms variation of 2.0%. This is comparable to the $\sim 7.5\%$ mean, 4.6%–13.6% range, and 2.2% rms measured at 230 GHz by Bower et al. (2003, 2005a). The range of observed polarization is lower at 340 GHz than it is at 230 GHz, and the mean is slightly lower as well. It is difficult to explain a lower observed polarization fraction (and comparable variability) at higher frequencies with beam depolarization models (Tribble 1991), as Faraday rotation and the

resulting dispersion in polarization directions decreases with increasing frequency. If the polarization fraction decrease is intrinsic to the source and not generated in the propagation medium, it suggests that the magnetic field becomes increasingly disordered at smaller radii, as these observations should probe slightly smaller radii than the 230 GHz data. But across only 0.2 decades in frequency we expect little change in intrinsic polarization, so the difference, if present, may be best explained by time variability in the source polarization. To resolve this question, simultaneous or nearly coincident polarimetry at multiple frequencies with interferometer resolution is clearly desirable.

Bower et al. (2005a) used the apparent stability of the 230 GHz polarization fraction to argue that the observed variations in the 230 GHz polarization position angle were more likely to be the result of changes in the rotation measure than due to intrinsic source changes. While our results do not refute this conclusion, they demonstrate that the polarization fraction is not stable, even over a single night. Note that two substantial excursions in the 230 GHz polarization fraction, one of which is labeled an “outlier” in Bower et al. (2005a), probably represent real variations similar to those seen here, but have lower significance because of the poorer sensitivity of their instrument.

The polarization fraction presented here is considerably lower than those measured in 1999 by Aitken et al. (2000): $13_{-4}^{+10}\%$ and $22_{-9}^{+25}\%$ at 350 and 400 GHz, respectively. However, to determine the flux density of Sgr A* Aitken et al. (2000) had to correct for the contamination from dust and free-free emission in their large primary beam ($14''$ – $12''.5$ at the highest frequencies), and it is possible that they over-corrected for the dust emission, which would make the polarized component

appear to be a larger fraction of the total flux density of Sgr A*. There is some support for this possibility from their measured flux densities: Sgr A* was found to be only 2.3 and 1 Jy at 350 and 400 GHz, while our data (see Table 4.2) and previous measurements between 300 and 400 GHz have found higher values of 2.6 – 3.8 Jy (Zylka et al. 1995; Serabyn et al. 1997; Pierce-Price et al. 2000). If we assume that their 350 GHz data are well calibrated (the 400 GHz calibration is more uncertain) and assume our 3.3 Jy flux density for Sgr A*, we can rederive the intrinsic polarization of Sgr A* using their Stokes Q and U decomposition method and find a polarization of 9% at 158° . The polarization fraction drops further as the assumed flux density for Sgr A* is increased, reaching 7.6% for 3.8 Jy. These values are within the polarization fraction variations we observe; one might expect that well-calibrated 400 GHz measurements could be interpreted similarly and that the polarization fraction need not rise steeply to high frequencies. In arriving at a flux density of 2.3 Jy for Sgr A*, Aitken et al. (2000) estimated the dust emission in their central pixel from the average of the surrounding pixels, so by increasing the contribution from Sgr A*, we are also suggesting that there is a deficit of dust emission in the central $14''$ at 350 GHz. Unfortunately, our observations are poorly sampled at short spacings, but the available visibilities shortward of $20 \text{ k}\lambda$ show little excess over the point-source flux density, consistent with such a central hole in the dust emission. The existence of this hole requires further confirmation, as could be achieved through simultaneous single-aperture and interferometer observations; our circumstantial evidence could be equally well explained if Sgr A* had a higher polarization fraction and lower flux density in 1999 (at the time of the Aitken et al. (2000) measurement) and if the emission in the central $30''$ is distributed smoothly

on scales smaller than $10''$.

We observe variability on internight and intraday intervals in both the polarization and total intensity. The single-night flux densities that we measure fall within the range of previous observations, and the rms variation of 0.3 Jy, or 10%, matches the recent results of Mauerhan et al. (2005) at 100 GHz. Within nights, the Stokes I light curves in Figure 4.3 show unambiguous variations on timescales of hours, reminiscent of those seen at 100 and 140 GHz by Miyazaki et al. (2004) and Mauerhan et al. (2005). This is slower than the variations seen in the near-infrared and X-ray (e.g., Baganoff et al. 2001; Genzel et al. 2003), which seem to vary on hour timescales, with some features requiring only minutes. These slow changes suggest that opacity is obscuring our view of the very inner regions of the accretion flow, regions unobscured at NIR/X-ray wavelengths, even at 340 GHz. At slightly higher frequencies the inner flow may become visible, although many estimates of the optically thin transition frequency place it at or above 1 THz, a frequency that is difficult to access from the ground. It should be possible to search for the transition to optically thin emission using the change in the variability timescale; the more frequently proposed technique of looking for the turnover in the spectrum relies on precise flux density calibration at high frequencies, which is problematic because of contaminating emission in single-aperture beams and lack of unresolved calibrators in interferometers. A few instruments may be able to make these difficult observations before the Atacama Large Millimeter Array (ALMA): the SMA, or perhaps the Submillimeter Common-User Bolometer Array (SCUBA; Holland et al. 1999) on the JCMT at 650 GHz, and the Submillimeter High Angular Resolution Camera (SHARC II; Dowell et al. 2003) on the Caltech Submillimeter Observatory

(CSO) at 650 or 850 GHz.

The intraday variations in the linear polarization shown in Figure 4.3 are the first linear polarization changes observed on intervals of hours rather than days. The three nights with time-resolved polarization measurements do not demonstrate a clear relationship between Stokes I and the polarization. For example, May 25 shows a very strong flare in I with m very close to our average values, followed in the second half of the track by a lower I and a below-average m . July 5 has the highest value of m of our six nights, along with 20% modulation in I , but the polarization fraction is not modulated significantly with the total intensity. Finally, on July 6 we see below-average m in a period of high I and above-average m with low I , the inverse of the relationship seen on May 25. That the polarization fraction may vary in multiple ways during flares in the total intensity could suggest that there are multiple mechanisms (of varying polarization) responsible for the submillimeter Stokes I variability, or that the I and m changes are not closely related. Diverse flare mechanisms could be expected to show different spectra at shorter wavelengths, so simultaneous infrared and X-ray data may be useful. However, on the basis of the infrequency of infrared and X-ray flares (Eckart et al. 2004) and the lack of coincident activity in these bands during the SMA observations on July 6 and 7 (Eckart et al. 2006a), it seems that the small changes we observe in the submillimeter are often imperceptible at shorter wavelengths. Therefore, the best way to determine whether the polarization changes are internal or external may be to increase the time resolution in the polarization light curves. In these data we observe changes in m on the shortest interval we can measure, around 3 hr (on July 6). This is close to the variability timescale observed in the total intensity, which suggests that,

given better time resolution, we may see that the changes in I and m have similar temporal characteristics and therefore arise from the same processes.

The m and χ curves seem to show more coordinated behavior than the total intensity and polarization do. Of the seven sub-night intervals plotted in Figure 4.3, five show position angles close to the observed quiescent χ -value of 140° . Only in the two intervals with the lowest polarization, on May 25 and July 6, does χ deviate from this value, and if the deviations are caused by RM changes, then both would represent increases in the RM. None of the intervals provide evidence for a RM through inter-sideband differences in χ , but the largest change in χ between intervals, -20.7 ± 3.8 on July 6, only requires a RM decrease of 5×10^5 rad m⁻², which is still below our detection limits. Here again we face the question of whether the source polarization or an external process is responsible for the variability we see. It is possible to explain the changes in χ with a two-component source, where the dominant polarization component is polarized close to the quiescent polarization direction and variable in amplitude, while the weaker component causes the polarization to deviate from 140° when the dominant component weakens. In this case we would expect to see a correlation between the polarization fraction and the position angle, something that is not excluded by our data. Such a source model is naturally identified with emission from a core and jet. A second model uses a turbulent plasma screen, in addition to the screen responsible for the putative mean RM (suggested by the difference in position angle between 230 and 340 GHz), to partially beam-depolarize the emission. The fact that χ seems to faithfully return to 140° implies that the source, or the source plus a stable RM component, is separated from the changes that cause the depolarization and position angle change.

With better time resolution and better sensitivity to RM, it should be possible to distinguish between these models.

4.5 Conclusions

Using the Submillimeter Array outfitted with polarization conversion hardware (D. P. Marrone, in preparation), we have made sensitive measurements of the polarization of Sgr A* at 340 GHz with angular resolution sufficient to separate the source from the surrounding contaminating emission. Our increased sensitivity has allowed us to make unequivocal measurements of the variability of the linear polarization of this source in both position angle and polarization fraction. This is the first reliable detection of variation in the linear polarization fraction. Moreover, we have made the first detection of linear polarization changes within a night. These changes do not show an obvious correlation with the observed changes in the total intensity, possibly because of the coarse time resolution available at our sensitivity limits. The polarization variations occur on the shortest intervals we sample, around 3 hr, which is comparable to the modulation time observed in the total intensity here and in Mauerhan et al. (2005) at 100 GHz. It is not clear from these data whether the polarization variability can be best explained by changes in the source emission or by changes in an external Faraday screen, but polarization light curves with better time resolution should clarify the issue. The observed polarization fraction at 340 GHz is comparable to, and perhaps lower than, that observed at 230 GHz. This contradicts the polarization spectrum measured from 150 to 400 GHz by Aitken et al. (2000), but we show that their polarization fraction at 350 GHz can be brought

into agreement with ours through changes in their correction for dust emission. Whether or not the polarization fraction rises steeply to high frequency, as predicted by synchrotron optical depth explanations of the early polarization results (Agol 2000; Melia et al. 2000), is no longer clear, but this question should be resolved by future submillimeter polarimetry at 650 GHz.

We have also measured the circular polarization of this source to be less than 0.5% for a time-stable component, and we do not detect CP at a slightly higher level in individual nights. This limit contradicts the predictions of the turbulence-driven polarization conversion model of Beckert (2003), which was designed to match the Aitken et al. (2000) linear polarization results, but can be matched to an earlier version of the model (Beckert & Falcke 2002) in which the CP originated in a fully turbulent jet.

By comparing the position angles in the two sidebands, we place new upper limits on the RM allowed for this source. In single nights we obtain 1σ upper limits of less than 10^6 rad m⁻² with our lowest limit of 7×10^5 rad m⁻² coming on July 5. This is comparable to the lowest limit obtained in any other polarimetric observations of this source and is well below the single-night limits of other interferometers. We can use a model accretion flow (with energy equipartition), parameterized only by the density power-law slope and the radius at which the electrons become relativistic, to convert this RM to a mass accretion rate limit, and we find that, for any density slope, Sgr A* is accreting at least an order of magnitude less matter than it should gravitationally capture on the basis of X-ray measurements (Baganoff et al. 2003) and may be accreting much less if the density profile is shallow. This result agrees with earlier interpretations of polarization detections. We note that the position

angle at 340 GHz seems to show a persistent stable state, much like that observed at 230 GHz (Bower et al. 2005a), and we combine these two values to infer a stable “quiescent” RM of -5×10^{-5} rad m⁻². This value is just below the detection limit of our observations. The possible proximity of the RM to the detection threshold, the need for more time-resolved polarimetry, and the potential for coordinated observations with other wavelengths suggests that expanded SMA capabilities may contribute considerably more to this study.

Acknowledgements

The authors thank the entire SMA team for their contributions to the array and to the new polarimetry system. In particular, we acknowledge the enormous contribution of K. Young for his work on the real-time software changes essential to these observations. We thank R. Narayan, E. Quataert, and G. Bower for useful discussions, and J. Greene for discussions and her help in developing the prototypes of the polarimetry system. D. P. M. was supported by an NSF Graduate Research Fellowship. We thank an anonymous referee for a thorough reading and helpful comments. Finally, we extend our gratitude to the Hawai’ian people, who allow us the privilege of observing from atop the sacred mountain of Mauna Kea.

Chapter 5

Sgr A*: Rotation Measure

Daniel P. Marrone, James M. Moran, Jun-Hui Zhao & Ramprasad Rao 2006, “An Unambiguous Detection of Faraday Rotation in Sagittarius A*”, *The Astrophysical Journal Letters*, submitted

Abstract

The millimeter/submillimeter wavelength polarization of Sgr A* is known to be variable in both magnitude and position angle on all time scales down to a few hours. The unstable polarization has prevented measurements made at different frequencies and different epochs from yielding convincing measurements of Faraday rotation in this source. Here we present observations made with the Submillimeter Array polarimeter at 227 and 343 GHz with sufficient sensitivity to determine the rotation measure at each band without comparing position angles measured at separate epochs. We find the rotation measure to be $(-5.6 \pm 0.7) \times 10^5$ rad m⁻², with no

evidence for variability at the level of the measurement error. We conservatively assign a 3σ upper limit of $2 \times 10^5 \text{ rad m}^{-2}$ to RM changes. This stability constrains interday fluctuations in the accretion rate to be less than 25%. The mean intrinsic position angle is $167^\circ \pm 7^\circ$ and we detect variations of 31_{-9}^{+18} degrees. The rotation measure restricts the accretion rate to the range $2 \times 10^{-7} M_\odot \text{ yr}^{-1}$ to $2 \times 10^{-9} M_\odot \text{ yr}^{-1}$, if the magnetic field is near equipartition and ordered. However, the apparent long-term stability of the sign of the rotation measure, its short-term stability, and past measurements of circular polarization suggest that a highly reversed field is also possible, which would substantially raise the upper and lower limits on the accretion rate.

5.1 Introduction

The linear polarization of Sgr A* was first detected by Aitken et al. (2000) above 100 GHz, after unsuccessful searches at lower frequencies (e.g. Bower et al. 1999a,c). Subsequent interferometer observations have shown the polarization to vary in position angle (Bower et al. 2005a) and fraction (Marrone et al. 2006), with variability occurring on timescales comparable to those of the previously observed total intensity variations (Marrone et al. 2006). The variability may be intrinsic to the source or due to propagation effects, but the short timescales suggest processes very close to the black hole and thus polarization should be a useful tool for the study of Sgr A*.

One aspect of the polarization that has yet to be exploited is its variation with frequency, particularly the frequency-dependent orientation change known

as Faraday rotation. The presence of polarization was used immediately after its detection to argue that the infalling plasma must be tenuous and the mass accretion rate low (less than $10^{-6} M_{\odot} \text{ yr}^{-1}$), as larger accretion rates would depolarize the emission through extreme Faraday rotation angles (Quataert & Gruzinov 2000a; Agol 2000). Further progress on determining the accretion rate and its variability has awaited measurement of the Faraday rotation measure (RM), a difficult task because of the significant variability of this source and the diminished effect of rotation at high frequencies. To date there have been three claims of a RM determination through non-simultaneous observations, although none of them is robust. Bower et al. (2003) used some of the available measurements to determine an RM of $-4.3 \times 10^5 \text{ rad m}^{-2}$, but the discovery of polarization variability rendered the result uncertain (Bower et al. 2005a). Marrone et al. (2006) compared average 230 and 345 GHz position angles to find $-5 \times 10^5 \text{ rad m}^{-2}$. Most recently, Macquart et al. (2006) estimated the RM to be $-4.4 \times 10^5 \text{ rad m}^{-2}$ from their 83 GHz polarization and all previous data. However, their analysis allows a much lower RM due to the 180° degeneracy of the polarization position angle (see § 5.3). Simultaneous measurements are a much more secure way to determine the RM, but the instantaneous frequency coverage of available instruments has not been adequate to show Faraday rotation. The lowest instantaneous upper limit on the magnitude of the RM is presently $7 \times 10^5 \text{ rad m}^{-2}$, using early Submillimeter Array¹ (SMA) 345 GHz polarimetric observations (Marrone et al. 2006).

¹The Submillimeter Array is a joint project between the Smithsonian Astrophysical Observatory and the Academia Sinica Institute of Astronomy and Astrophysics, and is funded by the Smithsonian Institution and the Academia Sinica.

Multi-frequency data can be used to determine the RM, the intrinsic polarization direction, and the variability of each. Isolating these changes is crucial to understanding the conditions in the inner accretion flow. The RM can be used to determine upper and lower limits on the accretion rate, while variations with frequency and time can be used to examine the structure of the flow. Here we report SMA measurements of the RM and intrinsic polarization changes of Sgr A*, the first observations to detect the RM with statistical significance and the only measurement made without resorting to comparisons between position angles measured at different epochs. The observations and calibration procedures are detailed in § 5.2, the RM and the variability of the RM and intrinsic polarization are examined in § 5.3, and we discuss the implications for the accretion rate and properties of Sgr A* in § 5.4.

5.2 Observations

The SMA made polarimetric observations of Sgr A* in 2005 June and July during polarimeter commissioning and as part of regular science programs. In the ten nights without weather or technical problems there are six (four) tracks in the 230 GHz (345 GHz) band. The 230 GHz observations used a local oscillator (LO) frequency of 226.9 GHz, providing simultaneous measurements of sidebands centered on 221.9 and 231.9 GHz, except one observations made at LO=225.55 GHz. The higher frequency data use LO=343 GHz. The weather was excellent in the usable nights, with a typical zenith opacity at 225 GHz of 0.06 – 0.08, or 0.19 – 0.27 when scaled to 343 GHz. All data were obtained with five to seven antennas in the compact configuration (7 – 70 meter baselines), resulting in a synthesized

beam width of $2''.0 \times 4''.0$ at 230 GHz and $1''.6 \times 3''.2$ at 345 GHz on Sgr A*. For the purposes of self-calibration and polarization extraction, baselines shorter than $20k\lambda$ were removed to exclude the extended emission around Sgr A*. Gain calibrators included J1743-038, J1733-130, J1924-292, and Ceres. Very similar polarization results were obtained when the calibrator gains were applied and when Sgr A* was self-calibrated. The flux density scale was derived from observations of planets and their moons, with an expected accuracy of better than 10%. Flux densities in each Stokes parameter were obtained through point-source fits to the visibilities. The observed properties of Sgr A* in all ten epochs are shown in Table 5.1. Stokes V (circular polarization) is not detected at the level of 1.5%.

To obtain full polarization information we used the SMA polarimeter, which was introduced in Marrone et al. (2006) and will be further described in a forthcoming paper (D. P. Marrone et al., 2006, in prep.). In 2005 a set of wave plates was added to the polarimeter to allow simultaneous polarimetry in the SMA 230 GHz and 690 GHz bands. These represent the first scientific data obtained with the new capabilities.

Measurement of polarization relies on precise determination of the fractional contamination (“leakage”) of each polarization state by the cross-handed polarization. Uncalibrated leakage contaminates the linearly polarized Stokes parameters (Q and U) with I . Leakages were measured each night by observing polarized quasars (3C 279 or 3C 454.3) over a large range of parallactic angle. The leakages are stable, approximately 1% in the upper sideband (USB) for each band, 4% for the 230 GHz lower sideband (LSB), and 2% for the 345 GHz LSB. The r.m.s. leakage variability is 0.3% at 230 GHz and 0.4% at 345 GHz. There are three potential sources of

Table 5.1. Polarization and Rotation Measure of Sagittarius A*

Date	ν (GHz)	I^a (Jy)	Q^a (mJy)	U^a (mJy)	m (%)	χ (deg)	RM (10^5 rad/m 2)	χ_0 (deg)
2005 Jun 4:	-6.7 ± 2.9	215 ± 29
USB ...	230.6	4.00 ± 0.04	100 ± 12	-176 ± 12	5.06 ± 0.29	149.8 ± 1.7		
LSB ...	220.6	3.91 ± 0.03	48 ± 11	-153 ± 11	4.08 ± 0.28	143.7 ± 2.0		
2005 Jun 6:	-23.1 ± 12.6	251 ± 56
USB ...	348.0	4.22 ± 0.04	126 ± 19	-177 ± 20	5.13 ± 0.47	152.7 ± 2.6		
LSB ...	338.0	4.14 ± 0.03	94 ± 16	-214 ± 15	5.62 ± 0.38	146.8 ± 1.9		
2005 Jun 9:	-5.0 ± 1.7	138 ± 17
USB ...	231.9	3.48 ± 0.02	-244 ± 9	-7 ± 8	7.01 ± 0.25	90.8 ± 1.0		
LSB ...	221.9	3.38 ± 0.02	-224 ± 8	28 ± 9	6.68 ± 0.24	86.4 ± 1.1		
2005 Jun 15:	-11.7 ± 13.6	192 ± 60
USB ...	348.0	3.31 ± 0.02	45 ± 16	-166 ± 16	5.18 ± 0.48	142.5 ± 2.7		
LSB ...	338.0	3.32 ± 0.02	29 ± 14	-181 ± 13	5.52 ± 0.41	139.6 ± 2.2		
2005 Jun 16:	-5.4 ± 1.8	174 ± 18
USB ...	231.9	3.94 ± 0.03	-93 ± 9	-196 ± 8	5.50 ± 0.22	122.3 ± 1.1		
LSB ...	221.9	3.79 ± 0.03	-109 ± 8	-157 ± 7	5.05 ± 0.19	117.6 ± 1.1		
2005 Jun 17:	-22.3 ± 7.4	246 ± 33
USB ...	348.0	2.95 ± 0.02	148 ± 14	-228 ± 14	9.21 ± 0.48	151.5 ± 1.5		
LSB ...	338.0	3.02 ± 0.02	109 ± 12	-276 ± 12	9.81 ± 0.41	145.8 ± 1.2		
2005 Jul 20:	-7.5 ± 1.6	209 ± 16
USB ...	231.9	3.82 ± 0.02	15 ± 6	-180 ± 6	4.73 ± 0.17	137.3 ± 1.0		
LSB ...	221.9	3.75 ± 0.02	-25 ± 6	-165 ± 6	4.45 ± 0.15	130.7 ± 1.0		
2005 Jul 21:	$+1.1 \pm 8.2$	154 ± 36
USB ...	348.0	3.87 ± 0.03	240 ± 18	-220 ± 17	8.39 ± 0.46	158.7 ± 1.6		
LSB ...	338.0	3.73 ± 0.03	225 ± 15	-203 ± 15	8.11 ± 0.40	159.0 ± 1.4		
2005 Jul 22:	-3.7 ± 1.8	152 ± 18
USB ...	231.9	3.37 ± 0.02	-91 ± 6	-120 ± 6	4.46 ± 0.18	116.4 ± 1.1		
LSB ...	221.9	3.34 ± 0.02	-105 ± 6	-110 ± 6	4.55 ± 0.17	113.1 ± 1.1		
2005 Jul 30:	-4.8 ± 1.4	133 ± 14
USB ...	231.9	4.16 ± 0.03	-223 ± 7	26 ± 6	5.39 ± 0.16	86.6 ± 0.8		
LSB ...	221.9	4.12 ± 0.03	-193 ± 7	53 ± 6	4.86 ± 0.15	82.4 ± 0.9		

^aStatistical errors only. Overall flux density scale uncertainty is 10%.

variability: (1) real instrumental polarization changes between nights, (2) finite signal-to-noise ratio, and (3) polarization leakage that is not constant across the sky, resulting in leakage determinations that depend on the hour angle coverage. The first of these may exist but is bounded by the small observed leakage variability. The second is expected to yield variations at the level of 0.1% in the 345 GHz leakages and less at 230 GHz. We know that the third effect is also present, at a level of around 0.2%, due to the fact that cross-polarization introduced skyward of the Nasmyth relay mirror is rotated relative to the feed as a source is tracked in elevation, while the cross-polarization of the wave plate and subsequent optics is fixed. This small additional leakage imprints itself on the polarization of the calibrator and its effect on the leakages derived in calibration (under the assumption of stationary leakage) changes with the elevation coverage of the calibrator. Fortunately, the resulting polarization changes are small. Leakage errors of 0.3%–0.4% contribute 0.2% fractional contamination to the instantaneous polarization, significantly less when averaged over a full track due to the parallactic angle rotation. For Sgr A*, which we measure to be 5%–10% polarized, this results in at most 1° of position angle error. We reduced the Sgr A* data using the average leakages at each frequency instead of the single-night values to confirm this estimate. More importantly for this purpose, the uncorrected instrumental polarization is very nearly constant across the sidebands because properties such as the illumination pattern on the antenna change slowly with frequency. We find the imprint of this additional leakage on the calibrator to be very consistent between sidebands, so although the absolute position angle varies by up to 1°, the inter-sideband difference varies only by 0.1°–0.2°. We take this as our systematic error for position angle differences, although it is much

lower than the thermal noise.

5.3 Rotation Measure and Intrinsic Polarization

Faraday rotation changes the observed polarization position angle (χ) as a function of frequency according to:

$$\chi(\nu) = \chi_0 + \frac{c^2}{\nu^2} \text{RM}, \quad (5.1)$$

where χ_0 is the intrinsic position angle. The rotation measure (RM) is proportional to the integral of the electron density and parallel magnetic field component along the line of sight. From the observed LSB and USB position angles we derive a RM and χ_0 for each observation. We plot χ in both sidebands against λ^2 for all ten epochs in Figure 5.1, along with the average RM and χ_0 . The larger errors in Table 5.1 for 345 GHz band RMs and χ_0 s result from the much smaller inter-sideband difference in λ^2 at the higher frequency. The average RM from all 10 epochs is $(-5.6 \pm 0.7) \times 10^5 \text{ rad m}^{-2}$, while the 230 GHz and 345 GHz points alone yield $(-5.4 \pm 0.7) \times 10^5 \text{ rad m}^{-2}$ and $(-13 \pm 5) \times 10^5 \text{ rad m}^{-2}$, respectively, consistent within their errors. The ten single-night RM values are consistent with a constant value ($\chi_r^2 = 1.21$, for 9 degrees of freedom). None of the 230 GHz points deviates from the average by more than 1.2 times its measurement error, while the largest deviation at 340 GHz is 2.2σ . We therefore place a conservative upper limit of three times the averaged σ , or $2.1 \times 10^5 \text{ rad m}^{-2}$ on RM variability. This agrees with the small RM fluctuations inferred from the constancy of polarization at 83 GHz (Macquart et al. 2006).

These observations also constrain the intrinsic polarization direction of Sgr A*. The average χ_0 in our ten measurements is $167^\circ \pm 7^\circ$, or $162^\circ \pm 7^\circ$ and $210^\circ \pm 21^\circ$ from 230 and 345 GHz observations, respectively. The χ_0 values vary by more than our measurement errors predict, suggesting intrinsic polarization changes. Assuming a constant χ_0 , we obtain $\chi_r^2 = 2.8$ (0.3% probability) using all data points, or $\chi_r^2 = 3.9$ (0.16%) for the 230 GHz points only. The scatter in the full data set suggests an intrinsic χ_0 dispersion of 31_{-9}^{+18} degrees, with very similar results obtained from just the 230 GHz points.

This represents the first reliable measurement of the RM of Sgr A*, and the only measurement made from simultaneous observations at multiple frequencies and therefore able to isolate source polarization changes. Macquart et al. (2006) derived an RM of -4.4×10^5 rad m⁻² from the average χ at four frequencies over the last several years. However, their interpretation requires a 180° unwrapping of the 83 GHz position angle and the non-wrapped position angle is not strongly excluded. They report a χ_r^2 of 2.1 for 3 degrees of freedom for the non-wrapped fit (RM= -1.9×10^5 rad m⁻²), which is only 90% confidence. Furthermore, this confidence level relies on their poorly measured USB polarization (just two of five measurements detect polarization at 3σ) and the standard error of the mean of just two measurements at 216 GHz in order to provide additional degrees of freedom. Discarding the former and using the 230 GHz variability to estimate the 216 GHz variability increases the probability of the non-wrapped position angle to 26%.

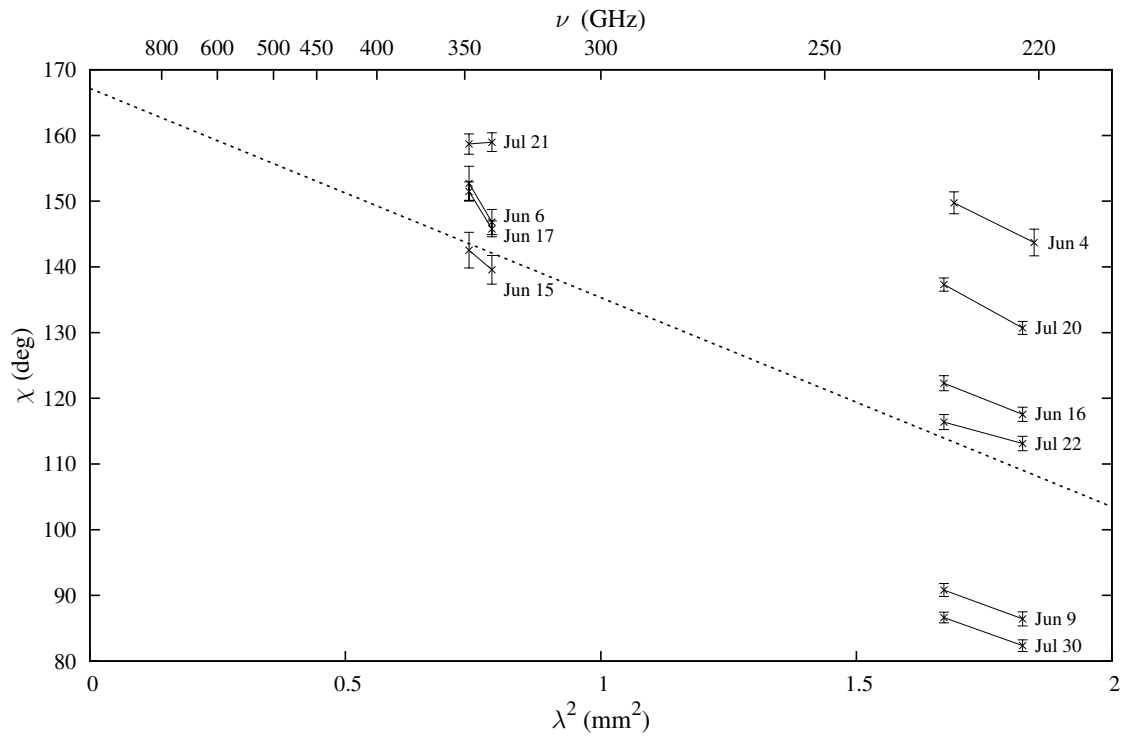


Fig. 5.1.— The position angles observed in each sideband on each of the ten epochs. The slope between the two sidebands at each epoch is proportional to the RM and the extrapolated intercept at the χ axis is χ_0 . The mean RM– χ_0 fit is also plotted. Variability in χ_0 is visible in the 230 GHz points (at right), which show slopes similar to the mean but are widely dispersed in χ .

5.4 Discussion

The RM we observe is too large to be produced by material beyond the accretion radius of Sgr A* (approximately $1''$ or 0.04 pc). Using the density determined by Baganoff et al. (2003), the RM in the dense inner $10''$ is just 8×10^3 rad m^{-2} assuming a 1 mG ambient field. RMs determined in nearby sources are as large as 70% of this estimate (e.g. Yusef-Zadeh & Morris 1987).

The RM can be used to determine the accretion rate at small radii around Sgr A* if assumptions are made about the nature of the accretion flow. The procedure is outlined in Marrone et al. (2006) and assumes a power-law radial density profile ($n \propto r^{-\beta}$) and ordered, radial, equipartition-strength magnetic fields. Our RM detection places upper limits that are 85% of those in their Figure 4. The important parameter for determining the range of upper limits is r_{in} , the radius at which electrons become relativistic and their RM contribution begins to be suppressed (Quataert & Gruzinov 2000a). In general, shallower density profiles approaching that of the convection-dominated accretion flow ($\beta \rightarrow 1/2$; Narayan et al. 2000; Quataert & Gruzinov 2000b) yield hotter central temperatures and thus larger r_{in} (Quataert 2003). Simulations favor this type of flow, for example, Igumenshchev et al. (2003) and Hawley & Balbus (2002) find $\beta = 1$, Pen et al. (2003) find $\beta = 0.72$, and the analytic model of Yuan et al. (2003) shows $\beta = 0.81$. The simulations with published temperature profiles show r_{in} between 30 and 100 Schwarzschild radii (r_{S}), yielding accretion rate upper limits of 2×10^{-7} to $5 \times 10^{-8} M_{\odot} \text{ yr}^{-1}$. Steeper profiles ($\beta \rightarrow 3/2$), as in Bondi-like or advection-dominated accretion flows (ADAF; Narayan & Yi 1995) are marginally relativistic to small radii and may have r_{in} of a few r_{S} ,

indicating an accretion rate upper limit of $1.5 \times 10^{-8} M_{\odot} \text{ yr}^{-1}$ for $r_{\text{in}} = 10r_{\text{S}}$. This has been used to rule out the original ADAF model, which has an accretion rate comparable to the Bondi rate ($10^{-5} M_{\odot} \text{ yr}^{-1}$ for this source; Baganoff et al. 2003).

Note that the assumptions of the Marrone et al. (2006) formalism, which were taken from previous related works (e.g. Melia 1992; Quataert & Gruzinov 2000a), are not constrained by existing observations. In particular, the assumption of equipartition-strength fields cannot be justified observationally, although simulations may show a tendency to reach equipartition fractions of a few percent (Igumenshchev et al. 2003). Magnetic fields that are a fraction ϵ of the equipartition strength will raise the accretion rate limits by $\epsilon^{-2/3}$ (a factor of 10 for $\epsilon = 3\%$).

The assumption of an ordered field is also potentially suspect. The direction of position angle change with frequency, and thus the sign of the RM, appears unchanged since the Aitken et al. (2000) measurements in 1999. Based on the observed stability of the sign of circular polarization (CP) and the large CP/LP ratio at low frequencies (Bower et al. 2002c), Ruszkowski & Begelman (2002) suggested that the observations could be explained by Faraday conversion of linear to circular polarization in a highly reversed field with a small directional bias. In this case the integrated product of the electron density and parallel magnetic field, without regard for direction along the line of sight, would be large, as would the accretion rate, but the net RM would be small and originate in the bias field. The bias field naturally creates stability in the CP and RM signs if the bias field (B_b), random field (B_{rms}), and number of reversals (N) satisfy $B_b \gg B_{\text{rms}}/\sqrt{N}$. Sign stability would not be expected from turbulent accretion flows due to the motion of randomly oriented field cells along the line of sight. Instead, such models must invoke a special geometry

(such as the axial region in model A of Igumenshchev et al. 2003) or a rigid field order (their model B) to create stability. The turbulent jet picture of Beckert & Falcke (2002) also uses a random field with a small bias to produce stability. If the stochastic field picture is correct, the accretion rate upper limits derived from our RM detection would no longer hold.

Our RM also allows us to place lower limits on the accretion rate; these are not subject to the caveats above since all of the uncertainties act to raise the minimum accretion rate. If we take r_{in} to be around $10r_{\text{S}}$ or $3r_{\text{S}}$ (smaller r_{in} yields smaller lower limits, so this is conservative for hot flows), we find that the accretion rate must be greater than $1 - 2 \times 10^{-8} M_{\odot} \text{ yr}^{-1}$ or $2 - 4 \times 10^{-9} M_{\odot} \text{ yr}^{-1}$, respectively. If the field is toroidal, reversed, or sub-equipartition, these lower limits are raised and may pose problems for very low accretion rate models. Our limit on RM variability (35%) also limits the accretion rate variability to 25% over two months.

Our detection of significant variability in χ_0 is the first clear separation of the effects of a variable RM and variable intrinsic polarization; disentangling these effects requires multi-frequency observations. In the optically thin limit χ_0 represents the intrinsic polarization direction of *Sgr A** at all frequencies. The dispersion in χ should be similar at 230 and 345 GHz as RM fluctuations of $7 \times 10^4 \text{ rad m}^{-2}$ produce only 7° and 3° changes, respectively, at these frequencies. However, comparing all previous measurements near 230 and 345 GHz (employing our RM to translate all observations to a single frequency), we find a dispersion of 22° in 16 observations at 230 GHz and just 8° in 11 epochs at 345 GHz (Aitken et al. 2000; Bower et al. 2003, 2005a; Marrone et al. 2006; this work). These two dispersions scale by approximately ν^{-2} , suggesting RM fluctuations, but the required changes ($2 \times 10^5 \text{ rad m}^{-2}$) are

disallowed by our data. The Macquart et al. (2006) 83 GHz measurements also show just 8° of variability, much less than predicted for RM fluctuations. Instead, the difference in the variability can probably be traced to opacity effects. Emission from Sgr A* appears to become optically thin around 300 – 400 GHz (Marrone et al., in prep), so the polarization at 345 GHz and higher frequencies represents structure just outside the black hole. In this picture, the greater dispersion at 230 GHz arises from changes in the polarization contribution from larger radii as the 230 GHz optical depth fluctuates. The relationship between opacity and polarization fluctuations was previously noted by Goldston et al. (2005).

Because we measure just two frequencies at a time, we cannot detect deviations from the ν^{-2} dependence expected for Faraday rotation. If the Faraday screen extends into the submillimeter emitting regions of the accretion flow (or jet), the magnitude of the RM would be expected to increase with frequency because of the decreasing optical depth. The difference between the Macquart et al. (2006) RM and ours is small but the difference is of the right sign, suggesting that non-relativistic plasma at small radii cannot be ruled out. Three-frequency observations, such as SMA 230/690 GHz data or joint observations with the SMA and the Combined Array for Research in Millimeter-wave Astronomy, may resolve this question.

Acknowledgements

The authors thank the SMA staff, particularly Ken Young, for assistance with the polarimeter, and Avi Loeb and Ramesh Narayan for useful discussions.

Chapter 6

Sgr A*: Submillimeter Spectrum

6.1 Introduction

Sagittarius A* is the source associated with what is now known to be a supermassive black hole at the center of our galaxy (e.g. Eisenhauer et al. 2005; Ghez et al. 2005a). Despite its proximity, Sgr A* is difficult to observe even at wavelengths where it is not obscured by Galactic extinction or the atmosphere because it sits amid a crowded field of sources. The detection of a bright and unresolved sub-arcsecond source at 2.7 and 8.1 GHz by Balick & Brown (1974) has been followed by high angular resolution imaging throughout the radio window (e.g. Falcke et al. 1998; An et al. 2005), which has demonstrated that Sgr A* has a rising spectrum across three decades in frequency up to 300 GHz. At higher frequencies, adaptive optics systems on ground-based telescopes and satellites have yielded detections of transient near-infrared and X-ray counterparts and placed limits on quiescent flux densities that are several orders of magnitude below the millimeter values (e.g. Genzel et al.

2003; Ghez et al. 2004; Baganoff et al. 2003). These data suggest that the primary peak in the spectral energy distribution (SED) lies between 300 GHz and the mid-infrared.

Submillimeter telescopes have been used to make observations of Sgr A* between 300 and 950 GHz. Higher frequency observations are precluded at nearly all ground-based telescopes by severe water vapor absorption (with a few notable exceptions, e.g. Marrone et al. 2004). There are single-aperture detections of Sgr A* up to 860 GHz (Serabyn et al. 1997; Yusef-Zadeh et al. 2006), including several around 670 GHz (Zylka et al. 1995; Aitken et al. 2000; Pierce-Price et al. 2000; Yusef-Zadeh et al. 2006). The scatter in these measurements and non-detections with the same telescopes (Dent et al. 1993; Serabyn et al. 1997) suggest variability in the source, as is seen at other wavelengths (Melia & Falcke 2001), but may also indicate the difficulty of extracting a flux density for Sgr A* from observations with angular resolution as coarse as $10 - 20''$ in the presence of contaminating dust and free-free emission. Submillimeter interferometers may enable us to finally measure the spectrum at these frequencies, an important constraint on emission models which presently must assume a peak emission frequency that could be incorrect by a factor of 10 or more. The turnover in the spectrum will indicate the transition to optically thin emission, so observations above this peak will probe plasma in the immediate vicinity of the black hole rather than larger photospheres.

Here we present measurements of the submillimeter spectrum of Sgr A* obtained through simultaneous observations at two frequencies. These data were obtained with the Submillimeter Array (SMA) and take advantage of its unprecedented submillimeter angular resolution and its ability to observe simultaneously at 230 and

690 GHz. These observations provide the first high-angular resolution measurements of the flux density of this source above 350 GHz. The accompanying 230 GHz data allow registration to previous measurements of the instantaneous lower-frequency spectrum of this source. In § 6.2 we describe the observations, their calibration, and the resulting flux densities in the two observing bands. In § 6.3 we place our data in the context of other measurements of this source and in 6.4 we discuss the implications of the submillimeter spectrum for the properties of Sgr A* and future submillimeter observations.

6.2 Observations and Results

The SMA¹ (Blundell 2004; Ho et al. 2004) was used to observe Sgr A* on three nights of excellent submillimeter weather in February and July 2005 (Table 6.1). The array was operated in its dual-frequency mode, with the 230 and 690 GHz receivers observing simultaneously at the frequencies listed in Table 6.1. There were between 5 and 7 antennas available in the two bands on each night. The 690 GHz band data sampled projected baselines between 20 and 158 k λ , while the 230 GHz data covered 6 to 55 k λ . Only baselines longer than 20 k λ have been used to extract the flux densities in order to exclude extended emission in this source (Bower et al. 2001). Typical synthesized beams were $5''.2 \times 2''.2$ and $2''.2 \times 0''.8$ in the 230 and 690 GHz bands, respectively. In February the 230 and 690 GHz receivers simultaneously

¹The Submillimeter Array is a joint project between the Smithsonian Astrophysical Observatory and the Academia Sinica Institute of Astronomy and Astrophysics, and is funded by the Smithsonian Institution and the Academia Sinica.

sampled orthogonal linear polarizations. The signal amplitude measured with such feeds is modulated across the sky due to the changing relative orientation of the feed and source polarizations (e.g. Shinnaga et al. 2004), but the amplitude of this modulation is limited to the polarization fraction, known to be $\lesssim 10\%$ in Sgr A* at 230–345 GHz (Aitken et al. 2000; Bower et al. 2005a; Marrone et al. 2006; Marrone et al. 2006b, submitted). In July, both sets of receivers alternated between left- and right-handed circular polarization (LCP and RCP, respectively) sensitivity; this polarization conversion was effected by the SMA polarimeter (Marrone et al. 2006, in prep.). Interferometric correlations of two RCP and two LCP elements measure Stokes $I + V$ and $I - V$, respectively, but their average yields Stokes I and the circular polarization (V) should be very small (e.g. Sault & Macquart 1999; Bower et al. 2002c; Marrone et al. 2006).

Calibration and flux density extraction were performed similarly in both receiver bands. At 230 GHz, gain calibration was performed at intervals of 8 – 15 minutes on combinations of the quasars J1733–130 (NRAO 530) and J1924–292, and the unresolved ($< 0.6''$) asteroid Ceres. Phase self-calibration on Sgr A* with a solution interval equal to the frequency of gain calibration was applied to correct small phase offsets introduced by the angular distance between the calibrators and Sgr A*. The flux density scales were derived from observations of the Solar system objects Ceres, Ganymede, Uranus, and Neptune. The brightness temperatures of these and other Solar system bodies underpin the flux density scale for all SMA data and their determination is an ongoing project of the SMA (Gurwell, in prep). The models account for limb darkening and the models of the gas giants also include corrections for brightness temperature changes due to CO lines. 230 GHz flux densities derived

from them should be accurate to 5%. Ceres is an exception because its brightness temperature changes significantly over its 10-hour rotation period, but on Feb 19 its brightness temperature was calibrated from observations of Ganymede and Callisto so that it could be used as flux density standard. Sgr A* flux densities were extracted using point-source fits to the visibilities (on baselines longer than $20 \text{ k}\lambda$).

At 690 GHz very few objects are bright enough to serve as gain calibrators. Gain calibration was derived from Ganymede and Ceres in February, Ceres and 3C 454.3 in July, during the exceptional outburst of this quasar (Villata et al. 2006). The signal-to-noise ratios in these calibrator observations were not always large enough for reliable gain amplitude calibration, so they were used for phase monitoring only. The observing strategy ensures that the lack of continuous (few-minute timescales) amplitude calibration should not significantly impact these measurements. After removal of atmospheric transmission effects (system temperature correction), pointing errors are the dominant contributor to gain amplitude variations. Pointing was therefore checked frequently, every 2 – 3 hours, with pointing measurements showing small ($3''$ r.m.s.) changes across the time intervals used for flux density extraction. For the $17''$ half-power beam width of the SMA telescopes at 684 GHz, the amplitude loss on a baseline where both telescopes are mis-pointed by $3''$ is 8%. Because pointing errors should be smallest immediately after pointing measurements, it is unlikely that the average pointing error was as large as $3''$ for the duration of the photometric periods. As at 230 GHz, phase self-calibration on Sgr A* was used to remove phase offsets from the calibrators. The flux density scale was derived from one or two of Ganymede, Neptune, and Uranus on each night. These objects were detected on all baselines (except at baseline lengths

where nulls were predicted by the model); the data matched the models well at all uv -distances, whether the planet was resolved (Uranus, Neptune, Ganymede) or unresolved (Ceres), indicating that we were not impaired by decoherence on the longer baselines. The calibrators were observed at elevation similar to that of Sgr A* to ensure that any elevation-dependent gain changes were well compensated. Gain calibrator flux densities were also constant over a larger range of elevations than the 25° – 41° spanned by the Sgr A* data. Flux densities were extracted from visibility fitting, yielding similar results when the sidebands were considered separately or together. Point source fitting to cleaned images also produced similar results.

The simultaneous flux densities in the two observing bands are shown in Table 6.2. The dominant error at both frequencies is the uncertainty in the flux density scale, rather than statistical errors. The 230 GHz measurements have a uniform fractional error of 5%, while the 690 GHz errors vary from 15% to 20% depending on the phase stability within the observing period. Because atmospheric phase fluctuations due to water are approximately three times larger at 690 GHz than at 230 GHz, periods of atmospheric instability were excised from the data. In July this excluded the first few hours of the tracks, nearly the entire pre-transit portion of the Sgr A* observations, due to unstable conditions before and just after sunset. The low-elevation portions of the tracks (below approximately 25°) were also generally poor for all sources. The remaining data segments have a typical duration of 2 hours, as shown in column 2. The February data were divided into two intervals because a significant change in flux density was evident in the 230 GHz light curve. The spectral index, α ($S_\nu \propto \nu^\alpha$), in each measurement epoch is provided in column 5. The spectral indices are derived from the flux densities in Cols. (3)

and (4), which are averages over the time interval listed in Col (2), not by averaging spectral indices measured on shorter timescales within each photometric interval. The duration of these averages is comparable to the variability timescales observed at 230 and 345 GHz (e.g., Marrone et al. 2006; Chapter 7), so these values should be similar to those that might be obtained over shorter averaging intervals. The spectrum between these frequencies is flat to declining, with a variance-weighted mean value of $\alpha = -0.18$.

6.3 Comparison with Previous Observations

6.3.1 Simultaneous Spectra

Observations of Sgr A* at radio frequencies show a slowly rising spectrum at low frequencies ($\alpha = 0.1 - 0.3$; Falcke et al. 1998; Zhao et al. 2001b; An et al. 2005), typical of an inhomogeneous optically thick synchrotron source. The spectrum is more difficult to characterize at higher frequencies because of the increasing variability of Sgr A*. Interday variations of 20%–40% are observed above 100 GHz (Zhao et al. 2003), with larger changes observed on few hour timescales (Miyazaki et al. 2004; Mauerhan et al. 2005; Marrone et al. 2006). Two multi-facility campaigns provide well-sampled simultaneous spectra of Sgr A* from ~ 1 GHz to 200–300 GHz (Falcke et al. 1998; An et al. 2005). These confirm the existence of a steeper “submillimeter bump” (Melia & Falcke 2001) at frequencies above ~ 10 GHz. The 8.5–236 GHz data of Falcke et al. (1998) show an average spectral index of $\alpha = 0.47$, while the An et al. (2005) data between 8.5 and 340 GHz indicate a spectral index of

Table 6.1. Observing Log

Date	MJD	ν_{230}	ν_{690}	τ_{225}	τ_{690}	N_{230}	N_{690}
(1)	(2)	(3)	(4)	(5)	(6)	(7)	(8)
2005 Feb 19	53420	224.0	684.0	0.034	0.55	6	6
2005 Jul 22	53573	226.9	684.0	0.045	0.78	7	5
2005 Jul 30	53581	226.9	684.0	0.044	0.76	7	5

Note. — Col. (2): Modified Julian Day. Col. (3) & (4): Observing frequencies (GHz) in the 230 and 690 GHz bands. Col. (5): Zenith opacity at 225 GHz, from the JCMT water vapor monitor (Weferling, B., Phillips, R. & Jenness, T., 2006, in prep.). Col. (6): Zenith opacity at the 690 GHz band local oscillator frequency, based on scaling relations derived from the *am* atmospheric model (Paine 2004). Col. (7) & (8): Number of antennas used in each band.

Table 6.2. Sagittarius A* Flux Densities

MJD	Span	S_{230}	S_{690}	α
(1)	(2)	(3)	(4)	(5)
53420.69	2.5	3.86 ± 0.19	2.62 ± 0.39	-0.35 ± 0.14
53420.80	1.9	3.40 ± 0.17	2.04 ± 0.41	-0.46 ± 0.18
53573.43	2.6	3.44 ± 0.17	3.52 ± 0.53	0.02 ± 0.14
53581.40	2.5	4.28 ± 0.21	4.65 ± 0.93	0.08 ± 0.19

Note. — Col. (1): Center of photometric window. Col. (2): Duration of photometric window (hours). Col. (3) & (4): Flux densities (Jy) at frequencies given in Table 6.1, respectively. Col. (5): Inter-band spectral index ($S_\nu \propto \nu^\alpha$). The errors are 1σ values, which are dominated by the uncertainties in the fluxes of the calibrators. See text for details.

0.41, or 0.47 between 8.5 and 43 GHz if the 340 GHz point is excluded. These data are plotted in Figure 6.1, along with the three power-law fits to the spectra. The agreement of these observations (the flux density normalizations match to within a few percent) across an interval of nearly seven years suggests that the mean Sgr A* spectrum is stable on long timescales. Yusef-Zadeh et al. (2006) also measured the relevant portion of the Sgr A* SED over four nights in 2004 Mar. However, during their observing period a radio transient (Bower et al. 2005b) just 3'' from Sgr A* interfered with flux density measurements at the lower frequencies, up to at least 43 GHz (see Figure 6.1). The contamination at these frequencies prevents a reliable measurement of the spectral index from these data.

The spectral index below 300 GHz in the submillimeter bump ($\alpha \simeq 0.5$) is clearly very different from that at lower frequencies (~ 0.2). At higher frequencies, the four SMA epochs show that the spectrum is also considerably flatter than and inconsistent with the bump index. The SMA measurements are shown with the other simultaneous data in Figure 6.1. Most of the SMA 230 GHz points fall very near to the extrapolated submillimeter bump spectra (ignoring the dot-dashed line that includes the 340 GHz point from An et al. 2005), indicating that they are representative of the typical Sgr A* SED. The exceptional 230 GHz point (2005 Jul 30) is also deviant at 690 GHz, suggesting that this measurement caught Sgr A* in a flare state, perhaps associated with an X-ray flare a few hours earlier (F. Baganoff, priv. comm.). The remaining epochs show 690 GHz flux densities that are between 2 and 4 Jy below the extrapolated ($\nu < 300$ GHz) spectra and even fall below the spectral fit that includes the 340 GHz point (dot-dashed line). We therefore conclude that these observations straddle the peak in the Sgr A* SED.

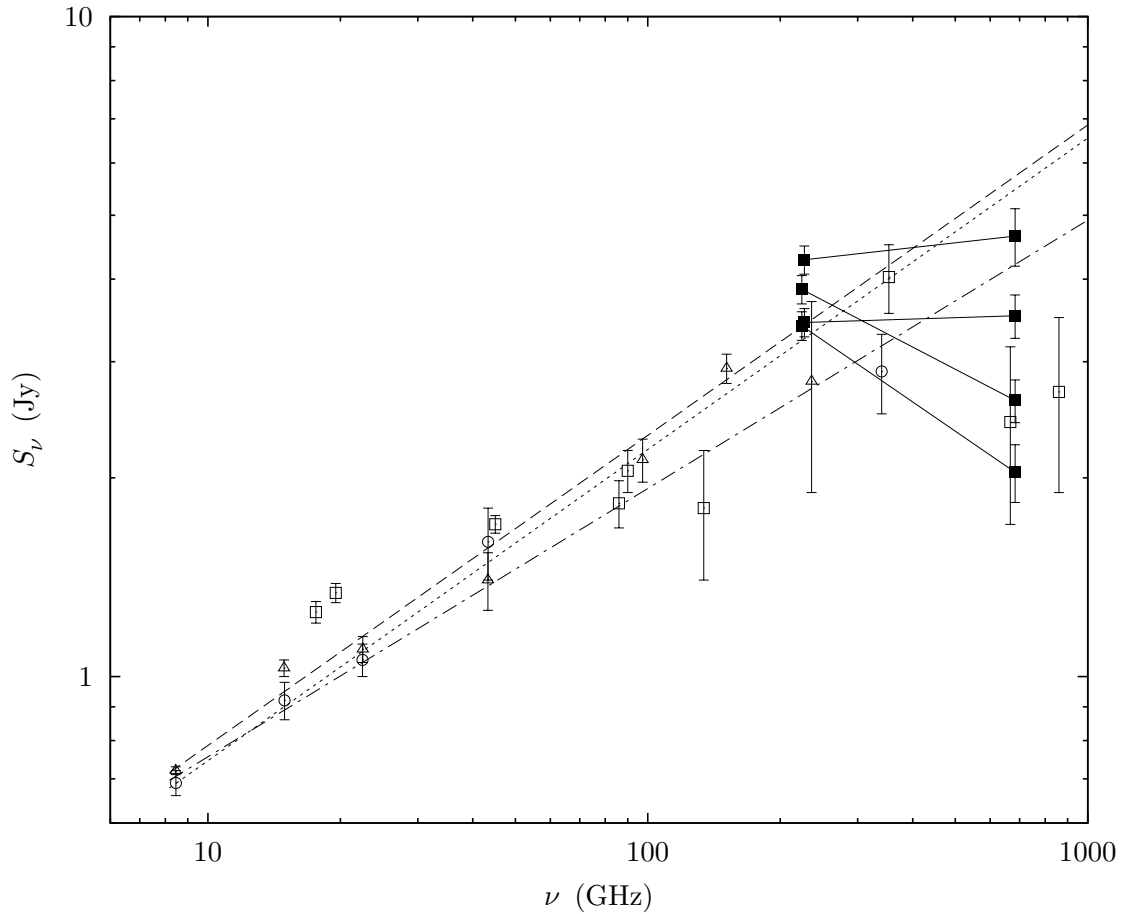


Fig. 6.1.— The 8 – 1000 GHz SED of Sgr A* from simultaneously measured flux densities. Data from the Falcke et al. (1998), An et al. (2005), and Yusef-Zadeh et al. (2006) campaigns are shown as open triangles, open circles, and open squares, respectively. The dashed line is a fit to the Falcke et al. (1998) spectrum from 8.5 to 236 GHz. The dot-dashed line is a fit to the An et al. (2005) spectrum, including the 340 GHz point, while the dotted line excludes this point. The four epochs of SMA observations from Table 6.2 are plotted as filled squares, with each epoch connected by a solid line. The SMA points near 690 GHz have been plotted with *half- σ* error bars for clarity.

6.3.2 High-Frequency Photometry

These observations are the first to measure the high-frequency ($\nu > 400$ GHz) flux density of Sgr A* with sufficient angular resolution to separate this source from the surrounding emission. However, previous single-aperture measurements with the James Clerk Maxwell Telescope (JCMT, 8'' resolution) and the Caltech Submillimeter Observatory (CSO, 11'') have also detected Sgr A* near 690 GHz (Dent et al. 1993; Zylka et al. 1995; Pierce-Price et al. 2000; Yusef-Zadeh et al. 2006) and can be used to test our results. These authors found flux densities between 1 and 3 Jy (with one upper limit of 1.5 Jy), the upper half of this range overlapping with our measurements. The single-aperture measurements will overestimate the emission from Sgr A* if they are not corrected for contamination from the surrounding emission and can underestimate the emission if the contamination is approximated from nearby pixels but the central pixel has below-average contamination (as was suggested by Marrone et al. 2006). In the SMA measurements, however, contamination is unlikely to cause an overestimation of the flux density because the interferometric observations are insensitive to any contaminant without significant structure on arcsecond scales. The SMA observed very little contaminant emission at 340 GHz at similar resolution (Marrone et al. 2006) and higher sensitivity. Errors in the flux density scale could push our measurements (or those from the JCMT and CSO) in either direction, but the independently calibrated single-aperture measurements provide no evidence that we are underestimating the 690 GHz flux density. Instead, historical observations of Sgr A* at this frequency seem to support the idea of a turnover in the SED below 600 GHz.

Over the last several years the SMA has been used to observe Sgr A* many times at 230 and 345 GHz; these high-angular resolution flux density measurements, while not simultaneous with the spectral measurements presented here, can be used to examine the average spectrum between these frequencies. Using a partially-completed SMA, Zhao et al. (2003) found $S_{230} = 2.61 \pm 0.67$ Jy over 24 epochs. With six additional epochs from Marrone et al. (2006b, submitted; Chapter 5) and two more unpublished monitoring observations, the average increases to 2.85 ± 0.74 Jy in 32 epochs. At 345 GHz, in 15 epochs (An et al. 2005; Marrone et al. 2006; 2006b, submitted; plus unpublished data), the average flux density is 3.21 ± 0.43 Jy. While the variability precludes any convincing detection of a decrement in flux density at 345 GHz, the average flux in this band is above the 230 GHz average and below the 3.95-4.15 Jy expected from the low-frequency extrapolation of the Falcke et al. (1998) and An et al. (2005) data, consistent with a turnover between 230 and 690 GHz.

6.3.3 Angular-Size Measurements

Observations of Sgr A* with very-long-baseline interferometry (VLBI) at frequencies between 40 and 100 GHz have been used to determine its intrinsic size (Bower et al. 2004; Shen et al. 2005). Krichbaum et al. (1998) may also have measured an intrinsic size at 215 GHz. At these and lower frequencies the image of Sgr A* is broadened by strong scattering, with the angular size varying as ν^{-2} (Bower et al. 2006). The intrinsic size is inferred from deviations from the expected scatter-broadened size at the highest frequencies. These sizes depend sensitively on the assumed form and normalization of the scattering law (Bower et al. 2006). Nevertheless, from the

factor of 2–4 in frequency over which the intrinsic size can be discerned, the implied frequency dependence of the size of the photosphere (r) appears to be between $r \propto \nu^{-1.1}$ and $\nu^{-1.7}$. A rough estimate of the frequency at which the emission becomes optically thin can be obtained by extrapolating the size-frequency relations to $r = 2r_S$, the diameter of a Schwarzschild black hole. Using the frequency-size relationship of Shen et al. (2005) ($\nu^{-1.1}$) this size occurs at $\nu = 530$ GHz, while the results of Bower et al. (2006) imply a steeper ($\nu^{-1.5}$) frequency-size relation that reaches $2r_S$ at 340 GHz. Both of these results are very consistent with our spectral measurements.

6.4 Discussion

Evidence from new SMA observations of the spectrum of Sgr A* above 200 GHz, older data at these frequencies, and angular size measurements indicate that the peak in the SED occurs between 230 and 690 GHz. The spectrum between these frequencies can be represented by a parabola in $\log \nu$ and $\log S_\nu$ coordinates. This choice of functional form is somewhat arbitrary, but it includes just three parameters (two of which are fixed by the flux densities) and should be a reasonable approximation for more physically-motivated spectral shapes over this narrow range in frequency. To completely determine the model we impose the constraint that the spectral slope at 230 GHz be 0.5, the spectral index measured in the submillimeter bump. Using the average flux densities in the two bands (Table 6.2) the peak frequency and flux density are 350 GHz and 4.2 Jy, or 330 GHz and 3.9 Jy if the outlier 2005 Jul 30 data are excluded. These numbers are higher than the historical

average of SMA data at 345 GHz, but this is unsurprising because the 230 GHz flux density in these four epochs is also higher than the 2.85 Jy average of all SMA 230 GHz measurements. The average 230 GHz flux density is also somewhat below the extrapolation of the simultaneous spectra (3.3 – 3.4 Jy), so even this frequency may be deviating from the submillimeter bump spectrum. Given the uncertainties in the 230, 345, and 690 GHz flux densities and the average submillimeter bump spectrum due to the significant variability of this source, we estimate that the peak of the Sgr A* SED occurs between 300 and 350 GHz, with a flux density between 3.5 and 4.2 Jy. The peak in νS_ν falls between 700 and 830 GHz. A similar peak in νS_ν was estimated by Yusef-Zadeh et al. (2006), based on the average of several epochs of non-simultaneous 350 and 670 GHz observations and their single 850 GHz detection of Sgr A*.

With the peak in the SED measured, we can estimate the luminosity of Sgr A*. Note that the largest contribution to the luminosity originates near the peak in νS_ν , so the unknown shape of the spectrum just above this frequency may introduce errors into our estimate. However, the spectrum between 690 GHz and the near-infrared band is approximately $S_\nu \propto \nu^{-1.3}$, steep enough that the error around the peak in νS_ν should be small. We have taken the “quiescent” state data of Genzel et al. (2003) as representative flux densities at 1.7 – 3.8 μm (6.4 – 2.8 mJy), although even these values may represent low-level flaring in this source and the actual emission could be weaker. This spectral extrapolation falls under the mid-infrared (30 – 8.4 μm) upper limits of Telesco et al. (1996), Cotera et al. (1999), and Eckart et al. (2006a). The quiescent X-ray emission measured by Baganoff et al. (2003) indicates a similar average spectral index (–1.4) all the way to X-ray energies, consistent with the

spectral index measured across the 2–10 keV band ($-1.7_{-0.9}^{+1.3}$). Assuming a constant spectral index of -1.3 above 690 GHz, the integrated luminosity at high frequencies converges to $135 L_{\odot}$ (assuming a distance of 8.0 kpc), with 75% of this luminosity emitted between 690 GHz and $3.8 \mu\text{m}$ (79 THz). From the parabolic fit above, the luminosity between 230 and 690 GHz is an additional $34 L_{\odot}$. Using the $\nu^{-0.5}$ extrapolation between 10 and 230 GHz we recover another $11 L_{\odot}$. Lower frequencies contribute insignificant luminosity, yielding a total of $180 L_{\odot}$, $7 \times 10^{35} \text{ ergs s}^{-1}$, or 1.5×10^{-9} of the Eddington luminosity for a $3.5 \times 10^6 M_{\odot}$ black hole. The assumption of a constant spectral index between 690 GHz and $3.8 \mu\text{m}$ agrees well with the accretion flow model of Yuan et al. (2003). The jet model of Falcke & Markoff (2000) produces a spectrum with significant curvature in this range, which would increase the luminosity by perhaps 20%.

The submillimeter bump in the spectrum of Sgr A* is attributed to synchrotron emission from the innermost region around the black hole (Falcke et al. 1998), either the central portion of an accretion flow (e.g. Melia et al. 2000) or the base of a small jet (Falcke & Markoff 2000). The peak of this bump roughly indicates the frequency at which opacity effects become unimportant, although Broderick & Loeb (2006a) have shown that relativistic effects in an accretion flow with angular momentum create significant inhomogeneity in the opacity across the “disk” of the black hole. The low frequency of this transition is a favorable result for planned 230 GHz (and higher frequency) VLBI observations of Sgr A* (Doeleman & Bower 2004). Were the transition frequency as high as 1 THz, as assumed in many models, the resulting images would likely be fairly featureless rather than showing the relativistic shadow of the black hole (Broderick & Loeb 2006a).

The origin of the impression that the SED of Sgr A* should peak at or above 1 THz may be traced to the 850 GHz data of Serabyn et al. (1997). Using the CSO, these authors measured a large flux density (7 ± 2 Jy) at this frequency, the only published data from the highest-frequency atmospheric window accessible to most submillimeter telescopes. This observation has often been used as a constraint in emission models for this source (e.g. Falcke & Markoff 2000). In fact, Yuan et al. (2003) explicitly constrain their model parameters to match the 850 GHz flux density. However, Yusef-Zadeh et al. (2006) have now published a second measurement at this frequency, a much fainter 2.7 ± 0.8 Jy (shown in Figure 6.1). Although the higher-flux density detection is consistent with the extrapolated low-frequency ($\alpha = 0.5$) spectrum, it seems far more likely that this was obtained during a flare. Given the variability observed at the highest accessible frequencies, including the ranges near 690 and 345 GHz (including a 6.7 Jy flare at 345 GHz reported by Zhao et al. 2003), such a large flare is not surprising.

With the new constraints on the Sgr A* SED determined here, the normalization of many emission models should be revisited. For example, the model of Yuan et al. (2003) can match the lower frequency and luminosity at the peak of the submillimeter bump (a factor of two lower in νS_ν than they have assumed) by lowering the fraction of turbulent energy that heats the thermal electron population (thus lowering the central temperature). This may increase the rotation measure expected from the model, which is already large compared to the value measured in Chapter 5. This may be offset by increasing their parameter s , which specifies the variation of accretion rate with radius ($\dot{M} \propto r^s$), as a lower central density would be allowed by the lower luminosity. These changes affect the submillimeter

bump and therefore also slightly change the inverse-Compton peak in this model. However, this peak occurs around 40 eV, between the IR and X-ray constraints on the spectrum, so the change does not contradict any other observational constraints. The jet model of Falcke & Markoff (2000) would better fit the spectrum if the characteristic electron Lorentz factor were lowered by as much as 20%, similar to their Figure 3. This change has little effect at frequencies below the submillimeter bump, although it does reduce the quiescent emission from the jet in the IR and X-ray bands. The existence of truly “quiescent” emission in the IR is not yet certain, so an under-prediction relative to, e.g., the Genzel et al. (2003) data points is not a significant concern. Moreover, the quiescent X-ray emission is resolved (Baganoff et al. 2003), not the point source emission expected from the jet contemplated by this model. The X-ray spectrum is well-fit by thermal bremsstrahlung, which is likely arising in the plasma at the Bondi capture radius, so a reduction of jet X-ray emission is a favorable result, as acknowledged by Markoff & Falcke (2003).

Chapter 7

Sgr A*: Light Curves

7.1 Introduction

Studies of the variability of Sgr A* have been undertaken at all wavelengths where this source has been detected. The variability on timescales of hours to years is well studied at radio frequencies (Zhao et al. 2001a; Herrnstein et al. 2004) and appears to result from a combination of interstellar scintillation and intrinsic changes (Macquart & Bower 2006). At higher frequencies, external processes should be unimportant and observed changes should be intrinsic in origin. Variability at infrared and X-ray wavelengths is found on timescales of hours or less (e.g. Baganoff et al. 2001; Goldwurm et al. 2003; Genzel et al. 2003; Eckart et al. 2004, 2006a). The rise-times of tens of minutes in these observations are comparable to those expected from the innermost region around the black hole. Candidate periodic signals have been reported by Genzel et al. (2003) and Aschenbach et al. (2004), with Belanger et al. (2006) recently reporting nearly seven full cycles of a 22.2-minute period in an

X-ray flare.

Millimeter/submillimeter observations have also been examined for variability of Sgr A*. Above 100 GHz, extended monitoring observations have shown both interday (e.g. Miyazaki et al. 2003; Zhao et al. 2003) and intraday changes Miyazaki et al. (2004); Mauerhan et al. (2005); Marrone et al. (2006); Eckart et al. (2006a), with the latter observed on timescales of a few hours or less. Submillimeter emission should arise at the inner edge of the accretion flow in Sgr A* (Melia et al. 2001), making the frequencies accessed by the Submillimeter Array (SMA) particularly important for studies of this source. Moreover, both angular size (Bower et al. 2004; Shen et al. 2005) and spectral measurements (Chapter 6) indicate that the submillimeter emission from Sgr A* is optically thin, unlike lower-frequency emission, allowing direct observation of the interior changes.

The linear polarization of Sgr A* has yet to be used as a tool for understanding Sgr A* variability. The polarization changes should reflect changes in the magnetic field configuration and order in the emitting region, properties not constrained by any other observations. Very sensitive multi-frequency polarization observations may reveal RM fluctuations indicative of magnetic field or density changes; if these properties are coupled, as is so often assumed when interpreting RMs, the fluctuations can be directly translated into accretion rate changes. However, in Chapter 5 I already placed a limit of around 12% on such changes. In addition, as shown by Broderick & Loeb (2006b), the polarization changes during flares should be an essential signature of strong gravity. All of these things make submillimeter polarimetry immensely important, particularly at the highest accessible frequencies where optical depth changes will have the smallest impact on the polarization

properties. Unfortunately, the temporal resolution of past linear polarization observations has been limited to inter-day timescales by a lack of sensitivity at the frequencies where polarization is observed (above 85 GHz, including a recent NIR detection of polarization in a flare; Eckart et al. 2006b). The data of Marrone et al. (2006) (Chapter 4) were the first to measure changes in polarization position angle within a night and the first to confidently detect polarization fraction changes on any timescale. Thanks to SMA sensitivity improvements in the 345 GHz band and the addition of 230 GHz polarimetry hardware, it is now possible to examine polarization changes on timescales of minutes rather than hours or days with the SMA. Here I review the ten epochs of Sgr A* polarimetric observations from 2005, in which the rapid polarization changes of Sgr A* are revealed for the first time.

7.2 Observations and Calibration

The SMA made polarimetric observations of Sgr A* on thirteen nights in 2005 during commissioning of the 230/690 GHz upgrade to the polarimeter and as part of regular science observations, including coordinated multi-wavelength Sgr A* monitoring observations. Three of these nights were lost to weather or problems at the array. In the ten remaining tracks, six and four were observed in the 230 and 345 GHz bands, respectively. These tracks all enjoyed excellent weather, with zenith opacities at 225 GHz between 0.04 and 0.10, typically within the range 0.06 – 0.08. Scaled to 343 GHz, these ranges become 0.12 – 0.34 and 0.19 – 0.27, respectively. The SMA was in its compact array configuration at this time, with baselines up to 70 meters. During the Sgr A* observations, typically limited to elevations greater than 20°,

projected baselines in the 230 GHz band spanned 5 – 54 k λ and in the 345 GHz band 7 – 80 k λ . Baselines shorter than 20 k λ were excluded for self-calibration, polarization extraction, and imaging to remove the influence of extended structure on the derived properties. This practice is consistent with previous high-frequency observations of this source (e.g. Bower et al. 2005a; Marrone et al. 2006). Observing parameters for all ten nights are provided in Table 7.1

Gain calibration was performed using 1–3 of several suitable quasars (and/or an asteroid) in each track. The 230 GHz band calibrators included J1743–038, J1733–130 (NRAO 530), J1924–292, and Ceres, while at 345 GHz only the first two calibrators were used. Stokes I light curves were extracted from visibility fits to the gain calibrated data, after a phase-only self-calibration to remove small residual phase differences between the calibrators and Sgr A*. For periods when calibrator data were unavailable due to instrument or weather problems were excluded from the Stokes I light curves. Polarization light curves were generated from the data after two different calibration paths; in one technique the Sgr A* data were calibrated as described for the Stokes I light curve, while in the second technique only a phase self-calibration was applied to data. Results of the two methods are very similar, with the phase self-calibrated data producing slightly smaller inter-sample scatter and smaller errors. The phase self-calibrated data are thus the preferred source for the polarization light curves. Although these data may retain scale errors in the individual light curve samples, the weather and interferometer were stable enough to ensure that these errors were small and overall scale errors do not alter derived quantities such as the fraction of emission in Q , U , and V , the total fraction of linearly polarized emission (m), or the polarization position angle (χ). As in the

Table 7.1. Observing Parameters

Date	Frequency ^a	τ_{225} ^b	τ_{343} ^c	N_{ant}
2005 Jun 4	225.55	0.090	...	6
2005 Jun 6	343.00	0.055	0.18	6
2005 Jun 9	226.90	0.080	...	6
2005 Jun 15	343.00	0.050	0.16	6
2005 Jun 16	226.90	0.060	...	5
2005 Jun 17	343.00	0.055	0.18	7
2005 Jul 20	226.90	0.070	...	7
2005 Jul 21	343.00	0.075	0.25	7
2005 Jul 22	226.90	0.050	...	7
2005 Jul 30	226.90	0.045	...	7

^aLocal oscillator frequency (GHz).

^bNightly average values.

^cScaled from the 225 GHz opacity, when applicable.

Stokes I light curves, the polarization light curves are obtained by fitting a point source to the visibilities, with the constraint that it be located at the phase center. The linearly polarized flux (P) and fraction (m), each debiased through quadrature subtraction of the measured noise, and the position angle were derived from the flux densities extracted in each of the four Stokes parameters. The flux density scale was derived from observations of planets and their moons, with an expected accuracy of better than 10%.

These observations used the SMA polarimeter to allow measurement of full polarization information. This mode of observation was introduced in Marrone et al. (2006) and will be further discussed in a future paper (D. P. Marrone et al., 2006, in prep.; see also Chapters 2 and 3). The polarimeter served to emulate dual-circular polarization feeds in each antenna through conversion of the single linearly-polarized feed available in each observing band. The polarization conversion was achieved through a rotatable quarter-wave plate under computer control, which was positioned in one of two orientations 90° apart, generating right- or left-circular sky polarization sensitivity (RCP and LCP, or just R and L, respectively). Although just a single polarization state was measured instantaneously, the four polarized visibilities for each baseline (RR, RL, LR, and LL) were rapidly sampled through coordinated switching of the wave plates in each antenna. In a single 16-step cycle, each baseline measured each polarization state exactly four times. For the 230 GHz band observations this cycle required 4 minutes. For the 345 GHz band observations, a longer integration time increased the cycle duration to 5.5 minutes. The cycle durations are the minimum time required to measure all polarization states on all baselines and therefore form the smallest time intervals accessible to the light curves.

Polarization calibration was performed on all ten nights. Through observations of a polarized quasar (here 3C 279 or 3C 454.3) over a large range of parallactic angle, the instrumental and quasar polarizations were determined simultaneously. The instrumental polarization parameters, or “leakages”, are found to be stable between observations at the same frequency, with rms variability of 0.3% in the 230 GHz band and 0.4% in the 345 GHz band. For random variations about a true leakage value, such changes would be expected to contribute 0.14% and 0.16% to the instantaneous polarization for a six antenna array. For errors that are completely correlated across the antennas, the polarization error introduced in a snapshot observation may be as large as the full leakage error.

The leakage variations appear to have a systematic origin rather than random noise or uncorrelated changes in the antennas. These observations were performed during a recent outburst of 3C 454.3, during which its flux density in our receiver bands was 30 – 40 Jy. This allowed very sensitive calibration measurements to be made. From the signal-to-noise ratio on this source, the expected noise in the measured leakages is around 0.1% for the 345 GHz band and even smaller for the 230 GHz band. Instrumental changes are another potential source of leakage variability, but no evidence for such changes has been observed in SMA leakages, beyond the instabilities reported here. Instead, the measured leakage variability is the result of small changes in SMA leakages as a function of antenna position. Because of the relay optics required to illuminate the SMA receivers at a Nasmyth focus, cross-polarization introduced skyward of the elevation relay mirror rotates relative to the receiver, subtly changing the leakages. Leakages were derived from the calibrator observations assuming that the leakages remain fixed. Therefore

the leakage solution determined for a given observation depend sensitively on the parallactic and elevation angle sampling, particularly in the hour around transit when the parallactic angle of 3C 454.3 varies by more than 100° . Polarized light curves of bright quasars, particularly the two calibrators, showed polarization variations across the sky at the level of a few tenths of a percent, tracing out a repeatable pattern between nights. The amplitude of these changes and their stability indicates that a significant fraction of the leakage variation was the result of this systematic error. The peak-to-peak modulation of Q and U due to this effect is around 0.8%, with an rms modulation of 0.2% and a smooth variation with hour angle. Within the much smaller range of parallactic angle and elevation covered by Sgr A* the peak-to-peak modulation can be expected to be significantly smaller, perhaps 0.4% to 0.5%. Thus, in any polarization snapshot the systematic uncertainty is a few tenths of a percent, although on average the polarization error distribution across the tracks should be described by the 0.2% rms. When the polarization fraction is below 3%, the systematic error in the position angle may be 10° or more, if the polarization error happens to be directed circumferentially from the source polarization in the $Q-U$ plane.

7.3 Light Curves

Total intensity and polarization light curves for the ten epochs, extracted according to the procedures described above, are shown in Figures 7.1 to 7.10. All data for each band are plotted with the same range and scale for easy comparison. Significant variability is obvious in all ten epochs. The position angle during periods of low

polarization is subject to increased uncertainty because of the systematic error, although adjacent points should have very similar error polarization and can be reliably compared. Position angles are not shown when the polarization is very low (2σ or less) because of the great uncertainty in the U to Q ratio that determines χ . All 230 GHz light curves are plotted together in Figures 7.11 and 7.12, while the 345 GHz light curves are all plotted in 7.13 and 7.14. No obvious systematic errors (in the form of repeated patterns of variability) are evident in the light curves. The full set of polarization light curves expressed as fractional Q and U are also provided. In these coordinates, systematic deviations from elevation/parallactic angle dependent leakage errors might be more obvious since the relevant leakage errors produce Q and/or U polarization contamination. It is clear from these plots that the intrinsic source polarization variations dominate any changes due to systematic errors. The raw data for these plots are included in Appendix C.

The light curves shown here represent a significant advance in the time resolution of linear polarization measurements. Single samples include just a few minutes of data, reaching a typical precision of 0.5%–1.0% at 230 GHz and 1.3%–1.8% at 345 GHz. Several samples are obtained per hour, providing an order of magnitude finer sampling than that presented in the other time-resolved measurements (Marrone et al. 2006; Chapter 4). The only other published polarization data with sub-night sampling are the circular polarization measurements of Bower et al. (2002c) at centimeter wavelengths.

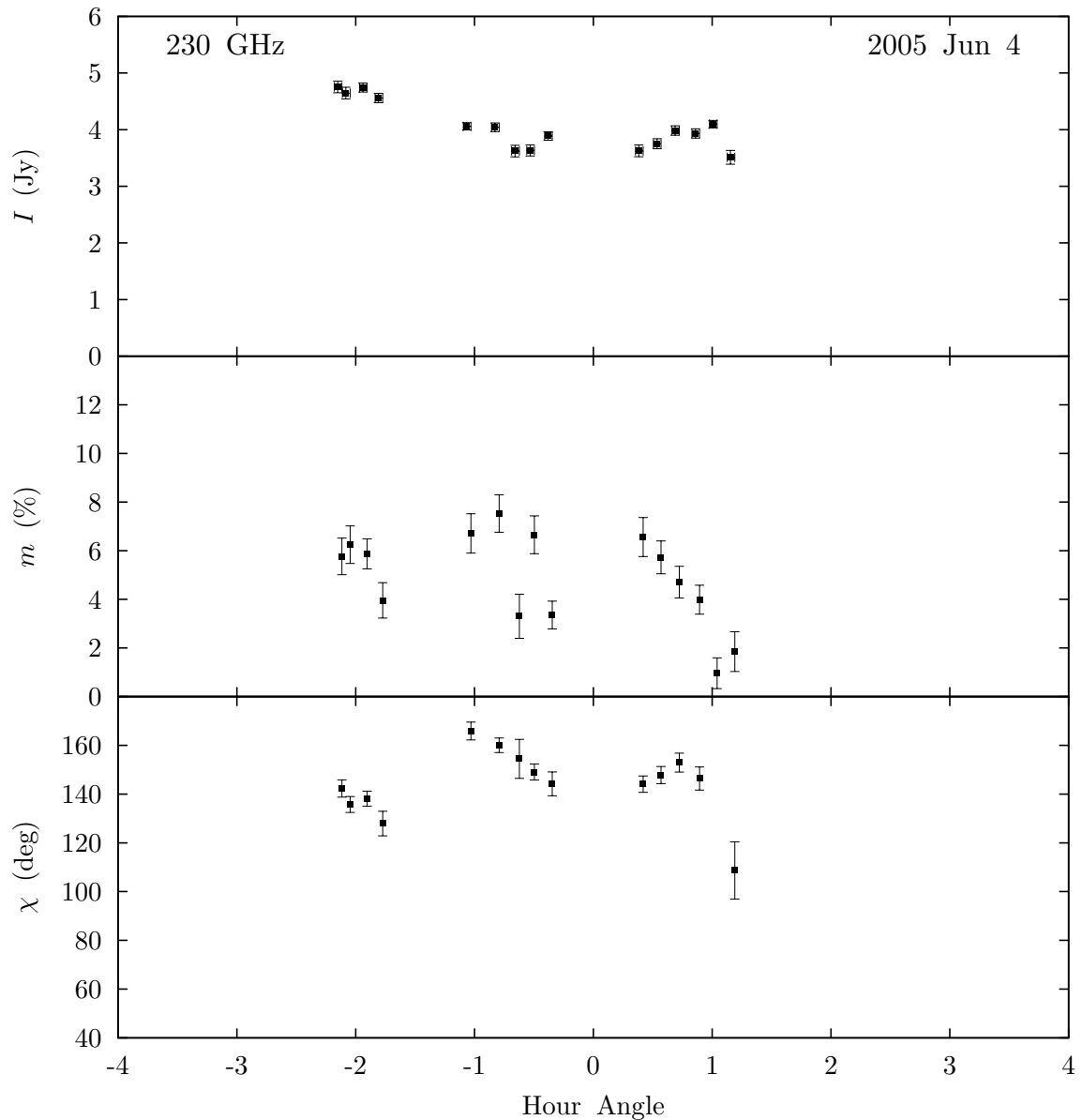


Fig. 7.1.— Polarization light curve for 2005 June 4. Points missing from the I light curve indicate a temporary lack of reliable gain calibrator observations. Points missing from both m and χ indicate observations obtained without the usual polarization switching. Points missing from χ alone are poorly constrained because of a weak polarization detection (less than 2σ).

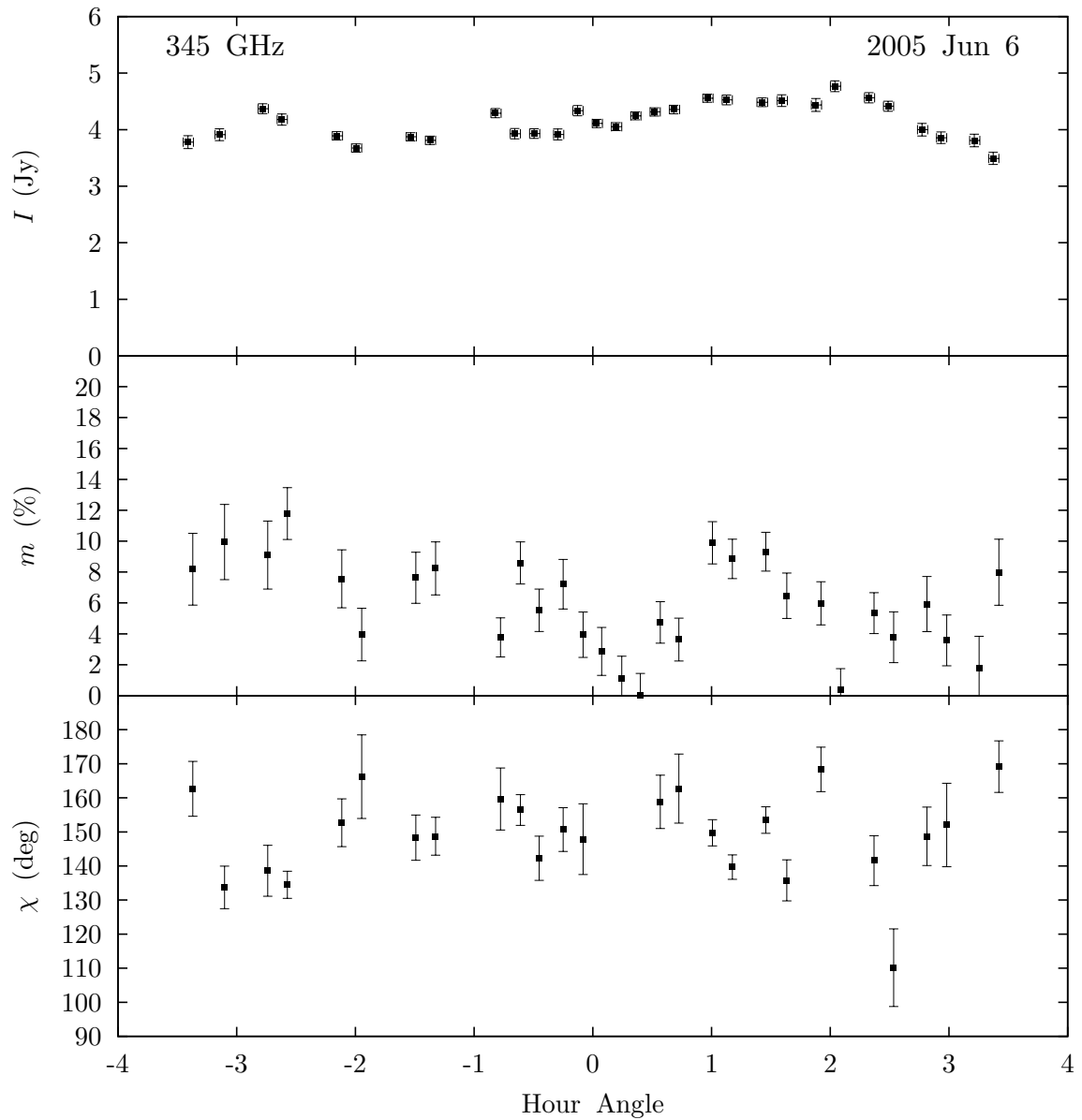


Fig. 7.2.— Light curve for 2005 June 6. See caption of Figure 7.1 for details.

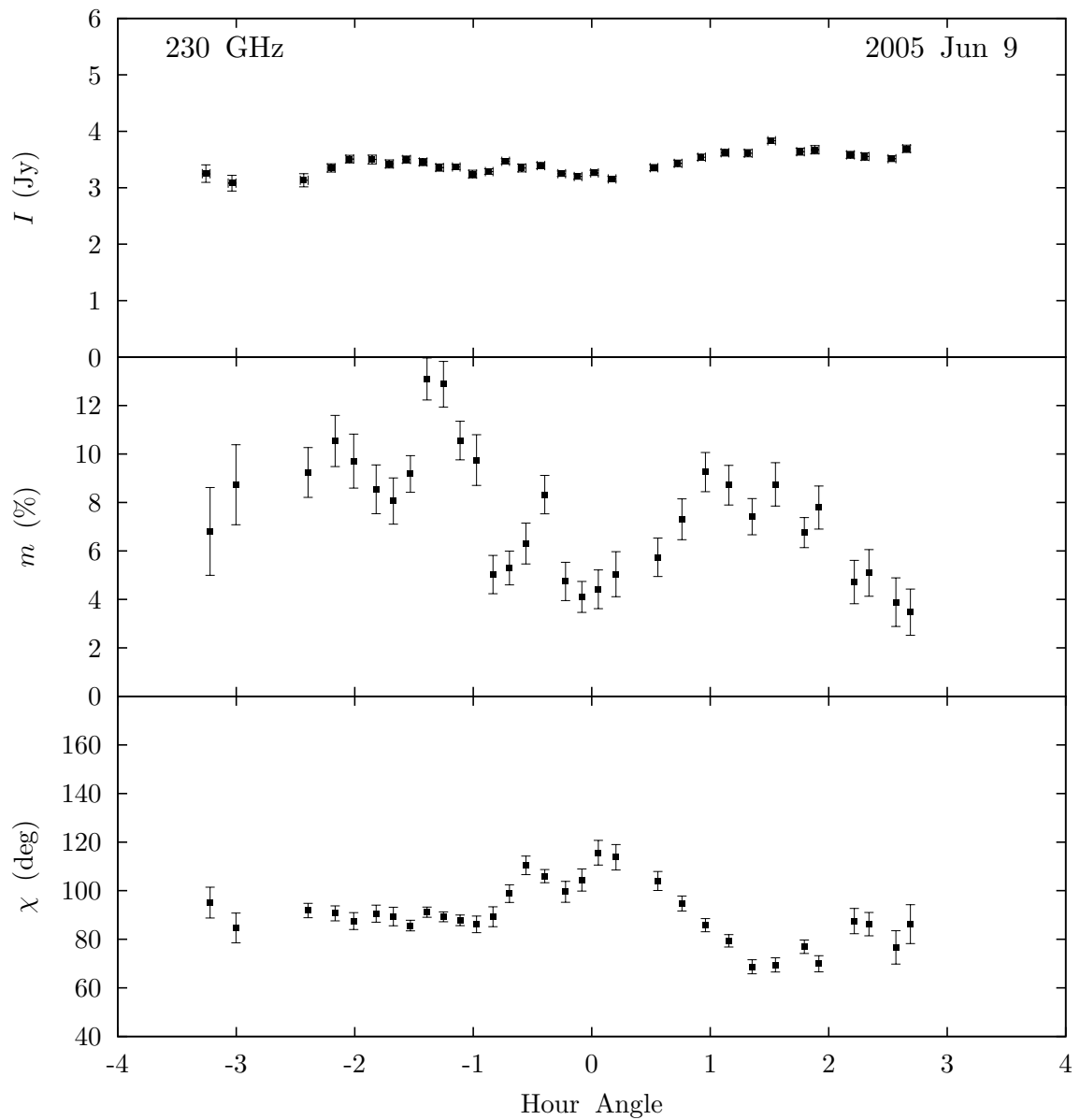


Fig. 7.3.— Light curve for 2005 June 9. See caption of Figure 7.1 for details.

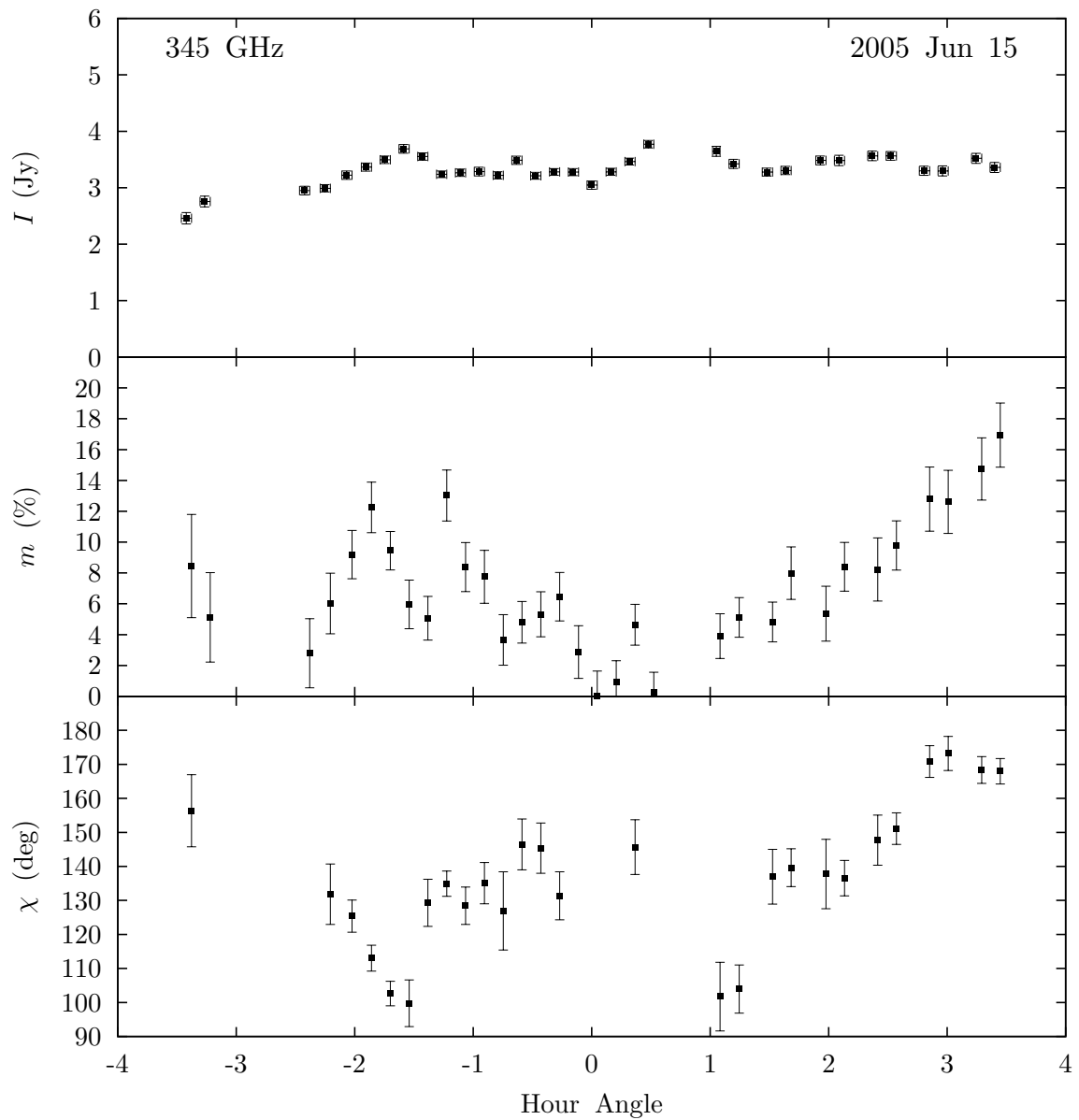


Fig. 7.4.— Light curve for 2005 June 15. See caption of Figure 7.1 for details.

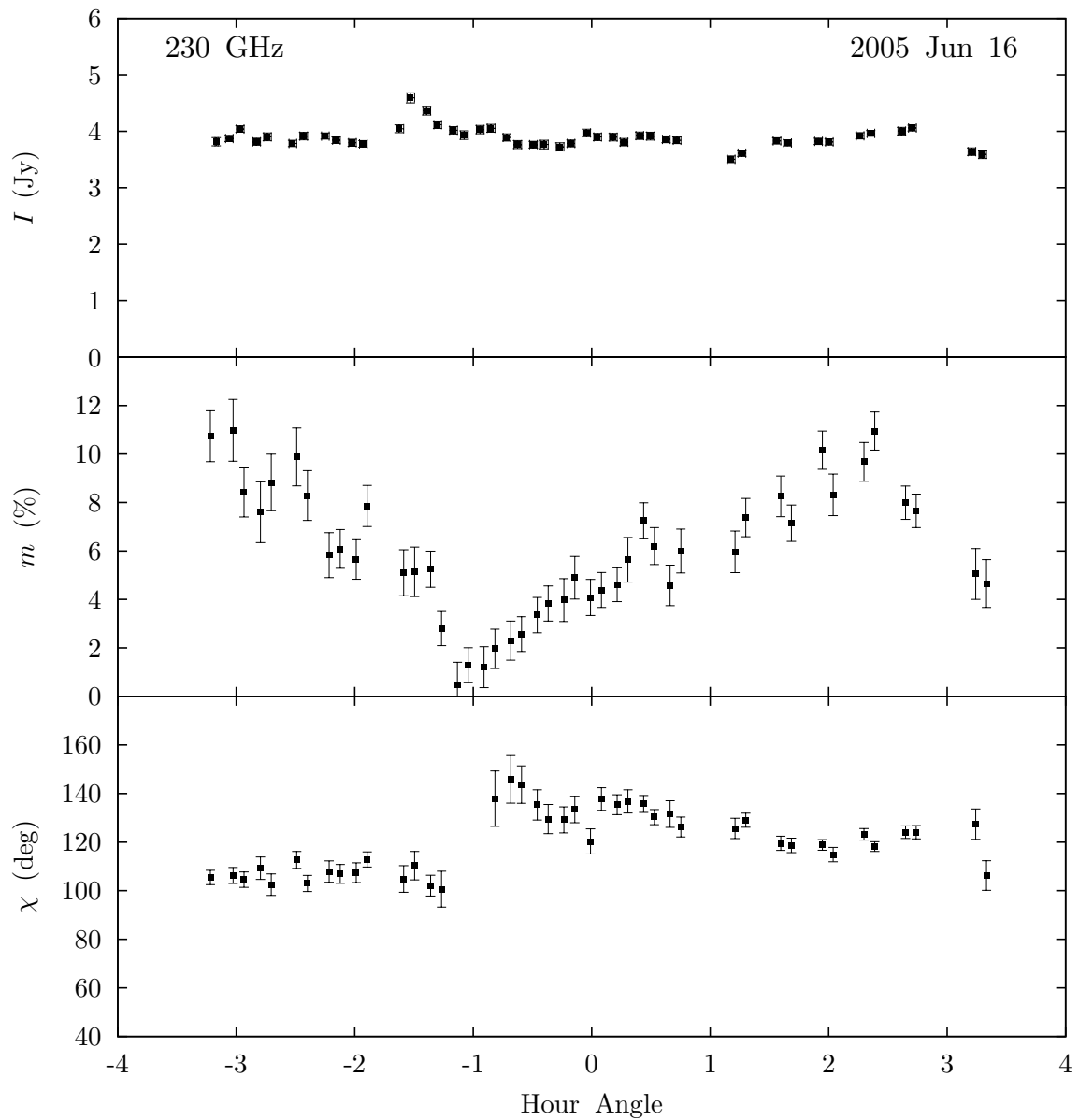


Fig. 7.5.— Light curve for 2005 June 16. See caption of Figure 7.1 for details.

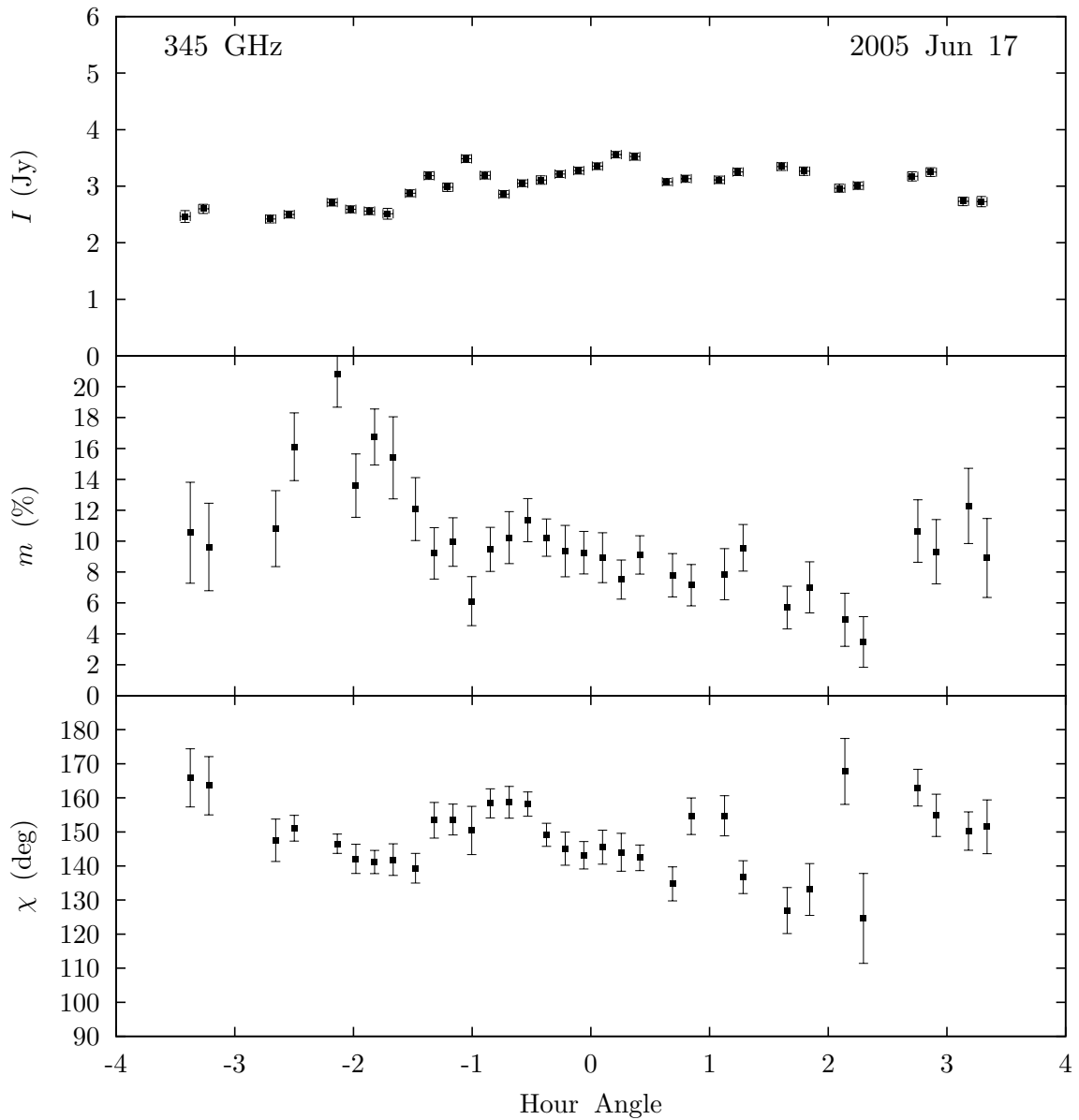


Fig. 7.6.— Light curve for 2005 June 17. See caption of Figure 7.1 for details.

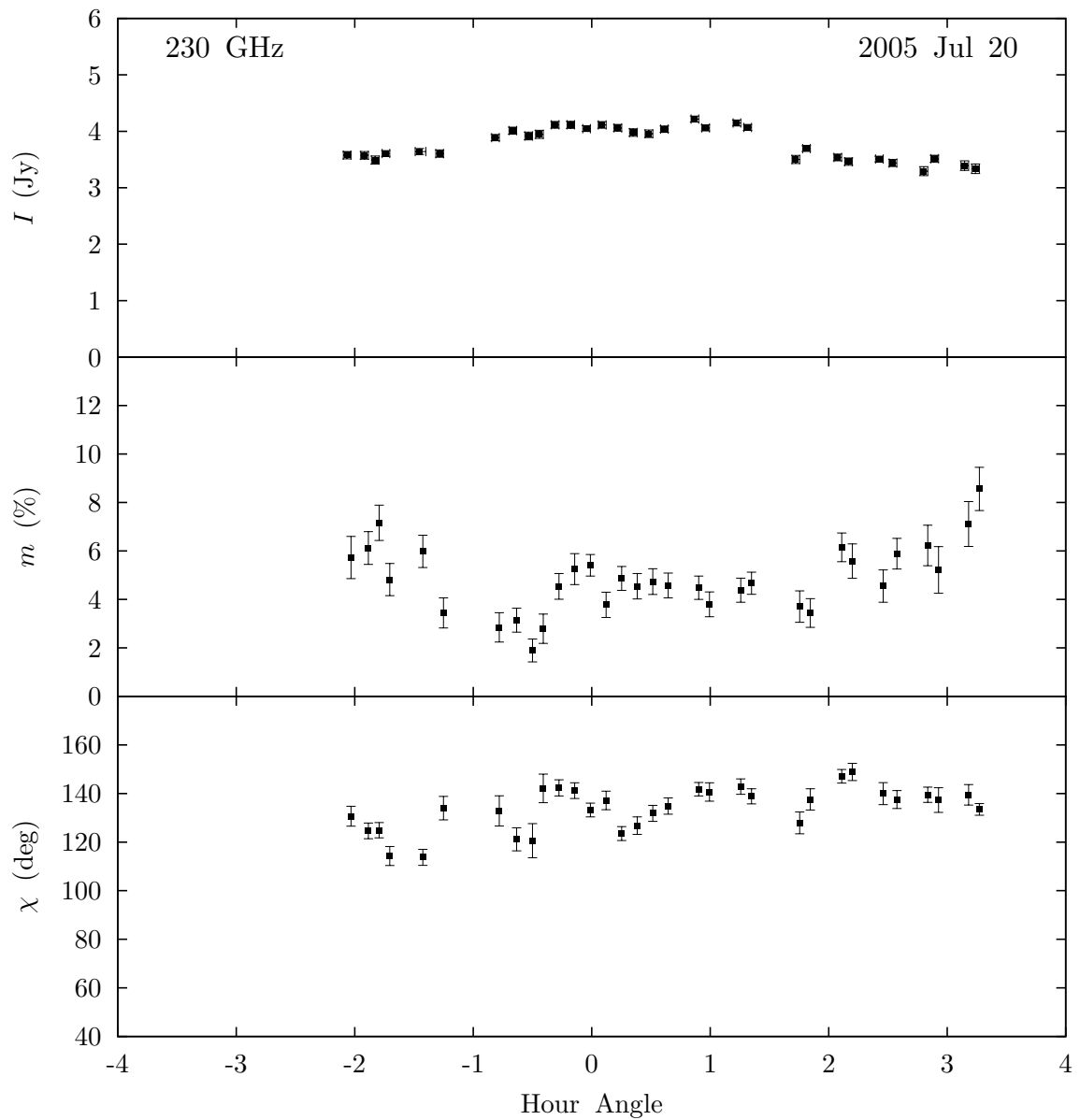


Fig. 7.7.— Light curve for 2005 July 20. See caption of Figure 7.1 for details.

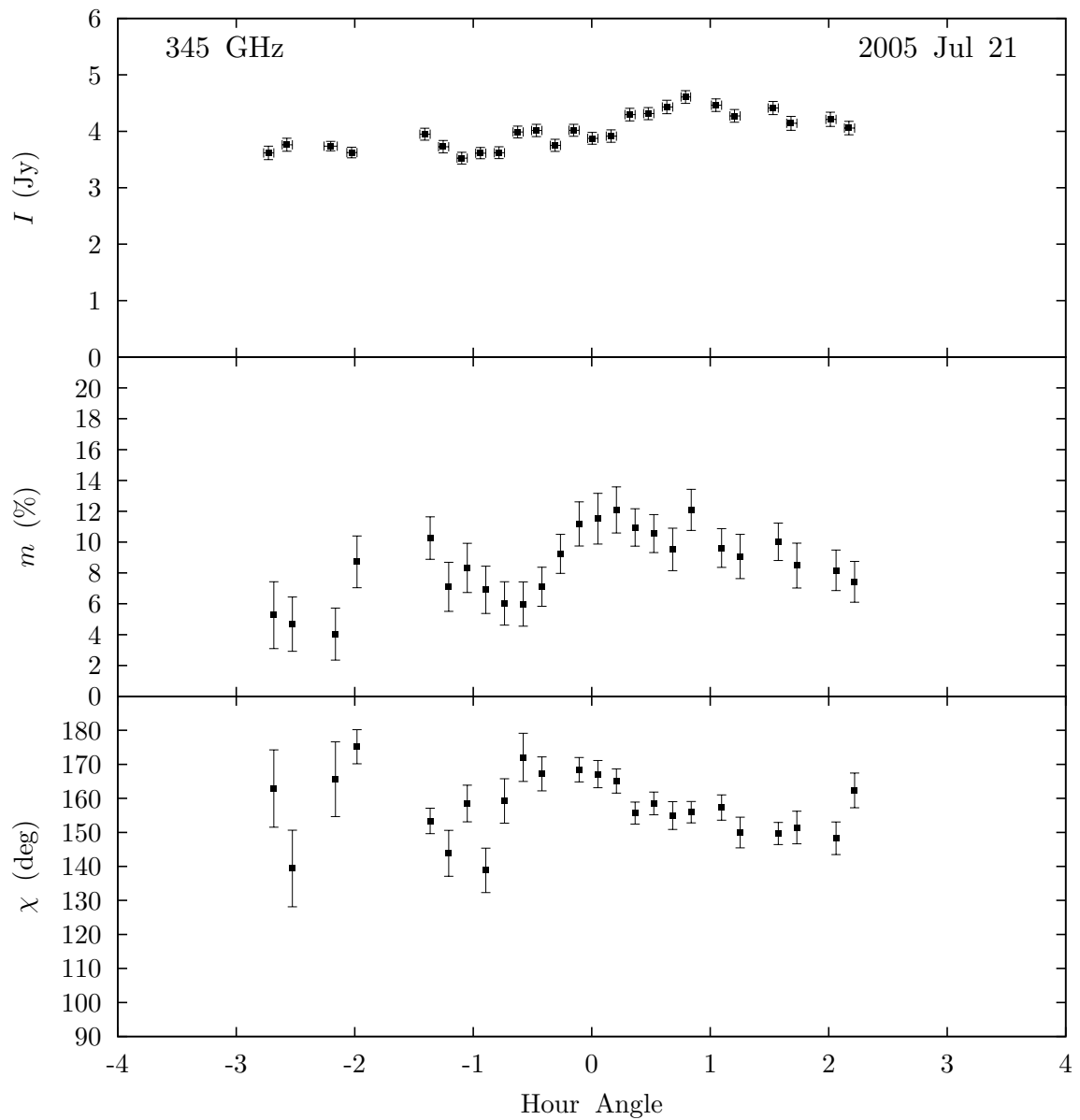


Fig. 7.8.— Light curve for 2005 July 21. See caption of Figure 7.1 for details.

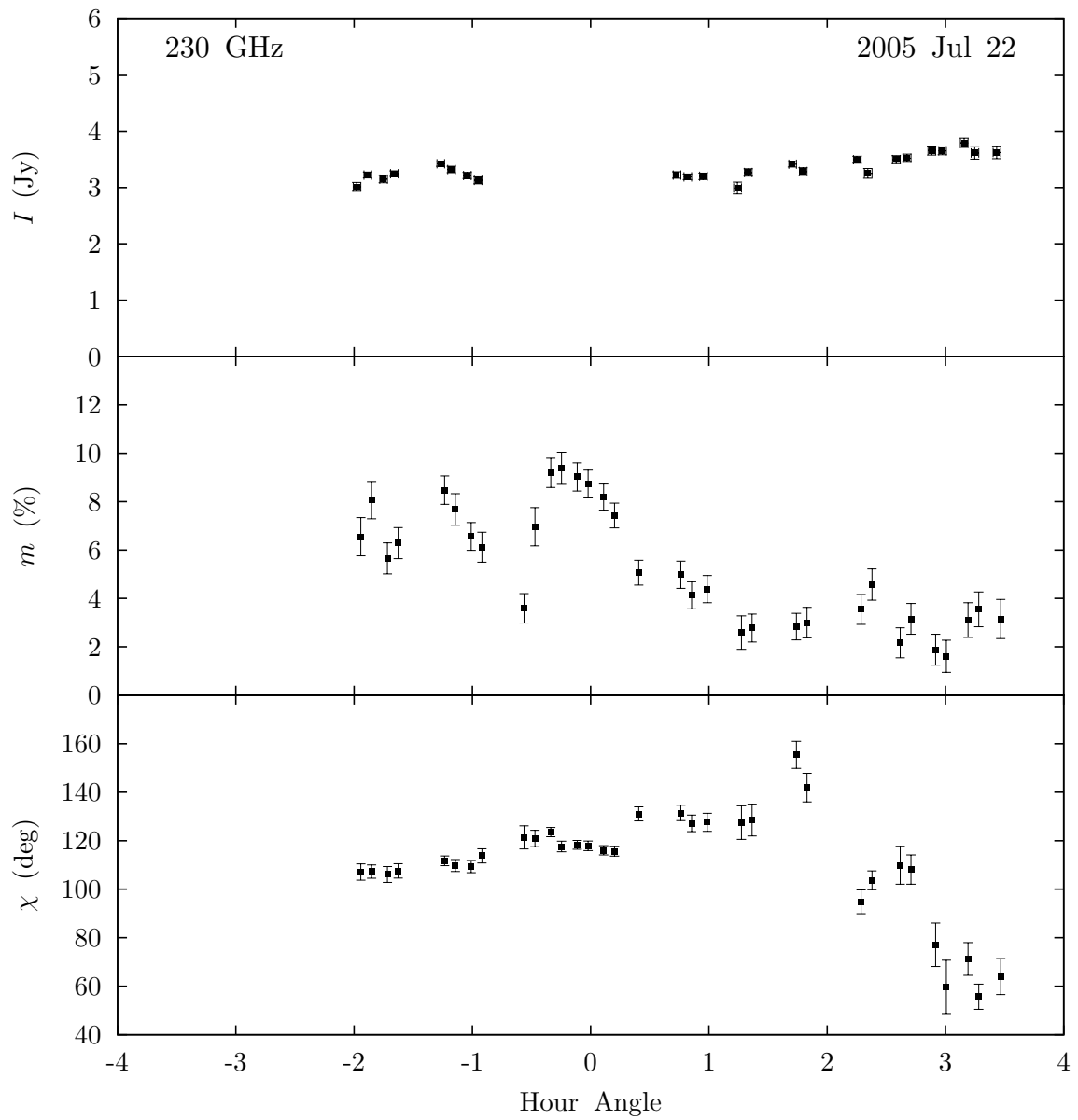


Fig. 7.9.— Light curve for 2005 July 22. See caption of Figure 7.1 for details.

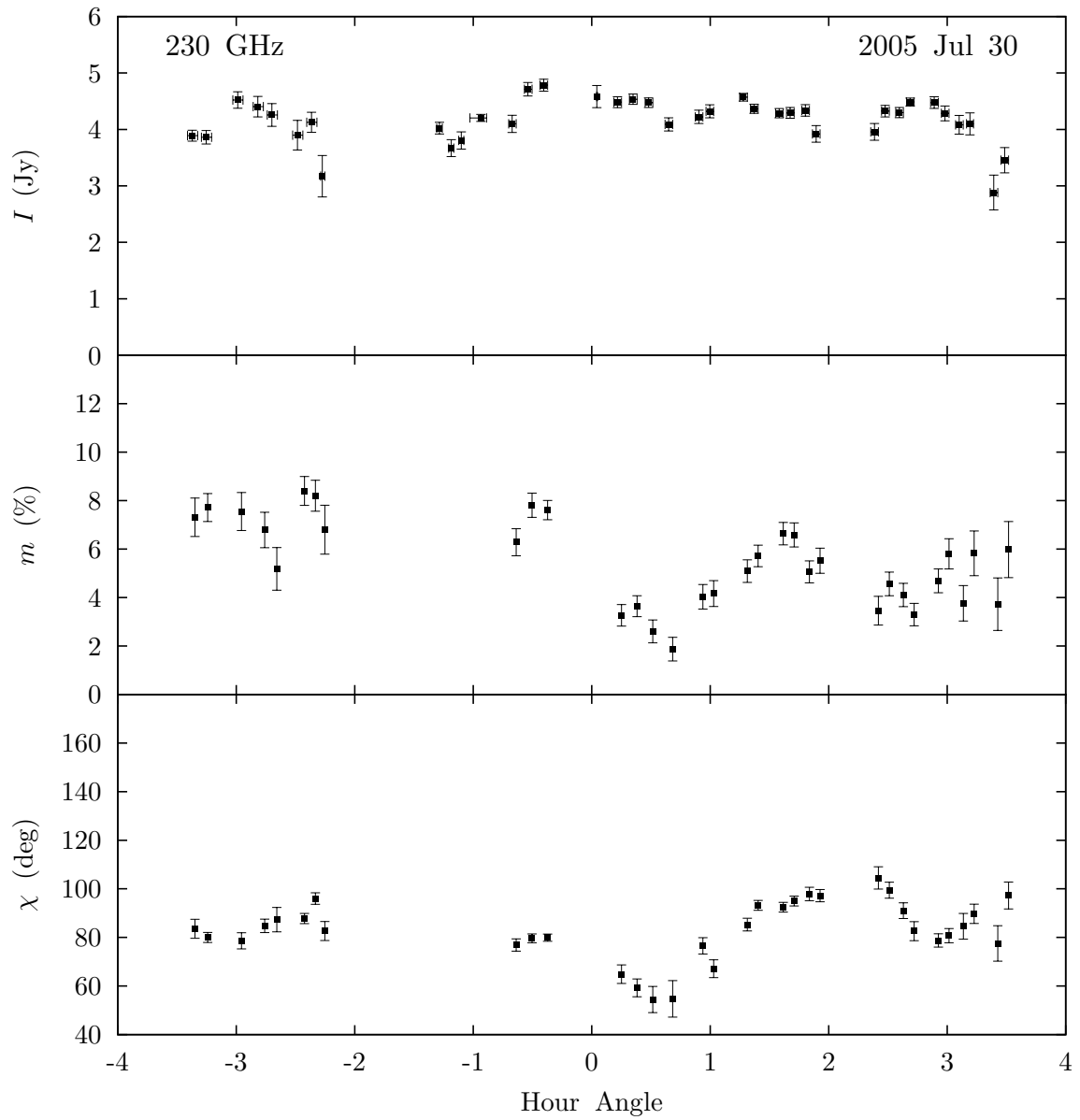


Fig. 7.10.— Light curve for 2005 July 30. See caption of Figure 7.1 for details.

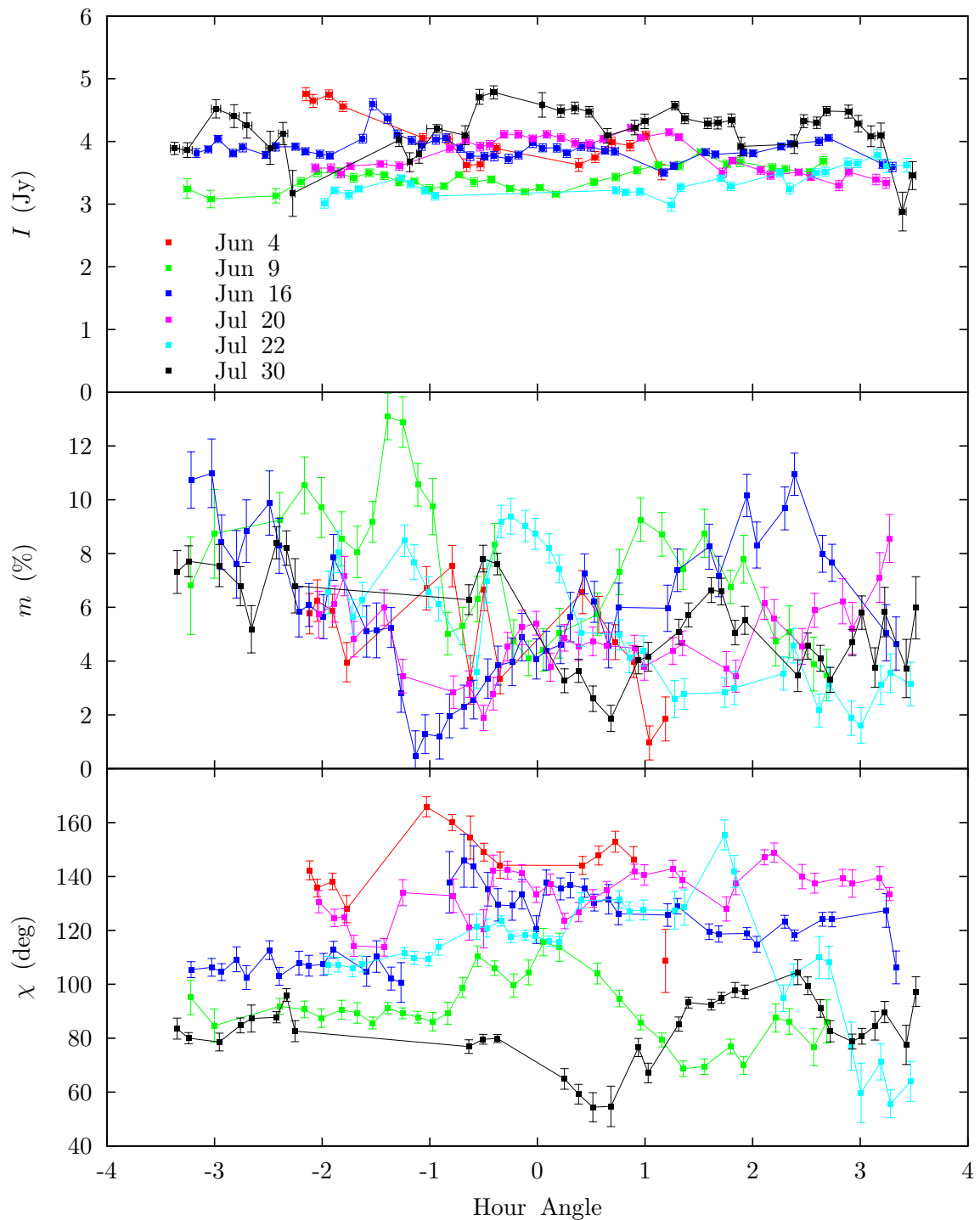


Fig. 7.11.— The full set of 230 GHz light curves from the summer of 2005. See Figure 7.1 for details.

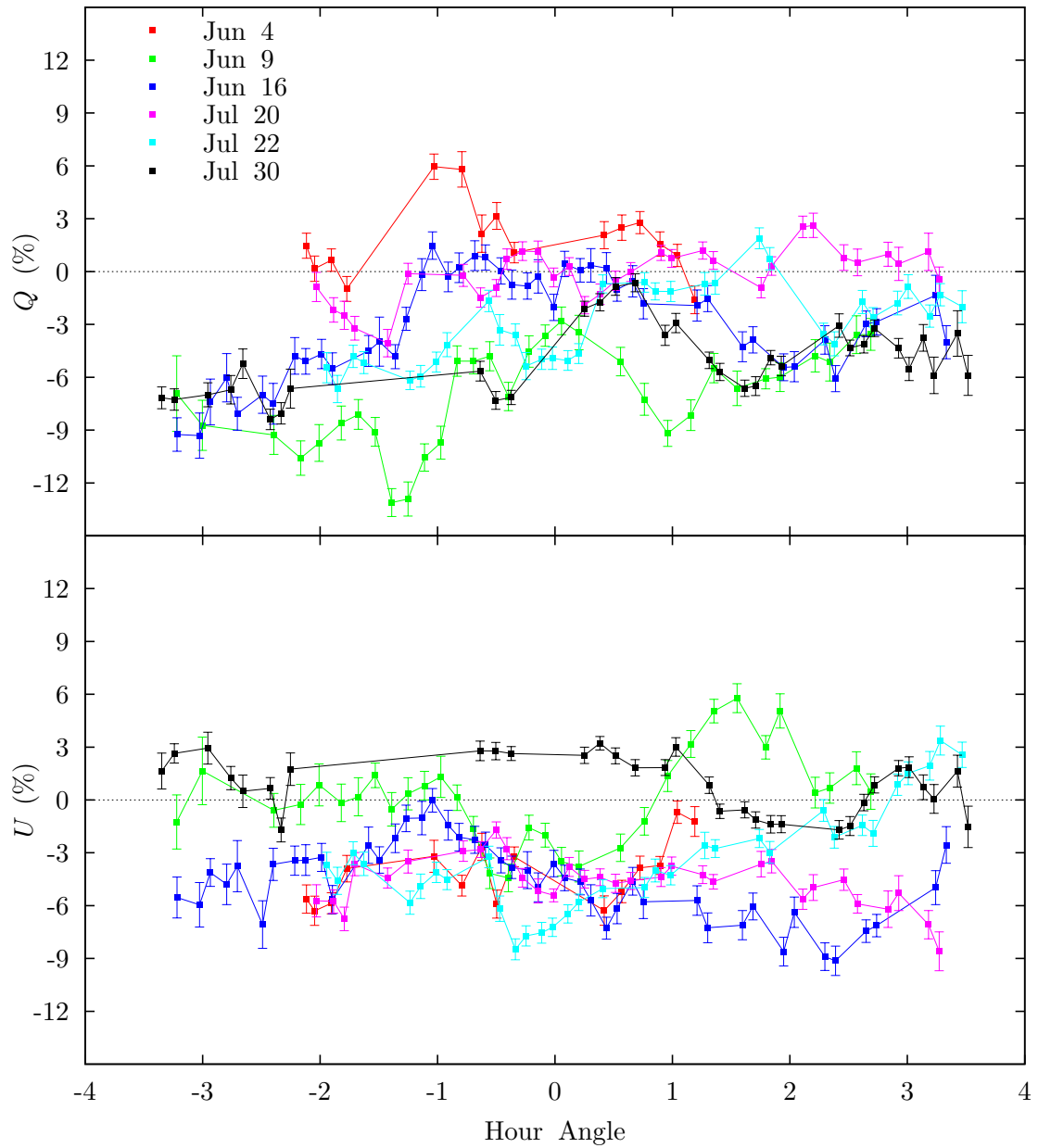


Fig. 7.12.— The full set of 230 GHz polarization light curves from the summer of 2005, plotted as fractional Q and U . In the event of leakage errors, these coordinates directly show fractional contamination from Stokes I .

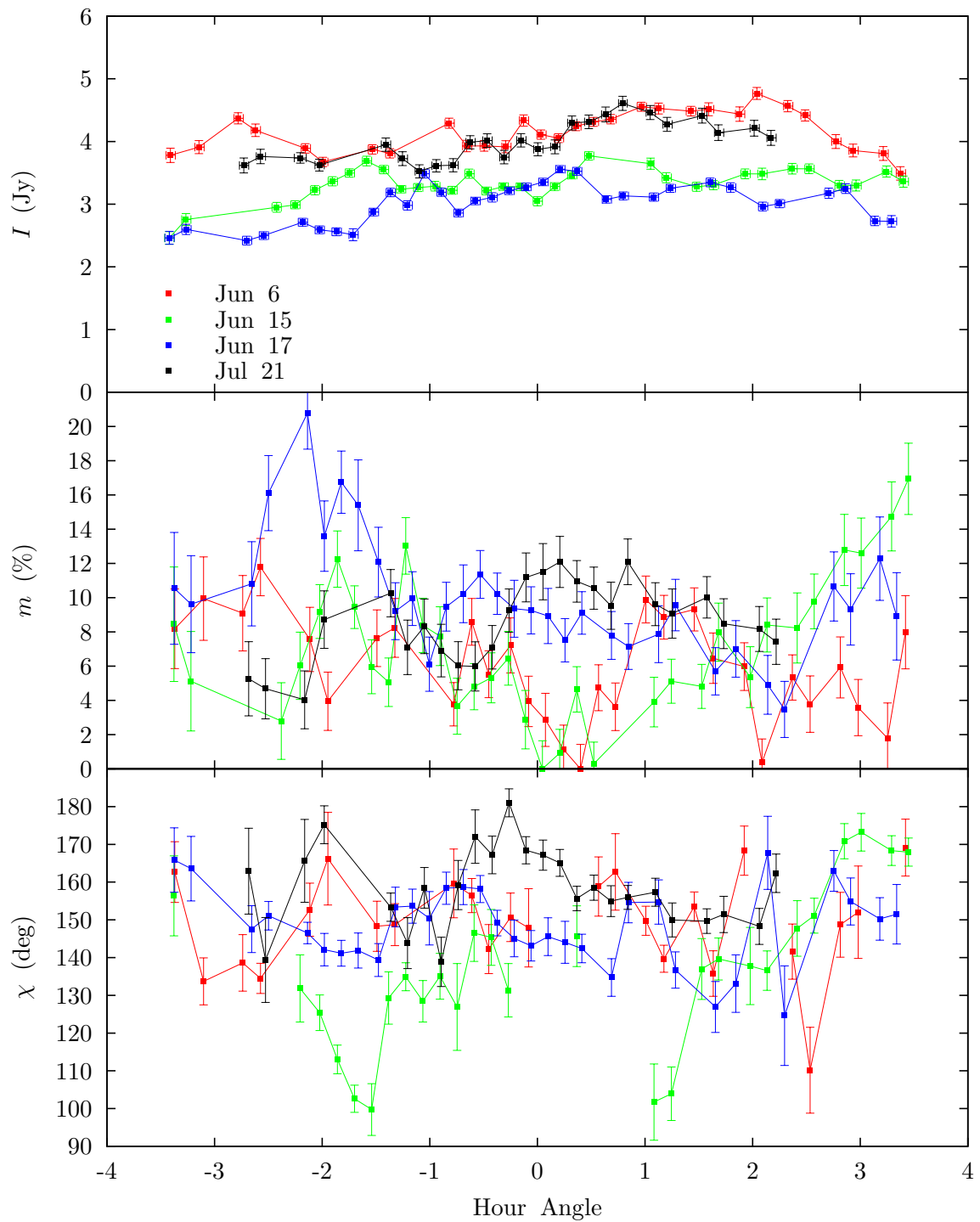


Fig. 7.13.— The full set of 345 GHz light curves from the summer of 2005. See Figure 7.1 for details.

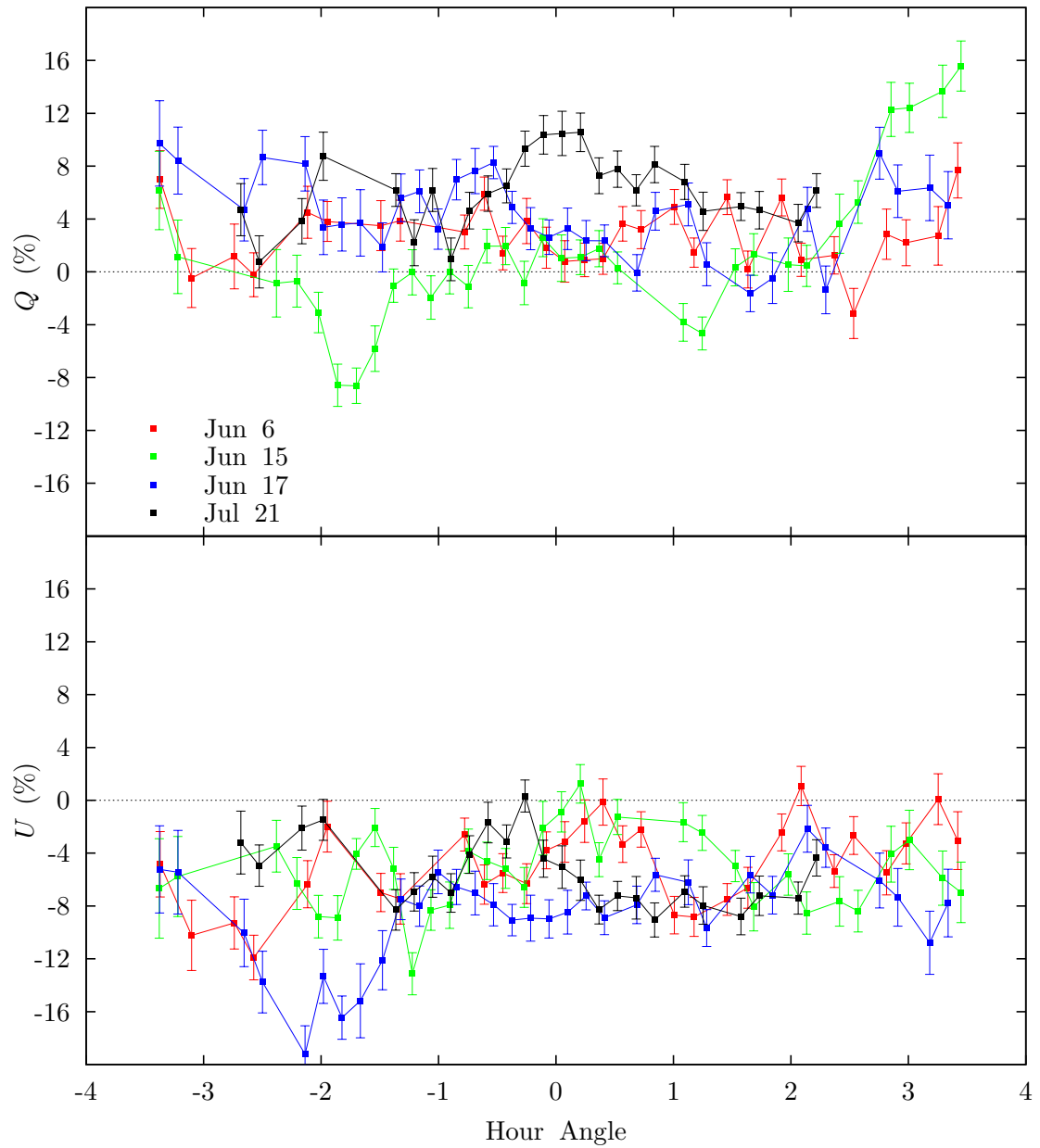


Fig. 7.14.— Like Figure 7.12, but showing the 345 GHz observations.

7.4 Variability Properties

The variability in these light curves is far more complex than anything previously observed in the polarization of Sgr A*. The region of the $m-\chi$ plane covered by the observed variability is shown in Figures 7.15 and 7.16. It is clear that the polarization variations do not uniformly cover these subsections of the plane. The polarization ranges of the individual nights cover even less of the plane, with most nights having clear preferred regions within the total area sampled on all nights. If the variability were dominated by power on timescales short compared to the seven-hour coverage of a single track, the polarization would be expected to be spread over a similar area in the $m-\chi$ plane on most nights, with the observed variability in full-night averages (Table 5.1 and § 5.4) possibly resulting from small contributions from power on longer timescales. Instead, significant variability appears to be present on timescales of a day or more, leading to offsets between the variations on different nights. This suggests that the full-night averages can contribute useful information to the study of polarization variability, information that is complementary to that obtained at fine temporal resolution.

Despite the substantial night-to-night variations in the mean polarization (the mean polarization for each night is shown in Table 5.1), the m and χ histograms show peaks for both frequencies. From all polarization samples (including those with low polarization), the noise-weighted average polarization fraction is 5.4% at 230 GHz and 7.5% at 345 GHz. The root-mean-square variation is substantial in both bands, 2.4% and 3.5% at 230 and 345 GHz, respectively. After removing those points with poorly detected polarization (less than 2σ), the noise-weighted average χ is 108.5°

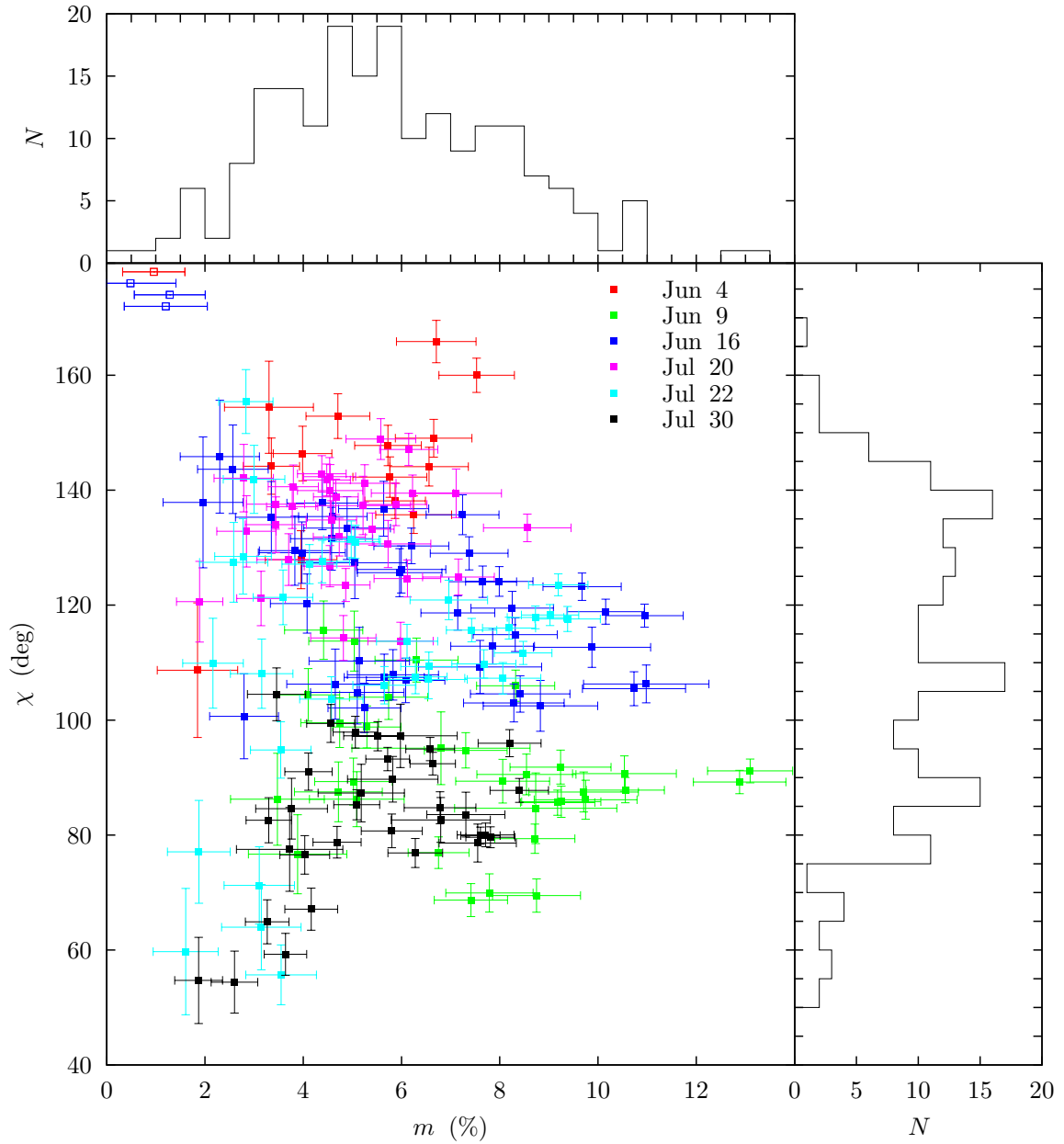


Fig. 7.15.— Short timescale polarization variability of Sgr A* at 230 GHz. Points are shown for each of the 4-minute polarization samples on six nights, 190 in all. The distribution of polarization fraction (m) is shown at top in 0.5% bins. The position angle (χ) distribution is compiled at right with 5° bins for all points where the polarization is detected at 2σ . The four points where the polarization falls below this threshold have very poorly constrained χ and are shown in the upper left at arbitrary χ .

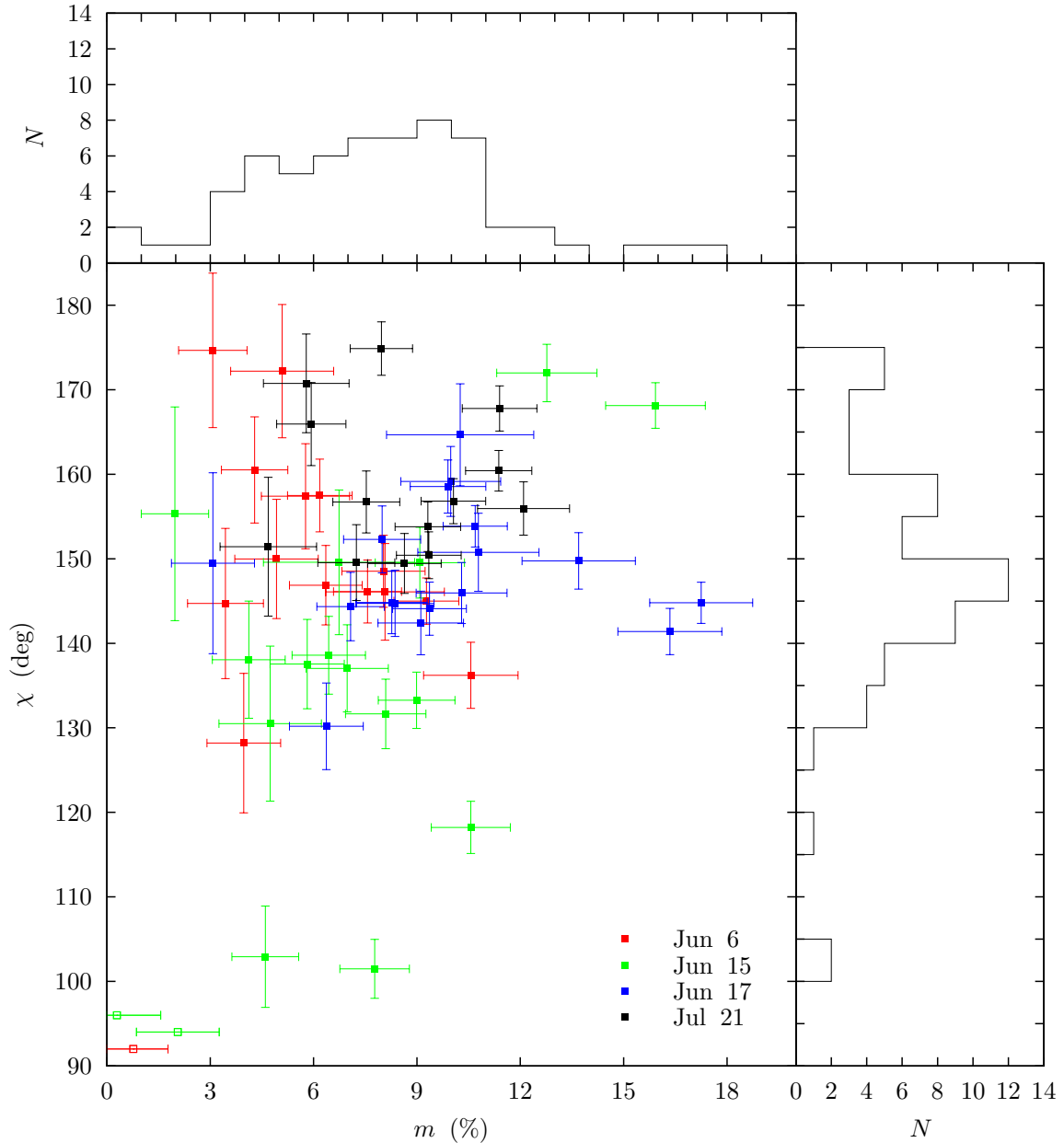


Fig. 7.16.— Short timescale polarization variability of Sgr A* at 345 GHz. The polarization samples shown here are averages of two adjacent (in time) 5.5-minute cycles to increase the signal-to-noise ratio of the points. The typical error in m after averaging is 1.0%–1.3%, within a factor of two of that achieved at 230 GHz. There are 62 averaged samples shown from the four nights. The distribution of polarization fraction (m) is shown at top in 1% bins, while the distribution of well-detected position angles is shown at right with 5° bins (see the caption of Figure 7.15 for more details). Three points have insignificant polarization and are shown at arbitrary χ in the lower left.

and 149.5° with rms variations of 25° and 15° at 230 and 345 GHz, respectively. The rotation measure inferred from these average angles is -7.3×10^5 rad m^{-2} , 30% higher than what was derived in Chapter 5. The origin of this discrepancy is clear, comparing averages relies on non-simultaneous measurements and is inherently unreliable in a source as variable as Sgr A*.

7.5 Polarization Orbits

7.5.1 Flares and Polarization Light Curves

Flare models for Sgr A* typically involve transient electron heating from processes such as magnetic reconnection, resulting in increased synchrotron emission in the submillimeter and synchrotron or synchrotron self-Compton emission in the infrared and X-ray (e.g. Markoff et al. 2001; Yuan et al. 2004; Liu et al. 2004). While the highest-energy electrons should quickly cool through synchrotron losses, those that emit at SMA frequencies can be expected to show emission for periods of hours (e.g. Eckart et al. 2006a). Synchrotron emission from a localized population of energetic electrons (a “hot spot”) should be significantly polarized; the polarization of synchrotron emission depends on the optical depth, electron energy distribution, and disorder in the magnetic field, but can reach 75% or more. Therefore, the small flares seen in the submillimeter, typically 10%–20% (Marrone et al. 2006), could contribute polarized emission of a few to 10% of the total flux density.

The signature of such a hot spot near the inner edge of a circularized accretion flow has been investigated by Broderick & Loeb (2006b). For hot spots located at

small radii, general relativistic magnification and multiple photon paths significantly affect the observed polarization during the flare. However, the temporal sampling accessible in the current observations is still a little coarse compared to the timescales relevant to very small radii. The orbital period (τ) for a hot spot at radius r around a black hole of spin parameter a is

$$\begin{aligned}\tau &= \frac{2\pi GM}{c^3} \left[\left(\frac{r}{r_g} \right)^{3/2} \pm a \right] \\ &= (108 \text{ s}) \left(\frac{M}{3.5 \times 10^6 M_\odot} \right) \left[\left(\frac{r}{r_g} \right)^{3/2} \pm a \right].\end{aligned}\quad (7.1)$$

Here r_g is the gravitational radius, GM/c^2 , half the Schwarzschild radius (r_S). The upper and lower signs refer to prograde and retrograde orbits, respectively. For a non-rotating black hole, the innermost stable orbit is at $6r_g$, a period of about 26.5 minutes, while a maximally rotating black hole has a prograde innermost stable orbit of $1r_g$, an orbital period of just 3.6 minutes (the innermost retrograde orbit is at $9r_g$ and requires 47 minutes, see Bardeen et al. 1972). Although the SMA can detect polarization in this source in just a few minutes, many samples would be required to measure an orbital signature well, so our light curves are not very sensitive to orbital periods shorter than an hour (radii greater than $10r_g$). For oscillatory behavior visible over many periods, like that possibly observed by Belanger et al. (2006), shorter periods may be accessible, although such a detection would be complicated by the irregular sampling of these light curves. At ten or more r_g from the black hole, the relativistic effects should be less important (except for viewing angles near the orbital plane) and a Newtonian picture can be considered. A hot spot with a fixed polarization direction in a co-rotating frame will appear as a rotating polarization vector added to the existing Sgr A* polarization. In the $Q-U$ plane this would show

up as a “polarization orbit” around the quiescent polarization. Note that this plane is a 360° mapping of the 180° -degenerate position angle, so two orbits in the $Q-U$ plane represent a single orbit in real space. This fact further increases the number of samples required for confident detection of such an orbit. Complexity can be added to the simple orbit picture in a variety of ways: synchrotron losses and the decay of the polarization contribution, radial motion, shearing, and relativistic effects. If these effects are important, they may make it difficult to observe a polarization orbit.

The July 30 light curve (Figure 7.10) stands out from the others because of the periodic-looking modulation in Stokes I and the correlated changes in m and χ . When the post-transit portion of the light curve is plotted in the $Q-U$ plane (Figure 7.17), the modulations resemble the polarization orbit described above. Over the last two hours the polarization completes nearly two complete circles of the mean polarization. The final points are closest to the mean, suggesting decay of the hot spot emission. If this is interpreted as an orbit, the period of roughly four hours (two $Q-U$ orbits per real space orbit) corresponds to a radius of $26r_g$ ($13r_s$) for all a . Plots of the full $Q-U$ -plane light curves on all ten nights are provided in Appendix C.

7.5.2 Future Prospects

Polarization orbits at very small radii would be extremely interesting for their power to constrain properties of the black hole and accretion geometry. Substantial effort in the submillimeter and near infrared is now being directed toward constructing instruments to observe Sgr A* at high-angular resolution with the goal of determining

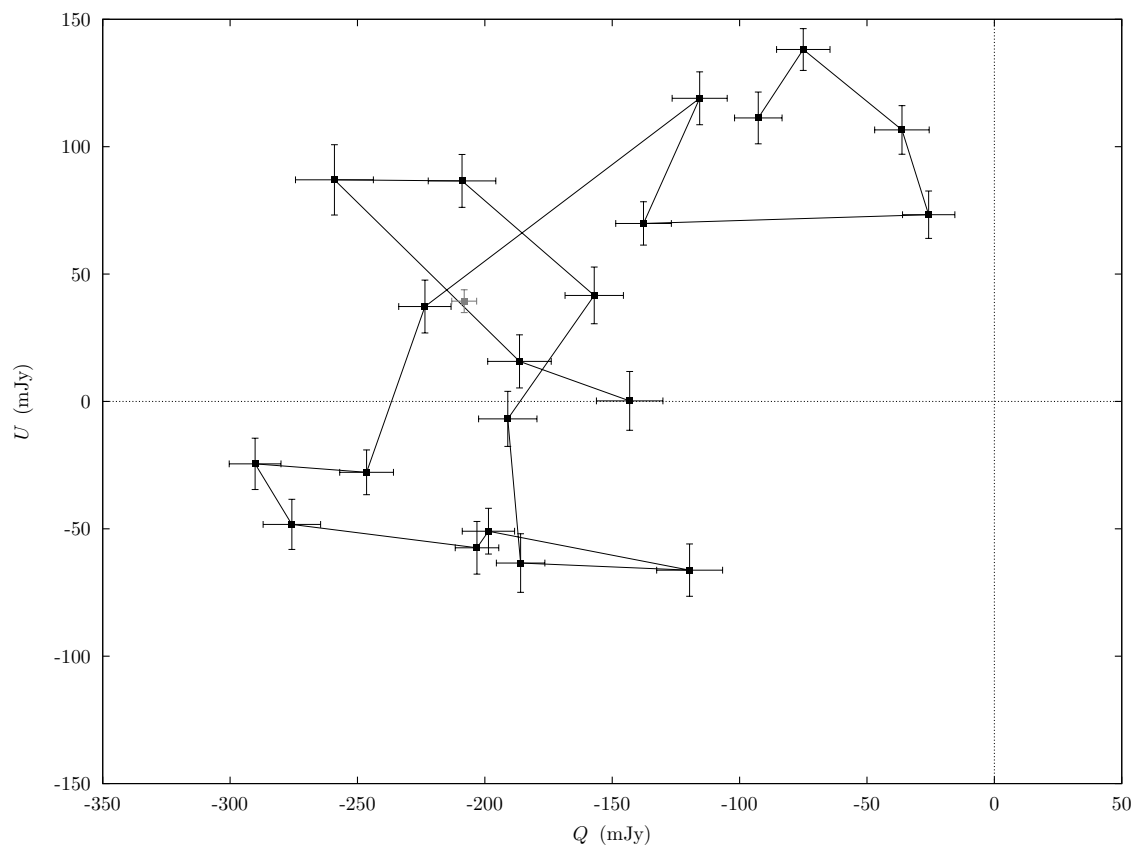


Fig. 7.17.— The post-transit portion of the 2005 July 30 polarization light curve (Figure 7.10), plotted in the $Q-U$ plane. The mean polarization for the track is marked with a grey cross, near $Q = -210$ mJy, $U = 40$ mJy. The time series proceeds from the start at the upper right to the end at center (near $Q = -140$ mJy, $U = 0$ mJy). *The individual light curve points are shown with half- σ error bars for clarity.* The final four points of the light curve, measured between 24° and 19° elevation, have significantly greater noise and therefore have been averaged together in pairs for this plot.

its spin through observations of hot spot motions and multiple images. Examples include a submillimeter VLBI project involving the SMA and the GRAVITY instrument for the Very Large Telescope Interferometer (Gillessen et al. 2006a). The prospects for such measurements are reviewed in Broderick & Loeb (2006c). These authors also note the promise of polarimetric measurements, as the polarization evolution is very sensitive to the properties of the spacetime through which the emission propagates. *It seems plausible that a flare at small radius observed with a sensitive submillimeter polarimeter could determine the spin of Sgr A* well in advance of the high-angular resolution measurements.*

The temporal resolution achieved in the measurements of this chapter can be improved upon in the near future with the SMA. Even polarization orbits at the smallest radii should be within reach of SMA polarimetry in a carefully designed experiment. Current SMA 230 GHz observations provide enough sensitivity in good weather to constrain the polarization to better than 1% in 4 minute samples. A purely polarimetric experiment can rely on self-calibration on Sgr A* to monitor the gains, with infrequent quasar observations to track gain amplitude changes. The polarization calibrator observations that greatly decrease the Sgr A* sampling at the beginnings and ends of the 2005 tracks can also be obviated due to the polarization stability of the system, further improving the coverage. The 15 samples per hour expected from continuous monitoring with four-minute cycles should be reachable. In addition, a hoped-for improvement in the correlator overhead would decrease the cycle time to 200 seconds, potentially allowing 18 cycles per hour with the same total on-source integration time. Because of the lower optical depth at higher frequencies, opportunities to detect hot spots at small radii should be better in the

345 GHz band. In the observations presented here, the sensitivity per 5.5-minute cycle is a factor of two poorer than in 4-minute cycles at 230 GHz. However, with the installation of the next SMA receiver band, dual-polarization observations will improve the polarization sensitivity (including reduced switching overhead) at 345 GHz by between $\sqrt{2}$ and $\sqrt{3}$, making it competitive with the 230 GHz band for polarimetry. With the correlator improvement, 1% sensitivity with 15 samples per hour should also be possible in this band. Based on the receiver installation schedule, this experiment should be feasible by the 2007 observing season.

Chapter 8

Conclusions

The completion of the Submillimeter Array (SMA) in 2003 dramatically improved the observational capabilities in the submillimeter band. In my graduate work I have attempted to make use of these new capabilities to examine Sagittarius A*, our local supermassive black hole. As the linear polarization of Sgr A* is an observable unique to the submillimeter, a portion of my work has been directed toward enabling polarimetry with the SMA. Here I summarize that effort and the scientific conclusions of the previous chapters. I also discuss results not included in this thesis, and a few additional lines of investigation accessible to the SMA and other instruments.

Results

SMA Polarimetry

The construction and commissioning of a facility polarimeter for the SMA is one of the significant achievements of this thesis. The polarimetry hardware and software employ very simple designs and have proven to be robust over the first two years of polarimetric observations. The cross-polarization of the system is well-measured, allowing diagnostic checks on the performance of the system. The frequency behavior of the leakages matches theoretical predictions, allowing a very precise measurement of the birefringence of the quartz used in the wave plates, which is otherwise poorly known. The leakages show no evidence of angular misalignment, which would increase the cross polarization, nor is there evidence that the alignment is changing over time, which might indicate degradation of the positioning system. Confidence in this conclusion is enhanced by the detection of a 0.3° orientation change in one positioner, likely due to a small change in the mounting surface of the instrument, which demonstrates the sensitivity of the measurements. Leakage variability appears to be dominated by a systematic effect resulting from the SMA optical design. Nevertheless, the stability in the leakages represents a factor of several improvement over that achieved at the Berkeley-Illinois-Maryland Association array (BIMA; Bower et al. 2002a), the closest analogue to this system. The stability will improve further when the calibration procedure is modified to remove the systematic error. The polarimeter system is presently being integrated into the new SMA calibration system, which will eliminate the need for manual installation of the polarimetry hardware before each polarization track.

The polarimeter now operates within the regular science program of the SMA. In the current observing semester, four PIs (myself excluded) have received polarimetric observing time, and seven other than myself have done so over the last year (Table 8.1). In addition to the observations of Sgr A* presented here, significant results in the field of star formation have been obtained from this instrument. Girart, Rao & Marrone (2006) found the first well-defined hourglass morphology in the magnetic field of a forming low-mass protostellar system, on the scales and with the properties predicted by the standard theory (Figure 8.1). The result confirms that star formation is slowed by the influence of magnetic fields. Other low- and high-mass protostars have been observed following this discovery and also show interesting magnetic properties.

Sagittarius A*

Our knowledge of the polarization properties of Sgr A* has advanced significantly over the three years since I began constructing the SMA polarimeter. SMA data have provided a second frequency with well measured polarization (345 GHz) and greatly improved upon the previous measurements at 230 GHz. In 2003, observations suggested that the polarization fraction rose like $m \propto \nu^{2.5}$ (Aitken et al. 2000; Bower et al. 2003). Now it is clear that m is quite flat between these two frequencies (Chapters 4 and 5), with a longer low-frequency tail than previously known (Macquart et al. 2006). Models and simulations that attempt to examine the polarization spectrum (e.g. Melia et al. 2000; Beckert & Falcke 2002; Yuan et al. 2003; Goldston et al. 2005) typically predict steep rises to high polarization fractions,

Table 8.1. Other SMA Polarization Projects

PI	Title	Tracks
R. Rao	Magnetic Field Structure in NGC 1333 IRAS 4A	2×345
E. Keto	Testing Theories for the Origin of the Galactic Center Arches	1×345
C. Brogan	Dust Polarization Observations of Cepheus A East	2×345
R. Rao	Mapping the Magnetic Field in the IRAS 16293 and NGC 7538 Protostars	3×345
R. Rao	Mapping the Magnetic Field in the L1551 IRS5 and HL Tau Protostars	2×345
Y.-W. Tang	Polarization Measurement of UCHII region G5.89-0.39	2×345
B. Matthews	Polarimetry of a Protostellar Core with Unique Polarization Properties	2×345^1
L. Greenhill	Submillimeter Water Masers as Tracers of Magnetic Fields in Orion BN/KL	1×345^1
M. Krejny	Probing Grain Size in TTS Disks via Multi-wavelength Polarimetry	1×230^1

¹Observations pending

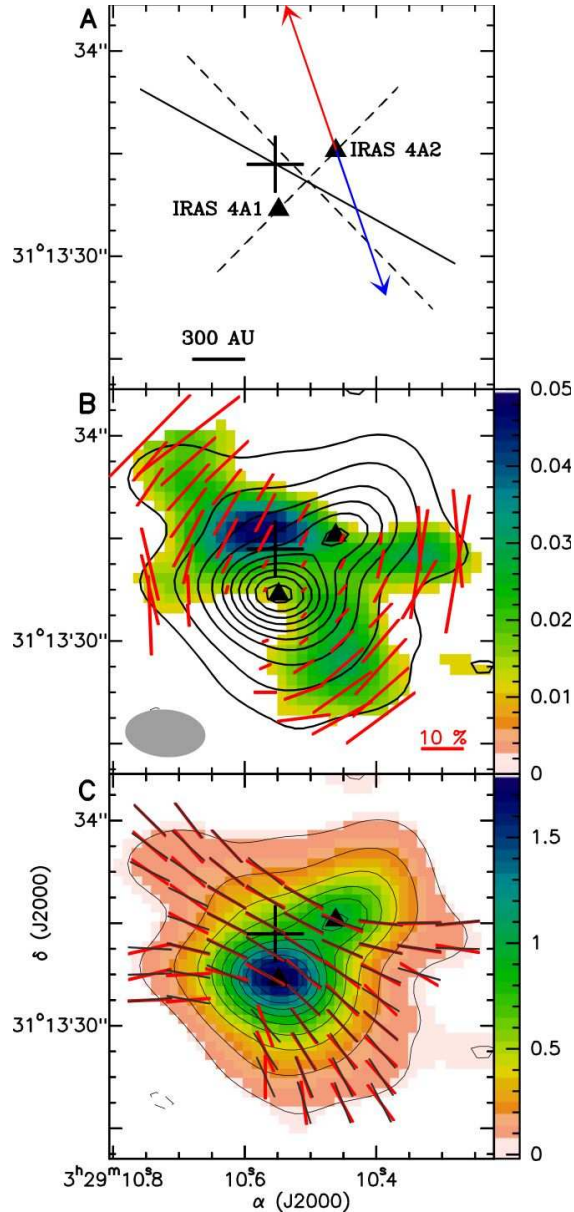


Fig. 8.1.— The pattern of polarization in NGC 1333 IRAS 4A, as measured by the SMA polarimeter. (A) Sketch of the axes of the system. The inter-core axis and its normal are drawn as dashed lines, the solid line is the axis of symmetry of the observed magnetic field. The red and blue arrows indicate the directions of the the molecular outflow. (B) Contour map of the 340 GHz dust emission (Stokes I) superimposed on the color image of the polarized flux intensity. Red vectors indicate the polarization direction, their length is proportional to the polarization fraction. Contour levels are 1, 3, 6, 9, ... 30×65 mJy per beam. (C) Contours and color scale trace the dust emission, while the magnetic field orientation (orthogonal to the polarization position angle) is shown with red vectors. The accompanying black vectors show the best-fit parabolic model for the magnetic field. This is the first clear detection of an hourglass-shaped magnetic field on the scales expected for isolated star formation. See Girart et al. (2006) for further details.

which may be hard to reconcile with these observations.

Polarization variability was not discovered until Bower et al. (2005a) found position angle changes and even then the origin of these changes was ambiguous. The first SMA observations at 340 GHz found clear variability in the polarization fraction, in addition to the position angle, indicating that intrinsic polarization changes were occurring (Chapter 4). Previously, the apparent stability of m at the sensitivity of the data suggested that Faraday rotation measure (RM) fluctuations were the more likely explanation. Subsequent SMA data at 230 and 345 GHz (Chapter 7) showed that the polarization, like most aspects of Sgr A*, varies dramatically on both interday and intraday timescales. Variations in the intrinsic polarization angle (χ_0), corrected for Faraday rotation, have also been detected (Chapter 5), confirming our earlier inference.

The RM of Sgr A* was estimated through selective use of the available data by Bower et al. (2003) and a more robust determination of the RM was the original motivation for this work. The discovery of polarization variability made simultaneous multi-frequency measurements essential to determining the RM. The 230 GHz polarization system allowed us to determine the RM from simultaneous data, the first measurement of Faraday rotation in this source (Chapter 5). The RM appears very stable, all 230 GHz epochs agree with the mean value of $(-5.6 \pm 0.7) \times 10^5 \text{ rad m}^{-2}$ to within 1.2σ and we place an upper limit of roughly 35% on the variations. This can be converted to a 25% limit on variation in the accretion rate, assuming that the density and magnetic field vary together. A formalism for deriving accretion rates from RM limits and detections was introduced with the first SMA results. It allows

consideration of the skeletal outlines of a continuum of models and simulations of Sgr A*. According to this formalism the accretion rate onto the black hole must lie in the range $10^{-7} - 10^{-9} M_{\odot} \text{ yr}^{-1}$. Exceptions for special geometries are allowed. The unknown radial temperature structure and equipartition fraction, orientation, and order in the magnetic field within the plasma surrounding Sgr A* remain unknown and soften the upper limit on the accretion rate.

The spectrum of Sgr A* has been difficult to measure because of its variability, particularly near the expected peak where the fluctuations increase and the atmosphere becomes opaque. Using the factor-of-three instantaneous spectral coverage of the SMA, we have now measured this spectral peak (Chapter 6). Based on the observed peak the luminosity of Sgr A* is just $200 L_{\odot}$, or $1.5 \times 10^{-9} L_{\text{E}}$, similar to previous estimates.

Ongoing Work

Coordinated Monitoring

In both 2004 and 2005, the SMA participated in coordinated observations of Sgr A*, with the goal of understanding the physics of the flaring emission observed at near-IR and X-ray wavelengths. The 2004 campaign was built around two 50 ks *Chandra* observations and results were reported in Eckart et al. (2006a). The VLA, SMA, VLT, and Keck telescopes provided contemporaneous observations at 43 and 340 GHz and in the near-IR. One significant X-ray flare was observed, during a period when Sgr A* was visible only to the VLT, and associated NIR variability

was detected. A decaying emission component was visible during the VLA and SMA observations beginning 2–3 hours after the flare, consistent with a model based on the standard van der Laan (1966) description of an expanding synchrotron source. No simultaneous flaring was observed in the IR and submillimeter bands and the submillimeter polarization was remarkable only for the low (2%) polarization fraction on July 7, following the X-ray flare.

The 2005 campaign was significantly larger, with five 50 ks *Chandra* observations; both the SMA and CSO provided submillimeter data between 230 and 690 GHz. Two X-ray flares were seen in four observations, again at times when only the VLT could observe Sgr A*, while the fifth observation was aborted because of a solar flare. Although we planned to coordinate IR and submillimeter polarimetry, after the VLT triggered SMA polarimetric observations on July 30 degraded seeing at the VLT prevented overlap between the two wavelengths. The VLT polarimetric observations were well-timed and provided the first detection of IR polarization in Sgr A* during one of the X-ray/IR flares (Eckart et al. 2006b). The SMA data were also unusual, as discussed in Chapter 7. Further results of the campaign are not yet known because the various data sets have not been aggregated.

Yusef-Zadeh et al. (2006) also conducted coordinated observations of Sgr A* primarily using the CSO, VLA, XMM, and *Hubble* telescopes to cover a similar frequency range. Although they did detect two X-ray flares, one with simultaneous IR observations, neither occurred while the CSO was providing submillimeter data. Although the X-ray and IR data are useful, particularly when spectral indices can be derived with both bands (a main focus of the Keck observing strategy for these observations), the models used to explain these flares have substantial

freedom to adjust parameters because the luminosity and evolution of the flare in the submillimeter band is not known. The freedom to relocate the peak of the flare emission across a decade in frequency prevents a complete characterization of the emission process. In particular, the relative roles of direct synchrotron and inverse Compton emission in producing the IR flare are undetermined, leaving the trigger for the flare completely unknown (e.g. Markoff et al. 2001; Yuan et al. 2003; Liu et al. 2004; Eckart et al. 2004, 2006a; Yusef-Zadeh et al. 2006).

The previous flare detections have generally lacked spectral information at IR wavelengths, important to the synchrotron/IC question, and have not managed to catch a flare across the full submillimeter/IR/X-ray range. In a July 17, 2006 make-up observation for the lost *Chandra* time from the summer of 2005, the SMA and CSO joined Keck in observing Sgr A*. The very recently reduced X-ray data are shown in Figure 8.2 with the simultaneous 230 GHz SMA light curve. The flare has a duration of 63 minutes and is a factor-of-22 increase over the quiescent emission. There is a substantial delay between the two observing bands, approximately 1.5 hours. The rise and fall of the 230 GHz light curve resembles the simple expanding, self-absorbed synchrotron plasma model of van der Laan (1966), although the delay in the onset of the rise requires a very large initial optical depth in the plasmon, or a very hard particle spectrum, or a slow rate of expansion. The flat spectral index in the submillimeter and X-ray bands is also consistent with a very hard electron spectrum. The Keck observations failed to observe the peak in the flare, although past observations have always found that the X-ray and IR flares occur simultaneously. Within these observations we can examine the temporal evolution of the flare and its change with wavelength, the spectral index in the

submillimeter between 230 and 350 GHz, the IR spectral index from three-color Keck measurements, and the X-ray spectral slope. The examination of these data is just beginning, but they will likely yield the best constraints ever obtained on the flare mechanism in Sgr A*.

New Experiments

The RM determination presented here is the first of its kind, but there remains a great deal to be learned from further measurements. Variability in the RM can constrain the accretion rate fluctuations in Sgr A* and the timescales observed in the variability can be used to infer the radial location of the Faraday screen, as noted by Bower et al. (2005a). Any measurement of variability timescales will require instantaneous measurements of the RM, like those presented here, rather than statistical measurements. Based on the stability inferred from past observations, the typical $3\text{--}5\sigma$ RM detections achieved at 230 GHz with the SMA will be inadequate for detecting RM changes. However, SMA 230/690 GHz measurements can increase the RM sensitivity by a factor of several. These observations were a primary goal of mine as I designed the upgrade to the polarimeter in early 2005. Although I spent a great deal of time in Hawaii in 2005 attempting to make this measurement, the weather did not reach the opacity and phase stability required. The best opportunity thus far arose on April 8, 2006, during my last observing trip, when the opacity was extremely low ($\tau_{225} \simeq 0.03$) and the atmosphere was very stable. Unfortunately, this weather came on the heels of a period of record wetness that had prevented SMA observations for nearly six weeks, and very little of the 690 GHz system was working

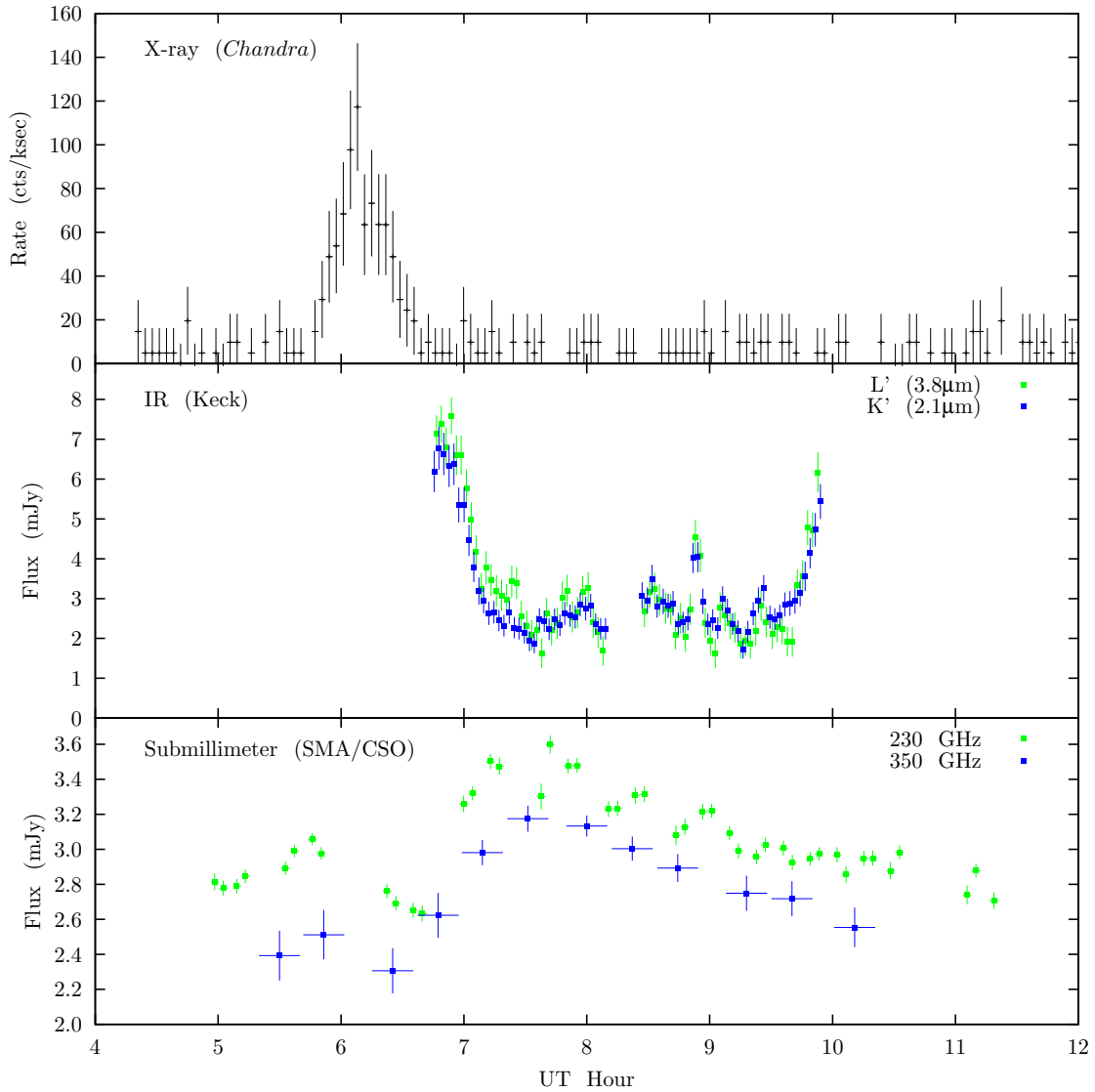


Fig. 8.2.— The July 17, 2006, flare of Sgr A* in the X-ray, IR, and submillimeter bands. The missing period in the 230 GHz (SMA) light curve during the peak of the flare resulted from a pointing measurement and leakage calibration observations. The missing 350 GHz (CSO) data are also due to unfortunately-timed calibration observations. The X-ray data are binned at 3.5 minute intervals and plotted from zero with an arbitrary scale. The peak in the 230 GHz light curve occurs approximately 1.5 hours after the 0608 UT peak in the X-ray data.

on that night. From the three antennas that produced usable data it appears that a polarization detection in Sgr A* at 690 GHz should be possible, although polarization calibration could not be performed with just three baselines. I intend to continue pursuing these observations in the coming year, both to determine the 690 GHz polarization fraction and to precisely measure the RM. In the near future, the SHARP polarimeter (Novak et al. 2004) will begin science observations at 650 and 850 GHz on the CSO. From past coordinated monitoring observations with the SMA and CSO we can determine the excess 650 GHz flux density in the CSO beam at the position of Sgr A* and determine the polarization contribution of dust at this location (expected to be low), so joint SMA-CSO observations at 230 and 650 GHz could also determine the RM to high precision with less stringent weather requirements. Through my ongoing collaboration with the Northwestern University SHARP team, I hope to attempt these observations in the coming year.

Although it is assumed that the variation of position angle with frequency follows the ν^{-2} curve expected from Faraday rotation with a single RM, this has never been measured and deviations from this behavior would be extremely interesting. One origin for such a deviation could be a changing intrinsic polarization direction (χ_0) with frequency resulting from a magnetic field geometry that changes with optical depth (equivalent to a radial coordinate through an accretion flow or a jet nozzle, or a coordinate along a jet). A second origin would be a change in RM with frequency, which would result from RM contributions from cooler than expected plasma or very dense, mildly-relativistic plasma at small radii or near the base of a jet. Although this is not predicted in most current models, it would be expected from the original ADAF model, which could escape the accretion rate limits derived

from the RM if the magnetic field is very tangled. As mentioned in Chapter 5, the RM chosen by Macquart et al. (2006) is lower than observed by the SMA, as would be expected in this scenario. Non-detection of this effect would confirm that there is stable χ_0 across the measured frequencies, a constraint for simulations, and eliminate the possibility of marginally-relativistic plasma in the inner accretion flow. A detection could be interpreted according to either of the two models proposed here and would constrain the magnetic field morphology at small radii or require cool plasma.

Observations with the SMA can provide polarimetry at three frequencies simultaneously using the 230/690 GHz wave plates. However, the effect of RM at 690 GHz is so small (6° total rotation for the RM derived in Chapter 5) that this frequency is unsuitable for detecting frequency-dependent changes in the RM. Now that linear polarization has apparently been discovered at 83 GHz (Macquart et al. 2006), more sensitive measurements of the RM should be possible at low frequencies where the span in ν^{-2} between sidebands is very large. Using the SMA at 230 GHz and CARMA near 100 GHz in a coordinated observation would yield four frequencies (or five with SMA 690 GHz data) and two measurements of the local slope of the χ versus ν^{-2} curve, the local RM. This type of measurement also has the advantage of distinguishing between frequency-dependent RM and χ_0 . Because it is observationally simple, this experiment should be attempted as soon as the existing 3 mm BIMA polarimetry hardware (now part of CARMA) is usable.

Finally, as discussed in Chapter 7, the SMA polarization sensitivity is sufficient to make very well-sampled light curves of polarization variations in Sgr A* at 230 GHz, with the 345 GHz sensitivity expected to be comparable in the coming

year. Rapid modulation of the polarization that is attributed to noise in the 2005 light curves may be resolved into “polarization orbits” under more uniform and continuous sampling. The radiative transfer models needed to predict the path of true polarization orbits, accounting for the effects of the strong gravity in the vicinity of a black hole, have been developed by Broderick & Loeb (2006b), and realistic complications (e.g., radial motion, expansion, decay) now being added to better represent real flares. We intend to propose focused polarimetric monitoring observations of Sgr A* designed to search for such signatures, as outlined in Chapter 7. These observations could be joined with the coordinated SMA/CARMA polarimetry described above without significant adverse impact for either program.

Appendix A

SMA Polarimetry System: Schematics and Part Lists

A.1 Hardware Components

A.1.1 Commercially Available Components

The following commercial components are used in each instrument. Miscellaneous ICs, connectors, and simple components are excluded from this list. Each part is listed with a short description, manufacturer, and part number.

- Drive gear
Spur gear (pin hub), Precision Industrial Components, MSG16-42
- Gear (mounted to rotation stage, must be modified after purchase: a $\varnothing 69$ mm clear aperture must be opened and screw holes added)
Spur gear (hubless), Precision Industrial Components, MHS8-168
- Optical brake

Opto-interrupter, Omron, EE-SX672

- Rotation stage for wave plate
Polarizer holder, Opto-Sigma, 114-0250
- Drive motor
DC micromotor, Faulhaber/MicroMo, 1319T024S+14/1
- Reduction gearhead (purchased with motor)
Gearhead, Faulhaber/MicroMo, 246:1+X0437
- Control computer, 486DX with 64MB RAM and 10/100 ethernet
PC104 computer, Micro/Sys, SBC0486 + 0486OPT3 + 0486OPT20
- Primary power supply
24V power supply, Acopian, 24WB125
- 24V to 5V DC-DC converter
DC-DC converter, Semiconductor Circuits, SC15A11-300-24
- Motor driver chip
Dual motor driver IC, Allegro, UDN2998W

The electrical schematic for the system is shown in Figure A.1.

A.2 Wave Plates

A.2.1 Wave Plate Specifications

- 230/690 GHz quartz quarter-wave plates
 - X-cut quartz
 - Assumed indices: $n_o = 2.106$, $n_e = 2.154$ (Birch et al. 1994)
 - 6.800 ± 0.003 mm thick
 - Nominal center frequency: 229.67/689 GHz
 - $\varnothing 50.8 \pm 0.1$ mm
 - Optically polished
 - Fast axis direction marked with flat on perimeter

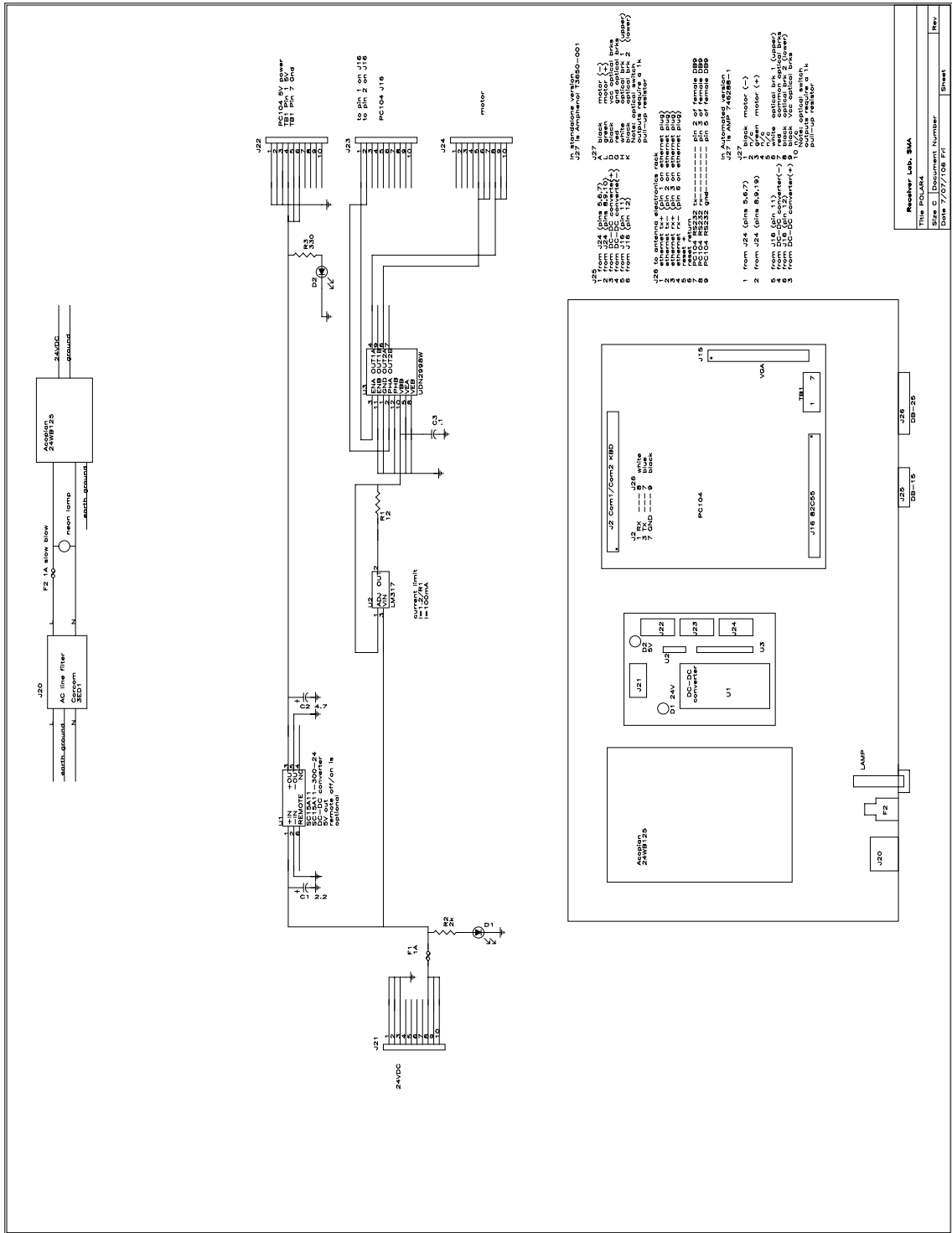


Fig. A.1.— Electrical schematic for the SMA polarimeter.

- 345 GHz quartz quarter-wave plates

X-cut quartz

Assumed indices: $n_o = 2.106$, $n_e = 2.154$ (Birch et al. 1994)

4.566 ± 0.003 mm thick

Nominal center frequency: 342 GHz

$\varnothing 50.8 \pm 0.1$ mm

Optically polished

Fast axis direction marked with flat on perimeter

- 345 GHz sapphire quarter-wave plates

A-cut Hemlux sapphire

Assumed indices: $n_o = 3.064$, $n_e = 3.404$ (Afsar 1987)

0.640 ± 0.006 mm thick

Nominal center frequency: 345.5 GHz

$\varnothing 50.8$ mm

100-70 polish

Fast axis direction marked with flat on perimeter

A.2.2 Anti-Reflection Coating Specifications

Nominal properties, based on $n = 1.514$ (Lamb 1996):

- 230/690 GHz coatings: $215\mu\text{m}$
- 345 GHz coatings: $144\mu\text{m}$

A.2.3 Vendors

The recommended vendor for quartz products is Boston Piezo-Optics:

Boston Piezo-Optics, Inc.
 38 B Maple Street
 Bellingham, MA 02019
 (508) 966-4988

BPO manufactured all of the 230/690 GHz quartz pieces and four of the 345 GHz pieces. In addition to the eight 230/690 plates in use, one additional piece was coated and machined to the proper thickness and remains as a spare, while three other pieces with a “fine polished” finish (translucent, but optically dull) remain unused.

Three 345 GHz pieces were also purchased from U-Oplaz Technologies (or Photop Technologies, Inc.), a distributor for the Chinese manufacturer JDSU CASIX. Delivery was very late on these pieces and another vendor (BPO) was sought.

The final 345 GHz wave plate is a sapphire plate purchased from Crystal Systems in 1993.

Crystal Systems, Inc.
27 Congress St.
Salem, MA 01970
(978) 745-0088

Five sapphire plates were purchased, three have been coated for use in the SMA. The last two are unavailable.

Polyethylene coatings were made with low density polyethylene sheets of various thicknesses purchased from Goodfellow.

Goodfellow Corp.
237 Lancaster Ave.
Suite 252
Devon, PA 19333
(800) 821-2870

A.2.4 Measured Coating Properties

Tables A.1 and A.2 list the measured thicknesses of the wave plate anti-reflection coatings. The serial number of the wave plate positioner that holds each plate is also provided. Because the 230/690 GHz wave plate coatings are turned down to their final thickness in a lathe, they do not have measurable coating thickness gradients. The coating on each side of these plates can be measured independently, while the coatings on the 345 GHz plates can only be measured as (two-side) total thickness increases.

A.3 Software Interface

The positioners are controlled through the remote procedure call (RPC) interface from `ha19000`. The RPC client program is located in `/application/wvpltCode` on this machine and is called `wave`. The usage of this program is provided if it is invoked without arguments:

Table A.1. 230/690 GHz Waveplate Coatings

Plate SN	Positioner SN ^a	Thickness ^b (μm)	Thickness ^c (μm)
1	1	224	218
2	2	216	221
3	3	234	229
4	4	231	231
5	5	231	229
6	6	229	231
7	7	218	221
8	8	218	224
9	Spare	216	218

^aWave plate assembly associated with each plate

^bMeasured thickness on receiver side of plate

^cMeasured thickness on sky side

Table A.2. 345 GHz Waveplate Coatings

Plate SN	Positioner SN ^a	Thickness ^b (μm)	Wedge ^c (μm)
CASIX1	6	143	6
CASIX2	4	142	8
CASIX3	5	140	3
BPO1	1	160	14
BPO2	2	152	14
BPO3	8	155	14
BPO4	7	152	14
S1 ^d	Spare	132	11
S2 ^d	Spare	133	7
S3 ^d	3

^aWave plate assembly associated with each plate

^bAverage single-side thickness (half of the total)

^cHalf of the thickness gradient across the plate

^dSapphire wave plate

```

wave -a<m> -o<n> [-s<C>] [-t] [-g | l]

-a <m> Antenna number m (m=1..8)

-o <n> Operation n:

    1 -> initialize waveplate and set new state

    2 -> set new state

    3 -> shut down waveplate

-s <C> State C (C = R, L, H, V), not needed for -o 3

-t Test mode (just return 0 after each request)

-l Location: LAB. Server is polarX.cfa.harvard.edu

-g Location: GUIDESCOPE. Server is optelX.cfa.harvard.edu

    Location defaults to polarX.sma.hawaii.edu

    If both -l and -g are used, last one wins.

-<other> Print usage

```

The location changing flags (-l, -g) are unnecessary for operation at the SMA site, they exist only for testing purposes. For operation in the Receiver Lab, the -l option is required. During normal observing these calls are made automatically by the `polar` control code, although occasionally a wave plate positioner must be reset after a reboot or installation of a plate by shutting down and reinitializing the control software (`wave -a<m> -o3`, followed by `wave -a<m> -o1 -s<C>`). There are a variety of improper behaviors that will be caught by the program and reported with informative errors if the call was made from the command line (instead of through `polar`). Such failures are rare, but should be corrected by reinitializing. The most common failures are “Operation failed to find Flag 1 in home routine.”, which likely indicates that the positioner is not connected to the computer or the

motor is not being powered, and “Operation completed too quickly. State likely invalid.”, which is usually caused when a wave plate is installed and a flag is left rotated into the beam of an optical brake.

The computers lack hard disks, their filesystems are stored on `ono.sma.hawaii.edu`. In the Receiver Lab they have been served from `other1.cfa.harvard.edu`.

The individual `polarX.sma.hawaii.edu` computers run the server program, `wave_server`. This program is automatically started when these computers are rebooted. The `polarX` computers have the usual root password and are located at IPs 128.171.116.161 to 128.171.116.168 for `polar1` to `polar8`. Notes on compiling the program for `hal9000` and for the `polarX` computers are included in `wvplt.h` in the code directory. The server program must be compiled on an external linux machine and copied to the `polarX` computers.

Appendix B

Optimal Walsh Functions

In polarimetric observations the SMA feeds are switched between right- and left-circular polarization sensitivity to completely sample the sky polarization on each baseline. This switching is done efficiently by assigning a Walsh function switching pattern to each antenna. An explanation of the origins and properties of these orthogonal functions can be found in § 7.5 of Thompson et al. (2001). The period-16 Walsh functions are labeled $wal(n, t)$, where the sequence number (n) ranges from 0 to 15, in order of increasing switching frequency. This order corresponds to alternating $cal()$ and $sal()$ (even and odd) sequences of the same number, i.e., $cal(0, t)$, $sal(1, t)$, $cal(1, t)$, $sal(2, t)$, and so on.

The following are the Walsh sequences that should be chosen to maximize the number of baselines where all four polarization states are sampled in every quarter of the 16-step cycle. The seven-antenna sequences are provided in Table B.1, while Table B.2 shows the polarized visibilities that these sequences produce on all 21 baselines. Tables B.3 and B.4 show the equivalent information for an eight-antenna

array. The set of sequences for the eight-antenna case is the same as that for seven antennas with the addition of sequence 10. The choice of R and L is arbitrary and the two states can be interchanged.

In the seven-antenna case, 16 baselines sample all four polarizations within each quarter cycle, four baselines (A-B, A-C, D-E, F-G) require a half-cycle to sample all states, and one baseline (B-C) requires a full cycle. In the eight-antenna case, 22 baselines sample four polarizations each quarter cycle, four require a half cycle (A-B, A-C, D-F, G-H), and two require the full cycle (B-C, E-F).

Table B.1. Walsh Sequencies for Seven Antennas

Antenna						
A	B	C	D	E	F	G
Sequency						
5	6	7	8	11	12	15
R	R	R	R	R	R	R
R	R	R	L	L	L	L
L	L	L	L	L	R	R
L	L	L	R	R	L	L
L	R	R	R	L	L	R
L	R	R	L	R	R	L
R	L	L	L	R	L	R
R	L	L	R	L	R	L
L	L	R	R	R	R	R
L	L	R	L	L	L	L
R	R	L	L	L	R	R
R	R	L	R	R	L	L
R	L	R	R	L	L	R
R	L	R	L	R	R	L
L	R	L	L	R	L	R
L	R	L	R	L	R	L

Table B.2. Polarization Cycle for Seven Antennas

Baseline																				
A-B	A-C	A-D	A-E	A-F	A-G	B-C	B-D	B-E	B-F	B-G	C-D	C-E	C-F	C-G	D-E	D-F	D-G	E-F	E-G	F-G
RR	RR	RR	RR	RR	RR	RR	RR	RR	RR	RR	RR	RR	RR	RR	RR	RR	RR	RR	RR	RR
RR	RR	RL	RL	RL	RL	RR	RL	RL	RL	RL	RL	RL	RL	RL	LL	LL	LL	LL	LL	LL
LL	LL	LL	LL	LR	LR	LL	LL	LL	LR	LR	LL	LL	LR	LR	LL	LR	LR	LR	LR	RR
LL	LL	LR	LR	LL	LL	LL	LR	LR	LL	LL	LR	LR	LL	LL	RR	RL	RL	RL	RL	LL
LR	LR	LR	LL	LL	LR	RR	RR	RL	RL	RR	RR	RL	RL	RR	RL	RL	RR	LL	LR	LR
LR	LR	LL	LR	LR	LL	RR	RL	RR	RR	RL	RL	RR	RR	RL	LR	LR	LL	RR	RL	RL
RL	RL	RL	RR	RL	RR	LL	LL	LR	LL	LR	LL	LR	LL	LR	LR	LR	LL	LR	RL	RR
RL	RL	RR	RL	RR	RL	LL	LR	LL	LR	LL	LR	LL	LR	LL	RL	RR	RL	LR	LL	RL
LL	LR	LR	LR	LR	LR	LR	LR	LR	LR	LR	RR	RR	RR	RR	RR	RR	RR	RR	RR	RR
LL	LR	LL	LL	LL	LL	LR	LL	LL	LL	LL	RL	RL	RL	RL	LL	LL	LL	LL	LL	LL
RR	RL	RL	RL	RR	RR	RL	RL	RL	RR	RR	LL	LL	LR	LR	LL	LR	LR	LR	LR	RR
RR	RL	RR	RR	RL	RL	RL	RR	RR	RL	RL	LR	LR	LL	LL	RR	RL	RL	RL	RL	LL
RL	RR	RR	RL	RL	RR	LR	LR	LL	LL	LR	RR	RL	RL	RR	RL	RL	RR	LL	LR	LR
RL	RR	RL	RR	RR	RL	LR	LR	LL	LR	LL	RL	RR	RR	RL	LR	LR	LL	RR	RL	RL
LR	LL	LL	LR	LL	LR	RL	RL	RR	RL	RR	LL	LR	LL	LR	LR	LR	LL	LR	RL	RR
LR	LL	LR	LL	LR	LL	RL	RR	RL	RR	RL	LR	LL	LR	LL	RL	RR	RL	LR	LL	RL

Table B.3. Walsh Sequencies for Eight Antennas

Antenna							
A	B	C	D	E	F	G	H
Sequency							
5	6	7	8	10	11	12	15
R	R	R	R	R	R	R	R
R	R	R	L	L	L	L	L
L	L	L	L	L	L	R	R
L	L	L	R	R	R	L	L
L	R	R	R	L	L	L	R
L	R	R	L	R	R	R	L
R	L	L	L	R	R	L	R
R	L	L	R	L	L	R	L
L	L	R	R	L	R	R	R
L	L	R	L	R	L	L	L
R	R	L	L	R	L	R	R
R	R	L	R	L	R	L	L
R	L	R	R	R	L	L	R
R	L	R	L	L	R	R	L
L	R	L	L	L	R	L	R
L	R	L	R	R	L	R	L

Table B.4. Polarization Cycle for Eight Antennas

Baseline																												
A-B	A-C	A-D	A-E	A-F	A-G	A-H	B-C	B-D	B-E	B-F	B-G	B-H	C-D	C-E	C-F	C-G	C-H	D-E	D-F	D-G	D-H	E-F	E-G	E-H	F-G	F-H	G-H	
RR	RR	RR	RR	RR	RR	RR	RR	RR	RR	RR	RR	RR	RR	RR	RR	RR	RR	RR	RR	RR	RR	RR	RR	RR	RR	RR	RR	
RR	RR	RL	RL	RL	RL	RL	RR	RL	RL	RL	RL	RL	RL	RL	RL	RL	RL	LL	LL	LL	LL	LL	LL	LL	LL	LL	LL	
LL	LL	LL	LL	LL	LR	LR	LL	LL	LL	LL	LR	LR	LL	LL	LR	LR	LL	LL	RR	RR	RL	RL	RR	RL	RL	RL	RR	
LL	LL	LR	LR	LR	LL	LL	LL	LR	LR	LR	LL	LL	LR	LR	LR	LL	LL	RR	RR	RL	RL	RR	LL	LL	LR	LL	LR	
LR	LR	LL	LR	LR	LR	LL	RR	RL	RR	RR	RR	RL	RL	RR	RR	RR	RL	LR	LR	LR	LL	RR	RR	RL	RR	RL	RL	
LR	LR	LL	LR	LR	LR	LL	RR	RL	RR	RR	RR	RL	RL	RR	RR	RR	RL	LR	LR	LR	LL	RR	RR	RL	RR	RL	RL	
RL	RL	RL	RR	RR	RL	RR	LL	LL	LR	LR	LL	LR	LL	LL	LR	LL	LR	LL	RL	RL	RR	RL	LL	LR	LL	LR	RR	
RL	RL	RR	RL	RL	RR	RL	LL	LR	LL	LL	LR	LL	LR	LL	LL	LR	LL	RL	RL	RR	RR	RR	LR	LR	LR	RR	RR	
LL	LR	LR	LL	LR	LR	LR	LR	LR	LL	LR	LR	LR	RR	RL	RR	RR	RR	RL	RR	RR	RR	RR	LR	LR	LR	RR	RR	
LL	LR	LL	LR	LL	LL	LL	LR	LL	LR	LL	LL	LL	RL	RR	RL	RL	RL	LR	LL	LL	LL	RL	RL	RL	LL	LL	LL	
RR	RL	RL	RR	RL	RR	RR	RL	RL	RR	RL	RR	RR	LL	LR	LL	LR	LR	LR	LR	LL	LR	LR	RL	RR	RR	LR	LR	RR
RR	RL	RR	RL	RR	RL	RL	RL	RR	RL	RR	RL	RL	LR	LL	LR	LL	LL	RL	RR	RL	RL	LR	LL	LL	RL	RL	LL	
RL	RR	RR	RR	RL	RL	RR	LR	LR	LR	LL	LL	LR	RR	RR	RL	RL	RR	RR	RL	RL	RR	RL	RL	RR	LL	LR	LR	
RL	RR	RL	RL	RR	RR	RL	LR	LL	LL	LR	LR	LL	RL	RL	RR	RR	RL	LL	LR	LR	LL	LR	LR	LL	RR	RL	RL	
LR	LL	LL	LL	LR	LL	LR	RL	RL	RL	RR	RL	RR	LL	LL	LR	LL	LR	LL	LR	LL	LR	LL	LR	LR	LL	LR	RR	
LR	LL	LR	LR	LL	LR	LL	RL	RR	RR	RL	RR	RL	LR	LR	LL	LR	LL	RR	RL	RR	RL	RL	RR	RL	LR	LL	RL	

Appendix C

2005 Sgr A* Light Curve Data

C.1 Raw Data

The following ten tables contain the raw data for the polarization light curves in Chapter 7 and the $Q-U$ tracks in the following section. The polarization quantities were measured as described in § 7.2. No position angle (χ) is reported for polarization samples where the polarization is not detected at 1.5σ .

Each table includes the polarization measured in every 16-step switching cycle on Sgr A* (4 and 5.5 minute averaging intervals in the 230 and 345 GHz bands, respectively). The average polarization properties of each track are reported in the last line.

Table C.1. Polarization data for 2005 June 4

UT Hour	Hour Angle	E (deg)	I (Jy)	Q (mJy)	U (mJy)	m (%)	χ (deg)
9.1172	-2.1162	32.4	4.744 ± 0.106	69.4 ± 33.6	-266.9 ± 38.0	5.76 ± 0.75	142.3 ± 3.5
9.1860	-2.0472	32.9	4.648 ± 0.085	7.5 ± 33.4	-292.5 ± 38.5	6.25 ± 0.77	135.7 ± 3.3
9.3294	-1.9034	33.9	4.723 ± 0.097	30.6 ± 29.9	-277.1 ± 28.4	5.87 ± 0.62	138.2 ± 3.1
9.4600	-1.7725	34.8	4.527 ± 0.107	-44.7 ± 32.0	-176.6 ± 34.0	3.96 ± 0.73	127.9 ± 5.1
10.1996	-1.0306	38.9	3.964 ± 0.081	235.9 ± 28.6	-126.8 ± 36.0	6.71 ± 0.81	165.9 ± 3.7
10.4368	-0.7933	39.8	3.936 ± 0.083	228.2 ± 39.6	-191.5 ± 23.1	7.53 ± 0.77	160.0 ± 3.0
10.6062	-0.6230	40.3	3.639 ± 0.111	78.2 ± 38.6	-97.0 ± 28.1	3.30 ± 0.91	154.4 ± 8.0
10.7325	-0.4964	40.6	3.652 ± 0.075	115.2 ± 27.8	-215.9 ± 29.1	6.66 ± 0.78	149.0 ± 3.3
10.8827	-0.3454	40.9	3.949 ± 0.060	42.3 ± 23.0	-127.5 ± 22.2	3.35 ± 0.57	144.2 ± 4.9
11.6450	0.4189	40.8	3.503 ± 0.096	72.3 ± 27.0	-220.0 ± 29.1	6.56 ± 0.80	144.1 ± 3.4
11.7968	0.5699	40.5	3.598 ± 0.069	89.6 ± 26.0	-187.1 ± 22.9	5.72 ± 0.68	147.8 ± 3.5
11.9487	0.7230	40.1	3.806 ± 0.077	105.7 ± 24.0	-146.7 ± 25.4	4.71 ± 0.65	152.9 ± 3.9
12.1194	0.8941	39.5	3.798 ± 0.073	59.3 ± 26.3	-141.2 ± 19.5	3.99 ± 0.60	146.4 ± 4.8
12.2662	1.0415	38.9	3.985 ± 0.067	36.4 ± 25.2	-27.8 ± 25.3	0.96 ± 0.63
12.4143	1.1904	38.2	3.435 ± 0.086	-55.2 ± 27.1	-42.1 ± 29.1	1.85 ± 0.82	108.7 ± 11.7
10.8984	-0.3301	...	3.956 ± 0.028	73.9 ± 8.3	-164.5 ± 7.9	4.55 ± 0.20	147.1 ± 1.3

Table C.2. Polarization data for 2005 June 6

UT Hour	Hour Angle	E (deg)	I (Jy)	Q (mJy)	U (mJy)	m (%)	χ (deg)
7.7290	-3.3702	21.0	3.747 ± 0.128	262.0 ± 81.7	-181.4 ± 92.9	8.18 ± 2.33	162.6 ± 8.0
7.9943	-3.1028	23.7	3.658 ± 0.107	-17.0 ± 81.6	-374.0 ± 97.2	9.94 ± 2.44	133.7 ± 6.2
8.3569	-2.7390	27.1	3.819 ± 0.083	44.7 ± 93.5	-354.5 ± 75.6	9.09 ± 2.20	138.6 ± 7.5
8.5265	-2.5729	28.6	3.730 ± 0.076	-8.0 ± 62.0	-444.0 ± 63.0	11.79 ± 1.68	134.5 ± 4.0
8.9801	-2.1143	32.4	3.613 ± 0.117	163.0 ± 71.3	-229.5 ± 64.6	7.56 ± 1.88	152.7 ± 7.0
9.1500	-1.9467	33.6	3.544 ± 0.090	135.1 ± 53.4	-70.6 ± 68.1	3.95 ± 1.70	166.2 ± 12.3
9.6008	-1.4916	36.6	3.434 ± 0.101	120.1 ± 65.0	-239.7 ± 49.8	7.63 ± 1.66	148.3 ± 6.6
9.7716	-1.3241	37.5	3.414 ± 0.117	132.3 ± 52.9	-254.9 ± 65.1	8.24 ± 1.72	148.7 ± 5.6
10.3123	-0.7783	39.9	3.942 ± 0.119	118.8 ± 50.7	-102.3 ± 49.1	3.77 ± 1.27	159.6 ± 9.1
10.4836	-0.6093	40.4	3.690 ± 0.155	218.4 ± 46.2	-235.3 ± 54.9	8.59 ± 1.36	156.4 ± 4.5
10.6370	-0.4526	40.7	3.774 ± 0.134	53.8 ± 48.2	-208.0 ± 55.5	5.53 ± 1.37	142.3 ± 6.5
10.8337	-0.2506	41.0	3.803 ± 0.170	146.3 ± 65.0	-240.0 ± 57.5	7.21 ± 1.61	150.7 ± 6.4
11.0094	-0.0823	41.2	4.459 ± 0.114	81.5 ± 69.2	-169.0 ± 62.4	3.94 ± 1.47	147.9 ± 10.4
11.1635	0.0751	41.2	4.210 ± 0.089	33.4 ± 66.2	-133.0 ± 64.7	2.86 ± 1.55
11.3339	0.2433	41.0	4.208 ± 0.089	38.0 ± 53.2	-66.3 ± 67.7	1.13 ± 1.43
11.4876	0.4001	40.8	4.348 ± 0.106	43.0 ± 51.0	-5.8 ± 76.1	0.00 ± 1.43
11.6582	0.5683	40.5	4.497 ± 0.110	163.6 ± 58.7	-149.2 ± 62.2	4.74 ± 1.34	158.8 ± 7.8
11.8115	0.7250	40.1	4.474 ± 0.091	143.1 ± 64.6	-98.6 ± 60.0	3.63 ± 1.39	162.7 ± 10.1
12.0931	1.0076	39.0	4.750 ± 0.093	233.4 ± 62.6	-412.9 ± 67.2	9.89 ± 1.37	149.7 ± 3.9
12.2632	1.1751	38.3	4.747 ± 0.115	69.2 ± 52.5	-419.1 ± 69.8	8.86 ± 1.28	139.7 ± 3.6
12.5421	1.4576	36.8	4.660 ± 0.094	263.4 ± 61.4	-349.8 ± 55.8	9.31 ± 1.26	153.5 ± 3.9
12.7178	1.6338	35.7	4.758 ± 0.090	8.6 ± 66.4	-315.2 ± 73.8	6.46 ± 1.47	135.8 ± 6.0
13.0044	1.9214	33.8	4.637 ± 0.102	261.2 ± 64.7	-112.7 ± 64.7	5.97 ± 1.40	168.3 ± 6.5
13.1731	2.0874	32.6	5.041 ± 0.109	46.2 ± 63.3	54.6 ± 75.2	0.38 ± 1.37
13.4503	2.3685	30.3	4.914 ± 0.140	61.4 ± 69.4	-263.2 ± 60.9	5.34 ± 1.32	141.6 ± 7.3
13.6196	2.5346	28.9	4.829 ± 0.117	-151.8 ± 91.4	-128.8 ± 68.9	3.78 ± 1.64	110.2 ± 11.4
13.8957	2.8150	26.4	4.307 ± 0.130	122.7 ± 81.9	-236.6 ± 72.0	5.92 ± 1.78	148.7 ± 8.6
14.0643	2.9811	24.8	4.171 ± 0.156	92.0 ± 72.4	-136.0 ± 64.8	3.58 ± 1.64	152.0 ± 12.2
14.3341	3.2543	22.2	4.052 ± 0.132	110.4 ± 89.6	3.3 ± 78.1	1.78 ± 2.06
14.5022	3.4204	20.5	3.751 ± 0.120	288.1 ± 78.3	-114.6 ± 82.1	7.98 ± 2.14	169.2 ± 7.5
11.5113	0.4229	...	4.182 ± 0.024	109.9 ± 12.5	-195.3 ± 12.7	5.35 ± 0.30	149.7 ± 1.6

Table C.3. Polarization data for 2005 June 9

UT Hour	Hour Angle	E (deg)	I (Jy)	Q (mJy)	U (mJy)	m (%)	χ (deg)
7.6864	-3.2210	22.5	3.188 ± 0.074	-220.9 ± 68.3	-39.8 ± 48.9	6.80 ± 1.81	95.1 ± 6.3
7.9058	-3.0031	24.6	3.011 ± 0.142	-262.9 ± 42.7	49.6 ± 57.8	8.73 ± 1.65	84.7 ± 6.1
8.5124	-2.3942	30.1	2.998 ± 0.090	-278.1 ± 33.2	-17.7 ± 28.7	9.24 ± 1.03	91.8 ± 3.0
8.7413	-2.1648	32.0	3.152 ± 0.062	-333.7 ± 30.8	-8.0 ± 36.0	10.54 ± 1.06	90.7 ± 3.1
8.8964	-2.0088	33.2	3.308 ± 0.061	-322.0 ± 34.5	28.3 ± 39.3	9.71 ± 1.11	87.5 ± 3.5
9.0862	-1.8190	34.5	3.293 ± 0.069	-283.2 ± 31.6	-5.4 ± 34.9	8.54 ± 1.01	90.5 ± 3.5
9.2304	-1.6745	35.5	3.230 ± 0.052	-262.1 ± 27.4	5.8 ± 34.8	8.06 ± 0.96	89.4 ± 3.8
9.3750	-1.5300	36.4	3.324 ± 0.059	-302.5 ± 27.1	46.5 ± 23.3	9.18 ± 0.76	85.6 ± 2.2
9.5132	-1.3905	37.2	3.314 ± 0.051	-434.6 ± 26.2	-17.6 ± 31.4	13.10 ± 0.87	91.2 ± 2.1
9.6532	-1.2511	37.9	3.354 ± 0.065	-433.1 ± 32.4	11.6 ± 30.7	12.88 ± 0.94	89.2 ± 2.0
9.7933	-1.1108	38.6	3.391 ± 0.063	-358.0 ± 26.3	27.5 ± 27.6	10.56 ± 0.79	87.8 ± 2.2
9.9317	-0.9721	39.2	3.326 ± 0.084	-323.1 ± 31.2	43.7 ± 38.8	9.75 ± 1.05	86.2 ± 3.4
10.0688	-0.8334	39.7	3.294 ± 0.059	-167.4 ± 28.4	4.2 ± 23.9	5.02 ± 0.79	89.3 ± 4.1
10.2075	-0.6946	40.1	3.381 ± 0.056	-172.1 ± 24.2	-54.6 ± 22.9	5.29 ± 0.70	98.8 ± 3.6
10.3454	-0.5558	40.5	3.302 ± 0.078	-158.8 ± 27.1	-137.5 ± 28.7	6.30 ± 0.84	110.4 ± 3.8
10.5048	-0.3963	40.8	3.357 ± 0.056	-238.2 ± 27.0	-148.6 ± 26.3	8.32 ± 0.80	106.0 ± 2.7
10.6800	-0.2208	41.1	3.265 ± 0.058	-148.3 ± 29.1	-51.3 ± 22.9	4.74 ± 0.79	99.5 ± 4.3
10.8178	-0.0828	41.2	3.209 ± 0.046	-116.8 ± 19.3	-64.2 ± 21.8	4.10 ± 0.64	104.4 ± 4.6
10.9550	0.0553	41.2	3.222 ± 0.054	-90.4 ± 25.4	-112.8 ± 26.0	4.42 ± 0.80	115.7 ± 5.1
11.1040	0.2041	41.1	3.188 ± 0.053	-110.3 ± 31.1	-120.4 ± 28.1	5.04 ± 0.93	113.8 ± 5.2
11.4559	0.5578	40.5	3.376 ± 0.071	-172.6 ± 27.4	-91.7 ± 26.3	5.74 ± 0.80	104.0 ± 3.9
11.6592	0.7613	39.9	3.441 ± 0.061	-249.7 ± 31.1	-41.7 ± 27.0	7.31 ± 0.84	94.7 ± 3.1
11.8570	0.9597	39.2	3.548 ± 0.089	-326.0 ± 26.1	48.3 ± 31.3	9.25 ± 0.81	85.8 ± 2.7
12.0538	1.1567	38.4	3.687 ± 0.084	-300.7 ± 32.1	117.1 ± 28.2	8.71 ± 0.82	79.4 ± 2.6
12.2490	1.3538	37.4	3.745 ± 0.092	-205.3 ± 31.1	189.0 ± 25.1	7.41 ± 0.74	68.7 ± 2.9
12.4462	1.5506	36.3	4.006 ± 0.072	-265.6 ± 39.2	231.4 ± 32.9	8.75 ± 0.90	69.5 ± 2.9
12.6889	1.7937	34.7	3.769 ± 0.105	-229.5 ± 21.6	112.6 ± 25.2	6.75 ± 0.62	76.9 ± 2.7
12.8124	1.9173	33.8	3.670 ± 0.111	-220.0 ± 30.0	185.5 ± 35.6	7.79 ± 0.89	69.9 ± 3.3
13.1101	2.2157	31.6	3.628 ± 0.072	-173.5 ± 33.3	15.1 ± 31.6	4.72 ± 0.89	87.5 ± 5.2
13.2330	2.3393	30.6	3.637 ± 0.081	-186.8 ± 39.2	24.6 ± 31.3	5.09 ± 0.96	86.2 ± 4.8
13.4592	2.5665	28.6	3.773 ± 0.068	-135.3 ± 40.6	68.0 ± 35.3	3.89 ± 1.00	76.7 ± 6.9
13.5829	2.6894	27.6	3.821 ± 0.068	-136.4 ± 34.5	18.1 ± 38.5	3.47 ± 0.95	86.2 ± 8.0
10.9114	0.0113	...	3.432 ± 0.015	-234.2 ± 6.0	10.5 ± 6.0	6.83 ± 0.18	88.7 ± 0.7

Table C.4. Polarization data for 2005 June 15

UT Hour	Hour Angle	E (deg)	I (Jy)	Q (mJy)	U (mJy)	m (%)	χ (deg)
7.1279	-3.3778	20.9	2.854 ± 0.125	176.0 ± 84.7	-190.6 ± 107.5	8.45 ± 3.34	156.4 ± 10.6
7.2847	-3.2197	22.5	2.896 ± 0.114	33.0 ± 80.5	-167.2 ± 87.7	5.12 ± 2.90	140.6 ± 13.6
8.1242	-2.3799	30.2	3.151 ± 0.105	-27.1 ± 80.4	-109.5 ± 61.8	2.79 ± 2.24	128.1 ± 20.2
8.2960	-2.2059	31.7	3.255 ± 0.100	-22.8 ± 64.0	-204.9 ± 63.9	6.02 ± 1.96	131.8 ± 8.9
8.4789	-2.0226	33.1	3.461 ± 0.104	-106.3 ± 53.0	-304.7 ± 55.6	9.19 ± 1.57	125.4 ± 4.7
8.6423	-1.8587	34.2	3.585 ± 0.109	-307.6 ± 57.3	-319.1 ± 60.3	12.25 ± 1.64	113.0 ± 3.8
8.8008	-1.6998	35.3	3.705 ± 0.101	-319.3 ± 49.5	-150.3 ± 43.2	9.44 ± 1.25	102.6 ± 3.6
8.9592	-1.5409	36.3	3.708 ± 0.109	-215.6 ± 63.9	-76.4 ± 53.5	5.96 ± 1.58	99.8 ± 6.9
9.1180	-1.3821	37.2	3.592 ± 0.092	-37.4 ± 45.2	-185.1 ± 57.3	5.06 ± 1.42	129.3 ± 6.9
9.2761	-1.2231	38.1	3.289 ± 0.076	-1.1 ± 56.2	-431.7 ± 52.5	13.02 ± 1.65	134.9 ± 3.7
9.4346	-1.0642	38.8	3.232 ± 0.078	-62.7 ± 53.1	-268.5 ± 49.6	8.38 ± 1.59	128.4 ± 5.5
9.5931	-0.9054	39.4	3.272 ± 0.098	0.6 ± 55.0	-259.8 ± 57.4	7.75 ± 1.72	135.1 ± 6.1
9.7516	-0.7465	40.0	3.211 ± 0.074	-35.9 ± 51.5	-123.6 ± 53.7	3.66 ± 1.64	126.9 ± 11.5
9.9092	-0.5883	40.4	3.386 ± 0.097	65.8 ± 43.3	-155.4 ± 48.1	4.80 ± 1.35	146.5 ± 7.5
10.0677	-0.4294	40.8	3.181 ± 0.085	62.1 ± 44.9	-164.1 ± 48.0	5.32 ± 1.46	145.4 ± 7.4
10.2261	-0.2705	41.0	3.314 ± 0.077	-27.9 ± 54.4	-218.6 ± 50.0	6.46 ± 1.57	131.4 ± 7.1
10.3853	-0.1109	41.1	3.401 ± 0.086	88.1 ± 48.8	-71.8 ± 69.1	2.87 ± 1.71	160.4 ± 15.6
10.5430	0.0473	41.2	3.180 ± 0.103	33.0 ± 56.1	-27.9 ± 48.6	0.00 ± 1.64
10.7022	0.2068	41.1	3.431 ± 0.092	37.9 ± 45.2	42.7 ± 50.1	0.92 ± 1.39
10.8607	0.3657	40.9	3.549 ± 0.085	62.3 ± 48.5	-159.5 ± 45.6	4.64 ± 1.32	145.7 ± 8.1
11.0191	0.5246	40.6	3.824 ± 0.087	11.6 ± 46.3	-48.4 ± 50.9	0.29 ± 1.27
11.5877	1.0833	38.7	3.411 ± 0.095	-130.3 ± 48.5	-56.5 ± 50.3	3.90 ± 1.45	101.7 ± 10.1
11.7375	1.2450	37.9	3.201 ± 0.089	-149.3 ± 39.9	-78.9 ± 42.3	5.12 ± 1.28	103.9 ± 7.1
12.0179	1.5261	36.4	3.031 ± 0.066	10.4 ± 42.5	-150.8 ± 35.9	4.82 ± 1.29	137.0 ± 8.0
12.1740	1.6829	35.4	2.991 ± 0.083	39.2 ± 47.2	-241.1 ± 54.7	7.99 ± 1.70	139.6 ± 5.6
12.4681	1.9776	33.4	3.156 ± 0.074	17.1 ± 63.6	-177.3 ± 49.5	5.36 ± 1.78	137.8 ± 10.2
12.6245	2.1343	32.2	3.074 ± 0.096	14.1 ± 47.9	-262.4 ± 49.2	8.40 ± 1.58	136.5 ± 5.2
12.9040	2.4147	30.0	3.382 ± 0.093	123.2 ± 75.8	-258.9 ± 63.3	8.23 ± 2.05	147.7 ± 7.4
13.0603	2.5715	28.6	3.335 ± 0.089	176.2 ± 53.8	-279.7 ± 52.6	9.78 ± 1.60	151.1 ± 4.6
13.3399	2.8518	26.1	3.228 ± 0.083	396.9 ± 66.0	-131.6 ± 68.3	12.79 ± 2.08	170.8 ± 4.7
13.4963	3.0085	24.6	3.060 ± 0.078	379.9 ± 57.0	-91.8 ± 68.8	12.61 ± 2.05	173.2 ± 5.0
13.7787	3.2918	21.8	3.440 ± 0.089	470.2 ± 68.2	-202.7 ± 70.7	14.75 ± 2.02	168.3 ± 3.9
13.9349	3.4485	20.2	3.515 ± 0.097	547.6 ± 66.6	-244.9 ± 80.3	16.94 ± 2.08	167.9 ± 3.7
10.6226	0.1266	...	3.317 ± 0.017	37.0 ± 10.8	-173.8 ± 10.2	5.35 ± 0.32	141.0 ± 1.7

Table C.5. Polarization data for 2005 June 16

UT Hour	Hour Angle	E (deg)	I (Jy)	Q (mJy)	U (mJy)	m (%)	χ (deg)
7.2310	-3.2189	22.5	3.580 ± 0.049	-331.2 ± 33.9	-198.4 ± 41.6	10.73 ± 1.05	105.5 ± 2.9
7.4237	-3.0259	24.4	3.695 ± 0.084	-344.2 ± 47.5	-220.0 ± 46.7	10.98 ± 1.27	106.3 ± 3.3
7.5146	-2.9346	25.3	3.853 ± 0.097	-285.4 ± 50.1	-158.8 ± 30.4	8.42 ± 1.01	104.5 ± 3.2
7.6537	-2.7951	26.6	3.633 ± 0.099	-219.0 ± 49.8	-174.2 ± 41.7	7.60 ± 1.25	109.2 ± 4.6
7.7435	-2.7045	27.4	3.730 ± 0.104	-301.1 ± 34.8	-140.2 ± 54.2	8.83 ± 1.17	102.5 ± 4.4
7.9575	-2.4903	29.3	3.569 ± 0.111	-249.6 ± 37.6	-252.6 ± 48.3	9.88 ± 1.19	112.7 ± 3.5
8.0505	-2.3989	30.1	3.688 ± 0.129	-276.9 ± 42.6	-134.8 ± 33.6	8.29 ± 1.02	103.0 ± 3.3
8.2320	-2.2157	31.6	3.531 ± 0.114	-169.1 ± 36.7	-121.7 ± 29.2	5.83 ± 0.93	107.9 ± 4.4
8.3241	-2.1229	32.3	3.448 ± 0.121	-175.8 ± 25.2	-117.7 ± 30.0	6.08 ± 0.80	106.9 ± 3.9
8.4595	-1.9870	33.3	3.398 ± 0.130	-159.2 ± 28.3	-110.8 ± 27.0	5.65 ± 0.81	107.4 ± 4.1
8.5508	-1.8957	34.0	3.401 ± 0.119	-187.6 ± 30.7	-192.4 ± 27.3	7.86 ± 0.85	112.9 ± 3.1
8.8519	-1.5866	36.0	3.736 ± 0.146	-168.4 ± 32.8	-96.0 ± 38.5	5.10 ± 0.95	104.8 ± 5.5
8.9494	-1.4946	36.6	4.422 ± 0.105	-176.1 ± 61.6	-150.8 ± 33.2	5.14 ± 1.02	110.3 ± 5.8
9.0848	-1.3601	37.3	4.385 ± 0.167	-211.9 ± 29.9	-95.3 ± 35.6	5.25 ± 0.74	102.1 ± 4.3
9.1766	-1.2681	37.8	4.280 ± 0.139	-114.9 ± 27.8	-44.8 ± 32.4	2.80 ± 0.70	100.7 ± 7.4
9.3099	-1.1344	38.5	4.372 ± 0.133	-7.7 ± 39.4	-45.0 ± 41.6	0.48 ± 0.93
9.4012	-1.0431	38.9	4.259 ± 0.148	62.7 ± 33.3	-0.8 ± 28.4	1.28 ± 0.72
9.5351	-0.9086	39.4	4.343 ± 0.151	-13.2 ± 36.5	-62.4 ± 36.8	1.20 ± 0.84
9.6261	-0.8173	39.8	4.296 ± 0.146	9.2 ± 36.3	-90.7 ± 33.6	1.96 ± 0.81	137.9 ± 11.4
9.7595	-0.6836	40.2	4.145 ± 0.143	37.3 ± 35.1	-94.0 ± 31.8	2.30 ± 0.81	145.8 ± 9.8
9.8505	-0.5923	40.4	4.047 ± 0.150	32.1 ± 29.0	-103.0 ± 29.1	2.57 ± 0.72	143.7 ± 7.7
9.9832	-0.4593	40.7	4.098 ± 0.144	1.5 ± 30.6	-140.6 ± 29.2	3.35 ± 0.73	135.3 ± 6.2
10.0746	-0.3673	40.9	4.086 ± 0.174	-30.6 ± 33.7	-156.4 ± 25.9	3.83 ± 0.72	129.5 ± 6.0
10.2075	-0.2343	41.0	3.997 ± 0.165	-33.0 ± 29.8	-159.3 ± 42.0	3.97 ± 0.89	129.1 ± 5.4
10.2996	-0.1422	41.1	4.032 ± 0.144	-11.1 ± 38.2	-200.1 ± 33.0	4.89 ± 0.88	133.4 ± 5.5
10.4314	-0.0099	41.2	4.206 ± 0.170	-85.7 ± 31.4	-151.9 ± 31.4	4.08 ± 0.75	120.3 ± 5.2
10.5230	0.0821	41.2	4.156 ± 0.146	17.8 ± 30.0	-184.0 ± 30.0	4.39 ± 0.72	137.8 ± 4.7
10.6551	0.2144	41.1	4.159 ± 0.152	2.8 ± 27.7	-193.6 ± 30.5	4.60 ± 0.70	135.4 ± 4.1
10.7460	0.3058	41.0	4.040 ± 0.143	14.2 ± 38.4	-230.3 ± 35.8	5.64 ± 0.92	136.8 ± 4.8
10.8778	0.4379	40.8	4.105 ± 0.146	7.6 ± 36.3	-298.8 ± 25.5	7.24 ± 0.74	135.7 ± 3.5
10.9692	0.5292	40.6	4.100 ± 0.156	-41.8 ± 27.6	-252.8 ± 35.5	6.20 ± 0.76	130.3 ± 3.1
11.1011	0.6615	40.2	4.161 ± 0.148	-23.2 ± 37.0	-192.2 ± 32.8	4.58 ± 0.84	131.6 ± 5.5
11.1920	0.7528	40.0	4.099 ± 0.134	-75.2 ± 35.2	-237.0 ± 39.1	6.00 ± 0.90	126.2 ± 4.1
11.6473	1.2094	38.1	3.353 ± 0.137	-64.7 ± 29.7	-191.4 ± 28.1	5.96 ± 0.86	125.7 ± 4.2
11.7365	1.2999	37.7	3.391 ± 0.129	-52.2 ± 25.1	-246.2 ± 28.7	7.38 ± 0.79	129.0 ± 2.9
12.0324	1.5954	36.0	3.470 ± 0.124	-148.3 ± 29.5	-246.7 ± 28.8	8.25 ± 0.84	119.5 ± 2.9
12.1227	1.6860	35.4	3.451 ± 0.119	-134.0 ± 25.6	-208.7 ± 26.2	7.15 ± 0.75	118.7 ± 3.0
12.3829	1.9470	33.6	3.519 ± 0.116	-191.4 ± 26.8	-303.1 ± 28.7	10.16 ± 0.79	118.9 ± 2.2
12.4728	2.0376	33.0	3.518 ± 0.091	-190.1 ± 30.0	-224.3 ± 30.2	8.31 ± 0.86	114.9 ± 2.9
12.7334	2.2985	30.9	3.639 ± 0.110	-141.3 ± 29.5	-323.8 ± 28.6	9.68 ± 0.80	123.2 ± 2.4
12.8238	2.3891	30.2	3.675 ± 0.103	-223.6 ± 27.2	-335.7 ± 30.7	10.95 ± 0.79	118.2 ± 2.0
13.0825	2.6487	27.9	3.683 ± 0.109	-109.5 ± 27.1	-274.3 ± 23.5	7.99 ± 0.69	124.1 ± 2.6
13.1718	2.7392	27.1	3.714 ± 0.109	-106.2 ± 27.8	-264.9 ± 23.6	7.65 ± 0.69	124.1 ± 2.7
13.6721	3.2411	22.3	3.398 ± 0.077	-46.0 ± 38.6	-169.1 ± 32.8	5.05 ± 1.05	127.4 ± 6.3
13.7645	3.3324	21.4	3.412 ± 0.084	-136.9 ± 32.0	-87.2 ± 35.5	4.65 ± 0.99	106.3 ± 6.1
10.3530	-0.0883	...	3.862 ± 0.022	-101.1 ± 5.7	-176.4 ± 5.4	5.26 ± 0.14	120.1 ± 0.8

Table C.6. Polarization data for 2005 June 17

UT Hour	Hour Angle	E (deg)	I (Jy)	Q (mJy)	U (mJy)	m (%)	χ (deg)
6.9988	-3.3754	20.9	2.560 ± 0.103	248.8 ± 82.8	-133.9 ± 84.5	10.54 ± 3.27	165.9 ± 8.5
7.1550	-3.2186	22.5	2.653 ± 0.087	223.5 ± 67.2	-144.4 ± 84.1	9.62 ± 2.83	163.6 ± 8.6
7.7162	-2.6557	27.9	2.517 ± 0.062	118.3 ± 59.5	-252.7 ± 64.4	10.81 ± 2.46	147.5 ± 6.2
7.8728	-2.4989	29.2	2.579 ± 0.063	223.3 ± 53.0	-354.9 ± 60.3	16.11 ± 2.19	151.1 ± 3.8
8.2347	-2.1359	32.2	2.730 ± 0.066	223.2 ± 56.2	-524.8 ± 58.9	20.78 ± 2.11	146.5 ± 2.8
8.3911	-1.9792	33.4	2.666 ± 0.057	89.8 ± 55.0	-355.4 ± 54.6	13.60 ± 2.06	142.1 ± 4.3
8.5472	-1.8225	34.5	2.713 ± 0.084	97.4 ± 54.7	-446.4 ± 44.5	16.74 ± 1.82	141.2 ± 3.4
8.7036	-1.6658	35.5	2.562 ± 0.086	95.0 ± 64.5	-388.8 ± 71.8	15.39 ± 2.65	141.9 ± 4.6
8.8922	-1.4767	36.7	2.913 ± 0.080	54.0 ± 54.1	-352.7 ± 65.3	12.08 ± 2.04	139.3 ± 4.4
9.0504	-1.3192	37.6	3.128 ± 0.073	175.4 ± 56.4	-234.4 ± 48.1	9.21 ± 1.67	153.4 ± 5.2
9.2063	-1.1618	38.4	2.911 ± 0.091	177.5 ± 47.2	-233.2 ± 44.3	9.95 ± 1.57	153.6 ± 4.5
9.3633	-1.0043	39.0	3.284 ± 0.078	106.3 ± 50.1	-178.1 ± 54.2	6.11 ± 1.59	150.4 ± 7.1
9.5204	-0.8469	39.7	3.198 ± 0.070	223.2 ± 48.9	-209.7 ± 42.5	9.47 ± 1.43	158.4 ± 4.3
9.6779	-0.6887	40.2	3.067 ± 0.086	233.9 ± 52.5	-215.3 ± 50.8	10.23 ± 1.69	158.7 ± 4.7
9.8350	-0.5313	40.6	3.228 ± 0.068	267.1 ± 39.4	-255.1 ± 51.6	11.36 ± 1.40	158.2 ± 3.6
9.9920	-0.3738	40.9	3.293 ± 0.089	160.8 ± 40.2	-298.6 ± 39.3	10.23 ± 1.21	149.2 ± 3.4
10.1489	-0.2164	41.1	3.314 ± 0.066	108.4 ± 52.8	-295.6 ± 57.6	9.36 ± 1.66	145.1 ± 4.9
10.3061	-0.0589	41.2	3.402 ± 0.065	89.3 ± 44.5	-305.6 ± 49.3	9.26 ± 1.38	143.1 ± 4.0
10.4631	0.0985	41.1	3.377 ± 0.060	110.1 ± 53.2	-286.0 ± 55.9	8.93 ± 1.61	145.5 ± 5.0
10.6201	0.2560	41.0	3.478 ± 0.064	82.3 ± 52.8	-251.8 ± 36.5	7.51 ± 1.26	144.0 ± 5.6
10.7771	0.4134	40.8	3.488 ± 0.074	82.0 ± 42.0	-310.1 ± 44.7	9.11 ± 1.24	142.4 ± 3.8
11.0510	0.6881	40.2	3.159 ± 0.065	-2.3 ± 43.6	-250.1 ± 44.7	7.79 ± 1.40	134.7 ± 5.0
11.2080	0.8455	39.7	3.236 ± 0.091	148.6 ± 46.3	-182.4 ± 40.6	7.15 ± 1.34	154.6 ± 5.4
11.4899	1.1259	38.5	3.111 ± 0.083	158.9 ± 50.3	-193.1 ± 52.8	7.86 ± 1.66	154.7 ± 5.9
11.6439	1.2826	37.8	3.208 ± 0.072	18.6 ± 52.1	-310.2 ± 44.9	9.57 ± 1.51	136.7 ± 4.8
12.0139	1.6536	35.6	3.034 ± 0.066	-49.5 ± 41.9	-171.0 ± 42.0	5.70 ± 1.38	126.9 ± 6.7
12.2032	1.8434	34.4	2.864 ± 0.065	-13.7 ± 54.9	-205.8 ± 40.8	7.01 ± 1.65	133.1 ± 7.6
12.4993	2.1403	32.2	2.638 ± 0.050	124.8 ± 43.9	-56.8 ± 46.8	4.91 ± 1.72	167.7 ± 9.7
12.6556	2.2970	30.9	2.788 ± 0.048	-38.0 ± 50.3	-100.1 ± 41.5	3.47 ± 1.64	124.6 ± 13.2
13.1123	2.7550	27.0	2.954 ± 0.095	265.3 ± 58.1	-179.4 ± 61.2	10.65 ± 2.02	163.0 ± 5.4
13.2679	2.9110	25.5	3.012 ± 0.073	183.8 ± 59.9	-221.1 ± 65.8	9.32 ± 2.08	154.9 ± 6.2
13.5382	3.1822	22.9	2.448 ± 0.077	155.5 ± 60.7	-264.0 ± 58.6	12.28 ± 2.44	150.2 ± 5.6
13.6940	3.3381	21.3	2.343 ± 0.082	118.2 ± 59.7	-182.1 ± 59.9	8.91 ± 2.55	151.5 ± 7.9
10.3540	-0.0110	...	2.986 ± 0.015	128.6 ± 9.3	-251.9 ± 9.5	9.47 ± 0.32	148.5 ± 0.9

Table C.7. Polarization data for 2005 July 20

UT Hour	Hour Angle	E (deg)	I (Jy)	Q (mJy)	U (mJy)	m (%)	χ (deg)
6.1872	-2.0318	33.0	3.751 ± 0.058	-32.9 ± 31.0	-214.8 ± 34.3	5.73 ± 0.87	130.6 ± 4.1
6.3336	-1.8851	34.1	3.748 ± 0.079	-81.6 ± 26.1	-215.9 ± 24.7	6.12 ± 0.68	124.6 ± 3.2
6.4237	-1.7944	34.7	3.688 ± 0.055	-91.7 ± 29.4	-249.1 ± 24.6	7.16 ± 0.73	124.9 ± 3.1
6.5135	-1.7039	35.3	3.788 ± 0.073	-121.9 ± 25.4	-138.1 ± 25.0	4.82 ± 0.67	114.3 ± 3.9
6.7917	-1.4257	37.0	3.726 ± 0.069	-151.6 ± 29.0	-165.3 ± 21.2	5.98 ± 0.67	113.7 ± 3.3
6.9659	-1.2510	37.9	3.639 ± 0.053	-4.5 ± 21.5	-127.2 ± 23.8	3.44 ± 0.62	134.0 ± 4.8
7.4342	-0.7808	39.9	3.849 ± 0.055	-8.4 ± 24.3	-111.7 ± 22.3	2.85 ± 0.60	132.9 ± 6.2
7.5807	-0.6341	40.3	4.031 ± 0.049	-59.6 ± 22.0	-113.5 ± 18.2	3.14 ± 0.50	121.2 ± 4.7
7.7141	-0.5004	40.6	3.959 ± 0.045	-37.1 ± 19.1	-67.6 ± 18.3	1.89 ± 0.47	120.6 ± 7.0
7.8051	-0.4091	40.8	3.979 ± 0.060	27.8 ± 23.1	-110.1 ± 25.1	2.79 ± 0.60	142.1 ± 5.9
7.9378	-0.2761	41.0	4.092 ± 0.042	47.4 ± 21.7	-180.8 ± 21.6	4.54 ± 0.53	142.3 ± 3.3
8.0690	-0.1445	41.1	4.040 ± 0.053	45.9 ± 24.0	-208.7 ± 27.6	5.25 ± 0.64	141.2 ± 3.2
8.2015	-0.0116	41.2	4.079 ± 0.055	-13.8 ± 21.8	-220.9 ± 14.9	5.41 ± 0.44	133.2 ± 2.8
8.3335	0.1207	41.1	4.160 ± 0.049	11.8 ± 21.0	-158.1 ± 22.4	3.78 ± 0.52	137.1 ± 3.8
8.4647	0.2524	41.0	4.046 ± 0.044	-77.3 ± 19.8	-182.2 ± 20.2	4.87 ± 0.49	123.5 ± 2.9
8.5963	0.3838	40.9	3.924 ± 0.044	-50.8 ± 22.8	-172.2 ± 18.6	4.54 ± 0.53	126.8 ± 3.6
8.7264	0.5147	40.6	3.904 ± 0.071	-20.5 ± 21.4	-184.9 ± 20.1	4.74 ± 0.53	131.8 ± 3.3
8.8575	0.6456	40.3	3.997 ± 0.065	-1.1 ± 21.6	-183.9 ± 19.4	4.57 ± 0.51	134.8 ± 3.4
9.1133	0.9029	39.4	4.143 ± 0.050	43.8 ± 17.8	-181.5 ± 22.3	4.48 ± 0.48	141.8 ± 2.8
9.2045	0.9942	39.1	3.984 ± 0.061	29.7 ± 20.1	-149.7 ± 20.6	3.80 ± 0.51	140.6 ± 3.8
9.4670	1.2574	37.9	4.042 ± 0.059	48.2 ± 19.7	-171.5 ± 20.5	4.38 ± 0.50	142.8 ± 3.2
9.5580	1.3487	37.4	3.966 ± 0.066	24.8 ± 20.1	-184.2 ± 16.3	4.66 ± 0.46	138.8 ± 3.1
9.9633	1.7549	35.0	3.396 ± 0.088	-31.2 ± 19.7	-123.9 ± 24.6	3.71 ± 0.65	127.9 ± 4.5
10.0527	1.8447	34.3	3.586 ± 0.065	11.2 ± 19.0	-124.5 ± 23.8	3.44 ± 0.59	137.6 ± 4.4
10.3165	2.1093	32.4	3.437 ± 0.068	87.1 ± 20.9	-193.7 ± 19.8	6.15 ± 0.59	147.1 ± 2.8
10.4076	2.1999	31.7	3.365 ± 0.070	88.2 ± 23.1	-167.4 ± 24.6	5.58 ± 0.71	148.9 ± 3.5
10.6665	2.4602	29.6	3.436 ± 0.054	27.1 ± 25.0	-155.6 ± 20.9	4.55 ± 0.67	139.9 ± 4.5
10.7813	2.5752	28.6	3.417 ± 0.072	17.7 ± 26.0	-201.5 ± 18.1	5.89 ± 0.63	137.5 ± 3.7
11.0408	2.8354	26.2	3.298 ± 0.088	32.3 ± 22.4	-204.6 ± 34.0	6.22 ± 0.84	139.5 ± 3.1
11.1312	2.9267	25.4	3.533 ± 0.067	15.3 ± 33.2	-186.9 ± 34.8	5.22 ± 0.96	137.3 ± 5.1
11.3848	3.1805	22.9	3.450 ± 0.082	38.4 ± 36.6	-244.4 ± 27.8	7.11 ± 0.93	139.5 ± 4.2
11.4763	3.2719	22.0	3.434 ± 0.071	-16.0 ± 24.7	-295.1 ± 37.8	8.56 ± 0.89	133.4 ± 2.4
8.7951	0.5836	...	3.787 ± 0.013	-5.1 ± 4.3	-172.8 ± 4.3	4.57 ± 0.11	134.2 ± 0.7

Table C.8. Polarization data for 2005 July 21

UT Hour	Hour Angle	E (deg)	I (Jy)	Q (mJy)	U (mJy)	m (%)	χ (deg)
5.4617	-2.6835	27.6	3.620 ± 0.119	170.4 ± 71.5	-115.9 ± 86.2	5.26 ± 2.17	162.9 ± 11.4
5.6170	-2.5268	29.0	3.600 ± 0.145	27.4 ± 71.0	-177.9 ± 56.4	4.68 ± 1.76	139.4 ± 11.3
5.9944	-2.1626	32.0	3.720 ± 0.097	142.7 ± 63.8	-78.3 ± 62.0	4.04 ± 1.69	165.6 ± 11.0
6.1613	-1.9811	33.4	3.520 ± 0.087	308.1 ± 64.1	-52.1 ± 54.4	8.72 ± 1.68	175.2 ± 5.0
6.7765	-1.3642	37.3	3.729 ± 0.108	231.0 ± 46.3	-309.5 ± 57.2	10.26 ± 1.38	153.4 ± 3.7
6.9326	-1.2075	38.1	3.565 ± 0.083	78.7 ± 62.0	-247.2 ± 51.8	7.10 ± 1.59	143.8 ± 6.8
7.0889	-1.0508	38.9	3.345 ± 0.092	207.3 ± 54.5	-193.5 ± 52.1	8.33 ± 1.59	158.5 ± 5.4
7.2459	-0.8933	39.5	3.372 ± 0.077	32.0 ± 54.5	-236.5 ± 49.1	6.91 ± 1.53	138.9 ± 6.5
7.4026	-0.7359	40.0	3.346 ± 0.084	154.9 ± 46.4	-137.3 ± 47.7	6.03 ± 1.41	159.2 ± 6.5
7.5599	-0.5785	40.5	3.671 ± 0.092	217.4 ± 49.3	-61.9 ± 56.4	5.99 ± 1.44	172.1 ± 7.1
7.7167	-0.4210	40.8	3.649 ± 0.095	237.4 ± 46.8	-113.8 ± 45.7	7.10 ± 1.27	167.2 ± 5.0
7.8742	-0.2636	41.0	3.518 ± 0.078	328.0 ± 46.6	11.4 ± 42.5	9.24 ± 1.27	1.0 ± 3.7
8.0308	-0.1061	41.1	3.743 ± 0.094	388.1 ± 54.6	-165.6 ± 52.5	11.18 ± 1.43	168.4 ± 3.6
8.1873	0.0513	41.2	3.678 ± 0.085	385.4 ± 61.8	-185.9 ± 59.1	11.52 ± 1.64	167.1 ± 4.0
8.3453	0.2088	41.1	3.741 ± 0.100	395.3 ± 54.6	-226.5 ± 57.1	12.09 ± 1.49	165.1 ± 3.6
8.5026	0.3662	40.9	4.077 ± 0.102	296.7 ± 55.3	-337.2 ± 44.3	10.95 ± 1.21	155.7 ± 3.2
8.6601	0.5244	40.6	4.021 ± 0.078	312.7 ± 55.2	-291.2 ± 44.4	10.55 ± 1.23	158.5 ± 3.3
8.8172	0.6826	40.2	4.103 ± 0.079	253.5 ± 48.2	-302.9 ± 66.2	9.53 ± 1.38	155.0 ± 4.1
8.9744	0.8400	39.7	4.238 ± 0.092	344.3 ± 58.3	-383.8 ± 54.9	12.09 ± 1.33	155.9 ± 3.2
9.2289	1.0959	38.7	4.150 ± 0.088	282.6 ± 55.0	-286.4 ± 49.3	9.62 ± 1.25	157.3 ± 3.7
9.3860	1.2527	37.9	4.033 ± 0.075	184.8 ± 58.4	-321.1 ± 57.4	9.07 ± 1.44	150.0 ± 4.5
9.7087	1.5740	36.1	4.286 ± 0.094	211.8 ± 45.3	-377.1 ± 59.4	10.02 ± 1.21	149.7 ± 3.2
9.8622	1.7308	35.1	4.075 ± 0.083	190.3 ± 58.0	-294.4 ± 60.8	8.48 ± 1.46	151.4 ± 4.8
10.1931	2.0615	32.8	4.383 ± 0.130	162.0 ± 62.2	-324.5 ± 53.4	8.17 ± 1.32	148.3 ± 4.8
10.3487	2.2182	31.6	4.202 ± 0.100	258.5 ± 53.7	-183.3 ± 57.6	7.42 ± 1.32	162.3 ± 5.1
7.9359	-0.2025	...	3.803 ± 0.021	232.3 ± 11.6	-211.6 ± 11.6	8.26 ± 0.30	158.8 ± 1.1

Table C.9. Polarization data for 2005 July 22

UT Hour	Hour Angle	E (deg)	I (Jy)	Q (mJy)	U (mJy)	m (%)	χ (deg)
6.1440	-1.9431	33.6	2.948 ± 0.080	-161.0 ± 25.2	-109.1 ± 21.5	6.55 ± 0.79	107.1 ± 3.3
6.2352	-1.8518	34.3	3.139 ± 0.064	-209.4 ± 24.3	-144.2 ± 24.2	8.06 ± 0.77	107.3 ± 2.7
6.3678	-1.7188	35.2	3.084 ± 0.062	-148.6 ± 19.4	-93.3 ± 20.2	5.65 ± 0.64	106.1 ± 3.3
6.4596	-1.6275	35.8	3.146 ± 0.050	-162.6 ± 19.6	-114.1 ± 20.9	6.28 ± 0.64	107.5 ± 3.0
6.8504	-1.2349	38.0	3.176 ± 0.055	-196.2 ± 16.6	-185.3 ± 20.8	8.48 ± 0.58	111.7 ± 2.0
6.9413	-1.1437	38.4	3.051 ± 0.054	-181.3 ± 18.7	-149.7 ± 21.1	7.68 ± 0.65	109.8 ± 2.5
7.0749	-1.0099	39.0	3.085 ± 0.037	-158.6 ± 17.5	-126.9 ± 17.9	6.56 ± 0.57	109.3 ± 2.5
7.1663	-0.9186	39.4	3.072 ± 0.046	-127.6 ± 20.9	-139.1 ± 17.4	6.11 ± 0.62	113.7 ± 2.9
7.5210	-0.5628	40.5	3.174 ± 0.063	-53.0 ± 19.2	-102.7 ± 19.3	3.59 ± 0.61	121.3 ± 4.8
7.6122	-0.4715	40.7	3.087 ± 0.081	-102.2 ± 26.7	-190.6 ± 22.2	6.96 ± 0.79	120.9 ± 3.4
7.7487	-0.3377	40.9	3.340 ± 0.061	-119.8 ± 20.5	-283.3 ± 19.8	9.19 ± 0.60	123.5 ± 1.9
7.8361	-0.2464	41.0	3.316 ± 0.054	-178.0 ± 25.6	-256.0 ± 19.0	9.38 ± 0.67	117.6 ± 2.2
7.9687	-0.1133	41.1	3.348 ± 0.074	-166.9 ± 19.3	-252.7 ± 19.7	9.02 ± 0.58	118.3 ± 1.8
8.0612	-0.0214	41.2	3.197 ± 0.071	-157.4 ± 20.3	-231.1 ± 16.7	8.73 ± 0.57	117.9 ± 2.0
8.1921	0.1102	41.1	3.462 ± 0.056	-174.8 ± 19.4	-224.0 ± 18.0	8.19 ± 0.54	116.0 ± 1.9
8.2837	0.2022	41.1	3.424 ± 0.062	-159.4 ± 19.3	-198.9 ± 16.0	7.43 ± 0.51	115.7 ± 2.0
8.4875	0.4064	40.8	3.648 ± 0.044	-25.6 ± 18.7	-183.8 ± 18.5	5.06 ± 0.51	131.0 ± 2.9
8.8422	0.7623	39.9	3.576 ± 0.061	-22.1 ± 19.9	-177.8 ± 20.3	4.98 ± 0.56	131.5 ± 3.2
8.9330	0.8537	39.6	3.578 ± 0.064	-40.3 ± 17.2	-143.4 ± 23.2	4.13 ± 0.56	127.1 ± 3.4
9.0647	0.9859	39.1	3.497 ± 0.074	-39.6 ± 20.1	-149.4 ± 19.2	4.38 ± 0.56	127.6 ± 3.7
9.3536	1.2749	37.8	3.011 ± 0.102	-21.0 ± 19.3	-77.8 ± 22.6	2.58 ± 0.69	127.4 ± 6.9
9.4441	1.3655	37.3	3.274 ± 0.075	-20.9 ± 21.5	-90.5 ± 16.6	2.78 ± 0.58	128.5 ± 6.6
9.8165	1.7394	35.1	3.417 ± 0.063	64.5 ± 20.3	-74.7 ± 17.5	2.83 ± 0.55	155.4 ± 5.6
9.9068	1.8299	34.4	3.303 ± 0.068	24.1 ± 20.9	-98.3 ± 20.5	3.00 ± 0.63	141.9 ± 5.9
10.3626	2.2872	31.0	3.524 ± 0.048	-124.9 ± 21.7	-21.1 ± 21.7	3.54 ± 0.62	94.8 ± 4.9
10.4536	2.3785	30.3	3.285 ± 0.108	-134.8 ± 22.3	-69.7 ± 20.2	4.57 ± 0.65	103.7 ± 3.9
10.6928	2.6179	28.2	3.554 ± 0.080	-61.5 ± 23.3	-51.2 ± 20.7	2.16 ± 0.62	109.9 ± 7.8
10.7829	2.7085	27.4	3.602 ± 0.079	-93.6 ± 19.8	-68.5 ± 26.5	3.15 ± 0.64	108.1 ± 6.0
10.9912	2.9170	25.5	3.742 ± 0.087	-66.8 ± 25.2	32.4 ± 22.7	1.88 ± 0.64	77.1 ± 8.9
11.0816	3.0076	24.6	3.742 ± 0.086	-31.9 ± 25.2	56.7 ± 24.3	1.61 ± 0.66	59.7 ± 11.0
11.2643	3.1909	22.8	3.823 ± 0.079	-96.7 ± 24.2	74.2 ± 31.0	3.11 ± 0.72	71.2 ± 6.7
11.3545	3.2815	21.9	3.623 ± 0.097	-47.7 ± 22.8	122.2 ± 29.8	3.55 ± 0.72	55.7 ± 5.2
11.5393	3.4670	20.0	3.547 ± 0.094	-70.9 ± 32.3	90.9 ± 25.5	3.15 ± 0.81	64.0 ± 7.4
8.7392	0.6589	...	3.356 ± 0.013	-98.1 ± 4.1	-115.0 ± 4.3	4.50 ± 0.12	114.8 ± 0.8

Table C.10. Polarization data for 2005 July 30

UT Hour	Hour Angle	E (deg)	I (Jy)	Q (mJy)	U (mJy)	m (%)	χ (deg)
4.2189	-3.3486	21.2	4.214 ± 0.108	-302.1 ± 26.1	69.1 ± 42.9	7.31 ± 0.79	83.6 ± 3.9
4.3257	-3.2417	22.3	4.411 ± 0.093	-320.6 ± 26.8	116.5 ± 24.2	7.71 ± 0.58	80.0 ± 2.1
4.6204	-2.9562	25.1	3.811 ± 0.148	-266.8 ± 26.0	112.1 ± 34.5	7.55 ± 0.79	78.6 ± 3.3
4.8050	-2.7598	26.9	3.880 ± 0.195	-260.3 ± 31.5	48.3 ± 25.6	6.79 ± 0.73	84.7 ± 2.8
4.9072	-2.6584	27.8	3.943 ± 0.273	-206.3 ± 33.1	19.5 ± 36.3	5.18 ± 0.88	87.3 ± 5.0
5.1398	-2.4244	29.9	4.610 ± 0.199	-386.9 ± 26.8	30.3 ± 28.1	8.40 ± 0.59	87.8 ± 2.1
5.2374	-2.3323	30.6	4.355 ± 0.155	-350.4 ± 26.3	-74.3 ± 29.6	8.20 ± 0.64	96.0 ± 2.4
5.3263	-2.2528	31.3	3.568 ± 0.231	-237.2 ± 39.4	62.4 ± 33.0	6.80 ± 1.01	82.6 ± 3.9
6.9221	-0.6372	40.3	3.811 ± 0.147	-215.6 ± 21.3	106.3 ± 21.2	6.28 ± 0.56	76.9 ± 2.5
7.0548	-0.5042	40.6	4.231 ± 0.131	-309.6 ± 21.4	117.5 ± 20.9	7.81 ± 0.50	79.6 ± 1.8
7.1870	-0.3719	40.9	4.239 ± 0.061	-303.0 ± 17.0	111.6 ± 16.8	7.61 ± 0.40	79.9 ± 1.5
7.8083	0.2514	41.0	4.392 ± 0.064	-92.7 ± 18.6	111.3 ± 20.3	3.27 ± 0.44	64.9 ± 3.8
7.9387	0.3823	40.9	4.289 ± 0.066	-75.0 ± 21.0	138.1 ± 16.4	3.64 ± 0.43	59.2 ± 3.6
8.0709	0.5147	40.6	4.258 ± 0.067	-36.3 ± 21.4	106.6 ± 19.0	2.60 ± 0.47	54.4 ± 5.4
8.2387	0.6828	40.2	4.019 ± 0.086	-25.8 ± 20.5	73.3 ± 18.6	1.87 ± 0.49	54.7 ± 7.5
8.4929	0.9380	39.3	3.800 ± 0.092	-137.7 ± 21.8	69.9 ± 17.0	4.03 ± 0.51	76.5 ± 3.4
8.5848	1.0293	38.9	3.954 ± 0.083	-115.7 ± 21.6	119.0 ± 20.8	4.16 ± 0.54	67.1 ± 3.7
8.8674	1.3133	37.6	4.434 ± 0.047	-223.5 ± 20.5	37.2 ± 20.8	5.09 ± 0.47	85.3 ± 2.6
8.9577	1.4039	37.1	4.324 ± 0.058	-246.4 ± 21.1	-27.8 ± 17.5	5.72 ± 0.45	93.2 ± 2.0
9.1699	1.6167	35.8	4.377 ± 0.081	-290.2 ± 20.3	-24.5 ± 20.1	6.64 ± 0.46	92.4 ± 2.0
9.2609	1.7080	35.3	4.239 ± 0.086	-275.7 ± 22.6	-48.3 ± 19.7	6.58 ± 0.50	95.0 ± 2.0
9.3894	1.8367	34.4	4.154 ± 0.090	-203.1 ± 17.1	-57.5 ± 20.7	5.06 ± 0.45	97.9 ± 2.8
9.4800	1.9273	33.8	3.700 ± 0.111	-198.6 ± 20.5	-50.9 ± 18.0	5.52 ± 0.52	97.2 ± 2.5
9.9712	2.4198	29.9	3.898 ± 0.106	-119.6 ± 25.9	-66.2 ± 20.5	3.46 ± 0.59	104.5 ± 4.6
10.0616	2.5110	29.1	4.285 ± 0.077	-186.0 ± 19.0	-63.5 ± 23.0	4.56 ± 0.49	99.4 ± 3.3
10.1808	2.6304	28.1	4.622 ± 0.085	-191.0 ± 22.9	-6.8 ± 21.6	4.11 ± 0.48	91.0 ± 3.2
10.2709	2.7210	27.3	4.878 ± 0.077	-157.1 ± 22.9	41.6 ± 22.3	3.30 ± 0.46	82.6 ± 3.9
10.4748	2.9251	25.4	4.798 ± 0.118	-209.0 ± 26.5	86.6 ± 20.8	4.69 ± 0.49	78.8 ± 2.7
10.5651	3.0157	24.5	4.682 ± 0.155	-259.0 ± 30.6	87.0 ± 27.6	5.80 ± 0.62	80.7 ± 2.9
10.6848	3.1358	23.3	3.978 ± 0.134	-149.8 ± 30.2	28.7 ± 28.0	3.76 ± 0.73	84.6 ± 5.3
10.7754	3.2271	22.4	3.813 ± 0.111	-224.8 ± 39.6	2.2 ± 31.1	5.82 ± 0.92	89.7 ± 4.0
10.9744	3.4270	20.4	2.925 ± 0.207	-102.8 ± 37.8	47.9 ± 26.5	3.72 ± 1.08	77.5 ± 7.3
11.0661	3.5183	19.5	3.113 ± 0.224	-183.5 ± 35.3	-47.5 ± 36.6	5.98 ± 1.16	97.3 ± 5.5
8.1241	0.5670	...	4.140 ± 0.024	-208.1 ± 4.9	39.4 ± 4.5	5.12 ± 0.11	84.6 ± 0.6

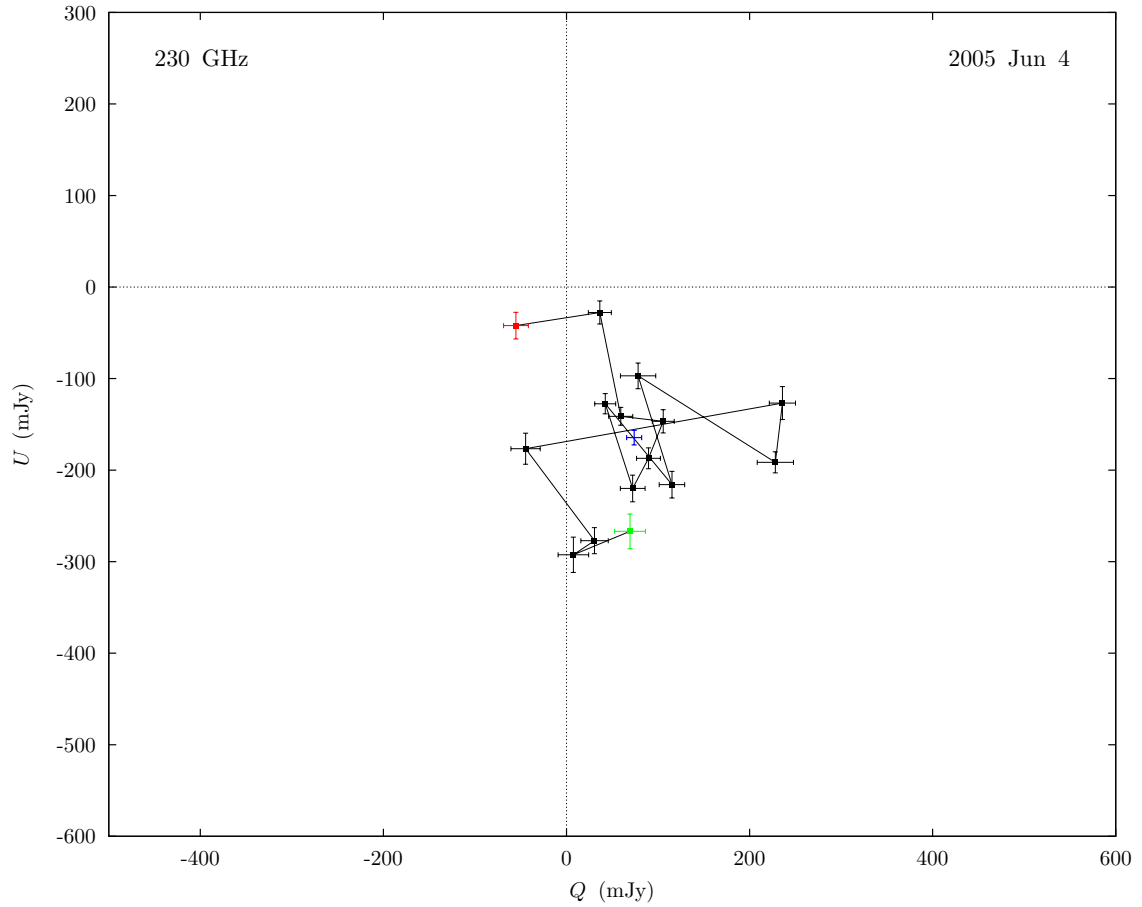
C.2 $Q-U$ Light Curves

Fig. C.1.— Polarization light curve for 2005 June 4, plotted in the $Q-U$ plane. The data are shown at full temporal resolution (one polarization switching cycle per point) as in Figure 7.1 and Table C.1. The mean polarization for the track is marked with a blue cross. The first and last points in the light curve are marked with green and red points, respectively. *The individual light curve points are shown with half- σ error bars for clarity.*

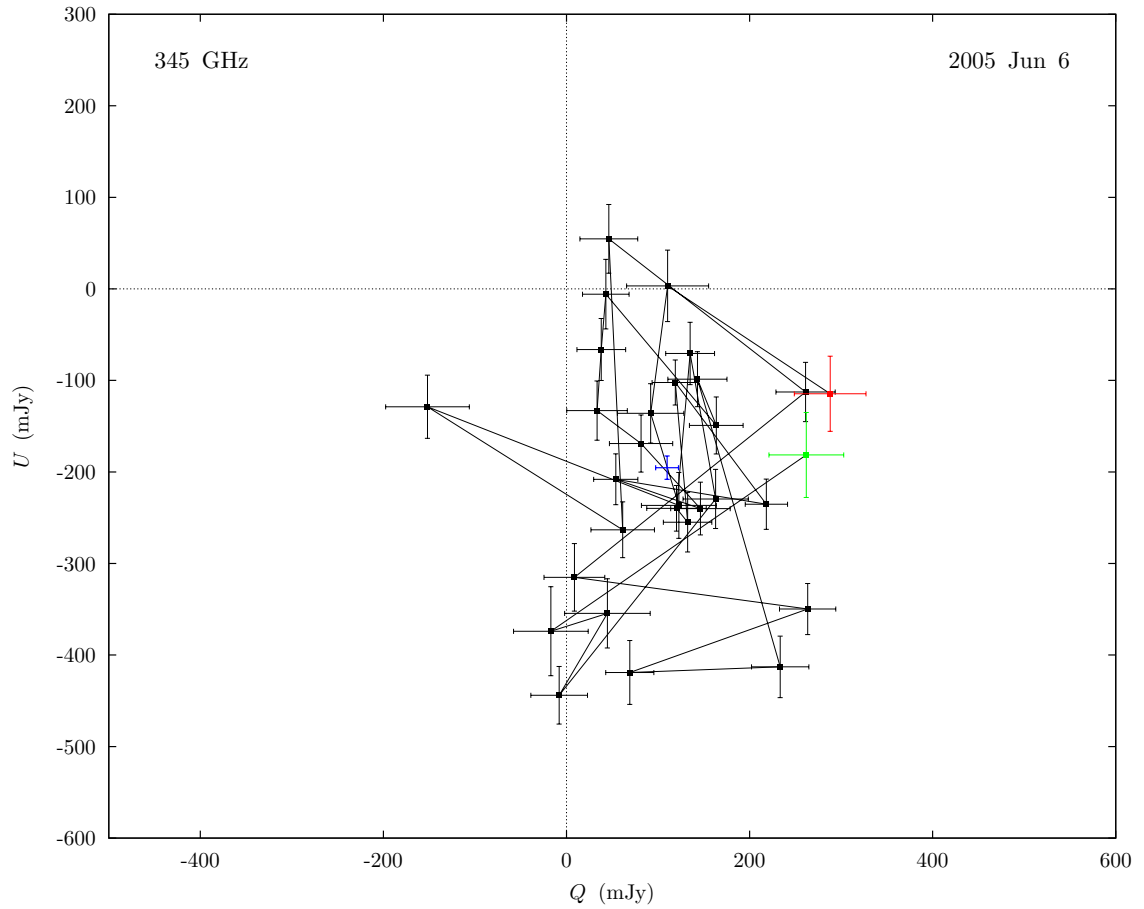


Fig. C.2.— Polarization light curve for 2005 June 6, plotted in the $Q-U$ plane. The data are shown at full temporal resolution (one polarization switching cycle per point) as in Figure 7.2 and Table C.2. See caption of Figure C.1 for details.

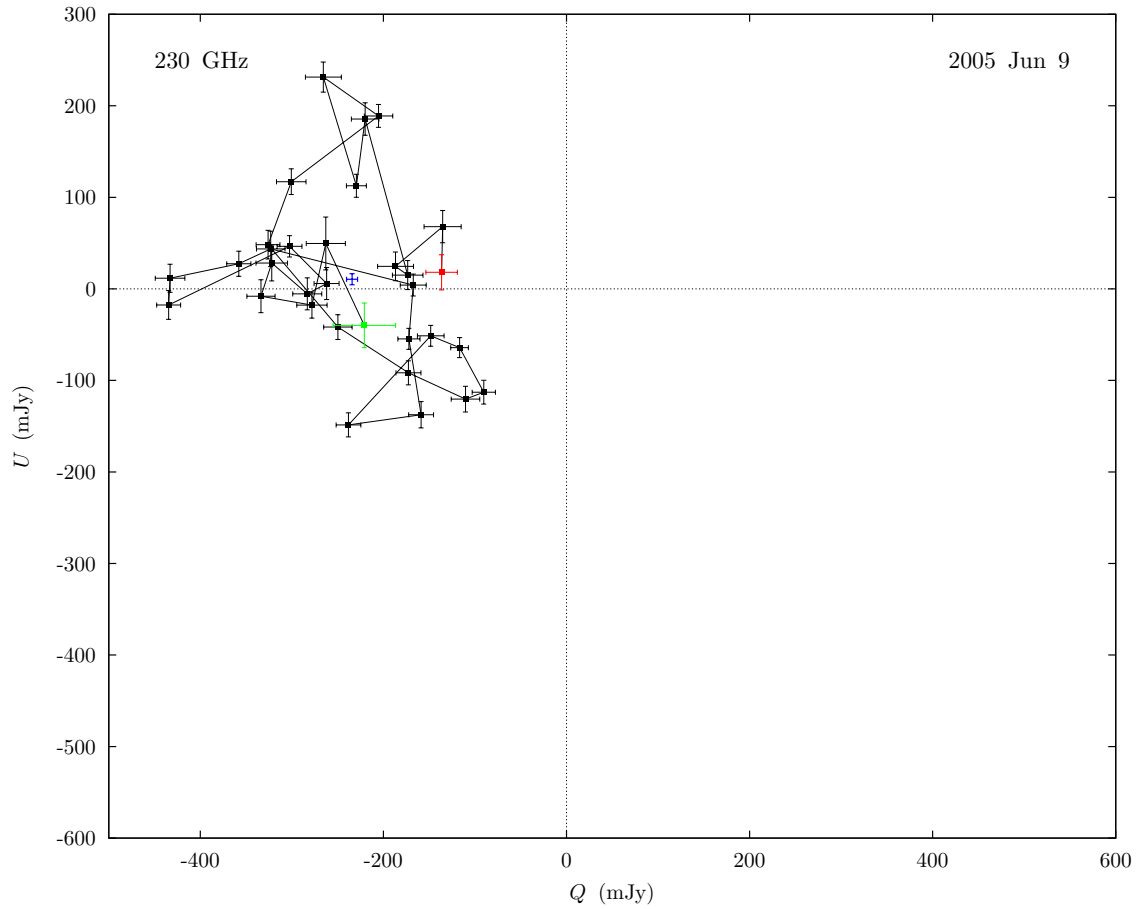


Fig. C.3.— Polarization light curve for 2005 June 9, plotted in the $Q-U$ plane. The data are shown at full temporal resolution (one polarization switching cycle per point) as in Figure 7.3 and Table C.3. See caption of Figure C.1 for details.

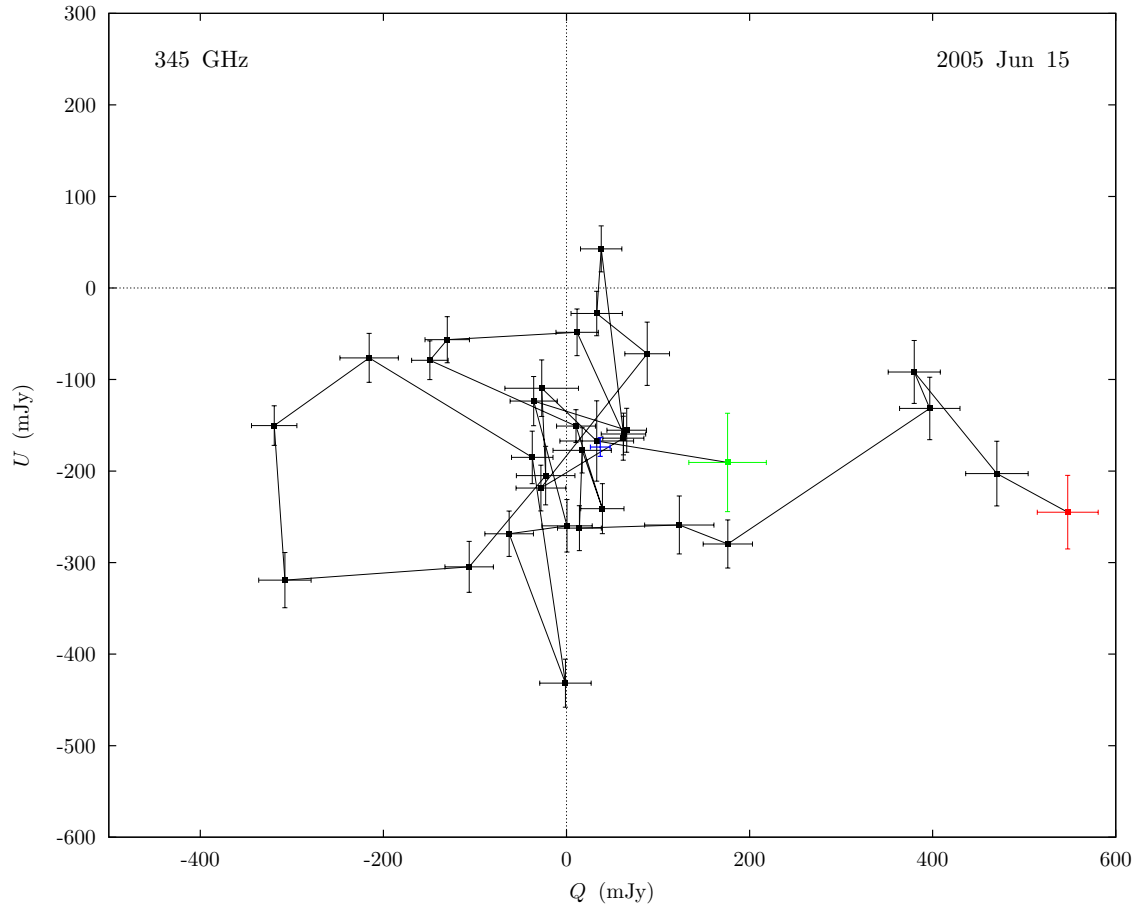


Fig. C.4.— Polarization light curve for 2005 June 15, plotted in the $Q-U$ plane. The data are shown at full temporal resolution (one polarization switching cycle per point) as in Figure 7.4 and Table C.4. See caption of Figure C.1 for details.

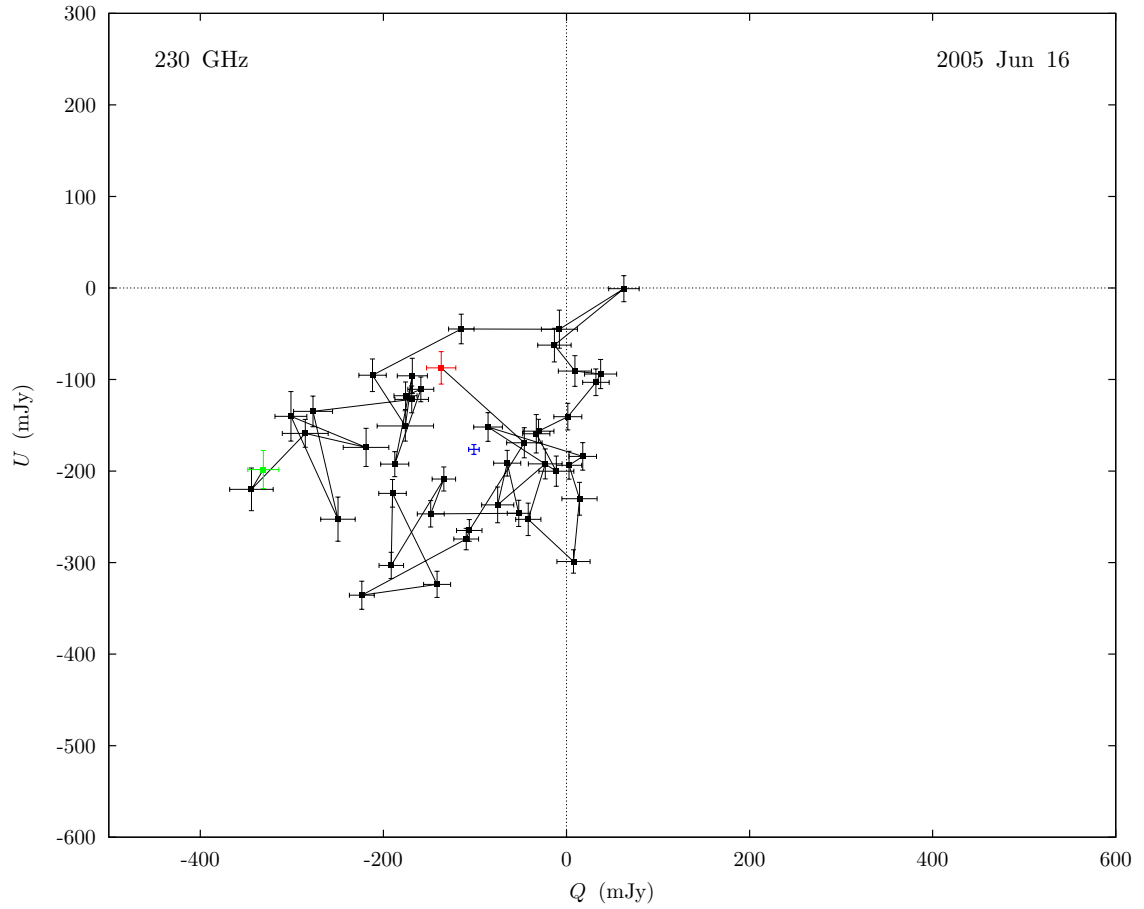


Fig. C.5.— Polarization light curve for 2005 June 16, plotted in the $Q-U$ plane. The data are shown at full temporal resolution (one polarization switching cycle per point) as in Figure 7.5 and Table C.5. See caption of Figure C.1 for details.

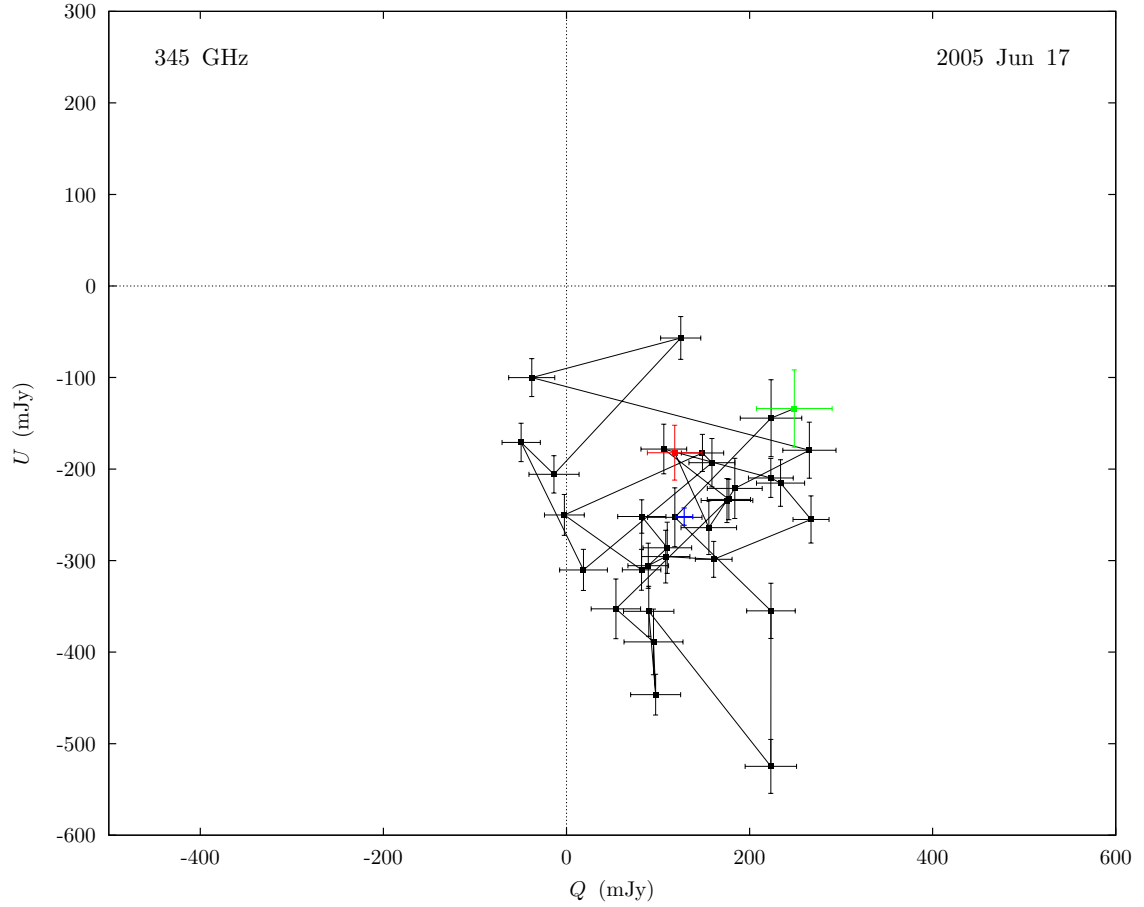


Fig. C.6.— Polarization light curve for 2005 June 17, plotted in the $Q-U$ plane. The data are shown at full temporal resolution (one polarization switching cycle per point) as in Figure 7.6 and Table C.6. See caption of Figure C.1 for details.

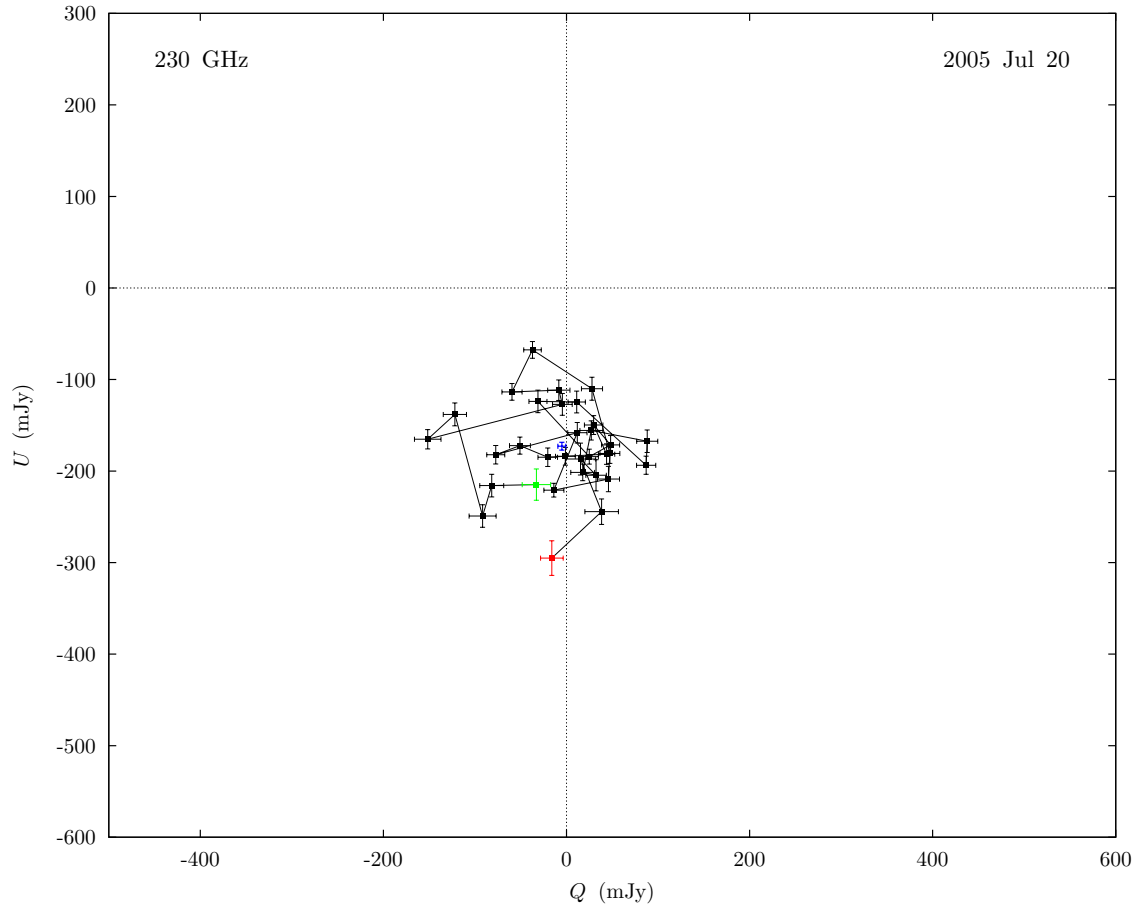


Fig. C.7.— Polarization light curve for 2005 July 20, plotted in the $Q-U$ plane. The data are shown at full temporal resolution (one polarization switching cycle per point) as in Figure 7.7 and Table C.7. See caption of Figure C.1 for details.

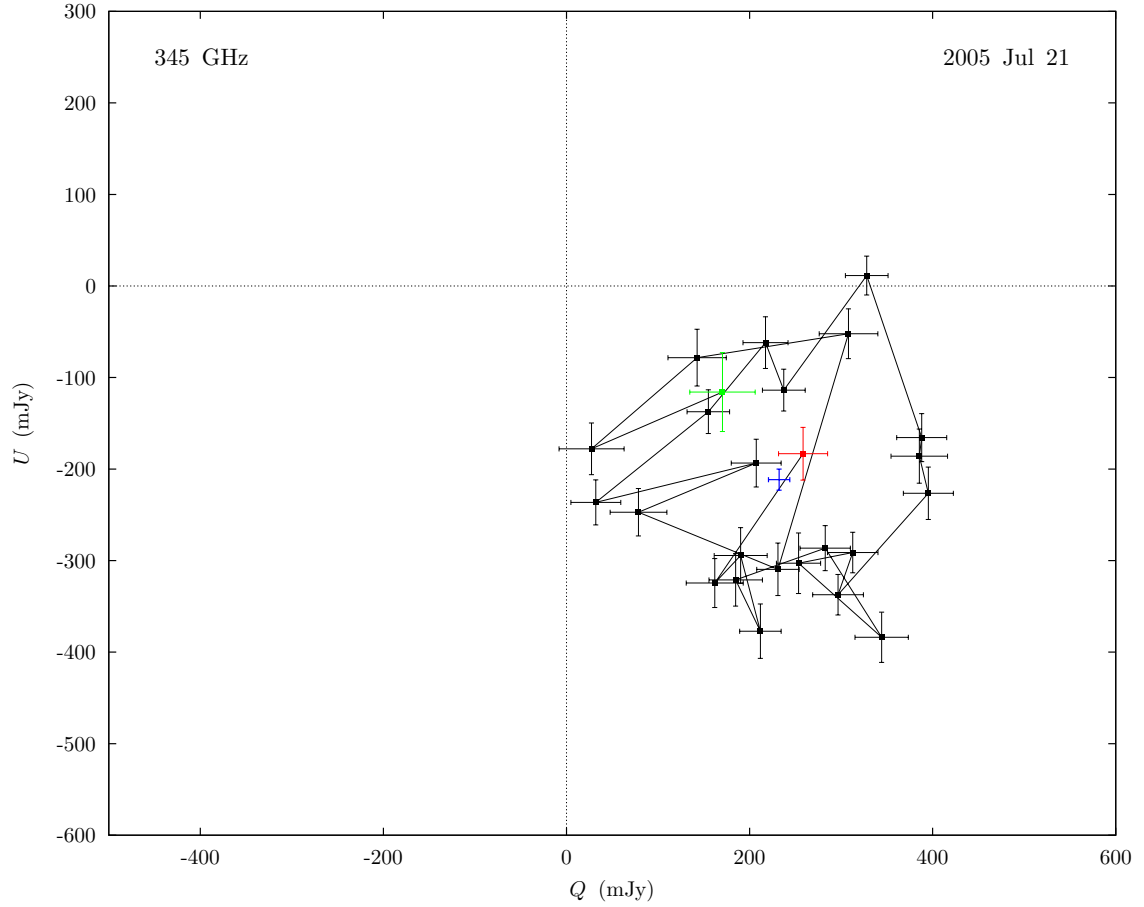


Fig. C.8.— Polarization light curve for 2005 July 21, plotted in the $Q-U$ plane. The data are shown at full temporal resolution (one polarization switching cycle per point) as in Figure 7.8 and Table C.8. See caption of Figure C.1 for details.

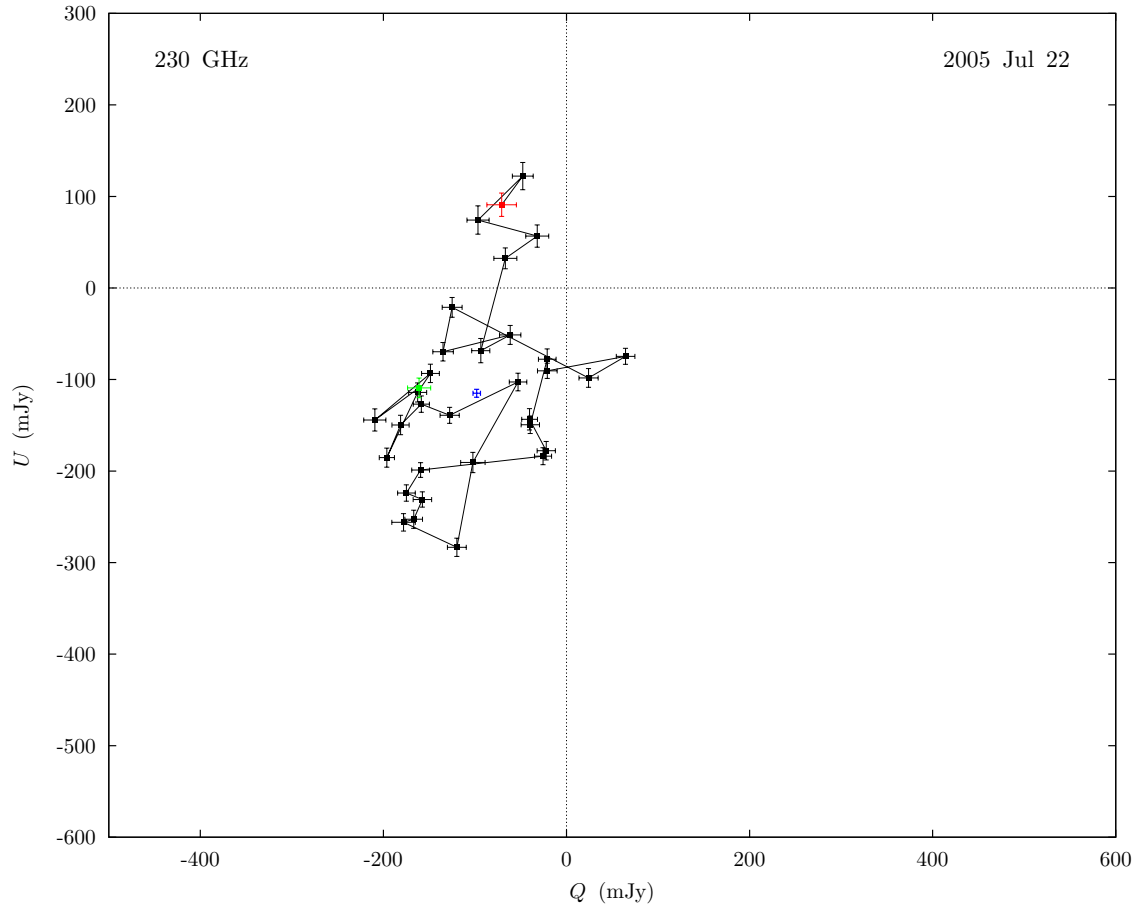


Fig. C.9.— Polarization light curve for 2005 July 22, plotted in the $Q-U$ plane. The data are shown at full temporal resolution (one polarization switching cycle per point) as in Figure 7.9 and Table C.9. See caption of Figure C.1 for details.

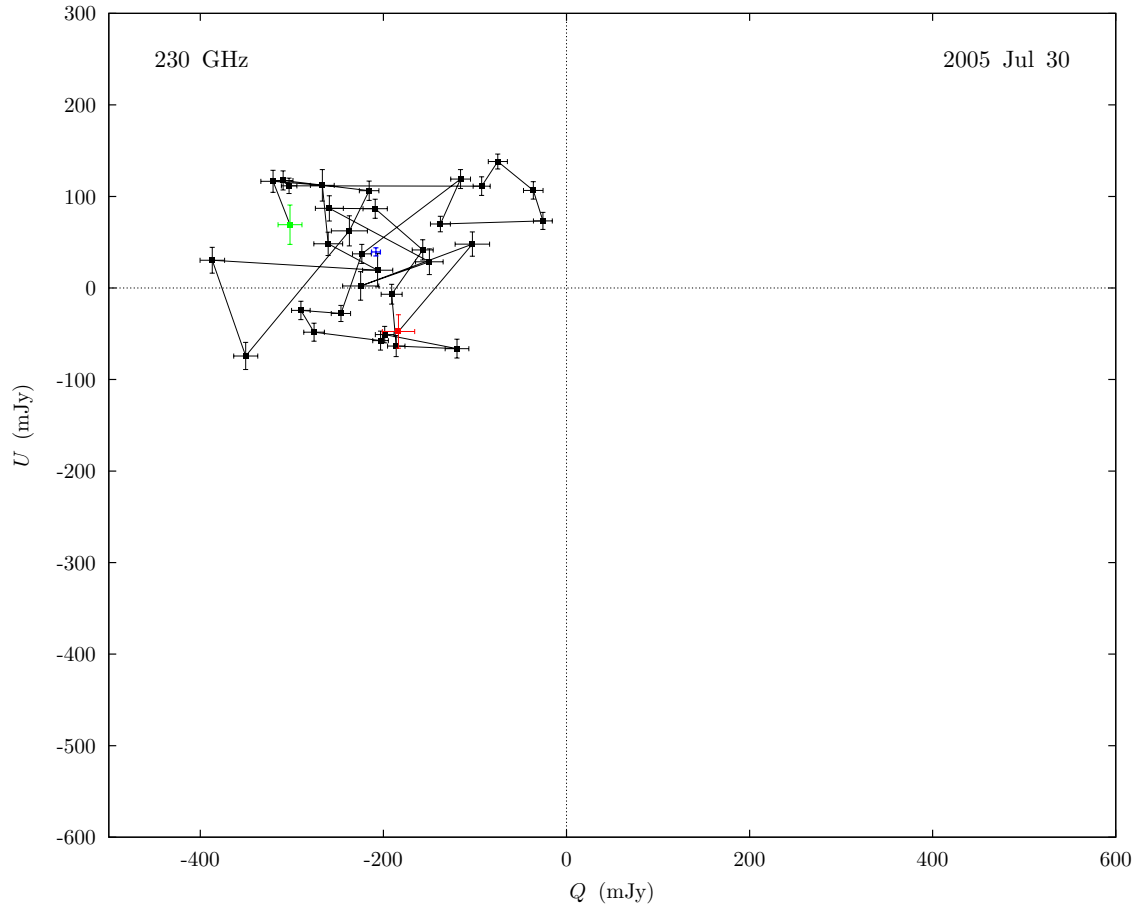


Fig. C.10.— Polarization light curve for 2005 July 30, plotted in the $Q-U$ plane. The data are shown at full temporal resolution (one polarization switching cycle per point) as in Figure 7.10 and Table C.10. See caption of Figure C.1 for details.

References

- Afsar, M. N. 1987, *IEEE Transactions on Instrumentation Measurement*, 36, 554
- Agol, E. 2000, *ApJ*, 538, L121
- Aitken, D. K., Greaves, J., Chrysostomou, A., Jenness, T., Holland, W., Hough, J. H., Pierce-Price, D., & Richer, J. 2000, *ApJ*, 534, L173
- Alberdi, A., Lara, L., Marcaide, J. M., Elosegui, P., Shapiro, I. I., Cotton, W. D., Diamond, P. J., Romney, J. D., & Preston, R. A. 1993, *A&A*, 277, L1
- Aller, M. F., Aller, H. D., & Hughes, P. A. 2003, *ApJ*, 586, 33
- An, T., Goss, W. M., Zhao, J.-H., Hong, X. Y., Roy, S., Rao, A. P., & Shen, Z.-Q. 2005, *ApJ*, 634, L49
- Aschenbach, B., Grosso, N., Porquet, D., & Predehl, P. 2004, *A&A*, 417, 71
- Backer, D. C., Zensus, J. A., Kellermann, K. I., Reid, M., Moran, J. M., & Lo, K. Y. 1993, *Science*, 262, 1414
- Baganoff, F. K. et al. 2001, *Nature*, 413, 45
- . 2003, *ApJ*, 591, 891
- Balick, B. & Brown, R. L. 1974, *ApJ*, 194, 265
- Bardeen, J. M., Press, W. H., & Teukolsky, S. A. 1972, *ApJ*, 178, 347
- Beckert, T. 2003, *Astronomische Nachrichten Supplement*, 324, 459
- Beckert, T. & Falcke, H. 2002, *A&A*, 388, 1106
- Bélanger, G., Goldwurm, A., Melia, F., Ferrando, P., Grosso, N., Porquet, D., Warwick, R., & Yusef-Zadeh, F. 2005, *ApJ*, 635, 1095

- Belanger, G., Terrier, R., De Jager, O., Goldwurm, A., & Melia, F. 2006, ArXiv Astrophysics e-prints
- Birch, J. R. et al. 1994, IEEE Transactions on Microwave Theory Techniques, 42, 956
- Blandford, R. D. & Begelman, M. C. 1999, MNRAS, 303, L1
- Blundell, R. 2004, in 15th International Symposium on Space Terahertz Technology, ed. G. Narayanan (Amherst: U Mass), 3, <http://www.stt2004.org>
- Bondi, H. 1952, MNRAS, 112, 195
- Born, M. & Wolf, E. 1999, Principles of optics : electromagnetic theory of propagation, interference and diffraction of light (New York : Cambridge University Press)
- Bower, G., Wright, M. C. H., & Forster, J. R. 2002a, Polarization Stability of the BIMA Array at 1.3mm, BIMA Memo 89, Berkeley-Illinois-Maryland Association
- Bower, G. C. & Backer, D. C. 1998, ApJ, 496, L97
- Bower, G. C., Backer, D. C., Zhao, J.-H., Goss, M., & Falcke, H. 1999a, ApJ, 521, 582
- Bower, G. C., Falcke, H., & Backer, D. C. 1999b, ApJ, 523, L29
- Bower, G. C., Falcke, H., Herrnstein, R. M., Zhao, J.-H., Goss, W. M., & Backer, D. C. 2004, Science, 304, 704
- Bower, G. C., Falcke, H., & Mellon, R. R. 2002b, ApJ, 578, L103
- Bower, G. C., Falcke, H., Sault, R. J., & Backer, D. C. 2002c, ApJ, 571, 843
- Bower, G. C., Falcke, H., Wright, M. C., & Backer, D. C. 2005a, ApJ, 618, L29
- Bower, G. C., Goss, W. M., Falcke, H., Backer, D. C., & Lithwick, Y. 2006, ApJ, in press, astro-ph/0608004
- Bower, G. C., Roberts, D. A., Yusef-Zadeh, F., Backer, D. C., Cotton, W. D., Goss, W. M., Lang, C. C., & Lithwick, Y. 2005b, ApJ, 633, 218
- Bower, G. C., Wright, M. C. H., Backer, D. C., & Falcke, H. 1999c, ApJ, 527, 851

- Bower, G. C., Wright, M. C. H., Falcke, H., & Backer, D. C. 2001, *ApJ*, 555, L103
- . 2003, *ApJ*, 588, 331
- Broderick, A. E. & Loeb, A. 2006a, *ApJ*, 636, L109
- . 2006b, *MNRAS*, 367, 905
- Broderick, A. E. & Loeb, A. 2006c, in *From the Center of the Milky Way to Nearby Low-Luminosity Galactic Nuclei*, ed. R. Schödel et al. (Institute of Physics), astro-ph/0607279
- Brown, R. L. & Lo, K. Y. 1982, *ApJ*, 253, 108
- Brunthaler, A., Bower, G. C., & Falcke, H. 2006, *A&A*, 451, 845
- Brunthaler, A., Bower, G. C., Falcke, H., & Mellon, R. R. 2001, *ApJ*, 560, L123
- Coker, R. F. & Melia, F. 1997, *ApJ*, 488, L149
- Cotera, A., Morris, M., Ghez, A. M., Becklin, E. E., Tanner, A. M., Werner, M. W., & Stolovy, S. R. 1999, in *ASP Conf. Ser. 186: The Central Parsecs of the Galaxy*, ed. H. Falcke, A. Cotera, W. J. Duschl, F. Melia, & M. J. Rieke, 240
- Cuadra, J., Nayakshin, S., Springel, V., & Di Matteo, T. 2005, *MNRAS*, 360, L55
- Cuadra, J., Nayakshin, S., Springel, V., & di Matteo, T. 2006, *MNRAS*, 366, 358
- Davidson, J. A., Werner, M. W., Wu, X., Lester, D. F., Harvey, P. M., Joy, M., & Morris, M. 1992, *ApJ*, 387, 189
- Davies, R. D., Walsh, D., & Booth, R. S. 1976, *MNRAS*, 177, 319
- Dent, W. R. F., Matthews, H. E., Wade, R., & Duncan, W. D. 1993, *ApJ*, 410, 650
- Doeleman, S. & Bower, G. 2004, *Galactic Center Newsletter*, 18, 6
- Doeleman, S. S. et al. 2001, *AJ*, 121, 2610

- Dowell, C. D. et al. 2003, in *Millimeter and Submillimeter Detectors for Astronomy*. Edited by T. G. Phillips & J. Zmuidzinas. Proc. SPIE, 4855, 73
- Eckart, A., Baganoff, F. K., Schödel, R., Morris, M., Genzel, R., Bower, G. C., Marrone, D., Moran, J. M., Viehmann, T., Bautz, M. W., Brandt, W. N., Garmire, G. P., Ott, T., Trippe, S., Ricker, G. R., Straubmeier, C., Roberts, D. A., Yusef-Zadeh, F., Zhao, J. H., & Rao, R. 2006a, *A&A*, 450, 535
- Eckart, A. & Genzel, R. 1996, *Nature*, 383, 415
- . 1997, *MNRAS*, 284, 576
- Eckart, A., Genzel, R., Ott, T., & Schödel, R. 2002, *MNRAS*, 331, 917
- Eckart, A., Schödel, R., Meyer, L., Trippe, S., Ott, T., & Genzel, R. 2006b, *A&A*, 455, 1
- Eckart, A. et al. 2004, *A&A*, 427, 1
- Eisenhauer, F. et al. 2005, *ApJ*, 628, 246
- Falcke, H. 1999, in *ASP Conf. Ser. 186: The Central Parsecs of the Galaxy*, ed. H. Falcke, A. Cotera, W. J. Duschl, F. Melia, & M. J. Rieke, 113
- Falcke, H., Biermann, P. L., Duschl, W. J., & Mezger, P. G. 1993a, *A&A*, 270, 102
- Falcke, H., Goss, W. M., Matsuo, H., Teuben, P., Zhao, J.-H., & Zylka, R. 1998, *ApJ*, 499, 731
- Falcke, H., Mannheim, K., & Biermann, P. L. 1993b, *A&A*, 278, L1
- Falcke, H. & Markoff, S. 2000, *A&A*, 362, 113
- Falcke, H., Melia, F., & Agol, E. 2000, *ApJ*, 528, L13
- Fan, X. et al. 2006, *AJ*, 132, 117
- Ferrarese, L. & Merritt, D. 2000, *ApJ*, 539, L9
- Gardner, F. F. & Whiteoak, J. B. 1966, *ARA&A*, 4, 245
- Gebhardt, K. et al. 2000, *ApJ*, 539, L13
- Genzel, R., Schödel, R., Ott, T., Eckart, A., Alexander, T., Lacombe, F., Rouan, D., & Aschenbach, B. 2003, *Nature*, 425, 934

- Genzel, R., Thatte, N., Krabbe, A., Kroker, H., & Tacconi-Garman, L. E. 1996, *ApJ*, 472, 153
- Genzel, R. & Townes, C. H. 1987, *ARA&A*, 25, 377
- Ghez, A. M., Becklin, E., Duchjne, G., Hornstein, S., Morris, M., Salim, S., & Tanner, A. 2003, *Astronomische Nachrichten Supplement*, 324, 527
- Ghez, A. M., Klein, B. L., Morris, M., & Becklin, E. E. 1998, *ApJ*, 509, 678
- Ghez, A. M., Morris, M., Becklin, E. E., Tanner, A., & Kremenek, T. 2000, *Nature*, 407, 349
- Ghez, A. M., Salim, S., Hornstein, S. D., Tanner, A., Lu, J. R., Morris, M., Becklin, E. E., & Duchêne, G. 2005a, *ApJ*, 620, 744
- Ghez, A. M. et al. 2004, *ApJ*, 601, L159
- . 2005b, *ApJ*, 635, 1087
- Gillessen, S. et al. 2006a, in *Ground-based and Airborne Telescopes*. Edited by Stepp, Larry M.. *Proceedings of the SPIE*, Volume 6268, pp. 626811 (2006).
- Gillessen, S. et al. 2006b, *ApJ*, 640, L163
- Girart, J. M., Crutcher, R. M., & Rao, R. 1999, *ApJ*, 525, L109
- Girart, J. M., Rao, R., & Marrone, D. P. 2006, *Science*, 313, 812
- Goldston, J. E., Quataert, E., & Igumenshchev, I. V. 2005, *ApJ*, 621, 785
- Goldwurm, A., Brion, E., Goldoni, P., Ferrando, P., Daigne, F., Decourchelle, A., Warwick, R. S., & Predehl, P. 2003, *ApJ*, 584, 751
- Greaves, J. S. et al. 2003, *MNRAS*, 340, 353
- Guesten, R., Genzel, R., Wright, M. C. H., Jaffe, D. T., Stutzki, J., & Harris, A. I. 1987, *ApJ*, 318, 124
- Gwinn, C. R., Danen, R. M., Tran, T. K., Middleditch, J., & Ozernoy, L. M. 1991, *ApJ*, 381, L43
- Hamaker, J. P., Bregman, J. D., & Sault, R. J. 1996, *A&AS*, 117, 137
- Hanany, S., Hubmayr, J., Johnson, B. R., Matsumura, T., Oxley, P., & Thibodeau, M. 2005, *Appl. Opt.*, 44, 4666

- Hawley, J. F. & Balbus, S. A. 2002, *ApJ*, 573, 738
- Heiles, C. E. & Drake, F. D. 1963, *Icarus*, 2, 281
- Herrnstein, R. M., Zhao, J.-H., Bower, G. C., & Goss, W. M. 2004, *AJ*, 127, 3399
- Ho, L. C. 1999, *ApJ*, 516, 672
- Ho, P. T. P., Moran, J. M., & Lo, K. Y. 2004, *ApJ*, 616, L1
- Holdaway, M., Carilli, C., & Owen, F. 1992, Possible Algorithms to Improve the VLA's Polarization Performance, VLA Memo 163, National Radio Astronomy Observatory
- Holland, W. S. et al. 1999, *MNRAS*, 303, 659
- Hornstein, S. D., Ghez, A. M., Tanner, A., Morris, M., Becklin, E. E., & Wizinowich, P. 2002, *ApJ*, 577, L9
- IAU. 1974, Transactions of the International Astronomical Union, 15B, 166
- Igumenshchev, I. V., Narayan, R., & Abramowicz, M. A. 2003, *ApJ*, 592, 1042
- Johnson, B. R. et al. 2003, *New Astronomy Review*, 47, 1067
- Jones, R. C. 1941, *Journal of the Optical Society of America*, 31, 488
- Kellermann, K. I., Shaffer, D. B., Clark, B. G., & Geldzahler, B. J. 1977, *ApJ*, 214, L61
- Kesteven, M. 1997, Field rotation due to an antenna's pointing model, ATNF Memo 39.3/071, Australia Telescope National Facility
- Krabbe, A., Iserlohe, C., Larkin, J. E., Barczys, M., McElwain, M., Weiss, J., Wright, S. A., & Quirrenbach, A. 2006, *ApJ*, 642, L145
- Kraus, J. D. 1966, *Radio astronomy* (New York: McGraw-Hill, 1966)
- Krichbaum, T. P. et al. 1993, *A&A*, 274, L37
- . 1998, *A&A*, 335, L106
- Lamb, J. W. 1996, *Int. J. IR and Millimeter Waves*, 17, 1997
- Li, Y. et al. 2006, *ArXiv Astrophysics e-prints*

- Liu, S., Petrosian, V., & Melia, F. 2004, *ApJ*, 611, L101
- Lo, K. Y., Backer, D. C., Ekers, R. D., Kellermann, K. I., Reid, M., & Moran, J. M. 1985, *Nature*, 315, 124
- Lo, K. Y., Cohen, M. H., Readhead, A. S. C., & Backer, D. C. 1981, *ApJ*, 249, 504
- Lo, K. Y., Schilizzi, R. T., Cohen, M. H., & Ross, H. N. 1975, *ApJ*, 202, L63
- Lo, K. Y., Shen, Z.-Q., Zhao, J.-H., & Ho, P. T. P. 1998, *ApJ*, 508, L61
- Lu, J. R. et al. 2006, in *From the Center of the Milky Way to Nearby Low-Luminosity Galactic Nuclei*, ed. R. Schödel et al. (Institute of Physics)
- Lynden-Bell, D. 1969, *Nature*, 223, 690
- Macquart, J.-P. & Bower, G. C. 2006, *ApJ*, 641, 302
- Macquart, J.-P., Bower, G. C., Wright, M. C. H., Backer, D. C., & Falcke, H. 2006, *ApJ*, 646, L111
- Mahadevan, R. 1998, *Nature*, 394, 651
- Marconi, A. & Hunt, L. K. 2003, *ApJ*, 589, L21
- Markoff, S. 2006, in *From the Center of the Milky Way to Nearby Low-Luminosity Galactic Nuclei*, ed. R. Schödel et al. (Institute of Physics)
- Markoff, S. & Falcke, H. 2003, *Astronomische Nachrichten Supplement*, 324, 445
- Markoff, S., Falcke, H., Yuan, F., & Biermann, P. L. 2001, *A&A*, 379, L13
- Marrone, D. P., Battat, J., Bensch, F., Blundell, R., Diaz, M., Gibson, H., Hunter, T., Meledin, D., Paine, S., Papa, D. C., Radford, S., Smith, M., & Tong, E. 2004, *ApJ*, 612, 940
- Marrone, D. P., Blundell, R., Tong, E., Paine, S. N., Loudkov, D., Kawamura, J. H., Luhr, D., & Barrientos, C. 2005, in *Proc. 16th Inter. Symp. on Space Terahertz Technology*, ed. M. Ingvarsson, J. Stake & H. Merkel, 64–67, (astro-ph/0505273)
- Marrone, D. P., Moran, J. M., Zhao, J.-H., & Rao, R. 2006, *ApJ*, 640, 308
- Masson, J.-B. & Gallot, G. 2006, *Optics Letters*, 31, 265

- Mauerhan, J. C., Morris, M., Walter, F., & Baganoff, F. K. 2005, *ApJ*, 623, L25
- Melia, F. 1992, *ApJ*, 387, L25
- Melia, F. & Falcke, H. 2001, *ARA&A*, 39, 309
- Melia, F., Liu, S., & Coker, R. 2000, *ApJ*, 545, L117
- . 2001, *ApJ*, 553, 146
- Menten, K. M., Reid, M. J., Eckart, A., & Genzel, R. 1997, *ApJ*, 475, L111
- Miyazaki, A., Tsutsumi, T., & Tsuboi, M. 2003, *Astronomische Nachrichten Supplement*, 324, 363
- . 2004, *ApJ*, 611, L97
- Morris, M., Ghez, A. M., & Becklin, E. E. 1999, *Advances in Space Research*, 23, 959
- Morris, M. & Serabyn, E. 1996, *ARA&A*, 34, 645
- Mueller, H. 1948, *Journal of the Optical Society of America*, 38, 661
- Narayan, R. 2002, in *Lighthouses of the Universe*, ed. M. Gilfanov, R. Sunyaev, & E. Churazov (Berlin: Springer), 405
- Narayan, R., Igumenshchev, I. V., & Abramowicz, M. A. 2000, *ApJ*, 539, 798
- Narayan, R. & Quataert, E. 2005, *Science*, 307, 77
- Narayan, R. & Yi, I. 1994, *ApJ*, 428, L13
- . 1995, *ApJ*, 452, 710
- Narayan, R., Yi, I., & Mahadevan, R. 1995, *Nature*, 374, 623
- Nartallo, R., Gear, W. K., Murray, A. G., Robson, E. I., & Hough, J. H. 1998, *MNRAS*, 297, 667
- Nord, M. E., Lazio, T. J. W., Kassim, N. E., Goss, W. M., & Duric, N. 2004, *ApJ*, 601, L51
- Novak, G. et al. 2004, in *Astronomical Structures and Mechanisms Technology*. Edited by J. Zmuidzinas, W. S. Holland & S. Withington. *Proc. SPIE*, 5498, 278–289

- Ohsuga, K., Kato, Y., & Mineshige, S. 2005, *ApJ*, 627, 782
- Özel, F., Psaltis, D., & Narayan, R. 2000, *ApJ*, 541, 234
- Paine, S. 2004, The *am* Atmospheric Model, SMA Memo 152, Smithsonian Astrophysical Observatory, <http://sma-www.harvard.edu>
- Paine, S., Blundell, R., Papa, D. C., Barrett, J. W., & Radford, S. J. E. 2000, *PASP*, 112, 108
- Paine, S. N. 1992, Ph.D. Thesis
- Pancharatnam, S. 1955, *Proc. Indian Acad. Sci.*, A41, 137
- Pen, U.-L., Matzner, C. D., & Wong, S. 2003, *ApJ*, 596, L207
- Pierce-Price, D. et al. 2000, *ApJ*, 545, L121
- Porquet, D., Predehl, P., Aschenbach, B., Grosso, N., Goldwurm, A., Goldoni, P., Warwick, R. S., & Decourchelle, A. 2003, *A&A*, 407, L17
- Quataert, E. 2003, *Astronomische Nachrichten Supplement*, 324, 435
- . 2004, *ApJ*, 613, 322
- Quataert, E. & Gruzinov, A. 2000a, *ApJ*, 545, 842
- . 2000b, *ApJ*, 539, 809
- Rao, R. 1999, PhD thesis, University of Illinois, <http://cfa-www.harvard.edu/~rrao/thesis.ps.gz>
- Reid, M. J. 1993, *ARA&A*, 31, 345
- Reid, M. J. & Brunthaler, A. 2004, *ApJ*, 616, 872
- Roberts, D. H., Wardle, J. F. C., & Brown, L. F. 1994, *ApJ*, 427, 718
- Rogers, A. E. E. et al. 1994, *ApJ*, 434, L59
- Ruszkowski, M. & Begelman, M. C. 2002, *ApJ*, 573, 485
- Sault, R. J., Hamaker, J. P., & Bregman, J. D. 1996, *A&AS*, 117, 149
- Sault, R. J. & Macquart, J.-P. 1999, *ApJ*, 526, L85
- Sault, R. J., Teuben, P. J., & Wright, M. C. H. 1995, in *ASP Conf. Ser. 77: Astronomical Data Analysis Software and Systems IV*, 433

- Schödel, R., Ott, T., Genzel, R., Eckart, A., Mouawad, N., & Alexander, T. 2003, *ApJ*, 596, 1015
- Serabyn, E., Carlstrom, J., Lay, O., Lis, D. C., Hunter, T. R., & Lacy, J. H. 1997, *ApJ*, 490, L77
- Serabyn, E., Carlstrom, J. E., & Scoville, N. Z. 1992, *ApJ*, 401, L87
- Shakura, N. I. & Sunyaev, R. A. 1973, *A&A*, 24, 337
- Shen, Z.-Q., Lo, K. Y., Liang, M.-C., Ho, P. T. P., & Zhao, J.-H. 2005, *Nature*, 438, 62
- Shinnaga, H., Moran, J. M., Young, K. H., & Ho, P. T. P. 2004, *ApJ*, 616, L47
- Springel, V., Di Matteo, T., & Hernquist, L. 2005, *MNRAS*, 361, 776
- Taylor, G. B., Carilli, C. L., & Perley, R. A., eds. 1999, *Synthesis Imaging in Radio Astronomy II* (San Francisco: Astronomical Society of the Pacific)
- Taylor, G. B. & Myers, S. T. 2000, Polarization Angle Calibration Using the VLA Monitoring Program, VLBA Memo 26, National Radio Astronomy Observatory
- Telesco, C. M., Davidson, J. A., & Werner, M. W. 1996, *ApJ*, 456, 541
- Thompson, A. R., Moran, J. M., & Swenson, Jr., G. W. 2001, *Interferometry and Synthesis in Radio Astronomy* (2nd ed.; New York : Wiley)
- Title, A. M. 1975, *Appl. Opt.*, 14, 229
- Tribble, P. C. 1991, *MNRAS*, 250, 726
- Trippe, S. et al. 2006, in *From the Center of the Milky Way to Nearby Low-Luminosity Galactic Nuclei*, ed. R. Schödel et al. (Institute of Physics)
- Tsuboi, M., Miyahara, H., Nomura, R., Kasuga, T., & Miyazaki, A. 2003, *Astronomische Nachrichten Supplement*, 324, 431
- van der Laan, H. 1966, *Nature*, 211, 1131
- Villata, M. et al. 2006, *A&A*, 453, 817
- Walter, F. et al. 2003, *Nature*, 424, 406
- Wardle, J. F. C. & Kronberg, P. P. 1974, *ApJ*, 194, 249

- Wilner, D. 1998, Polarimetry with the SMA: Workshop Summary, SMA Memo 129, Smithsonian Astrophysical Observatory, <http://sma-www.harvard.edu>
- Wright, M. C. H. & Backer, D. C. 1993, *ApJ*, 417, 560
- Yuan, F., Markoff, S., & Falcke, H. 2002, *A&A*, 383, 854
- Yuan, F., Quataert, E., & Narayan, R. 2003, *ApJ*, 598, 301
- . 2004, *ApJ*, 606, 894
- Yuan, F., Shen, Z.-Q., & Huang, L. 2006, *ApJ*, 642, L45
- Yusef-Zadeh, F., Bushouse, H., Dowell, C. D., Wardle, M., Roberts, D., Heinke, C., Bower, G. C., Vila-Vilaró, B., Shapiro, S., Goldwurm, A., & Bélanger, G. 2006, *ApJ*, 644, 198
- Yusef-Zadeh, F. & Morris, M. 1987, *ApJ*, 322, 721
- Zhao, J., Young, K. H., Herrnstein, R. M., Ho, P. T. P., Tsutsumi, T., Lo, K. Y., Goss, W. M., & Bower, G. C. 2003, *ApJ*, 586, L29
- Zhao, J.-H., Bower, G. C., & Goss, W. M. 2001a, *ApJ*, 547, L29
- . 2001b, *ApJ*, 547, L29
- Zhao, J.-H., Herrnstein, R. M., Bower, G. C., Goss, W. M., & Liu, S. M. 2004, *ApJ*, 603, L85
- Zylka, R., Mezger, P. G., & Lesch, H. 1992, *A&A*, 261, 119
- Zylka, R., Mezger, P. G., Ward-Thompson, D., Duschl, W. J., & Lesch, H. 1995, *A&A*, 297, 83